Advanced Turbine Technology

ATTAP

Applications Project

DOE/NASA 0336-2
NASA CR-187039
EDR 14585

0137

1989 Annual Report

Allison
Gas Turbine Division
General Motors Corporation
P.O. Box 420
Indianapolis, Indiana 46206-0420

2 July 1990

Final

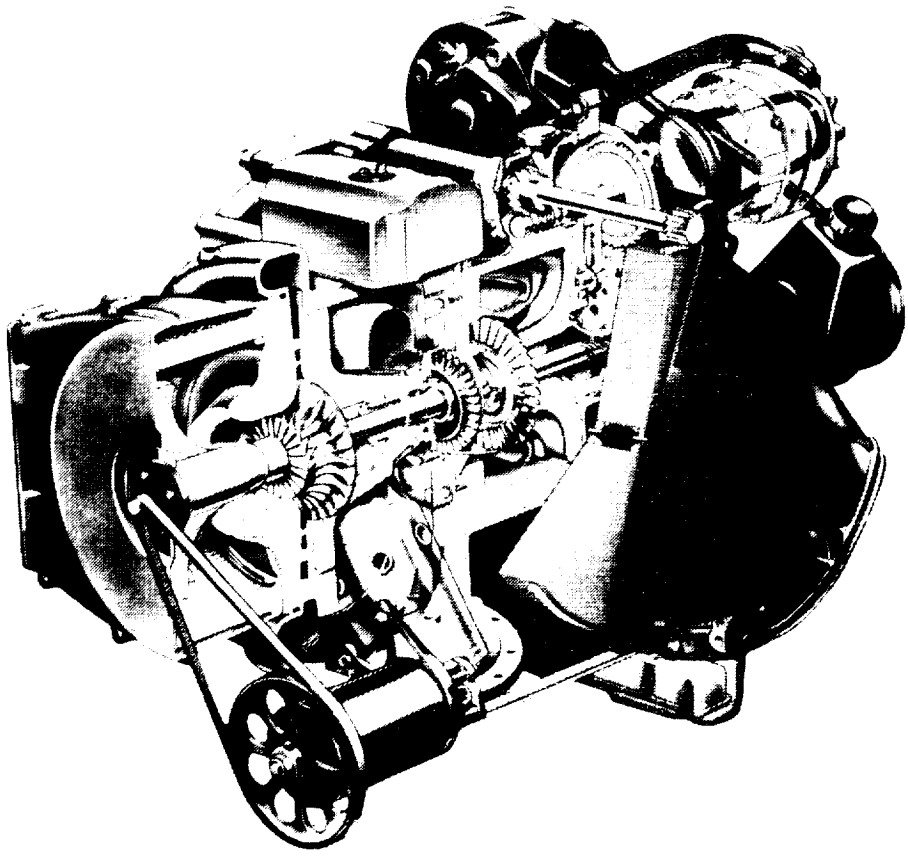

Prepared for
National Aeronautics
and Space Administration
Lewis Research Center
Cleveland, Ohio 44135
Contract DEN 3-336

For U.S. Department of Energy
Conservation and Renewable Energy
Office of Transportation Technologies

NOTICE

DOE/NASA 0336-2
NASA CR-187039
EDR 14585

Advanced Turbine Technology
ATTAP
Applications Project

1989 Annual Report

Allison
Gas Turbine Division
General Motors Corporation
P.O. Box 420
Indianapolis, Indiana 46206-0420

2 July 1990

Final

Prepared for
National Aeronautics
and Space Administration
Lewis Research Center
Cleveland, Ohio 44135
Contract DEN 3-336

For U.S. Department of Energy
Conservation and Renewable Energy
Office of Transportation Technologies

FOREWORD

This report presents a technical summary of work accomplished on the Advanced Turbine Technology Applications Project (ATTAP) under NASA contract DEN3-336 for calendar year 1989. This technology project is funded by the U.S. Department of Energy, Conservation and Renewable Energy, Office of Transportation Technologies, Office of Propulsion Systems, Advanced Propulsion Division. Project management and technical direction are provided by the NASA Lewis Research Center (LeRC), Aeronautics Directorate, Propulsion Systems Division, Terrestrial Propulsion Office.

The overall intent of the ATTAP is to bring the automotive gas turbine engine to a technology state at which industry can make commercialization decisions. Key to this goal is the development and demonstration of structural ceramic component technology as the critical high risk/high payoff element in this type of engine. Such ceramic technology is the prime ATTAP focus. Automotive gas turbine attractions include the following potential advantages:

- significantly increased fuel economy
- ability to meet federal emission standards with untreated exhaust
- ability to operate on a wide range of alternate fuels
- inherently smooth, low-vibration operation

General Motors (GM) is addressing the ATTAP with a team that draws on:

- the extensive ceramic design, analysis, and materials data base and expertise in place at Allison
- the substantial experience, design and test capabilities, automotive gas turbine technology and hardware, and test vehicle resources that were developed under GM funding as background to this project and are in place at GM's Advanced Engineering Staff (AES)
- the infrastructure of expertise and resources in place in the American ceramics industry and the working relationships between the industry and GM
- the unique capabilities and resources existing at universities and at national laboratories, such as the High Temperature Materials Laboratory at the Oak Ridge National Laboratory

In this arrangement, Allison serves as prime contractor. Major ceramic industry development subcontractors to date are: The Carborundum Company; GTE Laboratories Inc; Corning, Inc; Manville Corp; Ceramics Process Systems; and the Garrett Ceramic Components Division of Allied-Signal Aerospace Company.

TABLE OF CONTENTS

LIST OF ILLUSTRATIONS

LIST OF ILLUSTRATIONS (cont)

LIST OF ILLUSTRATIONS (cont)

LIST OF ILLUSTRATIONS (cont)

LIST OF ILLUSTRATIONS (cont)

LIST OF TABLES

SUMMARY

ATTAP activities during the past year were highlighted by test-bed engine design and development activities; ceramic component design; materials and component characterization; ceramic component process development and fabrication; component rig testing; and test-bed engine fabrication and testing. Although substantial technical challenges remain, all areas exhibited progress.

Test-bed engine design and development activity included engine mechanical design, power turbine flow-path design and mechanical layout, and engine system integration aimed at upgrading the AGT-5 from a 1038°C (1900°C) metal engine to a durable 1371°C (2500°F) structural ceramic component test-bed engine. The gearbox redesign was completed to meet the increased power output requirements of the ceramic engine. Associated engine components were modified to incorporate a two-stage, high temperature power turbine assembly. The final general arrangement, resulting from finite element method (FEM) temperature and stress modeling and aerodynamic analysis, represents the best configuration, within the existing confines of the test-bed engine envelope, to optimize engine performance and durability. The detailed aerodynamic designs of the power turbine vanes, rotor blades, and exhaust diffuser were completed. Engine/hot rig control software was modified and developed to limit engine speed and temperature excursions during start-up and shutdown, and an interactive data acquisition system for engine/hot rig durability testing was implemented. New high capacity fuel pumps meeting Reference Powertrain Design (RPD) operating conditions are under development, while candidate starter motors are undergoing evaluation. Combustion system design/development activities include the fabrication of an enhanced stability diffusion flame combustor that, while burning methanol fuel, meets current federal automotive emission standards and eliminates carbon formation. Additional combustor design activities include the layout of a low emissions premixing/prevaporizing combustor system that is being designed to meet the lowest proposed California emission standards while operating on diesel fuel.

ATTAP-defined ceramic and associated ceramic/metal component design activities completed include: the ceramic combustor body, the ceramic gasifier turbine static structure, the ceramic gasifier turbine rotor, the ceramic/metal power turbine static structure, and the ceramic power turbine rotors. A ceramitized standard diffusion flame AGT-5 combustor design was completed and analyzed for both start-up and maximum power operating conditions. Following some minor modifications (addition of swirl vanes, etc), the calculated probability of survival (POS) exceeded goal requirements and the resulting configuration possessed significant flexibility to aerodynamically "tune" the combustor flow field. Design concepts were prepared, FEM models were created, heat transfer and stresses were analyzed, and calculations of the POSs were completed for each ceramic component of the gasifier turbine static structure. Design goal (RPD) POSs were met for each ceramic component and optional materials were identified for individual parts. An acceptable design for the vane platform component was achieved only through use of Si_3N_4 material. The scroll design meets RPD POS goals for both SiC or Si_3N_4. A detailed 3-D FEM analysis was completed for the gasifier turbine vanes; again design tools were met with either SiC or Si_3N_4 materials. Twenty- and fifteen-bladed gasifier turbine rotor designs utilizing SiC and several varieties of Si_3N_4 were analyzed; both 2-D and 3-D FEM techniques were employed in the analysis. Minimum temperature gradients were produced in the 20-bladed gasifier turbine rotors and both the Norton/TRW-154 and Kyocera SN252 Si_3N_4 rotors meet RPD probability design goals. Extensive design permutation of the SiC 20-bladed rotor failed to produce a configuration that could be predicted to survive engine transient operation.

In a similar manner, design concepts were prepared, FEM models were created, heat transfer and stresses were analyzed, and calculations of the POSs were completed for each ceramic and metallic component of the power turbine assembly (static structure and rotors). Design goals were achieved for all ceramic (Si_3N_4) static and rotating components; however, analysis of the metallic static structure components during transient operating conditions revealed localized stress levels above the material yield strengths. These were reduced to acceptable levels by defining a less aggressive rate of acceleration during the transient cycle that will be used on the test stand until ceramic replacement parts are available. Shaft attachment

designs for the two power turbine rotors meet RPD design goals.

The materials and component characterization efforts included the testing and evaluation of several candidate ceramic materials and components being developed for use in the ATTAP. Material characterization activities have focused on microstructural, density, fracture toughness, and flexural strength evaluations of various candidate ceramic materials. Fracture surface analysis was also used to determine the nature and location of the strength-controlling defects. In addition, the time-dependent strength and oxidation resistance characteristics were evaluated for selected materials.

Ceramic component process development and fabrication activities are being conducted for the gasifier turbine rotor, gasifier turbine vanes, gasifier turbine scroll, extruded regenerator disks, and thermal insulation. Major ceramic industry development subcontractors are: The Carborundum Company; GTE Laboratories, Inc; Corning, Inc; Manville Corp; Garrett Ceramic Components Division of Allied-Signal Aerospace Company; and Ceramics Process Systems. Carborundum established process parameters for axial gasifier turbine rotor fabrication and delivered 15 initial hot isostatic pressed (HIPed) SiC rotors. Carborundum's gasifier turbine vane fabrication remains active. Their slip casting development efforts resulted in significant improvements in strength and capability; the scroll fabrication effort (α-SiC slip cast) is continuing. GTE fabricated and delivered PY6 Si_3N_4 gasifier turbine vanes while both AY6 and PY6 Si_3N_4 test bars were fabricated and also delivered. Process parameters were established for axial rotor fabrication through utilization of a specially designed HIPing test matrix experiment; PY6 Si_3N_4 gasifier turbine rotors with 30% SiC whiskers were also fabricated and are undergoing initial inspection. Corning delivered samples of extruded AS and MAS matrix for GM testing to be conducted early in 1990 to determine material characteristics and strength retention. Manville developed both an improved thermal insulation with enhanced radiation blockage using SiC and a surface hardening material and application technique for improved abrasion/erosion resistance. Manville also redesigned the injection mold to improve the insulation mold release. Garrett continues efforts to tailor their pressure slip casting techniques and mold technology to develop and fabricate GN-10 Si_3N_4 gasifier turbine rotors. HIPing parameters were developed for the rotors and statistical process control procedures were evolved to aid in their manufacture. Ceramics Process Systems is fabricating gasifier turbine vane platforms with integrally molded vane pockets. Their Quickset injection molding process is being utilized with CM200 sialon material. Initial moldings have recently been conducted; characterization of the sialon material is continuing.

Component rig testing activities include the development of the necessary test procedures and conduction of rig testing of the ceramic components and assemblies. All ceramic components are rig proof tested prior to engine test-bed installation. Currently, two component rigs, the hot gasifier rig and the regenerator cyclic sample rig, are being utilized. Developmental hot gasifier rig evaluations will continue until domestic ceramic components become available for testing. In the interim a hybrid nozzle assembly has been successfully tested, critical temperature measurements within the hot section have been recorded, and 400 hr of test time have been accumulated with turbine inlet temperatures exceeding 1204°C (2200°F) at 100% design gasifier speed. The rig durability cyclic testing has been automated and 348.6 test hr on a single ceramic rotor have been achieved without failure. A second ceramic rotor was retired in engine-ready condition at 364.9 test hr (330 hr of which were previously accumulated on an engine test-bed). The regenerator test rig is used to evaluate candidate ceramic and metal regenerator matrix samples by exposure to cyclic temperatures. Acceptable simulation of engine full throttle acceleration-deceleration thermal cycles was achieved and several candidate material samples were evaluated. Fe20Cr5Al-Ce catalytic metal alloy was determined to be an unsuitable regenerator material while Haynes 214 nickel base metal alloy shows promise. Hastelloy S and Haynes 230 are also scheduled for evaluation. NGK-Locke MAS was determined to have lost all flexural strength in bars cut from the hot face of the sample while Corning extruded AS matrix samples had adequate cross-corner compressive strength following thermal cyclic testing.

Test-bed engine fabrication, testing, and development supported improvements in ceramic component technology that will permit the achievement of program performance and durability goals. Both long-term cyclic and steady-state engine tests are being performed. Fabrication and test efforts in-

clude installation of a modified gearbox to evaluate vibration effects. Test-bed engine testing activities included shakedown durability testing of the AGT-5 durability test-bed engine; high temperature engine durability verification; and evaluation of ceramic hot flow-path component designs and engine insulation. A test cell dynamometer was automated for unattended durability schedule testing; engine oil flow rate requirements were determined and air filter intake configurations have been developed. The designated durability engine accumulated 359.3 hr of test time, 226.9 of which were on the General Motors gas turbine durability schedule. Tests were also conducted at idle, cruise, and full power conditions.

INTRODUCTION

This is the second of a series of annual reports documenting work performed on the Advanced Turbine Technology Applications Project (ATTAP). This work is being conducted by a team directed by General Motors (GM), with significant activities underway at GM's Allison Gas Turbine Division (which serves as prime contractor), at GM's Advanced Engineering Staff (AES) location at the General Motors Technical Center, and at the several domestic ceramic suppliers who are under development subcontracts. The U.S. Department of Energy sponsors this work, which is managed and technically directed by NASA under contract DEN3-336.

GOAL AND OBJECTIVES

ATTAP is intended to advance the technological readiness of an automotive ceramic gas turbine engine based on efforts begun in the Automotive Gas Turbine (AGT) Project, a DOE/NASA program executed between 1979 and 1987. This AGT project successfully demonstrated the feasibility of structural ceramic hot-section components in automotive-sized gas turbine engines. Specifically, ATTAP aims to develop and demonstrate the technology of structural ceramics that have the potential for competitive automotive engine life cycle cost and for operating for 3500 hr (automotive engine life) in a turbine engine environment at temperatures up to 1371°C (2500°F). Project objectives are the following:

- to enhance the development of analytical tools for ceramic component design using the evolving ceramic properties data base
- to establish improved processes for fabricating advanced ceramic components
- to develop improved procedures for testing ceramic components
- to evaluate ceramic component reliability and durability in an engine environment

PROGRAM SCHEDULE AND CONTENT

Figure 1 shows the scheduled activities in the 61-month program. Materials assessment occurred at the initiation of ATTAP and resulted in the targeting of ceramic component technology goals and the identification of materials, processes, and manufacturers to address those goals. Materials assessment activities are also scheduled during Years 3

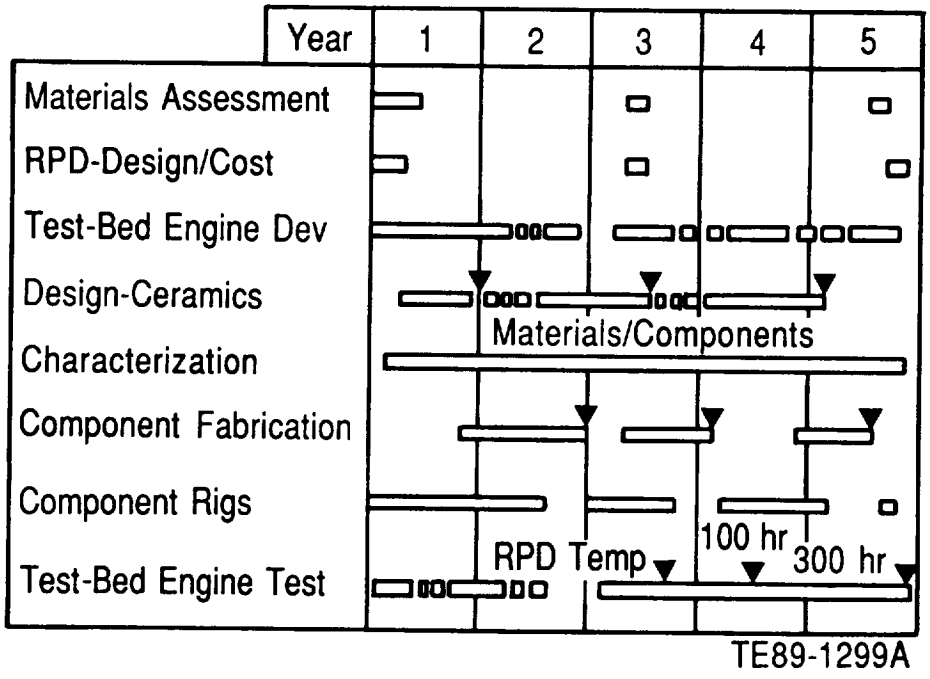

Figure 1. ATTAP schedule.

and 5, at which times the state of the art will be reassessed for each component and required technology improvements will be redefined. The identification and evaluation of materials, processes, and manufacturers are ongoing, continuous activities in ATTAP, and promising candidates are integrated into the program as merited. Similarly, those technologies and/or ceramic component suppliers which do not productively evolve to address program goals are truncated from ATTAP.

Reference Powertrain Design (RPD) activities include the preliminary design of a powertrain system which could meet performance, cost, and reliability design goals. Such a design was executed at the beginning of ATTAP using a high temperature derivative of the AGT-5 automotive gas turbine engine. The RPD is updated in Year 3 to reflect current ceramic component technology and goals, and again in Year 5 to provide a cost estimate of such a powertrain in production.

Test-bed engine development, shown in Figure 1 as an intermittent activity, includes those efforts aimed at ensuring the availability and functionality of the AGT-5 gas turbine engine as the test-bed for the high temperature ceramic components. Although engine development is not a primary focus of ATTAP, these activities recognize the need for continuing evolution of the engine to handle the power and thermal loads, as well as design changes resulting from the integration of a high temperature flow path.

Central to the logic of Allison's ATTAP approach is an iterative component development cycle. Three such cycles are shown in Figure 1 and include the design/fabrication/characterization/rigs/engine test sequences of activities. These three development cycles reflect anticipated improvements in ceramic materials and the associated component processing technologies, and the incorporation of laboratory characterization data and rig/engine test results into succeeding designs. The initial design activity, shown with a milestone at the end of Year 1, features then-current monolithic ceramic technology in the design of the gasifier turbine stage of the AGT-5 engine for 1371°C (2500°F) turbine inlet temperature (TIT) plus other required hot flow-path pieces. The second and third design phases incorporate toughened and advanced (e.g., from Oak Ridge's Ceramic Technology for Advanced Heat Engines [CTAHE] project) materials and processes as they become available, used in the same gasifier stage components. Additionally, these succeeding design phases include other necessary ceramic components in the high-temperature test-bed engine, notably power turbine flow path pieces. Component fabrication includes those process development activities executed by ceramic suppliers that result in the fabrication of engine-usable components. Characterization involves those laboratory activities both at suppliers and at Allison which measure and define the various properties and qualities of ceramic materials in both test bar form and in components. Examples are microstructural evaluation and measurements of density, strength, oxidation resistance, toughness, etc. Included are the development and application of nondestructive evaluation (NDE) techniques.

Component rig activity includes the development of rigs for component verification and testing (e.g., a hot gasifier turbine rig) as well as the actual testing activities. Test-bed engine test includes those testing activities associated with test-bed engine development plus the verification and development testing of the ceramic components. Note that each of the three component development cycles begins with design, followed by component fabrication, characterization, then rig testing, and finally engine testing. This rigorous development process, shown in Figure 2, is iterative between the users and the ceramic supplier community and ensures developing an understanding of the behavior of components in service and the continuous identification of areas for improvement.

TEST-BED ENGINE AND RPD

Figure 3 shows the automotive gas turbine engine being used as the ceramic component development test-bed for ATTAP. This GM-developed engine, the AGT-5, is a two-shaft, regenerative configuration with axial-flow gasifier and power turbines. The engine produces approximately 110 hp at its original full-power TIT of 1038°C (1900°F).

An RPD was completed at the outset of ATTAP in order to ensure that the AGT-5-type power plant has the potential to fulfill the overall fuel economy goals that underlie the DOE's sponsorship of automotive gas turbine technologies. This RPD is a preliminary engineering design of a powertrain system that integrates with vehicle characteristics to provide a system with the potential for meeting not only performance, but also cost and reliability

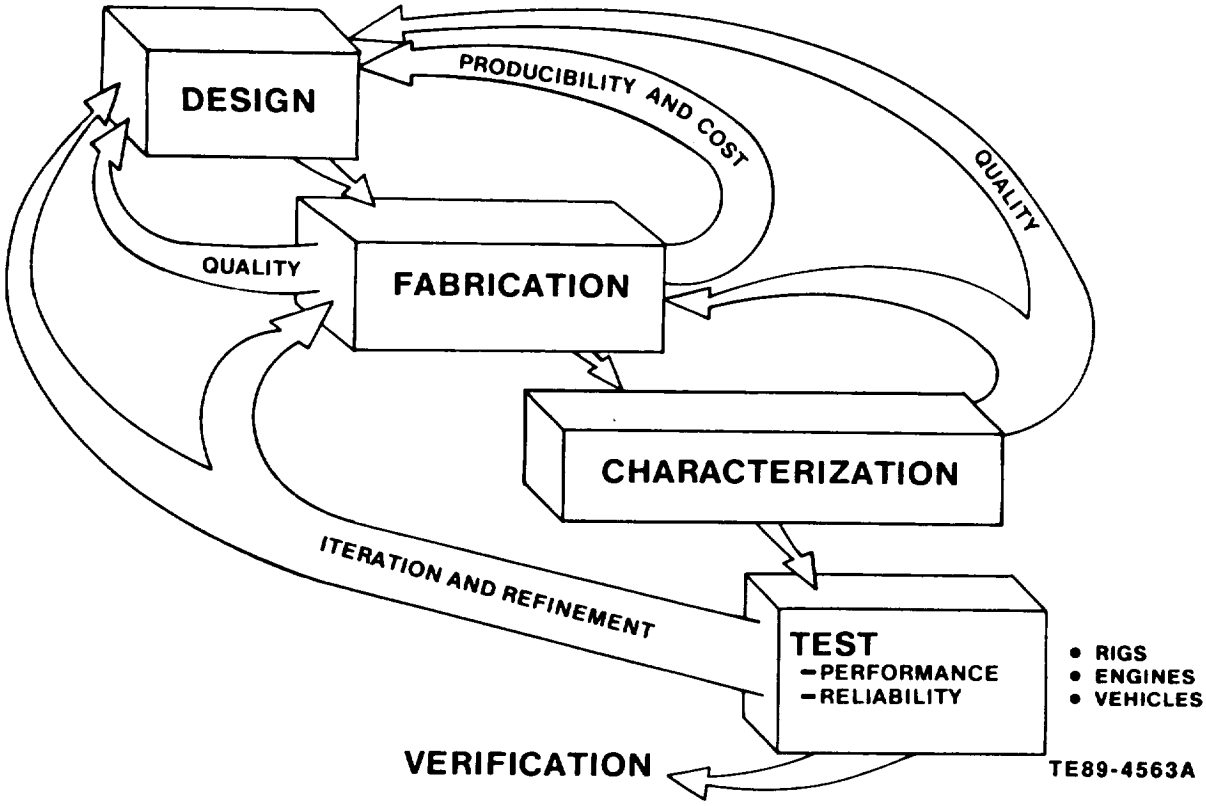

Figure 2. Ceramic component development cycle.

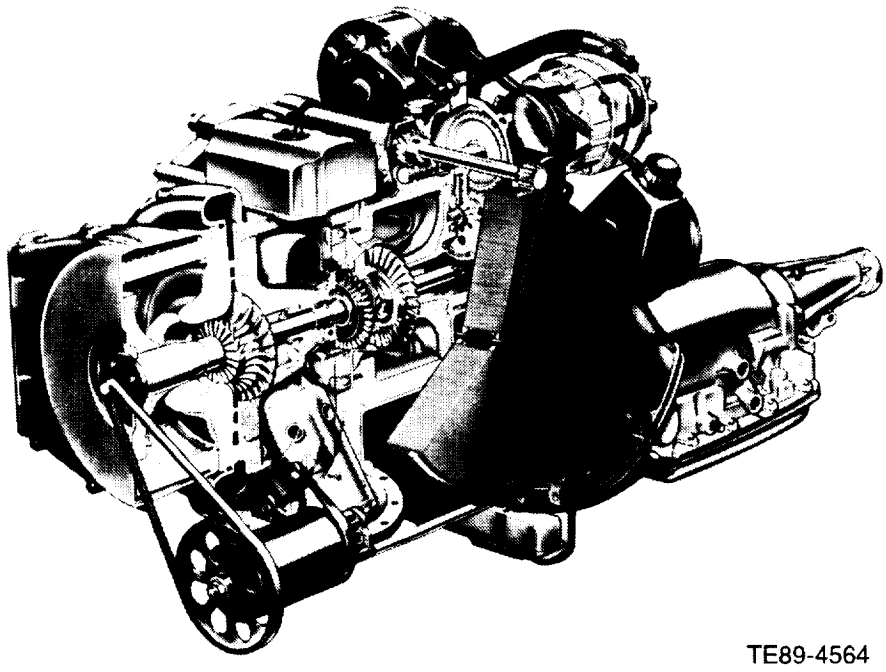

Figure 3. ATTAP test-bed engine--AGT-5 (GM AES).

goals. Specific performance goals are the following:

- 30% improvement in fuel economy over the reference 1988 Pontiac Grand Am equipped with a 2.5ℓ, 4-cylinder, spark-ignition engine over the combined Federal Driving Cycle
- competitive vehicle drivability and performance with the reference 1988 Grand Am
- gaseous emissions and particulate levels less than the following (based on diesel fuel No. 2):

  NO_X = 0.249 gm/km (0.4 gm/mile), HC = 0.255 gm/km (0.41 gm/mile), CO = 2.11 gm/km (3.4 gm/mile), particulates = 0.129 gm/km (0.2 gm/mile)

- ability to use a variety of alternate fuels

Table I shows the results of the RPD performance simulation, based on the AGT-5-type engine, versus the baseline reference vehicle.

Thus the RPD gas turbine equivalent vehicle outperforms the reference piston engine installation in critical fuel economy, performance, and drivability parameters.

The emissions and alternate fuels goals are considered achievable based on demonstrated GM experience. For example, the AGT 100 AGT engine's combustion system has displayed laboratory steady-state emissions of NO_X, CO, and unburned hydrocarbons well within Federal Emissions Standards using diesel fuel, jet fuel, and methanol. The AGT-5 engine has successfully run on dry powered coal. Although such systems have demonstrated the potential for low emission/alternate fuel gas turbine combustion, much work remains to achieve a fully-functional system suitable for automotive application. Such efforts are outside the scope of ATTAP. The definition of power plant cost and reliability goals, in addition to performance, is included in ATTAP.

CRITICAL COMPONENTS

Consistent with the strong ATTAP emphasis on ceramic component technology is the focus on specific gas turbine components as development/demonstration targets. Four ceramic components and the engine insulation have been identified as critical development components because: (1) their functional success is critical to the viability of the ceramic automotive gas turbine engine, and (2) each requires some further technological development to be proven reliable and durable in the automotive engine environment. These critical elements, shown in Figure 4, are the following:

- gasifier turbine rotor
- gasifier turbine vanes
- gasifier turbine scroll
- regenerator disks
- thermal insulation

For each component, specific areas and parameters requiring improvement have been identified and quantified where possible.

Table I.
Comparison of RPD vehicle performance to baseline Grand Am.

	Baseline--2.5ℓ spark-ignition	RPD--turbine
0-96.5 kmph (60 mph) time--sec	13.5	13.1
Top gear gradability at 88.5 kmph (55 mph)--%	7.9	10.9
Composite fuel economy--ℓ/100 km (miles/gal)	7.66 (30.7)	4.87 (48.3)

ORIGINAL PAGE
BLACK AND WHITE PHOTOGRAPH

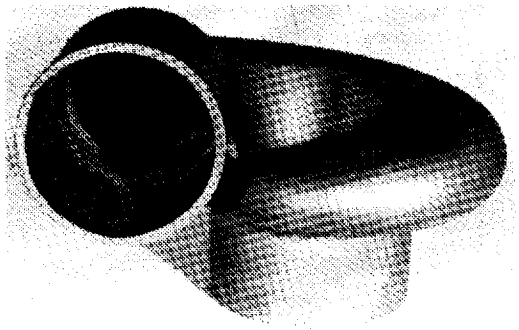

SCROLL

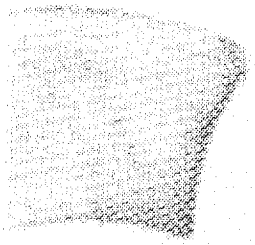

VANE

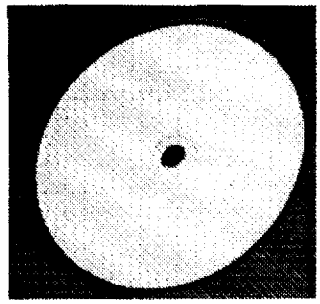

REGENERATOR

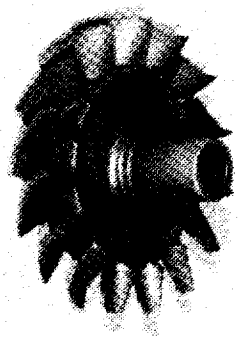

ROTOR

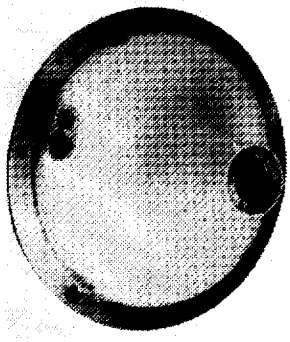

THERMAL INSULATION

TE89-4565A

Figure 4. Ceramic components selected for development.

I. ENGINE/POWERTRAIN DESIGN AND DEVELOPMENT, ANALYSIS, AND MATERIALS ASSESSMENT

1.4 TEST-BED ENGINE DESIGN AND DEVELOPMENT

The overall objective of this task is to perform the required preliminary and detail design activities to ensure that the AGT-5 ATTAP rig(s) and test-bed engine(s) can accept improved ceramic components and operate at the higher temperatures permitted by improved ceramics. Design activities are based on the Reference Powertrain Design (RPD) operating conditions. Specifically, efforts are concentrated in the following four areas:

- mechanical
- combustion systems
- alternate flow paths
- engine system integration

1.4.1 Mechanical

Objective/Approach

The objective of the mechanical design and development activity is to upgrade the AGT-5 from a 1038°C (1900°F) metal engine to a durable 1371°C (2500°F) structural ceramic component test-bed engine. Activity during 1989 primarily focused on gearbox redesign and ceramic power turbine mechanical design.

Accomplishments/Results

Accomplishments for the AGT-5 test-bed engine design and development activity are as follows:

- completed gearbox redesign
- completed ceramic power turbine mechanical design layout

Discussion

Gearbox. The gearbox redesign was directed toward increasing the load carrying capacity of the power turbine speed reduction (16.94:1) pinion/gear and chain system. This redesign was necessary due to the increased power output of the 1371°C (2500°F) engine.

The design layout of the upgraded gear case (Figure 5) retained the pinion/gear and chain approach used successfully on the metal 1038°C (1900°F) engine. New gear and pinion tooth bending and contact stress analyses, as well as Borg Warner Morse Chain Division's evaluation of its Hy-Vo chain design, were incorporated into the final detail design of the gearbox. All detail design drawings were completed and released for part procurement.

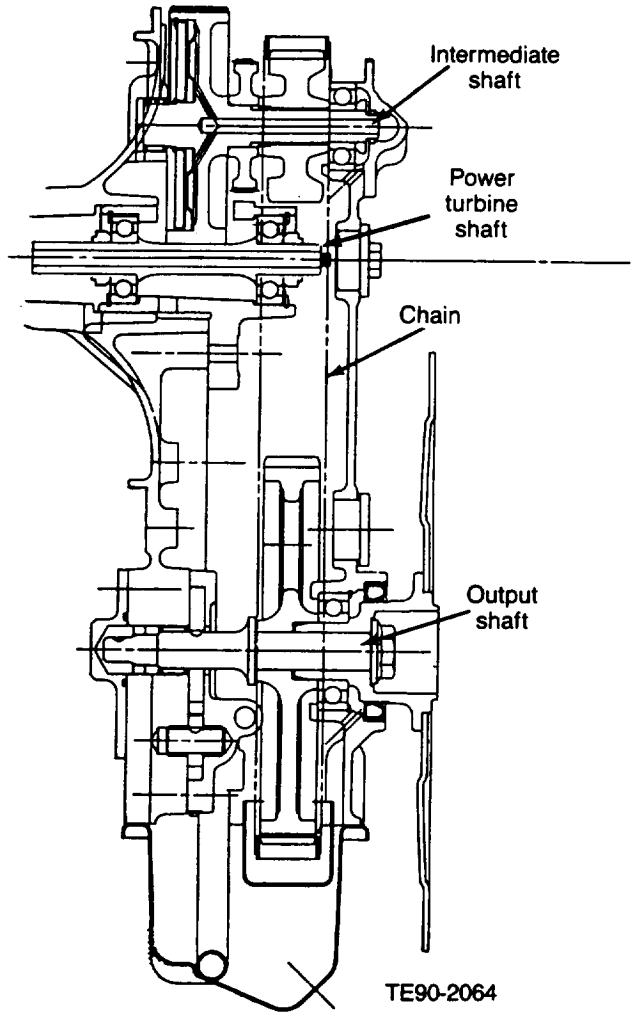

Figure 5. AGT-5 test-bed upgraded gearbox.

Power Turbine Assembly Layout. Incorporation of a two-stage, high temperature ceramic power turbine assembly into the AGT-5 test-bed engine required modification to the associated engine components. The increased trailing edge thickness of ceramic turbine blades (and vanes) requires a decrease in the number of airfoils in each blade row to maintain appropriate blockage levels. This, in turn,

requires a proportional increase in the axial length of each affected blade row to maintain proper aerodynamic parameters. Design modifications were undertaken to account for the required growth in the power turbine assembly's axial length.

The conceptual design of a general arrangement for the two-stage power turbine was initiated and several different configurations were conceived and reviewed. Rotor/shaft attachments (refer to subsection 2.1.5), bearing design/location, and incorporation of the required flow-path aerodynamics within the general confines of the existing AGT-5 engine block were prime concerns in determining the selection of the final arrangement. The redesigned power turbine general arrangement was analyzed using finite element method (FEM) techniques. Particular emphasis was assigned to those critical areas of the engine structure that dictated the design of the final arrangement.

Analysis of power turbine shaft dynamics resulting from bearing relocation and increased overhang of the turbine wheels required the development of a detailed FEM model of the new power turbine rotors/shaft/bearing system. Conclusions of the study indicated that the new configuration had acceptable levels of dynamic movement and, in fact, was dynamically similar to the original system.

FEM models were also used to estimate the heat flow and temperatures in the vanes, rotors, and wheel/shaft attachments. As both the first- and second-stage power turbine vanes will initially be made from metal, two-dimensional axisymmetric models were used to calculate heat transfer, resulting vane temperatures, and stresses to aid in the design and to ensure the survivability of these parts (refer to subsection 2.1.5 for details and results). Similar models were used in analyzing the power turbine rotors to calculate equivalent stresses and to estimate critical parameters such as burst speed. The analysis was conducted for both steady-state and worst-case transient conditions. Cold start to maximum power transient operating conditions are determined by a detailed computerized analysis of the engine test-bed dynamics which occur when the engine is subjected to full throttle operation. This full throttle operation is itself defined so that the vehicle acceleration goals specified by the Reference Powertrain Design are achieved. Results of these calculations and predicted probabilities of survival of the rotors are also presented in subsection 2.1.5. Finally, thermal analysis indicated that additional air cooling may be required at the second-stage wheel/shaft attachment. This can be accommodated by opening the labyrinth seal located between the second-stage vane and rotor wheel. The effects of opening this seal are also discussed in more detail in subsection 2.1.5.

The final ceramic power turbine general arrangement, as presented in Figure 6, incorporates results of both analyses described previously and additional analysis presented in subsection 1.4.3. Within the existing confines of the AGT-5 engine, this configuration represents the best design to optimize engine performance and durability. The design layout drawing has been completed and released for part procurement.

1.4.2 Combustion Systems

Objective/Approach

Combustion system development efforts contain both short- and long-term objectives. The short-term objective entails meeting current Federal automotive emission standards (1.0 gm/mi NO_x, 3.4 gm/mi CO, 0.41 gm/mi HC) while remaining carbon

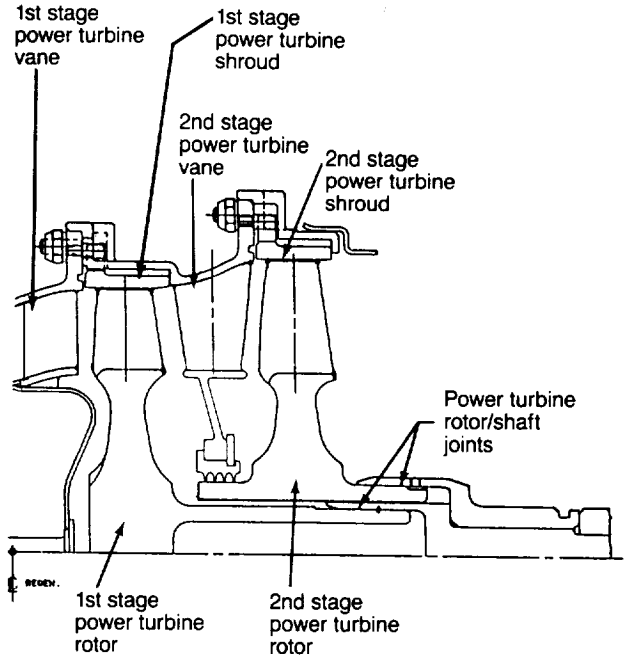

Figure 6. AGT-5 ceramic power turbine general arrangement.

free when burning methanol fuel by making minor changes to the AGT-5 test-bed diffusion flame combustor. The long-term objective is an ultra-low NO_x combustor that will meet the lowest proposed California NO_x standard of 0.2 gm/mi while operating on diesel fuel. A prevaporizing/premixing combustor is required to achieve this goal. Other requirements include fuel flexibility, combustion stability, carbon free operation, cold start capability, driveability, and reliability. An additional long-term objective is the development of an advanced combustion system that has the potential to meet emission goals without the benefit of exhaust gas treatment.

Accomplishments/Results

Accomplishments for the AGT-5 test-bed engine design and development activity are as follows:

- completed design and fabrication of enhanced stability diffusion flame combustor
- completed design of flow path for low emissions prevaporizing/premixing combustor

Discussion

Combustion system development effort during the reporting period was devoted to the design and fabrication of an enhanced stability diffusion flame combustor and to the design of a low emissions prevaporizing/premixing combustor.

Enhanced Stability Diffusion Flame Combustor. The standard AGT-5 test-bed diffusion flame combustor has met the current Federal emissions standards for CO (3.4 gm/mi) and HC (0.41 gm/mi) when burning diesel fuel, and for NO_x (1.0 gm/mi) when burning methanol. However, all three standards have not been met simultaneously. The standard combustor was modified to improve its combustion stability in an effort to reduce CO and HC emissions so that all emissions standards could be met on methanol fuel. Thumbnail louvers in the combustor dome were replaced with an axial swirler and the primary air admission jets were relocated to a plane farther downstream on the combustor body. The revised burner was named the enhanced stability combustor and is depicted in Figure 7.

The modifications are expected to significantly increase the recirculating mass flow rate in the combustor primary zone and to eliminate combustion instability as a potential cause of high CO and HC emissions when burning methanol. Testing of the enhanced stability combustor will differentiate between aerodynamics and atomization as the cause of previously observed increases in CO and HC when the fuel was changed from diesel to methanol. Fabrication of the enhanced stability combustor was completed in December 1989 with testing scheduled to begin in January 1990.

Low Emissions Prevaporizing/Premixing Combustor. A prevaporizing/premixing combustor will be required to meet the lowest proposed automotive NO_x standard of 0.2 gm/mi. Design of the flow path for such a combustor was completed in 1989 and is presented in Figure 8. The flow of air is directed through two concentric paths. The inner path contains the fuel preparation and reaction zones. The outer annular path channels dilution air around the reaction zone for mixing with combustion products just prior to entering the turbine scroll. The airflow split between the parallel flow paths is controlled by a variable geometry mechanism in which rectangular slots open and close as a rotating cover is moved. As combustion airflow is increased, dilution airflow is decreased; total flow area remains constant.

Material for the combustor is ceramic. The inner liner surrounding the reaction zone is uncooled except for external convection driven by dilution air passing around it. Mechanical design and fabrication of the low emissions combustor will take place in 1990.

Since the overall fuel/air ratio varies considerably over the operating envelope of the engine, variable geometry is required to maintain flame temperatures in the reaction zone within the narrow limits that will ensure both low CO and NO_x emissions. Carbon formation is precluded by the lean premixing approach. Emissions from the premixing/prevaporizing combustor were predicted using a perfectly stirred reactor (PSR) chemical kinetic model. Figure 9 indicates the effect of reaction zone temperature on CO and NO_x emissions at idle and rated power. CO is higher at rated power than at idle because of reduced residence time available for burnout. Also, CO reaches a minimum at some intermediate reaction zone temperature. At lower temperatures it increases due to reduced rates of reaction and at

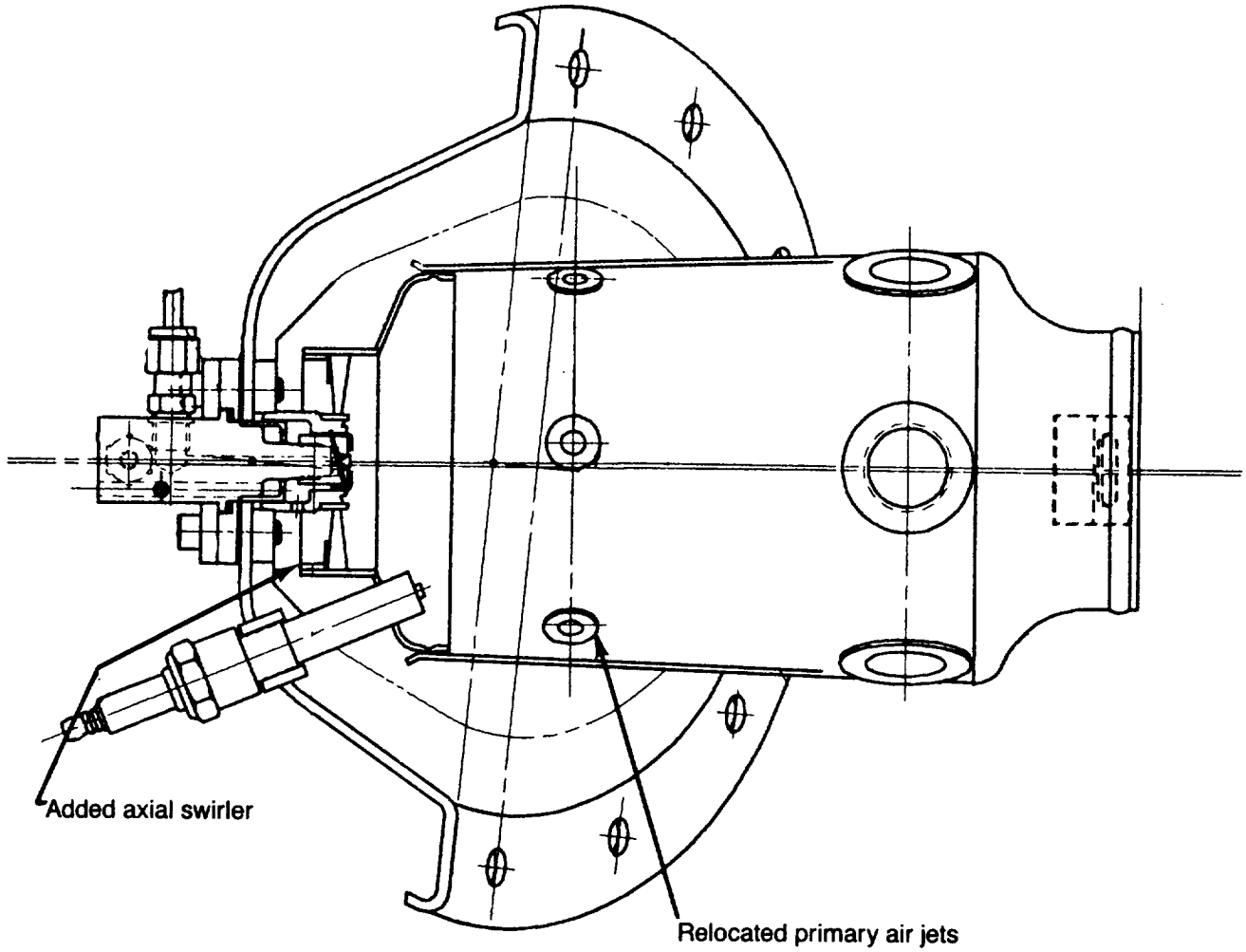

TE90-2075

Figure 7. AGT-5 test-bed enhanced stability diffusion flame combustor.

higher temperatures it also increases and becomes asymptotic with the equilibrium concentration. Assuming that the combustion technology scales to the RPD (i.e., similar flow residence times, etc) CO within an RPD engine combustor is projected to be substantially below current Federal regulations all the way down to reaction zone temperatures approaching the lean combustion stability limit at 1371°C (2500°F). NO_x produced within an RPD engine combustor increases monotonically with temperature, but is projected to be well below Federal or proposed California standards at the planned reaction zone temperature of 1538°C (2800°F). If actual NO_x emissions are higher than predicted, considerable margin exists to reduce reaction zone temperature without exceeding CO limits.

The effects of fuel nitrogen content and reaction zone temperature on NO_x emissions at idle and rated power are presented in Figures 10 and 11. Fuel nitrogen conversion to NO_x was assumed to be 100% and was added to the thermal NO_x predicted by the PSR kinetic code. Fuel nitrogen content results from the addition of cetane improvers to diesel fuel. Neat diesel fuel contains about 40 parts per million by weight (ppmw) of fuel bound nitrogen within its complex mixture of hydrocarbon compounds. However, diesel fuels with high levels of cetane improvers can have fuel bound nitrogen contents as large as 400 ppmw. Figures 10 and 11 indicate a substantial increase of NO_x emissions index with increasing content of cetane improvers. While NO_x emission goals (0.2 gm/mi) within an RPD engine could still be achieved, larger automotive gas turbine engines may be sub-

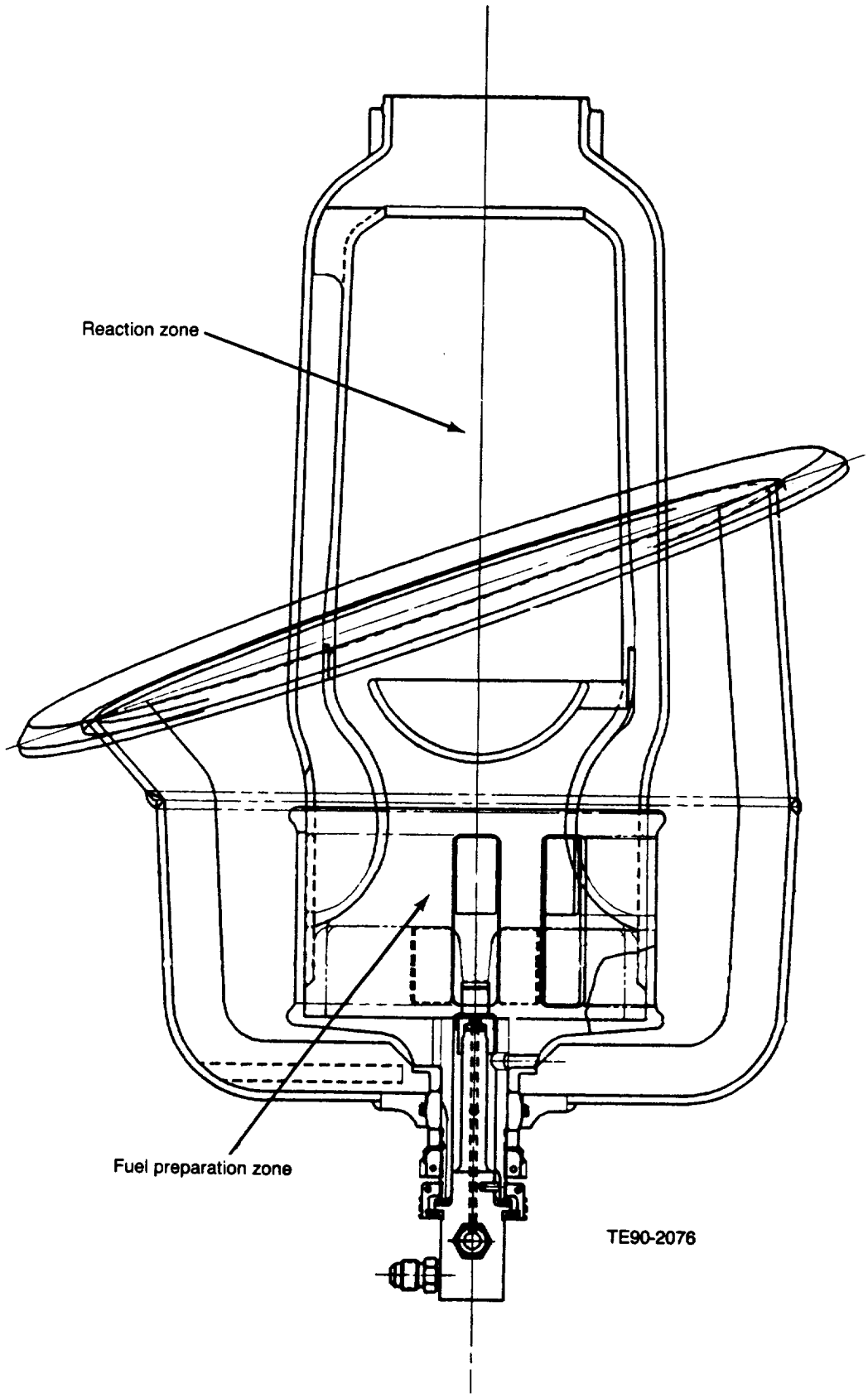

Figure 8. AGT-5 test-bed low emissions prevaporizing/premixing combustor.

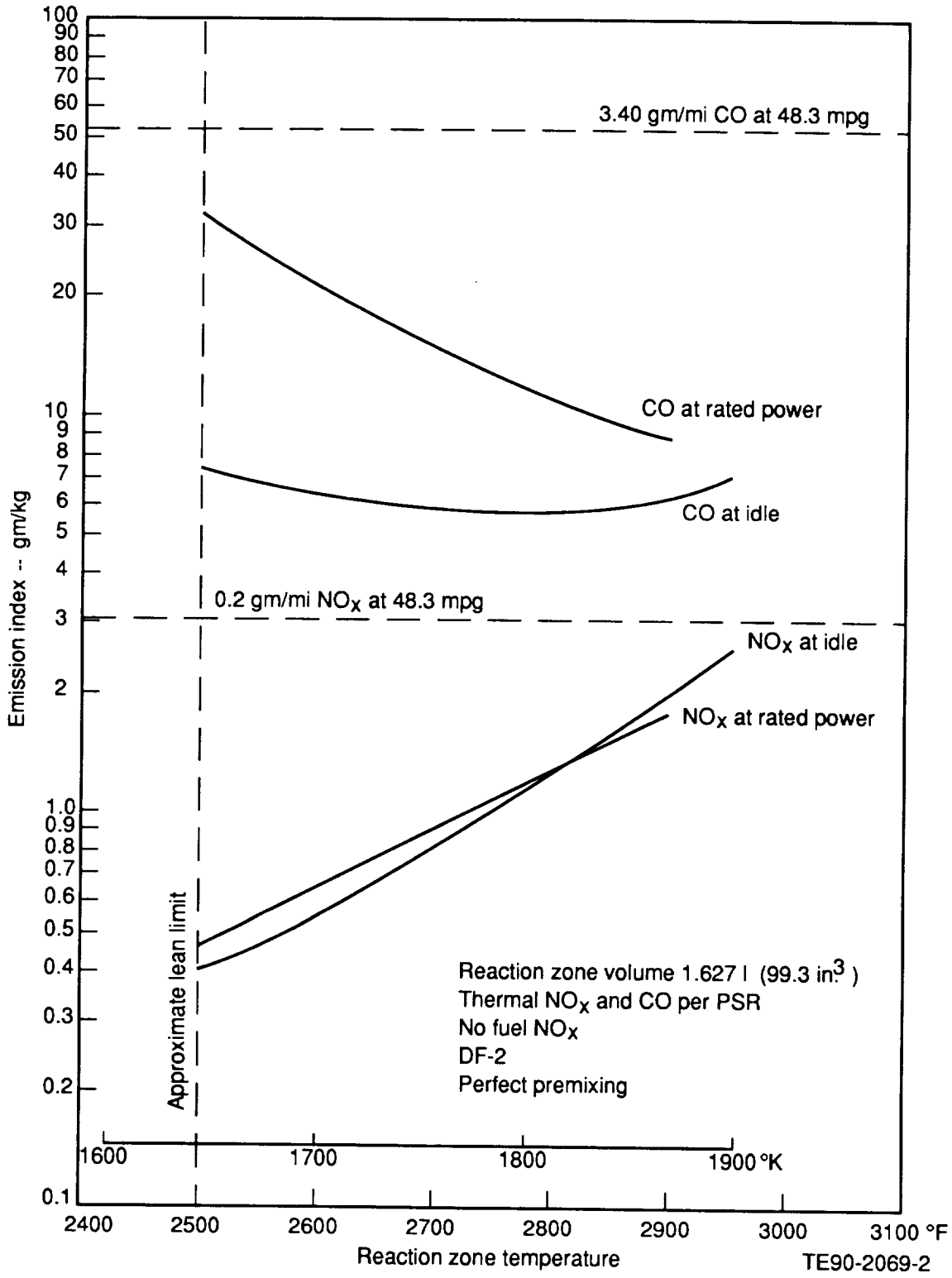

Figure 9. Effects of reaction zone temperature and residence time on CO and NO_x emissions, low emissions combustor.

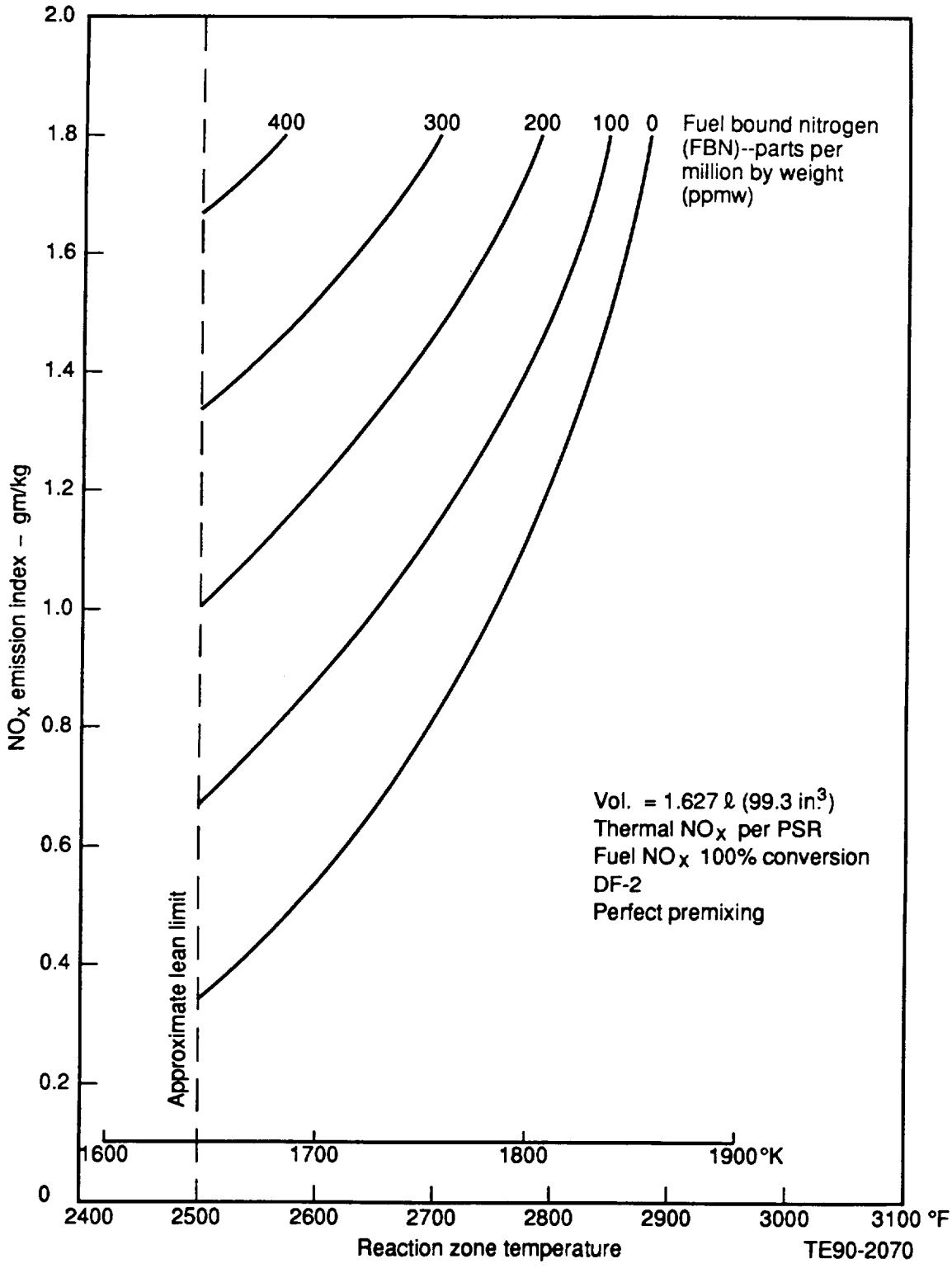

Fuel 10. Effect of fuel nitrogen content on NO_x emissions at idle, low emissions combustor.

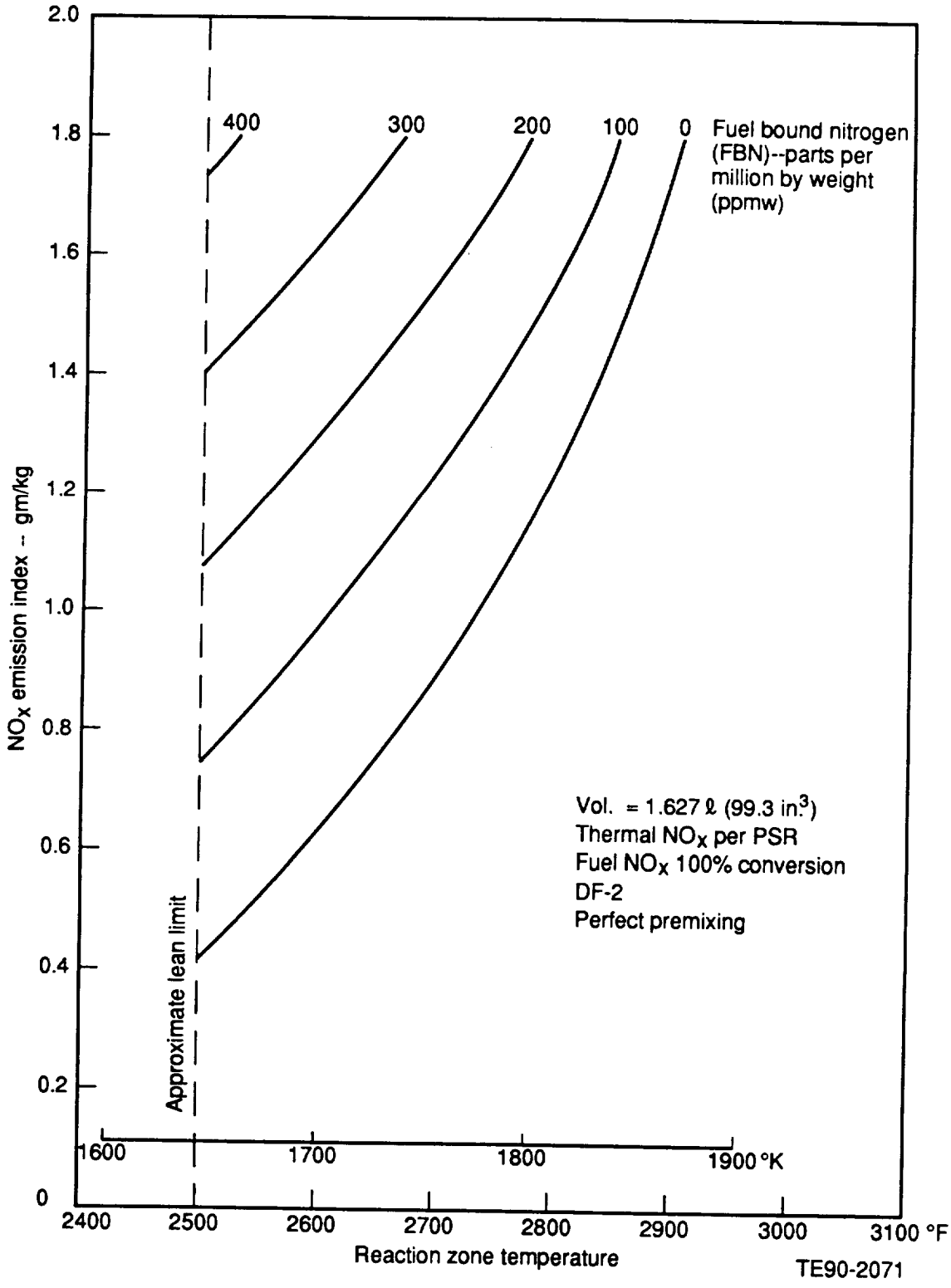

Figure 11. Effect of fuel nitrogen content on NO_x emissions at rated power, low emissions combustor.

jected to more severe duty cycles with a concomitant reduction of fuel economy and, thus, a corresponding increase in NO_x emissions reported on a gm/mi basis. At some point Federal NO_x emission standards from untreated exhaust may not be achievable with high levels of fuel bound nitrogen resulting from the addition of cetane improvers to diesel fuel. As the addition of these cetane improvers represent added fuel cost and are of no benefit to the gas turbine combustion system, it is reasonable to propose that automotive turbines need not and should not use the same (more expensive) pool of diesel fuel presently supplied for diesel engines.

The fuel preparation zone of the premixing-prevaporizing combustor must provide sufficient residence time for vaporization of the fuel and mixing of the fuel and air. Evaporation of diesel fuel was calculated using a code that considers fuel properties, droplet size distribution, convective effects, and droplet heat-up times. The atomizer was assumed to provide a spray with Sauter mean diameter (SMD) of 30 microns and a Rosin-Rammler distribution parameter of 2.5. The calculated results predict the mass fraction evaporated as a function of steady-state, acceleration, deceleration, and hot start conditions as related to the Reference Powertrain Design goals. Evaporation is predicted to be 100% for all deceleration conditions and nearly 100% for all steady-state conditions. During an acceleration most of the air is routed through the fuel preparation zone resulting in reduced residence times and fuel evaporation is only 70-90% complete. Under these conditions some droplets will escape into the reaction zone and NO_x emissions can be expected to be greater than that predicted in Figure 9. While the variable geometry could be adjusted to increase residence time, this would be at the expense of increasing the reaction zone temperature. The test program will identify the optimum position for minimizing NO_x emissions during an acceleration. Evaporation during a hot start is predicted to exceed 90% and will not adversely affect the ability to achieve ignition and to accelerate the gasifier. Because of very low ambient temperatures, evaporation rates of complex fuels, such as DF-2, are extremely difficult to analytically predict during a cold start. Precise droplet chemical composition, constituent distillation dynamics, and low temperature chemical kinetics must be computed in detail. To date, no adequate model exists to precisely predict cold start conditions. A rigorous analytical/experimental program to minimize cold start emissions may be required.

Although residence time in the fuel preparation zone is beneficial for evaporation and mixing, excessive residence time within this region will result in autoignition of the fuel. This must be avoided as it can cause increased NO_x emissions and possible damage to the combustor. The autoignition characteristics of diesel fuel, as determined from the data of References 1 and 2*, were used to optimally size the fuel preparation zone in order to provide the maximum possible residence time available for fuel/air mixing and fuel evaporation while simultaneously minimizing the risk of fuel droplet or fuel/air vapor autoignition. Operating conditions for the low emissions combustor representing steady-state, acceleration, and deceleration operation were examined. All operating points were predicted to lie within a region of autoignition nonoccurrence except that of the deceleration from the maximum power point. The fuel preparation zone was intentionally sized to be close to this autoignition boundary because this condition maximized the residence time available for evaporation and mixing. If autoignition is found to occur at this one condition, it can be eliminated by adjusting the variable geometry control to slightly reduce residence time.

Flame stabilization in the low emissions combustor is accomplished via a bluff body stabilizer. Premixed fuel and air flow around this dome shaped obstruction, which separates the fuel preparation and reaction zones. Hot combustion products recirculate behind this bluff body and continuously ignite the incoming fresh mixture. For any given bluff body geometry and set of flow conditions (pressure, temperature, and velocity), there exists a weak extinction equivalence ratio below which the flame will blow out. (Equivalence ratio is defined as the actual fuel/air ratio divided by the stoichiometric fuel/air ratio.) One of the major design requirements of the combustion system is that blowout should not occur over the operating range of the engine. Weak extinction equivalence ratios for the low emissions combustor were calculated using the methods of Reference 3 for starting, steady-state, acceleration, and deceleration operating conditions. Based on this

*References are at the end of this section.

analysis, blowout is not expected to occur in the low emissions combustor.

1.4.3 Alternate Flow Paths

Objective/Approach

Turbine aerodynamic development efforts are required to upgrade the power turbine of the existing 1038°C (1900°F) metal AGT-5 test-bed to meet the requirements of the 1371°C (2500°F) RPD operating conditions. Activities during 1989 focused on the aerodynamic definition of the power turbine flow path including design of the nozzle vanes, rotor airfoils, and exhaust diffuser.

Accomplishments/Results

Activities and accomplishments during 1989 were as follows:

- completed detailed analysis of absolute and relative velocities (velocity triangle) of the power turbine assembly
- completed power turbine first- and second-stage nozzle (vane) airfoil designs
- completed power turbine first- and second-stage rotor blade airfoil designs, meeting the surface velocity criteria and having both acceptable hub stresses and reasonable tooling formabilities of the airfoil shapes
- completed nozzle and rotor detailed drawings, which were released and sent to vendors

Discussion

Velocity Triangle Analysis of Power Turbine Assembly/Airfoil Design. Detailed velocity triangle calculations were initiated for the various configurations described in subsection 1.4.1. Two candidate configurations were analyzed in some detail. As indicated in subsection 1.4.1 various constraints dictated the general layout of the power turbine assembly. The envelope in which the power turbine flow path had to fit was dictated by the existing engine. The gasifier turbine hub and tip diameter, as well as the gasifier exit flow conditions, were already established. Further, the exit hub diameter of the power turbine second stage rotor was essentially restricted by its bearing location and bearing housing insulation thickness. The axial location of this same rotor was also restricted by the power turbine diffuser design requirements and exhaust cavity casting. Other existing engine test-bed constraints and design simplicity determined the rotor tip diameters of both power turbine stages.

The trailing edge diameter for both power turbine rotors was set through past experience with the gasifier rotor to a value that will provide adequate impact strength; the trailing edge requirement was the determining factor in the reduction of rotor blade number and rotor axial chord length. Preliminary calculations based on a guideline mean section blockage indicated each rotor should have approximately 27 blades.

An initial flow path was designed that used contoured outer and inner walls for both the first- and second-stage nozzles (Figure 12). Radial equilibrium flow calculations were performed using Allison's turbine design program 0S069. The total pressure loss profiles used in the calculations were obtained from those measured in an Allison helicopter power turbine (T800-LHT-800). The mass average total pressure loss for each component was scaled to match earlier predicted losses. The power turbine has to meet two major criteria: minimal exit swirl at design speed and a 110% overspeed stress capability resulting from wide-open throttle up-shifts. Since the second-stage rotor is the highest stress component in the power turbine design, it dictated the selection of the design speed at 57,000 rpm (with an overspeed of 62,700 rpm). Initial calculations for the blade root predicted an acceptable overspeed stress while the design speed exit swirl was 7 deg. Based on these acceptable values a detailed preliminary aerodynamic design was completed.

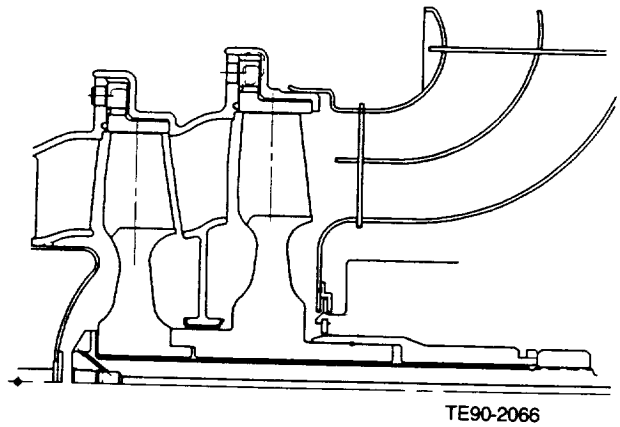

Figure 12. AGT-5 test-bed ceramic power turbine assembly--preliminary design.

This initial design was reviewed and several revisions were made (Figure 6). The flow acceleration on the outer wall of the first-stage nozzle was increased by changing the wall contours and vane design. These changes to the initial design (which had originally produced a 21% increase in velocity) increased the nozzle velocity another 9 percentage points. The contoured hub of the second-stage nozzle was replaced with a cylindrical hub, resulting in a slight increase in flow acceleration in the second-stage nozzle. The hub radius of the first-stage rotor was slightly raised and the hub of the second-stage rotor was slightly lowered to match the second-stage nozzle hub. As a result of the increases in nozzle flow acceleration, the rotor reaction levels were decreased by approximately one-third.

Nozzle velocity ratios and the resulting rotor reaction for the preliminary and final designs are presented in Figure 13. The decreased rotor hub reaction (indicating the potential for increased blade losses, i.e., production of adverse pressure gradients, etc) was an initial concern but rotor hub airfoil sections were redesigned to minimize this problem. The power turbine assembly speed remained at 57,000 rpm.

The total-to-static pressure isentropic efficiency calculated for the final power turbine assembly design is 0.75. The mean line exit swirl remains at 7 deg.

Tooling Formability of Power Turbine Airfoil Shapes. The nozzle airfoil vanes, initially to be made of metal, are to be constructed using conventional casting techniques. One of the major design criteria was to provide a smooth contoured outer wall between rotors. Airfoil sections were created and the surface velocities checked at both the design point and typical power point conditions. The first-stage vane has 20 airfoils and the second-stage vane has 27 airfoils.

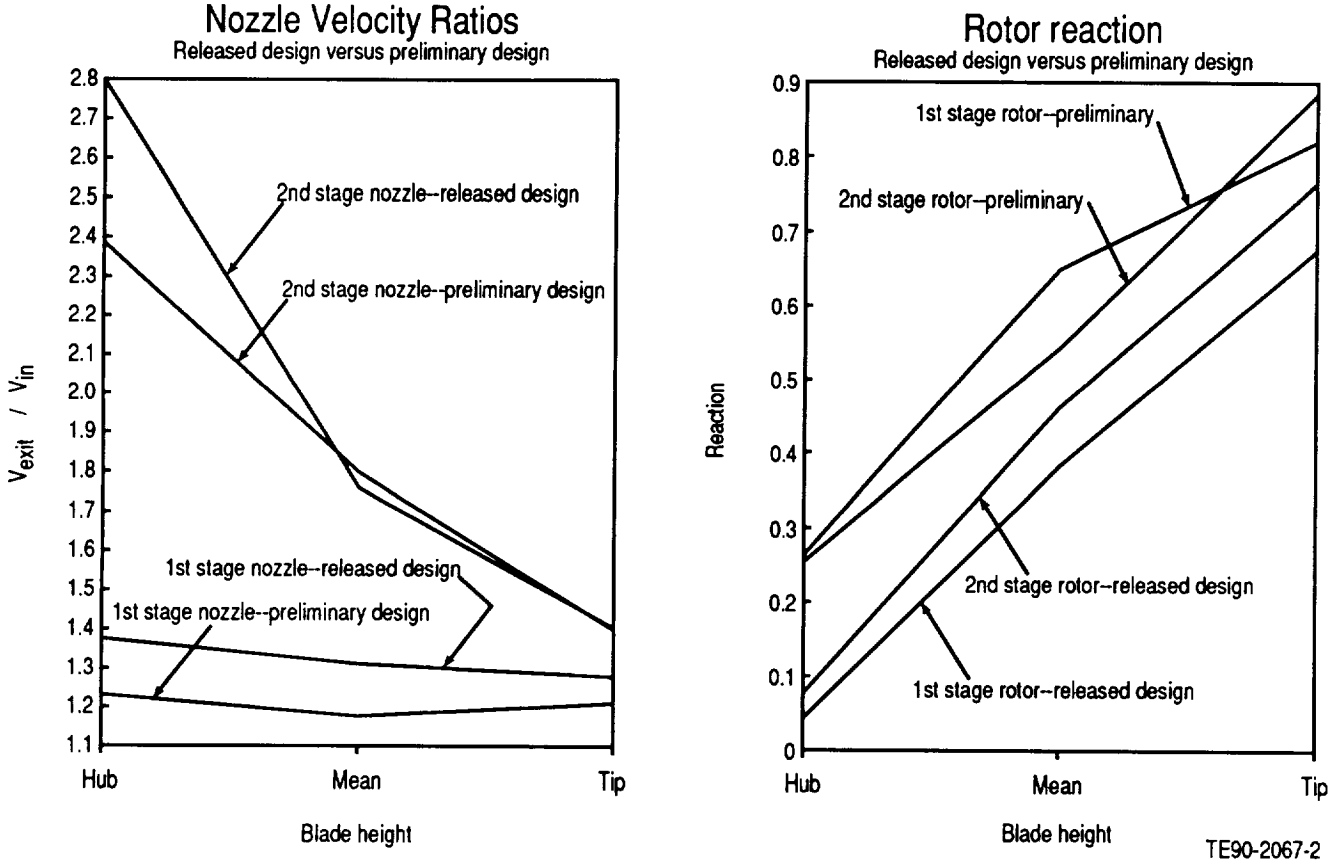

Figure 13. Nozzle velocity ratios and resulting rotor reaction for the preliminary and released design.

The rotor airfoil design was created using an iterative scheme that optimized aerodynamic shape and blade spacing formability. The airfoil surface velocities were calculated and a 3-D shape model created for each rotor. The tool path pullability was checked by viewing the 3-D model down the trailing edge of the airfoil. As an example, the first-stage rotor tool path view is illustrated in Figure 14. Creation of an airfoil with a pullable blade spacing requires the tangential chord of the hub section to be slightly increased while the tip section tangential chord is slightly decreased. The result is a hub section with a blade angle slightly greater than that desired from a pure aerodynamic design point. Conversely, the tip section has a blade angle slightly less than aerodynamically desirable. However, the overall airfoil efficiency is only slightly affected. The first-stage rotor now has 28 blades and the second-stage rotor has 26 blades.

1.4.4 Engine System Integration

Object/Approach

Development efforts on automatic control systems, fuel pumps, and starter motors are required to integrate ceramic components and 1371°C (2500°F) temperature capabilities into the AGT-5 rig(s) and test-bed engine(s). Activity during 1989 focused on modification and development of engine control software, development of an interactive data acquisition system for durability engine testing, design and initial procurement of a new generation of engine control system, and development of a high capacity fuel pump and automotive starter motor for the AGT-5 test-bed engine operating at RPD conditions.

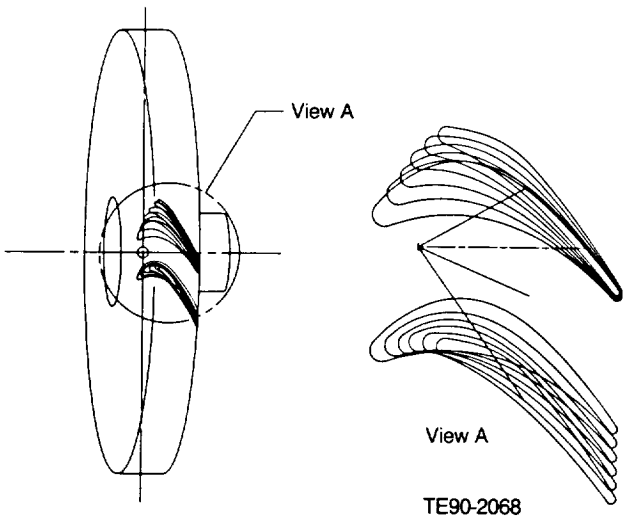

Figure 14. View of first-stage power turbine rotor tool path--blade space pullability.

Accomplishments/Results

Activities and accomplishments relating to engine system integration efforts during 1989 were:

- modification of software algorithms controlling rig/engine test-bed gasifier speed and temperature limits, start fuel delivery rates, fuel flow limits, and shutdown monitoring
- development of new software for the hot rig durability cycle test controller with interactive data acquisition system computer command of engine speeds
- modification of software algorithms controlling combustor fuel nozzle air assist dropout characteristics and development of new software for the hot rig motor-driven fuel pump controller
- design and initial procurement of the next generation of engine control system
- assembly, test, and calibration of various spur gear driven fuel pumps with motors supplied by two candidate sources (test results to date indicate continuing problems that have not been fully resolved)
- modification, installation, and initial testing of a Gerator type fuel pump as an alternative system
- evaluation and selection of candidate automotive starter motors for the test-bed engine (subsequent development work is under way)

Discussion

Software Modification/Control System Development. The integration of ceramic components and 1371°C (2500°F) temperature capabilities into the AGT-5 rig(s) and test-bed engines introduces new, unique requirements in rig/engine hardware, operation, and attendant data acquisition/control systems. The control system(s) have been and are being modified and updated to meet these new demands. Modifications are first bench tested, if necessary, before being installed in a rig or test-bed. Reliability and maintainability of the controllers have also been a prime consideration in control system requirements and development.

In response to the changing test requirements software algorithms controlling rig/engine test-bed gasifier speed and temperature limits, start fuel delivery rates, lower and upper fuel flow limits, and shutdown monitoring are undergoing modifications and revisions on an as required basis.

New software for the hot rig durability cycle test controllers permits the rig to follow a preprogrammed, operator free schedule of gasifier speed variation with time. The software permits schedule flexibility as required. The control concept was developed and implemented with interactive automated data acquisition system computer command of the engine schedule.

The present engine combustion system relies on high pressure air assist within the combustor fuel nozzle to aid fuel atomization and to enhance subsequent fuel ignition and flame stabilization. Loss of this high pressure air assist can adversely affect the engine start sequence. The control algorithm during start was modified to supply high pressure air assist via an auxiliary electric air pump, which is powered until the engine driven air pump attains sufficient speed to provide the nozzle assist air. Additionally, all of the rig(s) and test-bed(s) now use electric motor driven fuel pumps in which controllers deliver the fuel rate proportional to fuel pump shaft speed. Provision for changing calibration tables in the control software permits the use of a variety of fuel pumps.

Finally, the function control module (FCM) controllers currently in use are aging and will eventually become unreliable, especially as many of the controller components are either no longer available or are in rapidly diminishing supply. Consequently, a new generation of engine controller, the EDM-800, is under test and development. Replacement of the FCMs on a scheduled basis will begin early in the 1990 model year. The EDM-800 controller is faster than the FCM type and can handle far more complex control algorithms and input/output signals. It is also a smaller, more reliable unit and uses printed circuit boards for input/output (I/O) instead of wire-wrap.

Fuel Pump System. Development work during 1989 concentrated on a fuel pump/motor system that possessed a sufficient turn-down ratio to meet both the extremes of idle and maximum acceleration fuel flow rates. The speed/torque characteristics of motors from two different suppliers were evaluated using a control system which duplicated that of the engine electronic controller. The superior of the two motors was then mated to a fixed displacement spur gear pump, which had been sized to deliver the required maximum flow at the motor's highest speed. The pump/motor package, together with a speed feedback device, was evaluated at all operating speeds and flows. Difficulty was encountered at the low speed (idle flow) conditions in the form of "cogging" or start-stop rotation of the pump/motor. Attention has been focused on the low-speed frictional characteristics of the pump as well as the mechanical alignment of the pump and motor. Work is still progressing at this time, but full resolution of the problem has not yet been attained.

Because of the recurring problems with the spur-gear pump/motor system, the evaluation of an alternate pump design package that uses Gerator-type pumping elements was undertaken. Characterization of this pump/motor system is just beginning. In addition to determining its flow as a function of pressure, the system will also be evaluated for its low end torque requirements.

Starter Motors. An automotive starter motor was installed on a test-bed engine and successfully accelerated the gasifier during the start sequence. Although high current levels were experienced during the start sequence, the starter motor successfully performed 1380 engine starts without incident. Reliability dictates, however, that the current level should be reduced to more acceptable levels. Simply dropping supply voltage was unacceptable because the lower voltage was not compatible with that required for the engine controllers. Use of a lower power starter kept controller voltages at an acceptable level but resulted in excessive start times. The solution appears to be the use of a different starter motor with a power output appropriately selected between the two previously tested starters. Additionally, a different pulley ratio will be used with the new starter motor to optimize engine speed start-up acceleration. Parts manufacturing is presently in progress.

REFERENCES

1. Tacina, R. R., "Autoignition in a Premixing-Prevaporizing Fuel Duct Using Three Different Fuel Injection Systems at Inlet Air Temperatures to 1250°K," NASA TM-82938, May 1983.
2. TeVelde, J. A. and Spadaccini, L. J., "Autoignition Characteristics of No. 2 Diesel Fuel," NASA CR-165315, June 1981.
3. LeFebvre, A. H., *Gas Turbine Combustion*, Hemisphere Publishing Corporation, New York, 1983, pp 199-200.

II. CERAMIC COMPONENT DESIGN

2.1 DESIGN ACTIVITIES

The AGT-5 ATTAP test-bed engine is a two shaft regenerative engine designed to operate at Reference Powertrain Design (RPD) operating conditions, specifically at 1371°C (2500°F) turbine inlet temperature. Engine operation at this TIT requires heat resistant structural ceramic materials in the engine hot section. The overall objective of the ceramic component design activity is to create designs of the AGT-5 ceramic components that permit successful operation of the engine at the RPD operating conditions.

Specifically, the objectives of this activity are to do the following:

- complete designs of the *defined* ATTAP ceramic development components; turbine components include the gasifier scroll, gasifier vane(s) and vane platform, gasifier vane retaining ring, and the gasifier rotor
- complete designs of *associated* ceramic and metal components necessary to permit evaluation of the ATTAP development ceramic components in rig and engine environments at RPD operating conditions; included are the combustor body (ceramic) and associated components, two power turbine rotors (ceramic) and shafts, two power turbine rotor blade tip shrouds (ceramic), and the two power turbine nozzle assemblies and associated components
- prepare and present design reviews of selected components
- incorporate into the ceramic design activity "simultaneous engineering" which integrates component performance and reliability and related design activities, and component vendor fabrication technology development, to enhance the successful manufacture of cost-effective components

The overall approach utilized to design the ATTAP/AGT-5 test-bed ceramic components includes the following steps:

- establish operating condition(s) and reliability goals for ceramic engine components
- prepare conceptual designs of components
- complete detailed linear elastic, fast fracture probabilistic design analysis based on: certified material characteristics, i.e., two parameter characteristic strength and Weibull parameters generated from test bar fracture data; design reliability goals established from engine system reliability goals; and component failure probability analysis using finite element modeling and Weibull characterization of material strength
- iterate design configuration, materials, and operating requirements to achieve satisfactory preliminary component design
- iterate component design details with ceramic manufacturer(s) to correlate component requirements with processing capabilities
- finalize design layout and detail drawings

After progressing through further steps of the development cycle, as shown in Figure 2, the design function reviews component performance, cost, and reliability results and updates or modifies component designs as appropriate, to achieve overall design goals.

In addition to those ceramic components identified as requiring considerable development under ATTAP (i.e., the gasifier turbine assembly, regenerator disks, and engine insulation) the engine assembly also includes a ceramic combustor assembly and selected ceramic power turbine components (rotors). The gasifier turbine static structure, shown in Figure 15, consists of a scroll that guides the gas flow from the combustor to the turbine vane (nozzle) row. This row consists of loosely mounted vanes that act to accelerate the flow to rotor inlet conditions; a retaining ring surrounds the scroll outer shroud and covers slots within this shroud through which the vanes are inserted into the gas path. A vane platform forms the inner gas path boundary and positions the hub end of the vanes within machined pockets contained within this structure. The gasifier turbine rotor completes the gasifier turbine assembly. The gasifier turbine static structure is mounted to the engine structure by a combination insulating/locating subassembly, which inhibits heat flow from the gas path into the engine structure. Cross key features are utilized to accurately locate the static structure relative to the rotor blade tips while allowing free movement between ceramic and metallic components as unequal thermal expansion occurs.

The power turbine vane assemblies are attached to the engine housing by a bolted flange which main-

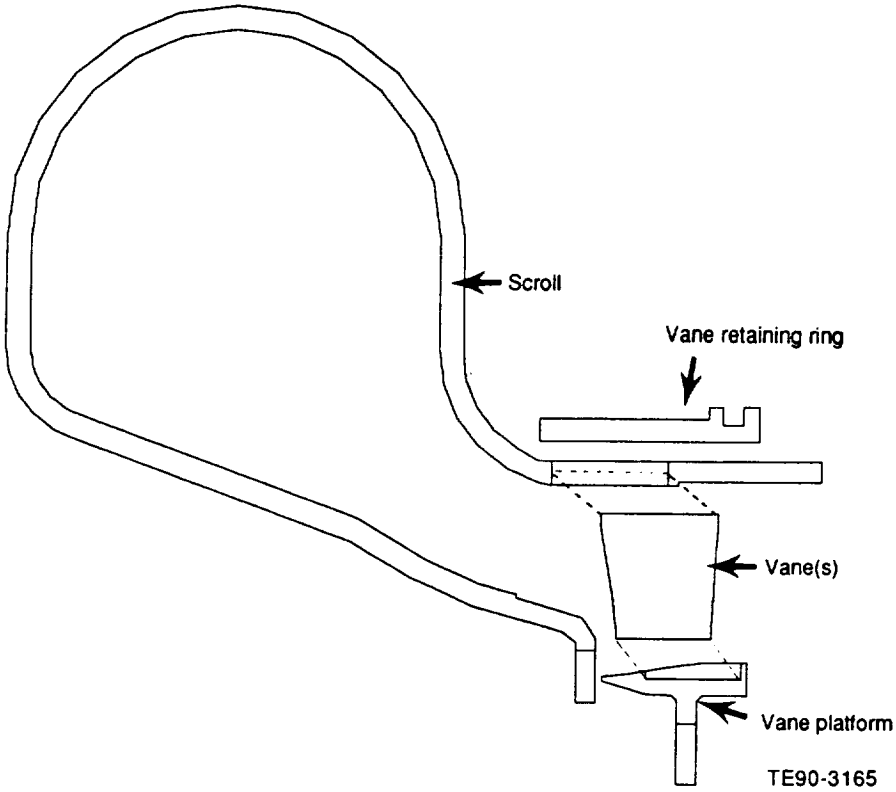

Figure 15. Gasifier turbine static structure.

tains concentricity between the vane assemblies and the power turbine rotors. The ceramic rotor tip shrouds are radially located in the vane assemblies by cross keys. The power turbine rotors are individually attached to metal shaft segments, which are in turn bolted together to form the turbine rotor assembly.

Overall engine design requirements impacting ceramic (and metal) turbine and combustor design are as follows:

- duty cycle, 100,000 miles life of which 55,000 miles operate on an urban cycle and the remainder (45,000 miles) is considered highway operation
  - 3,500 hr life
  - 12,000 starts
  - 33,600 low cycle fatigue (LCF) cycles
- gasifier turbine inlet temperature 1371°C (2500°F)
- rotor containment at maximum burst speeds
- meet automotive environmental, maneuver, and attitude requirements
- reliability goals to have less than 0.25 major engine system failures in 100,000 miles

Detailed design and analyses of the turbine assemblies and the combustor are described in the following subsections. Further, the probability of survival (POS) design goal for each ceramic engine component is based on the number of failure sites for that component in relation to the total number of failure sites in the complete engine assembly. The POS design goal for each ceramic component is also listed in those subsections describing that component.

2.1.1 Combustor

Objective/Approach

This activity focused on designing static structural ceramic components for the combustor that meet performance, mechanical strength and POS, and dimensional criteria for operating in the AGT-5 hot gasifier rig(s) and test-bed engine(s) at RPD conditions. Efforts included the construction of 2-D models to calculate component temperatures, stress profiles, and the resulting probabilities of survival. Extended operation at 1371°C (2500°F) exceeds the design capability of the metal (cooled) combustor assembly presently being used in the AGT-5 test-

bed engine. Successful operation of a ceramic combustor assembly in the AGT program formed the basis for choosing ceramics as a combustor body material.

Activity during 1989 focused on modification of the combustor to closely duplicate the existing metal combustor aerodynamic and mechanical design while substituting ceramic material for the combustor body and dome. The combustor outlet configuration was revised to permit assembly into the ceramic gasifier turbine scroll.

Accomplishments/Results

- The preliminary combustor design was completed and analyzed at maximum power and defined transient operating conditions; following several design iterations the ceramic combustor body POS exceeded goal requirements while the temperature of the metal attachment hardware was calculated to be acceptable.
- The combustor design was subsequently modified to address structural recommendations from the ceramic vendor as well as changing aerothermodynamic design considerations; the result was a less complex ceramic combustor body configuration possessing significant flexibility to "tune" the combustor flow field aerodynamically.

Discussion

The initial ceramic combustor assembly configuration, depicted in finite element model form, is shown in Figure 16. The one-piece ceramic body and dome incorporate six primary and six dilution air holes in the cylindrical portion of the body and eleven angled air swirler slots in the dome. There is an additional round hole in the dome (not shown) through which the igniter plug passes. The metal attachment that locates the dome (inlet) end of the combustor body consists of four semi-flexible fingers, which extend from the fuel nozzle holder to the lip on the dome.

Initial design calculations indicated excessively high temperatures in the metal combustor attachment components. Two combustor body design modifications were studied as a means to reduce the body temperature at the point of attachment and, consequently, the temperature of the metal attachment components. Isotherm plots of the combustor body temperatures at the maximum power operating condition for the three design configurations are presented in Figure 17. The body temperature at the attachment point in configuration numbers 2 and 3 was reduced as the length of the body was extended away from the combustion zone (combustor number two) and cooling air holes were added in the body extension (combustor number three). The calculated probability of survival at maximum power for each configuration exceeds the design goal of 0.9752 as noted in Figure 17. Calculations also revealed that application of a 0.020 to 0.040 in. thick thermal barrier coating to the surface of the metal attachment (finger) in contact with the ceramic dome would reduce the temperature of the metal component to an acceptable level. Therefore, the shorter body configuration (number 1), as shown in Figure 17, was chosen in combination with the thermal barrier coating on the metal attachment.

Heat transfer and stress analyses, combined with calculations of POS, were completed for combustor configuration number 1 simulating operation at both maximum power steady state and transient start-up conditions. The minimum calculated POS, 0.99936, occurred during the transient cycle (about 40 sec after start); this POS is greater than the design goal of 0.9752. Temperatures and principal stresses occurring at maximum power operation and at 40 sec

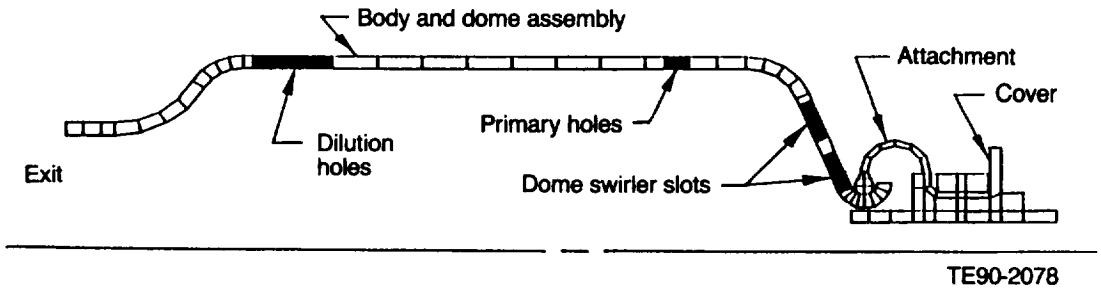

Figure 16. Cross section of ceramic combustor assembly.

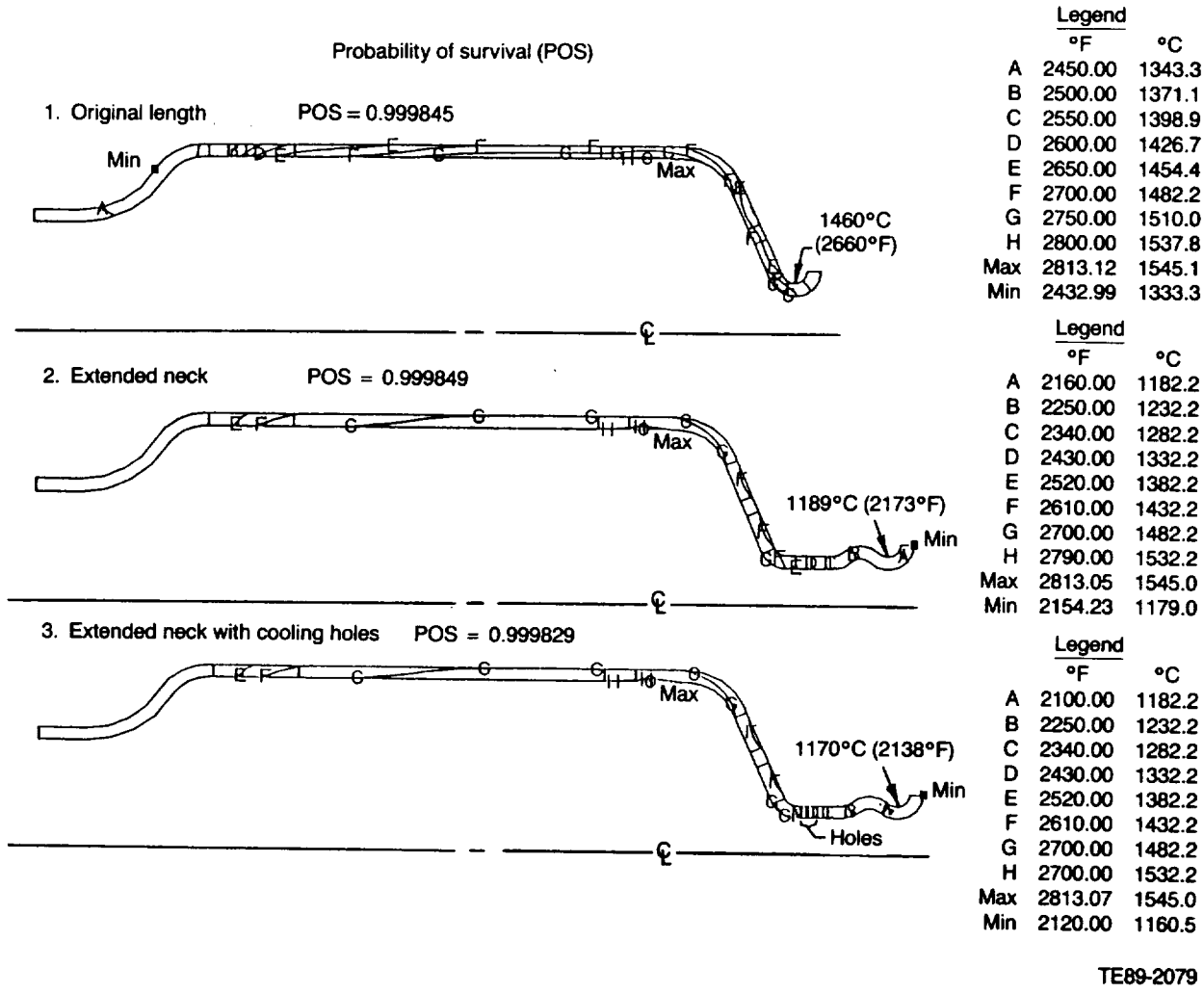

Figure 17. Isotherm plots for three ceramic combustor configurations at steady-state, maximum power 1371°C (2500°F) operating conditions.

into the start-up transient are presented, respectively, in Figures 18 and 19. The maximum calculated stress within the ceramic combustor body is less than 20 ksi (Figure 19) while the maximum calculated material temperature in the body is about 1538°C (2800°F) at maximum power (Figure 18). SiC is the material of choice for this operating temperature.

Reservations concerning both the aerodynamic performance and fabricability of angled slots in the ceramic combustor dome led to a further redesign. The resulting configuration incorporates a metal vaned swirler assembly surrounding the fuel nozzle, thus eliminating the slots in the ceramic dome. This redesign, as depicted in Figure 20, greatly simplifies the fabrication of the ceramic combustor body/dome component and provides a relatively simple means of "fine tuning" the airflow characteristics of the combustor if required.

2.1.2 Gasifier Turbine Static Structure

Objective/Approach

The objective of this activity is to design ceramic components in the gasifier turbine static structure that operate satisfactorily at ATTAP RPD turbine inlet temperature (1371°C, [2500°F]) conditions and achieve assigned probability of survival (POS) criteria. Design concepts are prepared, FEM models created, heat transfer and stress modes analyzed, and calculations of POS completed for each ceramic component of the gasifier turbine static structure.

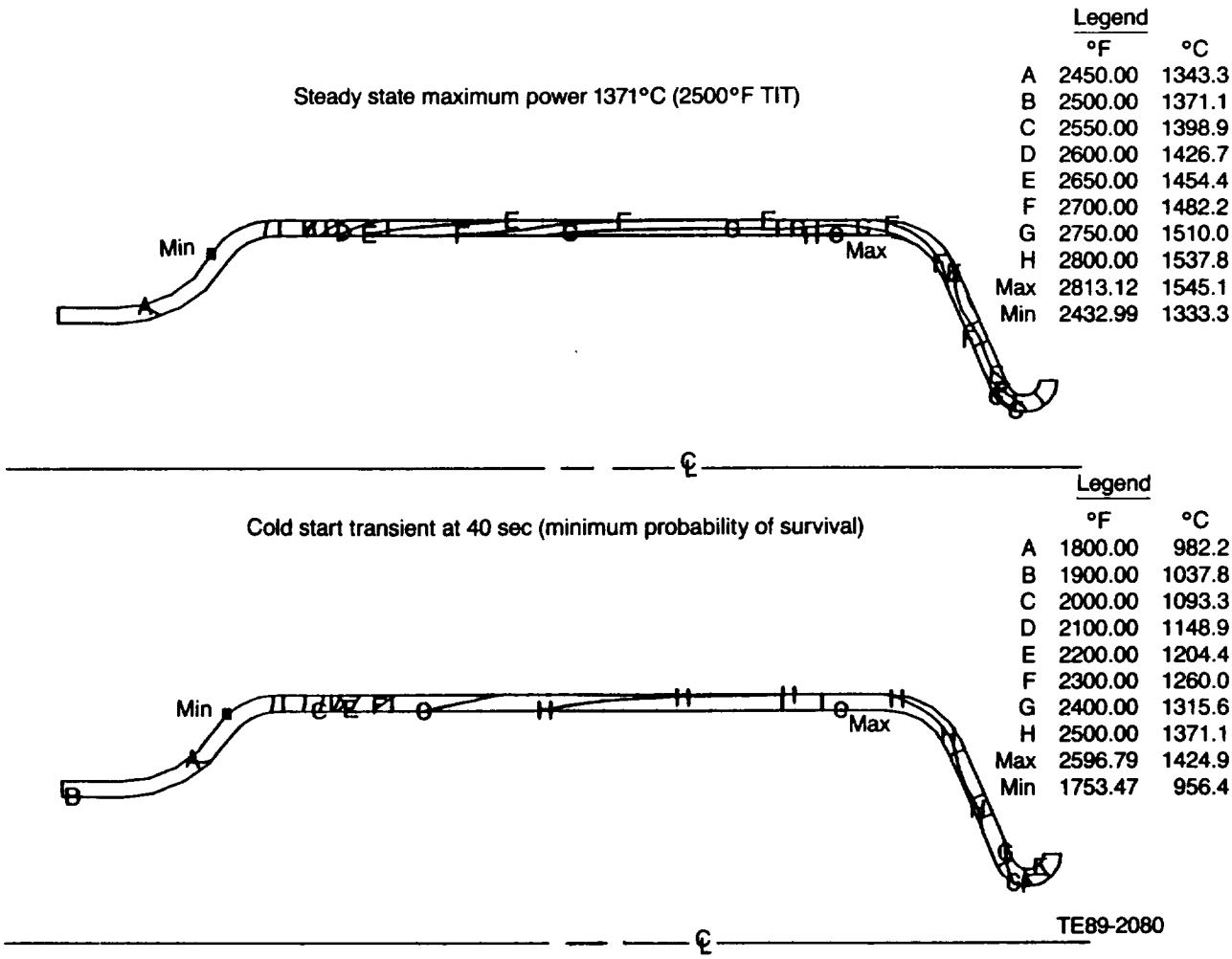

Figure 18. Ceramic combustor temperature distributions.

Accomplishments/Results

- Detail designs have been completed for each component of the gasifier turbine static structure.
- Two-dimensional FEM heat transfer and stress analyses have been completed for each static structure component.
- Design goal POS has been met for each ceramic component; optional materials have been identified for most components.
- An expanded analysis was completed on the vane platform component because α-SiC was found to have a deficient POS; two Si_3N_4 materials (SN251 and PY6) were predicted to be viable candidate materials for this component due to their increased strengths.
- Norton NC430 SiC material was evaluated as a potential scroll material; with a configuration change, NC-430 material was analytically determined to be able to meet design goals.
- A detailed 3-D FEM analysis was completed for the loosely fitted gasifier turbine vane permitting a more accurate prediction of the POS by utilizing real vane shape and flow conditions appropriate to either side of the vane; design goals can be met with either SiC or Si_3N_4 materials.

Discussion

Alpha SiC Scroll. An FEM transient heat transfer analysis was completed for the scroll assembly fabricated from alpha SiC material. The temperatures were used to calculate stresses and resulting Weibull POS for each of the parts in the assembly. The configuration was determined to yield satis-

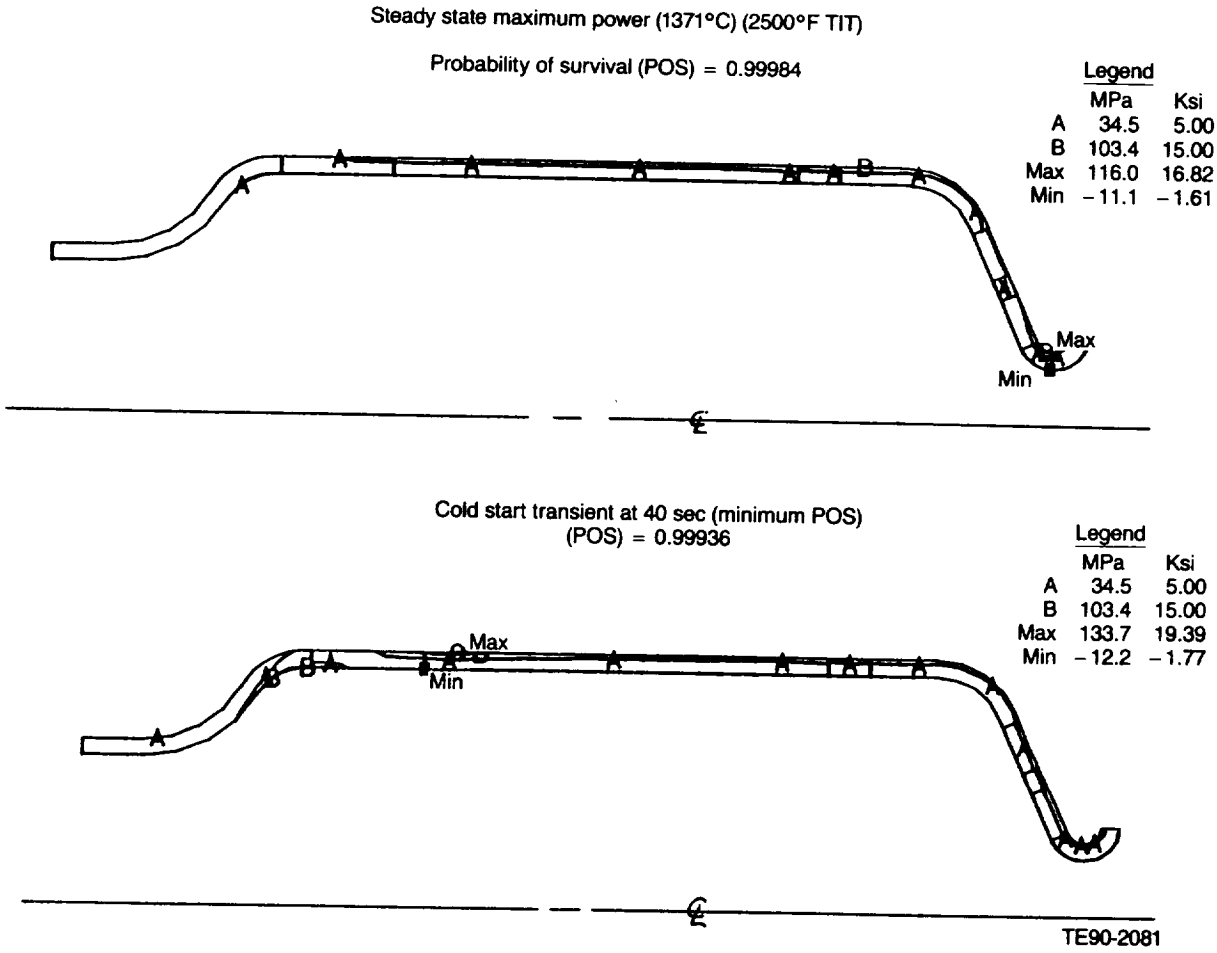

Figure 19. Ceramic combustor maximum principal stress.

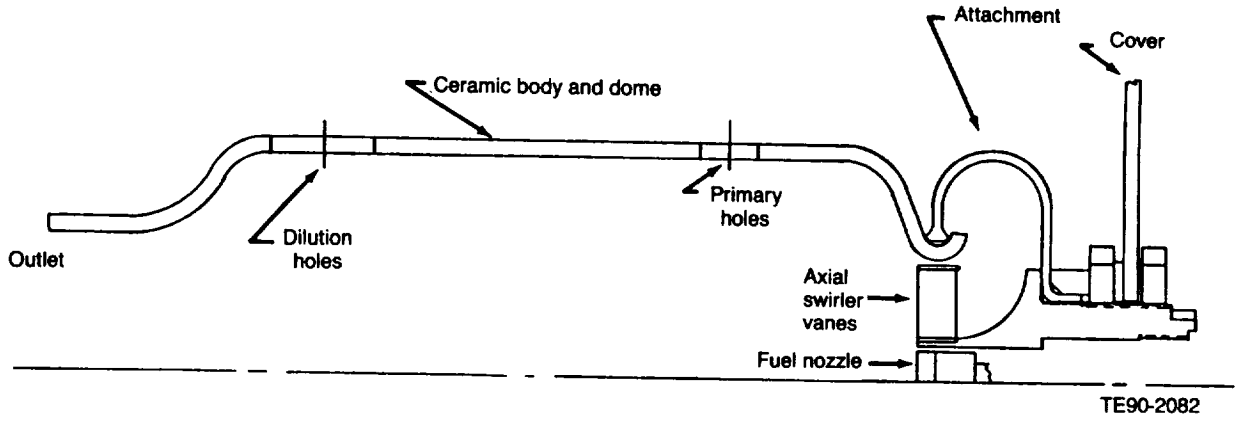

Figure 20. Combustor assembly with simplified ceramic body/dome and metal swirler vanes.

factory POS for the following: the scroll body, vane, and vane retaining ring. However, the vane platform did not meet the probability of survival criteria when made from alpha SiC material; an acceptable design was achieved by substituting GTE's PY6 Si_3N_4 as the vane platform material. Temperature plots are presented for the structural ceramic parts in Figure 21. Corresponding maximum principal stresses for these same parts are depicted in Figure 22. The probability of survival summary

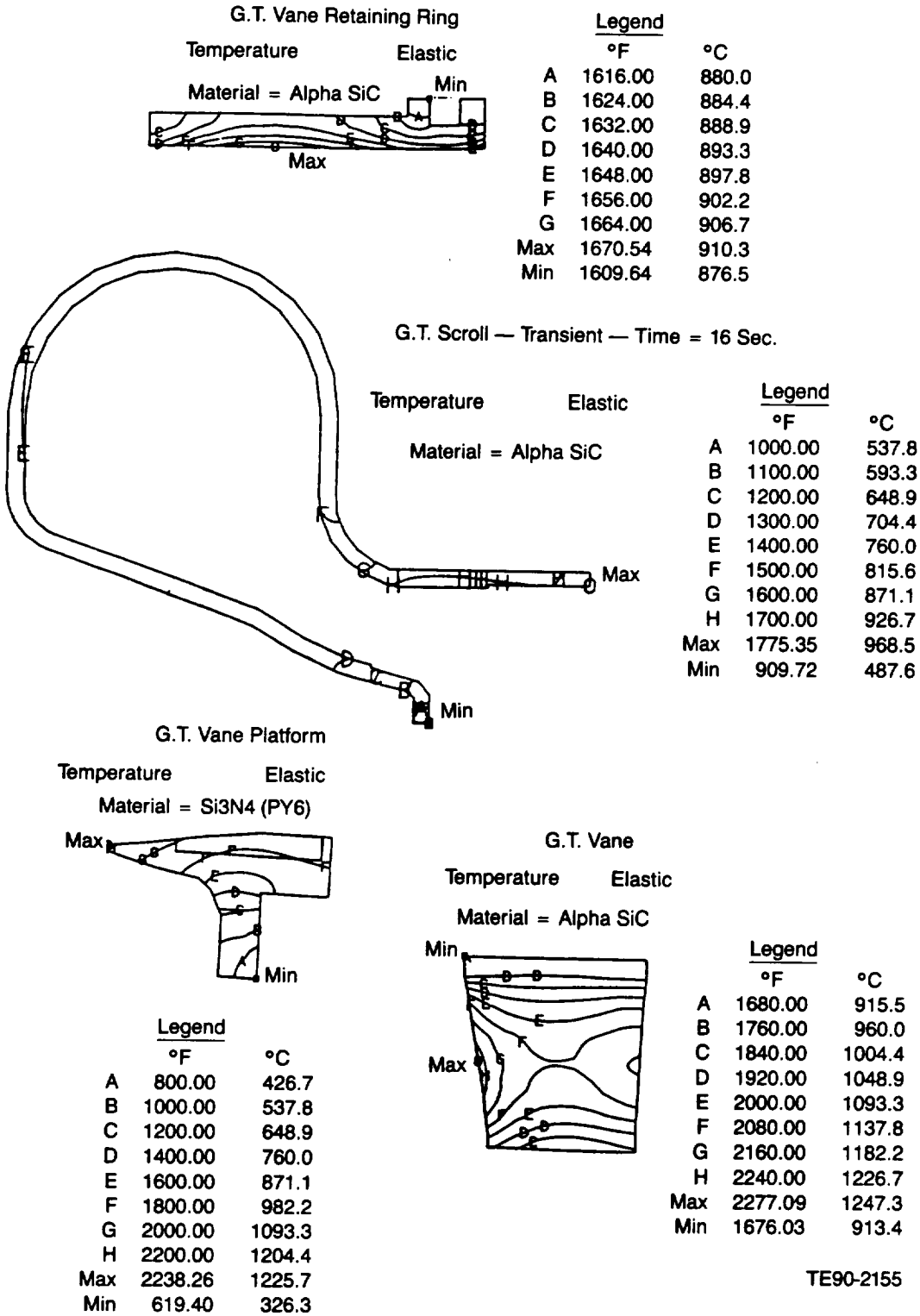

Figure 21. Scroll assembly temperature distributions (worst case transient condition).

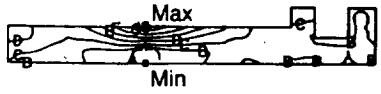

Legend	Ksi	MPa
A	-1.00	-6.89
B	0	0
C	1.00	6.89
D	2.00	13.79
E	3.00	20.68
F	4.00	27.58
G	5.00	34.47
H	6.00	41.37
Max	6.55	45.16
Min	-1.99	-13.72

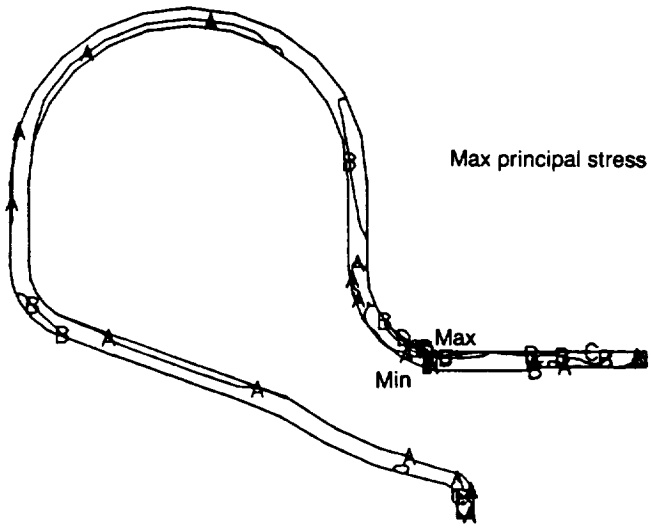

Legend	Ksi	MPa
A	0	0
B	4.00	27.6
C	8.00	55.2
D	12.00	82.7
E	16.00	110.3
F	20.00	137.9
G	24.00	165.5
Max	25.86	178.3
Min	-3.53	-24.34

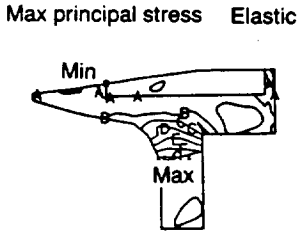

Legend	Ksi	MPa
A	0	0
B	10.00	68.9
C	20.00	137.9
D	30.00	206.8
E	40.00	275.8
F	50.00	344.7
G	60.00	413.7
H	70.00	482.6
Max	70.63	487.0
Min	-2.47	-17.0

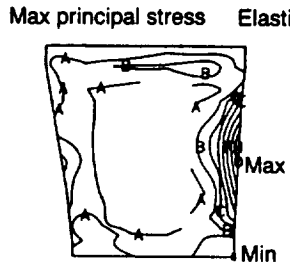

Legend	Ksi	MPa
A	3.00	20.7
B	6.00	41.4
C	9.00	62.1
D	12.00	82.7
E	15.00	103.4
F	18.00	124.1
G	21.00	144.8
H	24.00	165.5
Max	25.35	174.8
Min	0	0

TE90-2156

Figure 22. Scroll assembly stress distributions (worst case transient condition).

for this configuration, based on 2-D FEM analysis, is listed in Table II and compares the worst-case predicted values to the desired goals. The minimum POS was calculated at the worst operating condition for each part, whether at a particular time during the defined start-up transient, or at maximum power steady-state operation.

Si_3N_4 Scroll. The scroll assembly was also analyzed assuming fabrication from Kyocera's SN251 silicon nitride material. The scroll body, vane platform, and vane retaining ring were analyzed as being comprised of this material but the vane was analyzed assuming fabrication from GTE's PY6 silicon nitride. Maximum power steady-state and the cold start to maximum power transient conditions were used to generate FEM temperatures. These temperatures were then input into the structural FEM analysis for Weibull computation. The resulting probability of survival as a function of time is presented in Figure 23. The maximum principal stress plot for this configuration is illustrated in Figure 24. Clearly, the vane platform exhibits the lowest POS and an expanded analysis of this part was warranted.

Vane Platform Expanded Analysis. A comparison study was undertaken of the scroll assembly assuming platform fabrication from three different materials. Alpha SiC was the material assumed for the scroll, vanes, and retaining ring in all calculations while the platform material was varied. Steady-state and transient heat transfer analyses were performed for each assembly to include the effects of interaction of the platform with the other parts. In all cases the maximum principal stress and POS were essentially unchanged for the scroll, vanes, and ring. The POS for α-SiC, GTE PY6, and Kyocera's SN251 platforms as a function of time are presented in Figure 25. Maximum principal stresses for these same parts also as a function of time are illustrated in Figure 26. Clearly the Si_3N_4 vane platforms are superior with PY6 having the highest POS.

NC430 Scroll. The current design gasifier turbine scroll was also analyzed assuming fabrication from Norton's NC430 silicon carbide material. The analysis shows local high stresses relative to NC430 material strength at or near the slots in the scroll shroud where the vanes are positioned. These local stresses cause the calculated POS for the scroll to be very low for the transient and maximum power steady-state design operating conditions. However, if the slots in the scroll body are eliminated, requiring the vanes to be made integral with and located by the vane platform, the POS of the NC430 material scroll is predicted to be 0.9937 during even the most severe transient condition. The POS at steady-state maximum power rises to 0.9994 for this same configuration; the design goal POS for the scroll is 0.9826. Elimination of the slots through the scroll body, which caused stress concentrations, and a more favorable heat flow situation from the vanes to the scroll body are primarily responsible for improving the POS of the design. There is less heat flow into the scroll body than in the original case due to the clearance between the vanes and the scroll body. This results in reduced thermal gradients in the area above the vanes which originally caused an area of high stress. The 1371°C (2500°F) steady-state maximum power temperature and maximum principal stress distributions for a scroll without vane slots are presented in Figure 27. These distributions are also presented in Figure 28 for the worst case transient condition (lowest POS) which occurred at 30 seconds into start-up.

Table II.
Probabilities of survival summary: worst cases.

Component	Material	Time at min POS	Volume	Surface	Total	Goal total
Scroll	Alpha SiC	25 sec	0.9997	0.9998	0.9995	0.9826
Vane	Alpha SiC	10 sec	0.9999	0.9999	0.9998	0.9980
Platform	PY6 Si_3N_4	16 sec	0.9987	0.9931	0.9918	0.9836
Ring	Alpha SiC	Steady-state	0.9999	0.9999	0.9998	0.9990

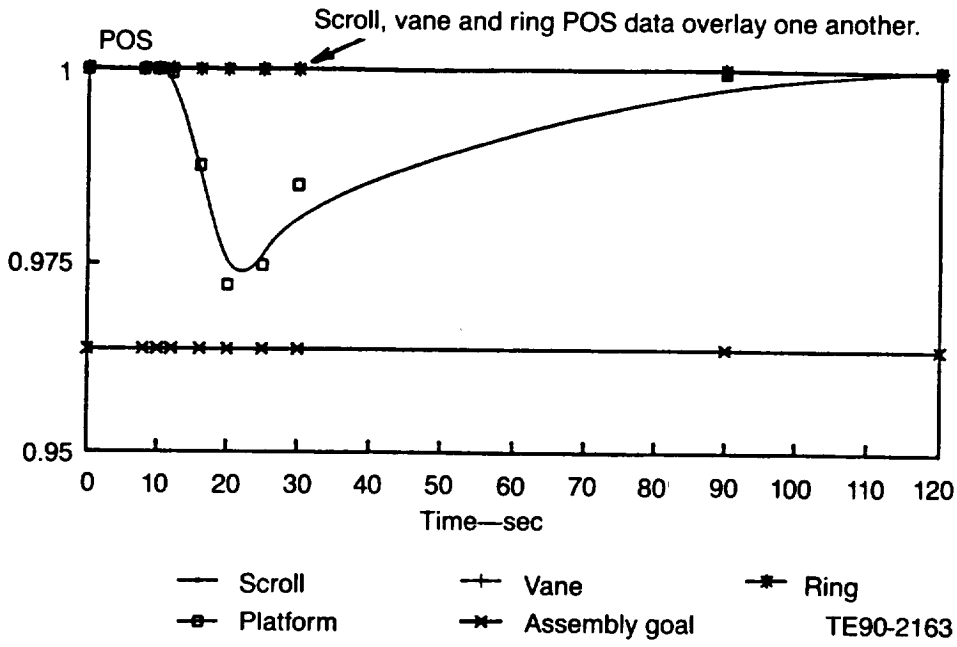

Figure 23. Probability of survival--SN251 scroll, ring, platform, and PY6 vane.

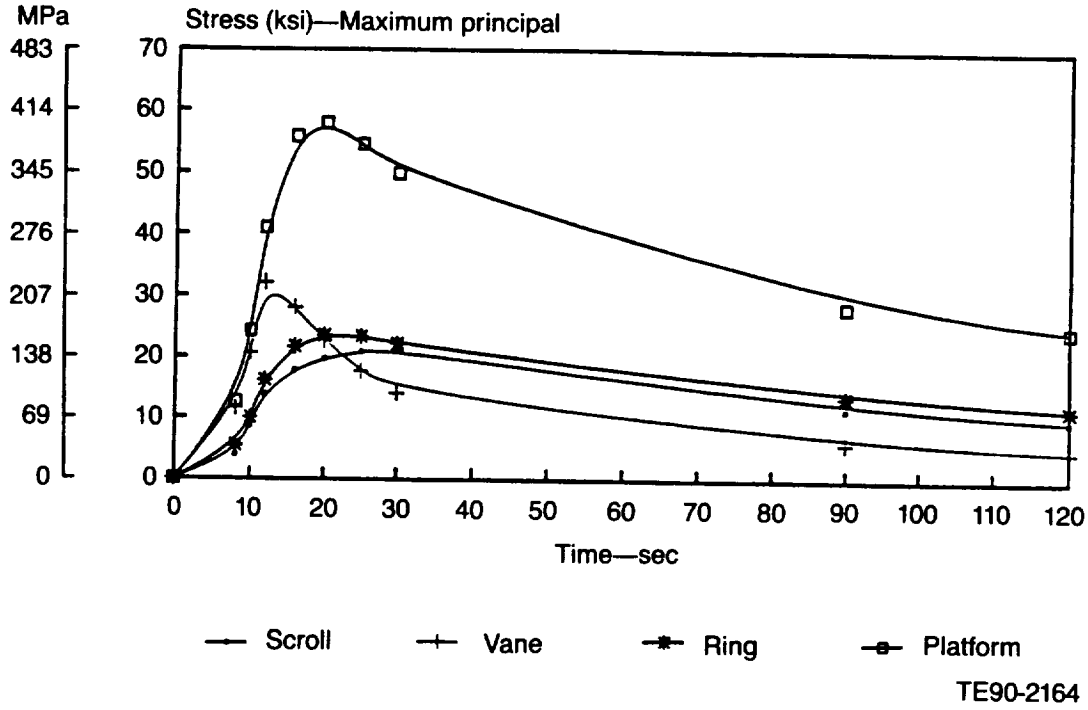

Figure 24. Transient stress--SN251 scroll, ring, platform, and PY6 vane.

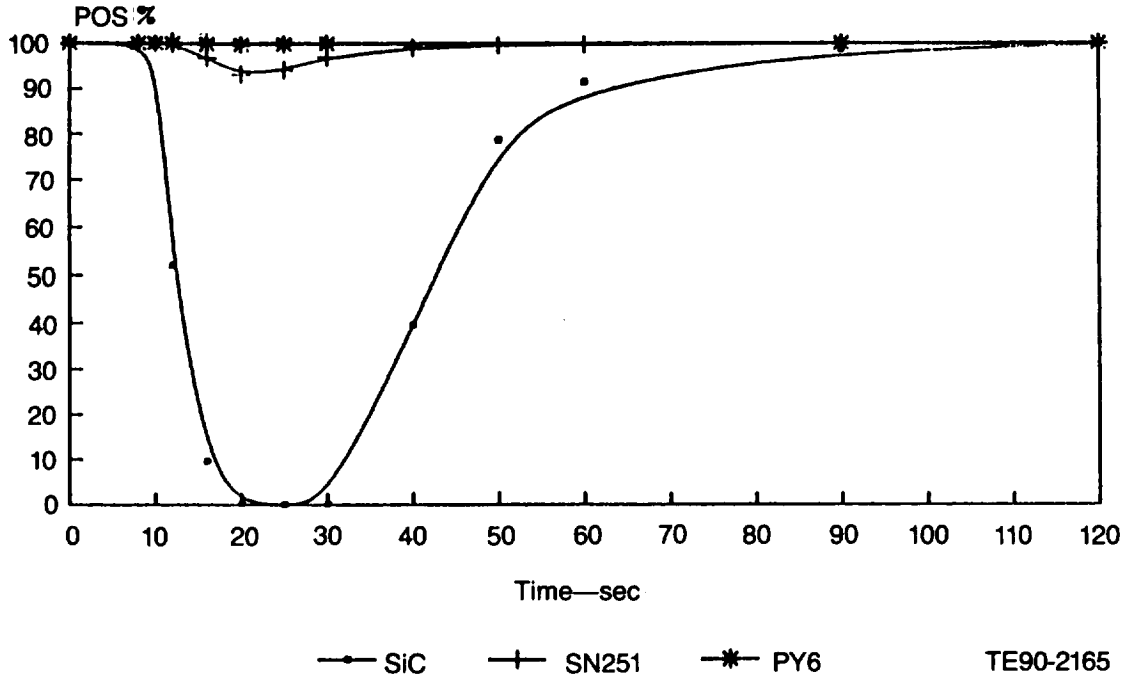

Figure 25. Vane platform POS--candidate materials.

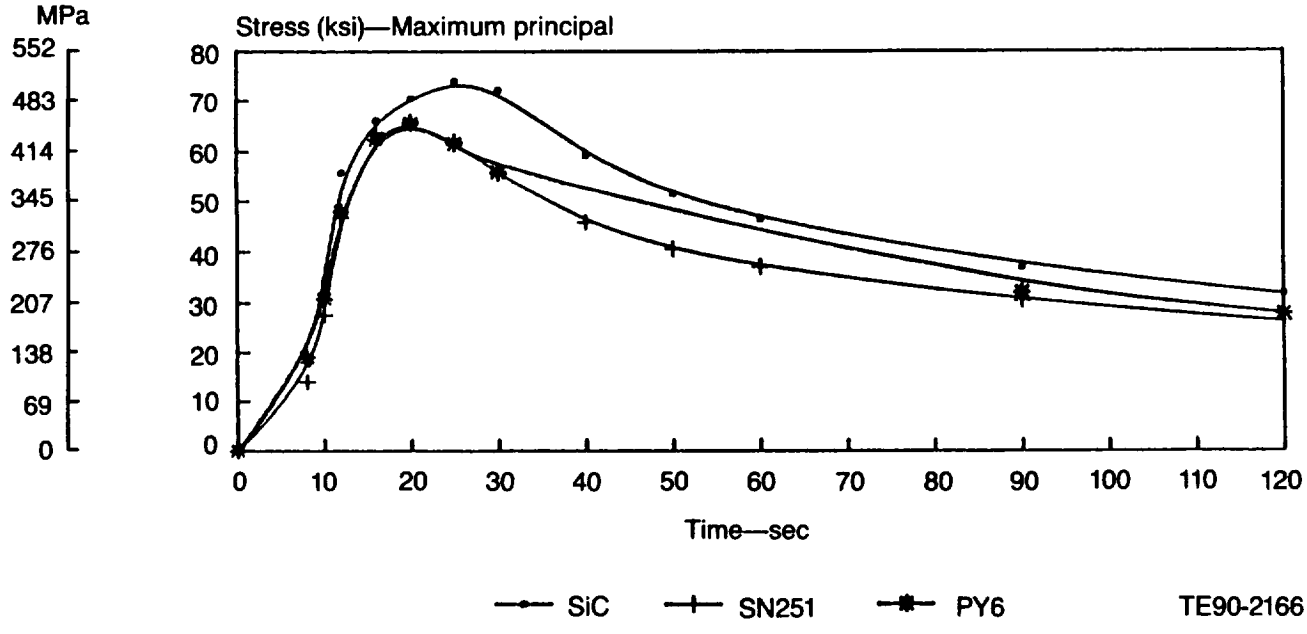

Figure 26. Vane platform transient stress--candidate materials.

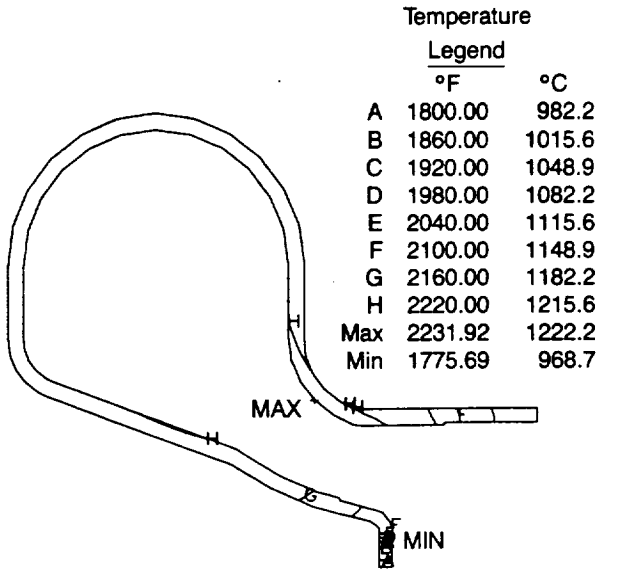

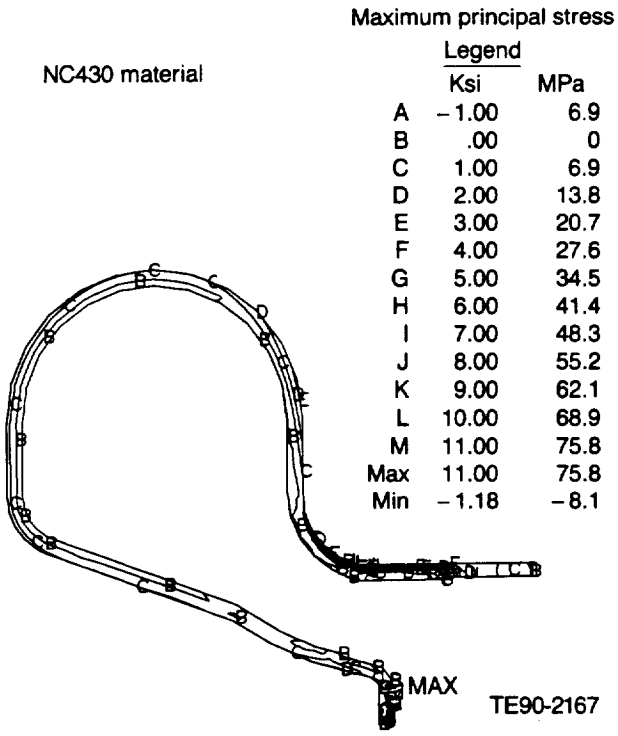

Figure 27. Temperature and stress distributions for gasifier turbine scroll without vane slots--steady-state maximum power condition.

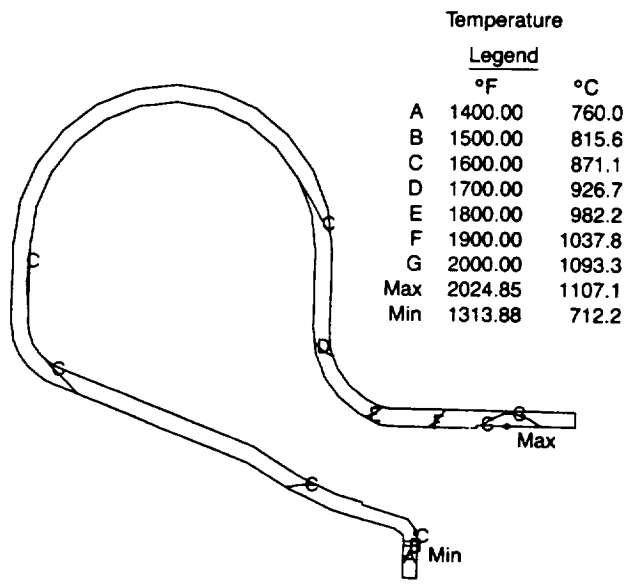

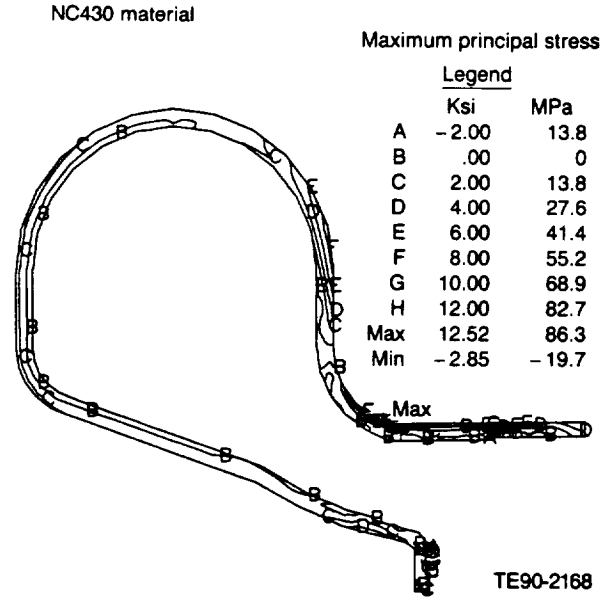

Figure 28. Temperature and stress distributions for gasifier turbine scroll without vane slots--cold start transient at 30 sec.

Future work scheduled for 1990 includes: a design activity to incorporate the nozzle vanes into the platform, and transient analyses to define deflections as a function of time using various candidate ceramic materials.

Vanes. A 3-D model was constructed to analyze the response of the ceramic gasifier turbine vane during the 1371°C (2500°F) TIT engine cycle (see Figure 29). The ceramic vane materials examined were Carborundum's α-SiC and GTE Laboratories' PY6 Si_3N_4. The goal POS for the ceramic vanes was calculated to be 0.9980. Three-dimensional finite element modeling results for both vane materials are summarized in Table III.

A detailed exploded view of the ceramic components in the gasifier turbine static structure has been illustrated in Figure 15. There are 14 individual vanes in the gasifier turbine assembly. They are inserted through a slot in the scroll and mounted loosely in pockets on the vane platform. The retaining ring holds the vanes in position. The α-SiC modeled vane maximum temperature was predicted to occur at approximately the mean section on the leading edge of the airfoil for both steady-state and start-up transient conditions. The maximum principal stress occurred at the mean section on the trailing edge for both time conditions. This was primarily due to the thin cross section at the trailing edge and the large thermal gradients projected to be present in this region. The calculated POS for the worst case transient condition, occurring at 14 sec after start-up, was 0.9951. The POS for the steady state condition was 1.000. Projected temperature and principal stress profiles for both steady state and transient conditions are illustrated in Figures 30 and 31, respectively.

The calculated maximum temperature and maximum principal stress for the PY6 Si_3N_4 vane are both located in approximately the same locations as computed for the silicon carbide vane. The computed POS for the worst case transient condition, occurring at 11.6 sec, was 0.9613. This value is 3.7% lower than the calculated POS goal of 0.9980. The lower POS is the result of low as-fired surface characteristic strength values used in the probabilistic calculations. The POS of the silicon nitride vane could be increased to 0.9933 by grinding the trailing edge smooth (free of surface roughness). GTE's PY6 material has surface strength values for longitudinally ground surfaces that are more than double those used for as-fired surfaces. The POS for the steady-state condition was 1.000. Projected temperature and principal stress profiles for both steady-state and transient conditions are presented in Figures 32 and 33, respectively.

This 3-D study concludes the design of the individual loosely mounted gasifier turbine ceramic vane. No further design activity is currently planned.

Table III.
Three-dimensional FEM ceramic vane results.

	alpha SiC	PY6 Si_3N_4
Steady-state		
• Max temperature–°C (°F)	1357.4 (2475.25)	1369.1 (2496.40)
• Max principal stress–Mpa (ksi)	59.2 (8.59)	56.3 (8.17)
• POS	1.0000	1.0000
Start-up transient		
• Time of maximum stress–sec	14.0	11.6
• Maximum temperature–°C (°F) (at maximum stress condition)	1253.0 (2287.38)	1311.4 (2392.45)
• Maximum principal stress–MPA(ksi)	401.6 (58.24)	338.3 (49.07)
• POS	0.9951	0.9613 (as-fired) 0.9933 (machined trailing edge)

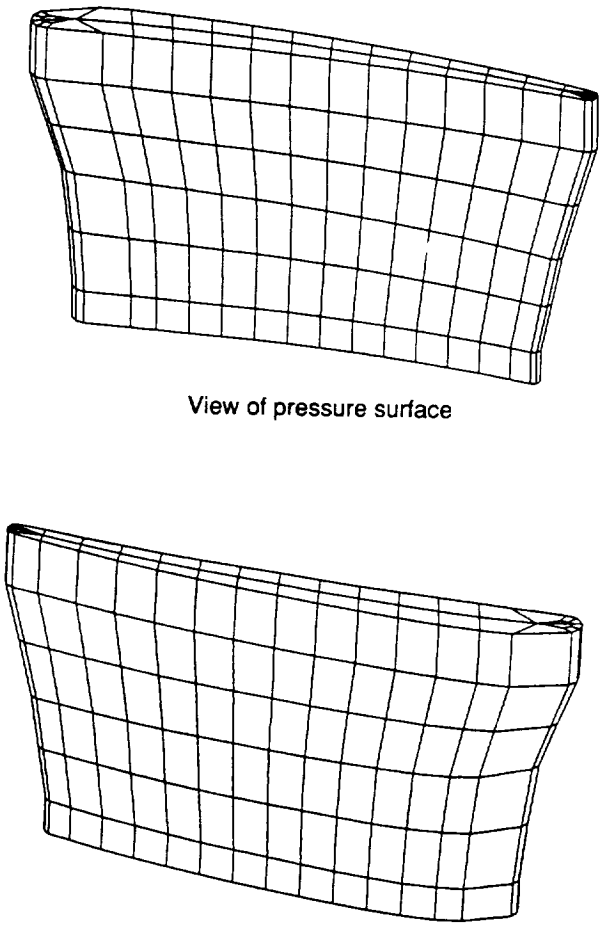

Figure 29. Three-dimensional gasifier turbine ceramic vane model.

2.1.3 Gasifier Turbine Rotor

Objective/Approach

This activity is focused on designing structural ceramic rotors for the gasifier turbine that meet performance, mechanical strength, and dimensional criteria for operating in the AGT-5 hot gasifier rig(s) and test-bed engine(s) at Reference Powertrain Design operating conditions. Efforts include the analytic assessment of the structural reliability (statistical basis) of gasifier rotor designs considering various ceramic material systems. The rotor design reliability goal is 0.9797. Twenty- and fifteen-airfoil designs utilizing silicon carbide and several varieties of silicon nitride were considered. Critical points in the engine operating cycle were analyzed, including 1371°C (2500°F) TIT maximum power steady-state and a cold start to maximum power transient.

Specific design requirements for the ceramic rotor were: 161,000 km (100,000 mi)/3500 hr life, 12,000 starts, 33,600 low cycle fatigue cycles, and the ability to endure engine generated foreign objects (primarily carbon debris). These requirements formed the design basis for the ceramic rotor. In particular: the airfoils were defined to aerodynamically satisfy the engine cycle; minimum trailing edge thickness was selected based on rig and engine test observations of foreign object survivability; the rotor/shaft attachment selection scheme was based on successful test experience; and the wheel web initial size and shape were determined by limiting the part stresses to approximately 207 MPa (30 ksi).

Finite element models were constructed for each rotor candidate in both two and three dimensions to calculate temperature and stress profiles and component POS.

Accomplishments/Results

- Two-dimensional design optimizations based on the POS were performed on the α-SiC gasifier turbine rotor.
- Two- and three-dimensional FEMs were developed for the 20-bladed rotor configuration and corresponding analytical results computed for various Si_3N_4 material types.
- A 3-D FEM was created for the 15-bladed gasifier rotor and analytical results computed for several ceramic materials.

The initial design optimizations performed for Carborundum's α-SiC ceramic rotor were computed in two dimensions. This was primarily due to the simplicity of the 2-D model and its corresponding lower cost compared to full 3-D models. Various configurations of this base rotor design were investigated in an unsuccessful attempt to analytically achieve a POS greater than the POS goal of 0.9797. The results from the 20-bladed rotor 2-D and 3-D models were used as a basis for the development of the 15-bladed models. Table IV summarizes the analytical results, displaying POS values for the various configurations, material systems, and operating conditions. Details are presented in the following discussion.

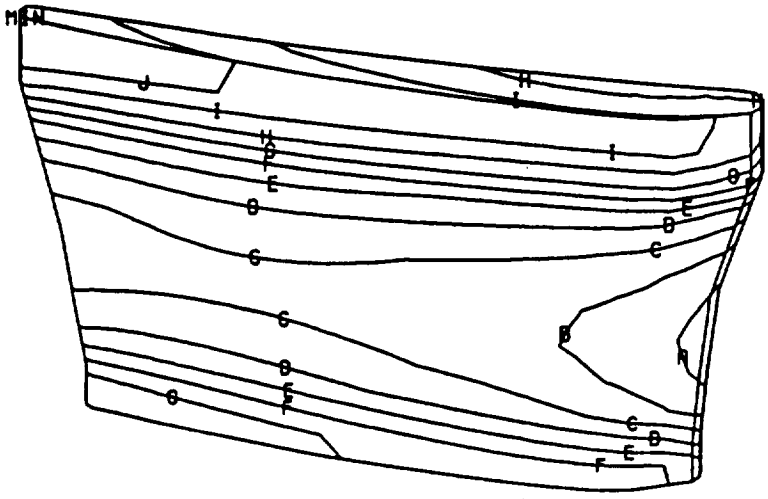

Temperature profile

Legend	°F	°C
A	2470.0	1354.44
B	2460.0	1348.89
C	2450.0	1343.33
D	2440.0	1337.78
E	2430.0	1332.22
F	2420.0	1326.67
G	2410.0	1321.11
H	2400.0	1315.56
I	2390.0	1310.00
J	2380.0	1304.44
*Max	2475.2	1357.36
Min	2370.9	1299.42

*Denotes hidden

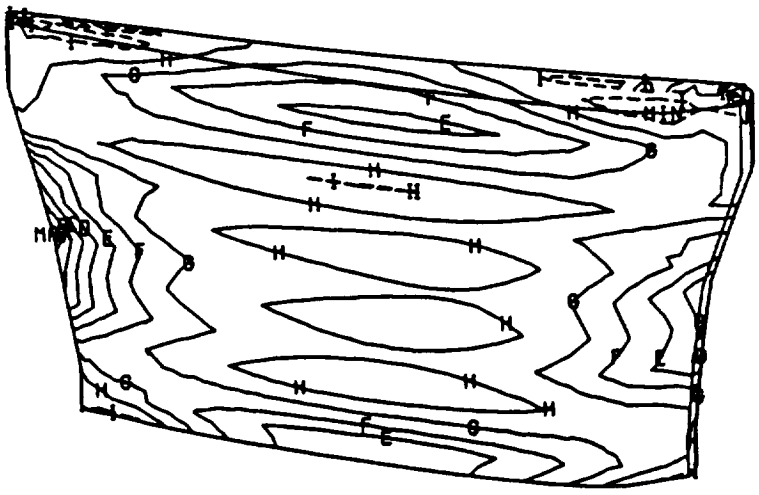

Maximum principal stress profile

Legend	Ksi	MPa
A	8.0	55.16
B	7.0	48.26
C	6.0	41.37
D	5.0	34.47
E	4.0	27.58
F	3.0	20.68
G	2.0	13.79
H	1.0	6.89
I	.0	.00
Max	8.6	59.23
Min	-.7	-4.75

TE90-2158

Figure 30. Temperature and stress profiles, α-SiC vane-steady-state condition.

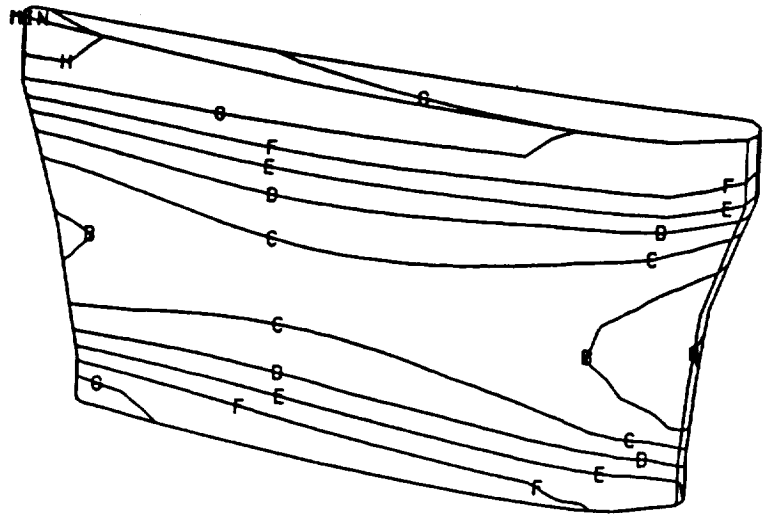

Temperature profile

Legend	°F	°C
A	2280.0	1248.89
B	2200.0	1204.44
C	2120.0	1160.00
D	2040.0	1115.56
E	1960.0	1071.11
F	1880.0	1026.67
G	1800.0	982.22
H	1720.0	937.78
*Max	2287.4	1252.99
Min	1695.4	924.14

*Denotes hidden

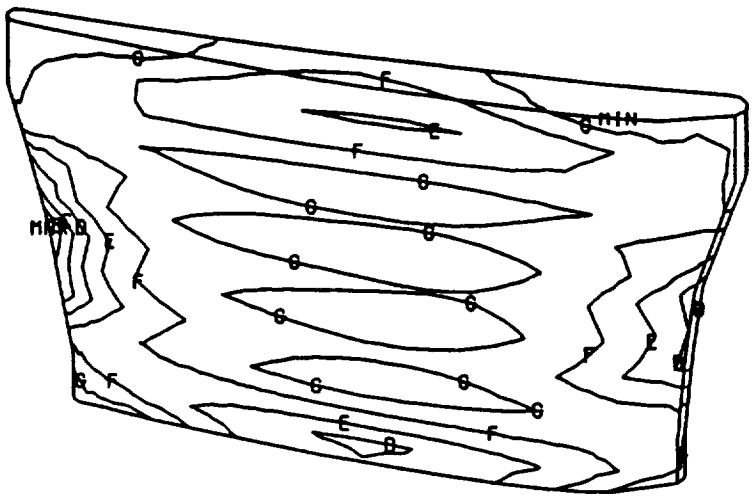

Maximum principal stress profile

Legend	Ksi	MPa
A	58.0	399.90
B	49.0	337.84
C	40.0	275.79
D	31.0	213.74
E	22.0	151.68
F	13.0	89.63
G	4.0	27.58
Max	58.2	401.58
Min	-2.9	-20.32

TE90-2159

Figure 31. Temperature and stress profiles, α-SiC vane-transient condition (T = 14 sec).

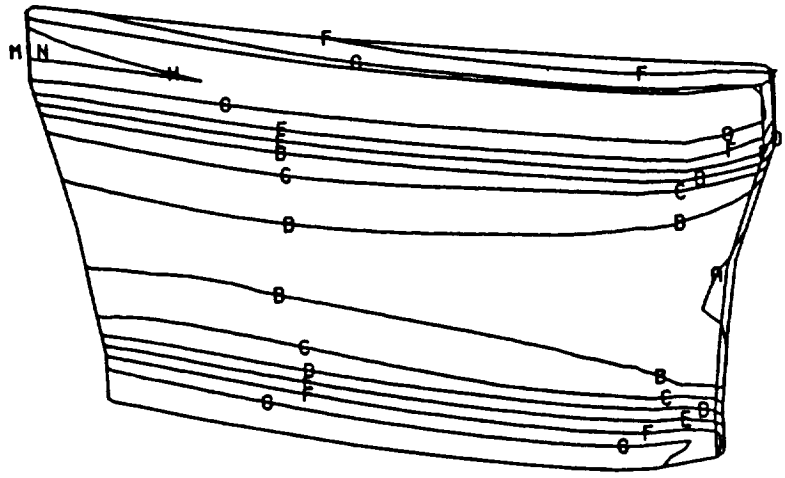

Temperature profile

Legend	°F	°C
A	2490.0	1365.56
B	2470.0	1354.44
C	2450.0	1343.33
D	2430.0	1332.22
E	2410.0	1321.11
F	2390.0	1310.00
G	2370.0	1298.89
H	2350.0	1287.78
*Max	2496.4	1369.11
Min	2344.2	1284.54

*Denotes hidden

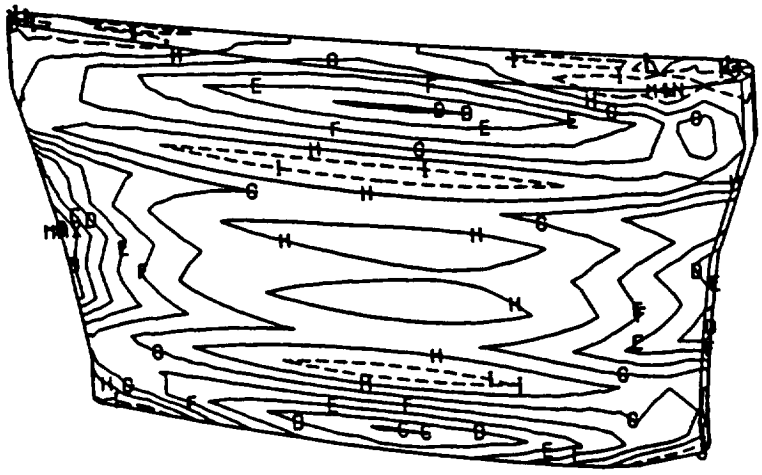

Maximum principal stress profile

Legend	Ksi	MPa
A	8.0	55.16
B	7.0	48.26
C	6.0	41.37
D	5.0	34.47
E	4.0	27.58
F	3.0	20.68
G	2.0	13.79
H	1.0	6.89
I	.0	.00
J	-1.0	-6.89
Max	8.2	56.33
Min	-1.3	-8.82

TE90-2160

Figure 32. Temperature and stress profiles, PY6 Si_3N_4 vane-steady-state condition.

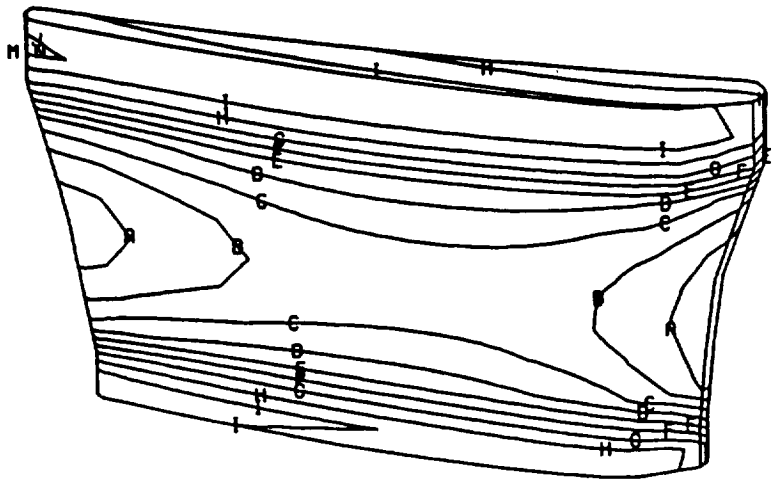

Legend	°F	°C
A	2300.0	1260.00
B	2200.0	1204.44
C	2100.0	1148.89
D	2000.0	1093.33
E	1900.0	1037.78
F	1800.0	982.22
G	1700.0	926.67
H	1600.0	871.11
I	1500.0	815.56
J	1400.0	760.00
*Max	2392.4	1311.36
Min	1384.9	751.62

*Denotes hidden

Temperature profile

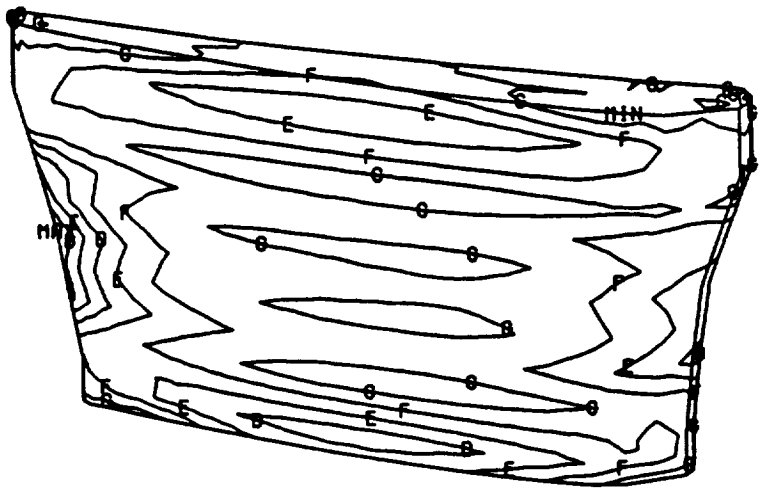

Legend	Ksi	MPa
A	49.0	337.84
B	41.0	282.68
C	33.0	227.53
D	25.0	172.37
E	17.0	117.21
F	9.0	62.05
G	1.0	6.89
Max	49.1	338.30
Min	-5.9	-40.55

Maximum principal stress profile

TE90-2161

Figure 33. Temperature and stress profiles, PY6 Si_3N_4 vane-transient condition (T = 11.6 sec).

Table IV.
Calculated probabilities of survival for ceramic gasifier rotors.

Gasifier turbine design reliability goal = 0.9797	Room temperature spin 100% N1	1371°C (2500°F) TIT	
		Steady state	Transient
20 airfoils			
• CBO, α-SiC, 2-D	0.9982	0.4610	0.0
• GTE PY6, 2-D	0.9995	0.9776	0.9950
• NTC NT-154			
• 2-D		0.9999	0.9997
• 3-D	1.0000	0.9998	0.9974
• GCCD GN-10, 2-D		0.9815	0.7540
• KYO SN252			
• 2-D	0.9998	0.9852	0.9576
• 3-D	0.9995	0.9556	0.8953
15 airfoils			
• GTE PY6			
• 2-D	1.0000		
• 3-D	0.9850	0.9880	0.6740
• NTC NT-154, 3-D	1.0	0.9987	0.9322
• KYO SN252			
• 2-D	1.0000		
• 3-D	0.9952	0.9973	0.6987

Discussion

α-SiC Rotor Analysis. The critical design modifications to the α-SiC gasifier rotor concentrated on increasing the rotor's survivability during the transient condition (that condition which occurs from engine start-up to maximum power). The steady state condition was, however, also examined as an initial reference point. All of the design changes were judged as either beneficial or detrimental based solely on the positive or negative effect that they had on the POS.

The original design of the α-SiC gasifier rotor did not meet the POS goal of 0.9797. During steady state operation, the silicon carbide rotor is predicted to incur a maximum principal stress of over 510 MPa (74 ksi) in a very localized area at the base of the ceramic shaft in the fillet region. The resulting overall POS was calculated to be 0.461 (see Figure 34). (The apparent maximum stress of 568.9 MPa [82.51 ksi] listed in Figure 34 actually occurs in the metal shaft and not in the ceramic component.) The maximum principal stress profile for this same rotor during transient operation is displayed in Figure 35. There are *large* regions of stress present on the aft face of the web that exceed 414 MPa (60 ksi), the material's characteristic strength, hence the overall calculated POS for this condition was 0.0.

As a result of these rotor evaluations, a redesign effort to improve the rotor survivability was initiated. A proposed first redesign of the α-SiC gasifier rotor is presented in Figure 36. The intent of this iteration was to reduce the stress profile by creating more isothermal conditions within the rotor. A larger shaft fillet tends to subdue thermal gradients and therefore reduce overall stress, while undercutting the wheel rim and increasing the web cross section was intended to help decrease the high observed principal stresses. Initial computations indicated that this first redesign effort slightly improved the POS, but the extent of improvement was insufficient to ensure survivability. Additional redesign efforts were undertaken.

Another redesign approach involved a different attempt to reduce the temperature gradients in the disk. The thermal path from the wheel rim to the

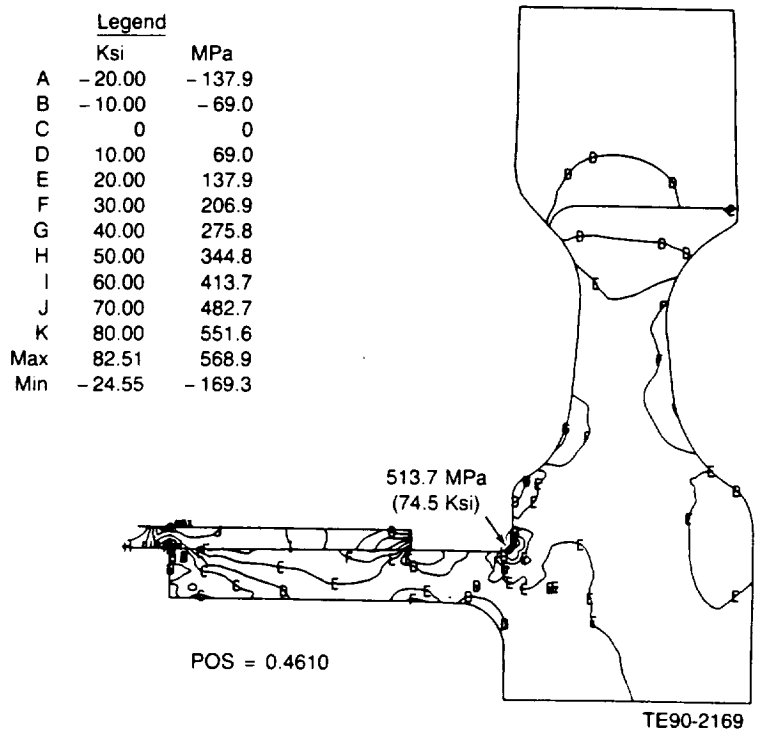

Figure 34. Principal stress plot, SiC material rotor, maximum power steady-state condition.

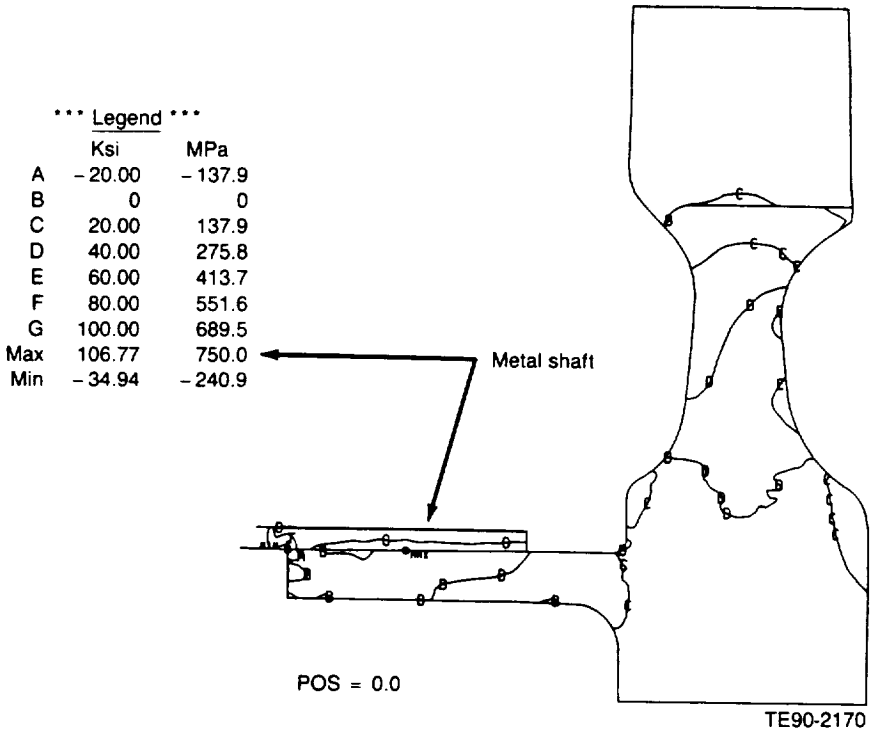

Figure 35. Principal stress plot, SiC material rotor, worst case transient condition.

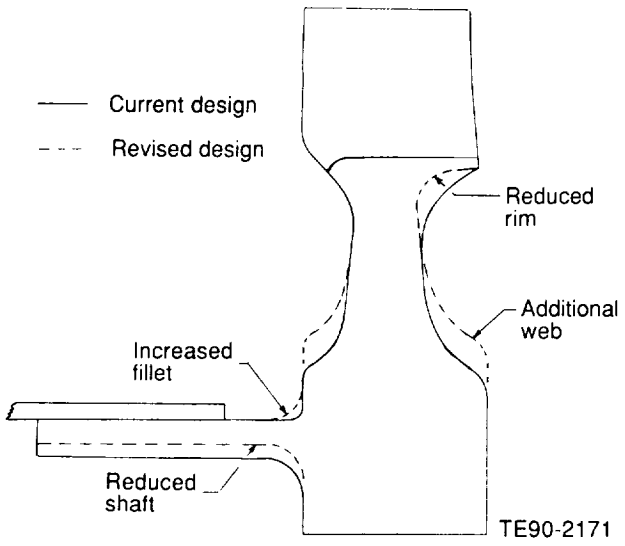

Figure 36. Proposed redesign of SiC gasifier rotor.

metal shaft was extended compared to that in the original design in an attempt to reduce the thermal gradients. This rotor design is shown in Figure 37; the resulting POS for steady state operation was 0.78. Analysis of this design for the transient condition, however, revealed large thermal gradients and a predicted POS, again of 0.0 (see Figure 38).

The rim in Figure 38 is about 871°C (1600°F) while the hub region is approximately 316°C (600°F). This creates a 555°C (1000°F) thermal gradient with an associated large stress profile leading to the predicted POS of 0.0.

As a result of these computations, an extreme condition was then examined (Figure 39) to determine if transient condition survivability was even possible. This design iteration featured a large rim area cross section to maximize thermal gradient reduction in the disk. While the steady state operation produced a calculated POS of 0.633, the maximum thermal gradients in the rotor during transient operation were still too large (approximately 427°C [800°F]), producing a corresponding predicted POS of only 0.102. This represented the only configuration modeled in α-SiC to obtain a non-zero POS for the transient condition. However, the POS value was still well below design specifications.

Although this was not a totally exhaustive study of the structural design of an α-silicon carbide rotor, it suggests that survival of an α-SiC rotor operating under the conditions of this engine test-bed is minimal. The stresses in this ceramic rotor are induced primarily by the thermal gradients in the

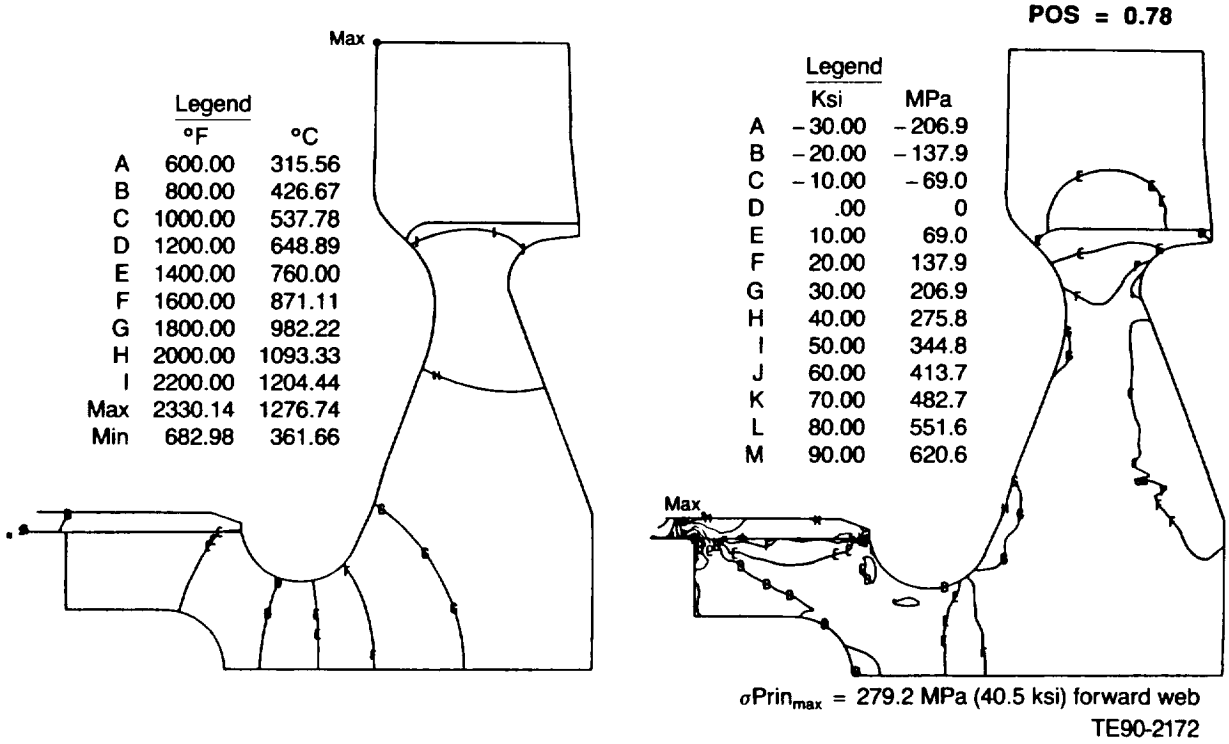

Figure 37. Temperature and stress profiles, SiC modified gasifier rotor, maximum power steady-state condition.

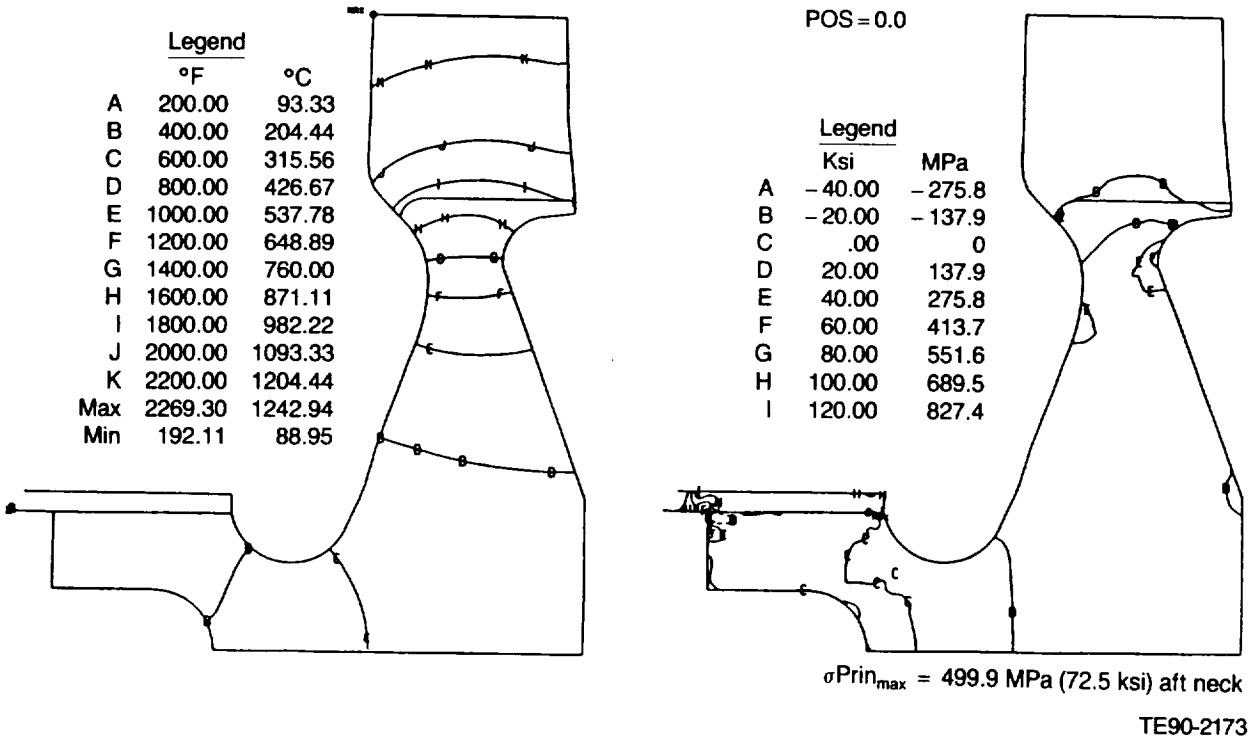

Figure 38. Temperature and stress profiles, SiC modified gasifier rotor, worst case transient condition.

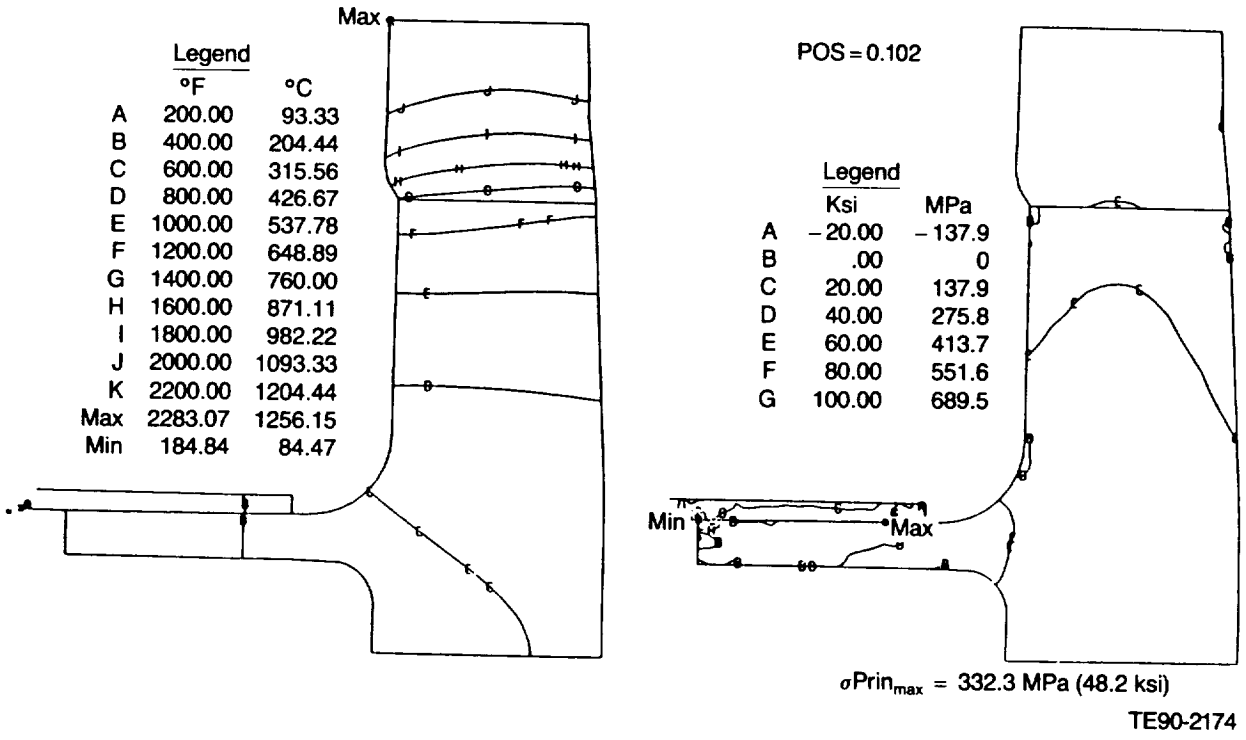

Figure 39. Temperature and stress profiles, SiC limiting configuration gasifier rotor, worst case transient condition.

wheel. In the original α-SiC rotor configuration, the observed maximum principal stress was greater than that in a silicon nitride rotor with the same geometry. The physical properties of the two materials, as listed in Table V, help to explain this phenomenon. Thermal induced stress can be defined as:

$$s_{Thermal} = f(E\alpha\, dT/dr)$$

The Eα product for α-SiC exceeds that of Si_3N_4 by nearly a factor of 2. Therefore, in the presence of similar thermal gradients (dT/dr) the resulting thermal stresses in silicon nitride rotors will always be less than those produced in silicon carbide rotors. Further, the MOR strength of α-SiC is much lower than that of silicon nitride, a further challenge to the successful design of an α-SiC rotor. This effect can be alleviated by designs in which the larger thermal conductivity of SiC can be successfully utilized to significantly reduce thermal gradients. This was not possible within the design constraints of the ATTAP AGT-5 test-bed engine.

Silicon Nitride Rotor Analysis. Both the 20- and 15-bladed rotor designs, modeled in several Si_3N_4 materials, are included in the matrix of ceramic gasifier rotors for which the POS has been calculated (refer to Table IV). The 20-bladed rotor was analyzed using both 2-D and 3-D techniques. Because of the geometric similarities between 20-bladed and 15-bladed models, detailed 2-D examination for all materials was suspended for the 15-bladed design. Rather, the simple 2-D geometry was used for establishing the boundary conditions for the more complex 3-D running conditions for both rotor designs. Sector models of 1/20 and 1/15 of the gasifier rotor were constructed for the 3-D analyses for the 20- and 15-bladed rotors, respectively.

A comparison of the 2-D and 3-D analyses is facilitated by reviewing the POS data listed in Table IV and for the 20-bladed rotor. In summary, the 3-D analysis calculates lower POS values than the 2-D approach, which is consistent with the nature of the calculations; the 2-D approach does not adequately consider the contribution of the airfoils to the total rotor survivability. Rather, the 2-D scheme models the cambered blade as a flat plate, and the calculated stress and POS values may not, therefore, always be realistic. The 3-D analysis accurately simulates the airfoil and the fillet radius joining the blade to the hub. In some cases involving steady-state operating conditions and very high strength materials, such as Norton/TRW's NT-154 silicon nitride, the predicted results between the 2-D and 3-D analyses are similar. For lower strength materials, such as Kyocera SN252, the differences in predicted results are amplified and the 3-D approach yields more accurate POS predictions. A specific example illustrating the requirement for 3-D analysis involves the POS predictions of the NT-154 silicon nitride 20-bladed rotor during transient operating conditions. The 2-D calculation result is presented in Figure 40, and the corresponding 3-D analytical solutions are displayed in Figures 41 and 42. The corresponding POSs for the 2-D and 3-D models, as listed in Table VI, are 0.9997 and 0.9974, respectively. The total rotor 3-D predicted POS is the product of the airfoil POS (= 0.9978) and the wheel POS (=0.9996). The stresses present in the root of the blade are significant and contribute extensively to the overall POS of the rotor. These effects are not adequately predicted by the 2-D analysis. As expected, the calculated POS values for the rotor body are, however, similar for both the 2-D and 3-D designs. For example, comparison of the data in Figures 40 and 41 indicates acceptable correlation of the 2-D and 3-D predicted maximum principal stresses in the aft web of the rotor.

Table V.
Summary comparison, ceramic material properties.

	Room temperature		1200°C (2192°F)	
	α-SiC	PY6	α-SiC	PY6
MOR, MPa (ksi)	413 (60)	944 (137)	413 (60)	586 (85)
m	8	9	8	9
E, GPa (msi)	407 (58.3)	296 (43.0)	382 (55.4)	270 (39.1)
a, mm/mm°C x 10^{-6}	1.04	0.75	1.52	1.06

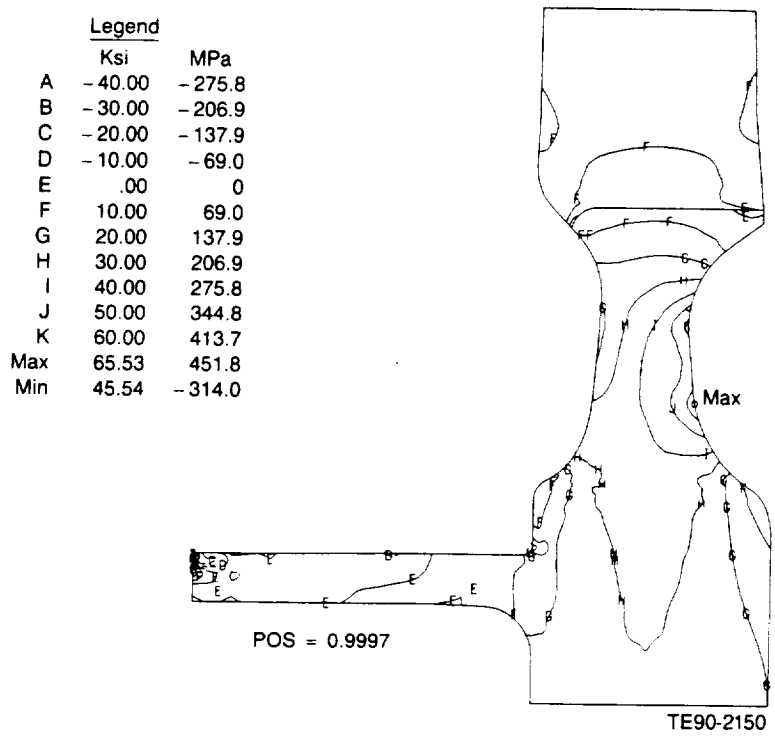

Figure 40. Stress profile for NT-154 Si_3N_4 20-bladed gasifier turbine rotor: 2-D model, worst case transient condition.

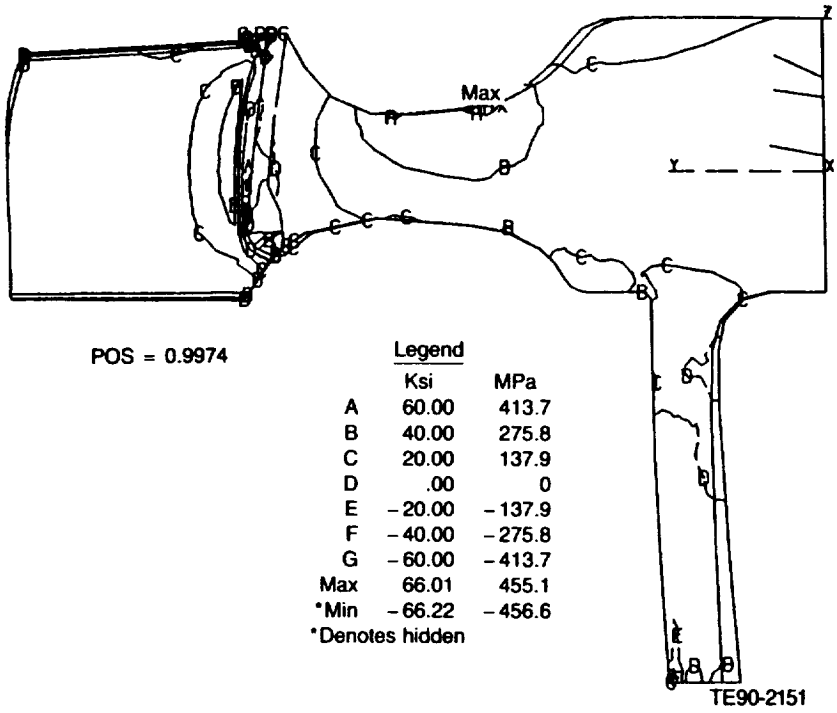

Figure 41. Stress profile for NT-154 Si_3N_4 20-bladed gasifier turbine rotor: 3-D model, worst case transient condition.

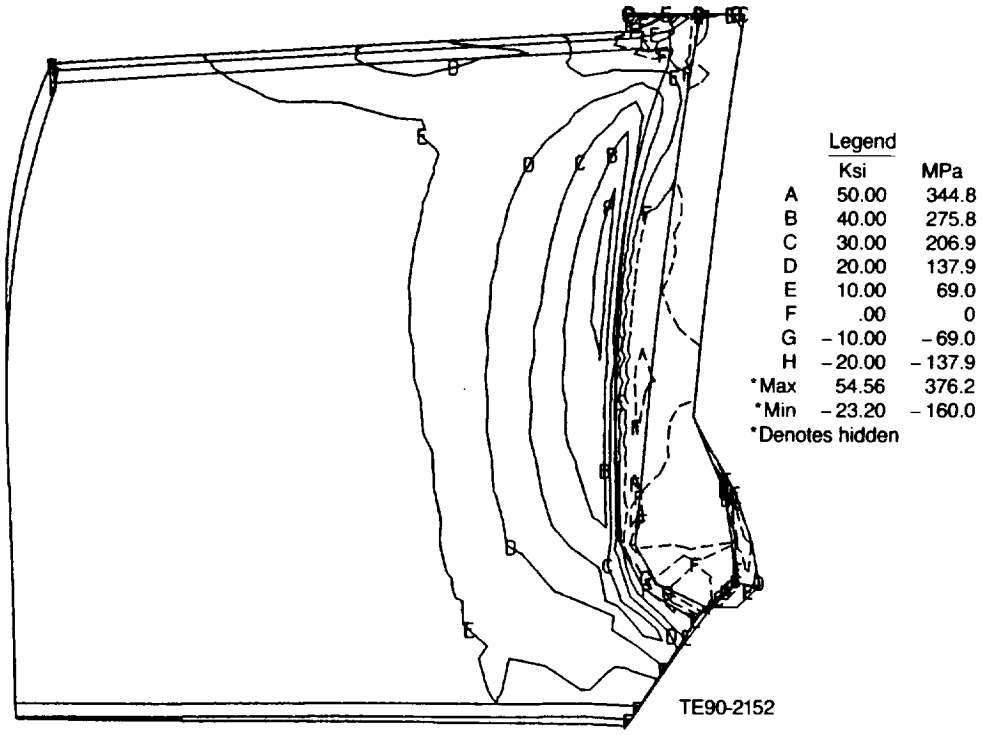

Figure 42. Stress profile for NT-154 Si_3N_4 airfoil from 20-bladed gasifier turbine rotor: 3-D model, worst case transient condition.

Table VI.
Analysis comparison between 2-D and 3-D FEM 20-bladed ceramic gasifier rotor (Norton/TRW NT-154 Si_3N_4).

	2-D	3-D
Steady state		
Max principal stress, MPa (ksi)	455.4 (66.05)	496.9 (72.06)
POS	0.99994	0.99981
Transient		
Max principal stress, MPa (ksi)	451.8 (65.53)	455.1 (66.01)
POS	0.9997	0.99735

As thermal effects substantially affect rotor survivability, heat transfer rates into the rim of the wheel as a function of the number of blades were investigated. The cross sections of the 15- and 20-bladed gasifier rotors are directly proportional at the same radius. The cross-sectional area at the blade hub (conduction area) and the airfoil surface area (convection area) as a function of the number of airfoils were calculated and plotted in Figure 43. An examination of the calculated temperature profiles for the 20- and 15-bladed ceramic rotors (Figures 44 and 45) indicate equivalent maximum temperatures, but the minimum temperature of the 20-bladed rotor is nearly 170°C (340°F) greater than that of the 15-bladed wheel. It was concluded that rotors with a larger number of blades tend to have heat transfer characteristics in which the conductive heat flux through the root of the airfoils to the web of the rotor appears "choked" in the transient condition. Since minimization of heat transfer is considered desirable, rotors with increased number of blades appear favorable; how-

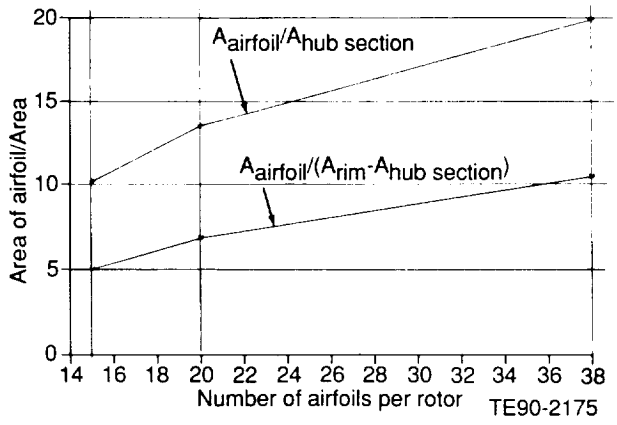

Figure 43. Airfoil area parameters.

ever, use of more blades also implies relatively thin airfoil cross sections, which are more vulnerable to foreign object damage (FOD).

The 20-bladed Norton/TRW NT-154 silicon nitride rotor, of all of those examined, is analytically the most likely to survive in the operating conditions of the AGT-5 engine test-bed. It exceeds the POS design goal and represents a reasonable compromise regarding blade number effects.

2.1.5 Power Turbine

Objective/Approach

The AGT-5 test-bed engine, operating at the elevated temperatures associated with the ATTAP program, requires a power turbine capable of delivering increased power while operating at increased rotor speed and inlet gas temperature (versus original 1038°C (1900°F) engine parameters). The objective of this activity is the design and analysis of power turbine structural ceramic components (both static and rotating) which meet performance, material behavior, dimensional criteria, and durability requirements necessary to allow operation of the ceramic gasifier components in the test-bed engine at Reference Powertrain Design operating conditions. The resulting power turbine design is in fact a hybrid of metal and ceramic components; these metal components necessary to support the ceramic structures were also designed and analyzed under this task, because extensive system analyses were executed in which all components and their interactive effects were considered. The power turbine design was examined at maximum power steady-state and worst case transient conditions to determine the ceramic components' survivabilities.

Accomplishments/Results

- detail designs completed for all major power turbine components
- heat transfer analyses completed for the maximum power steady-state operating condition and for the transient cold start-to-maximum power condition
- stress analyses, including probability of survival calculations for ceramic components, completed for maximum power and transient conditions: design goals were met for all *ceramic* components in the power turbine assembly; however, the analysis of the metallic static structure components for the transient operating condition revealed localized stress levels above material yield strengths
- maximum (local) stresses in *metallic* static structure components were reduced to levels below yield strengths by defining a less aggressive rate of acceleration to be used during test-stand transient cycle operation
- integrity of the ceramic rotor to metal shaft joints for both power turbine rotors was verified by analysis; the turbine design incorporates air cooling provisions for both rotor joints

Discussion

Static Structure. An initial FEM model was generated for a preliminary conceptual flow path version of the power turbine assembly. Since the flow path was expected to undergo modification as the aerodynamic design progressed, the FEM model was first used for calculating and assigning preliminary heat transfer coefficients and other initialization factors. As soon as the near-final flow path configuration was determined, the model was adjusted to match and detailed analysis was initiated. The preliminary power turbine FEM model is illustrated in Figure 46.

Both static and rotating components were included in the model; temperatures generated with later versions of this model were used as inputs for static and rotating stress models. By midyear the preliminary FEM model was updated to reflect the revised flow-path configuration. At this point the power turbine assembly design was sufficiently defined that subsequent changes were relatively mi-

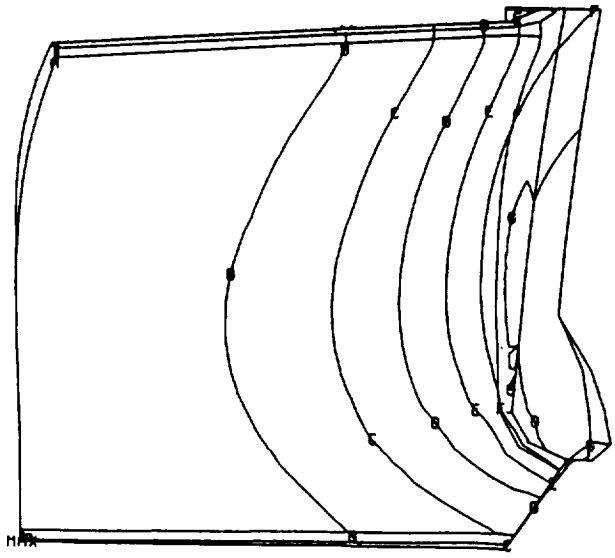

Legend	°F	°C
A	2310.00	1265.6
B	2210.00	1210.0
C	2110.00	1154.4
D	2010.00	1098.9
E	1910.00	1043.3
F	1810.00	987.8
G	1710.00	932.2
Max	2311.32	1266.3
*Min	1617.20	880.7

*Denotes hidden

• Temperature profile

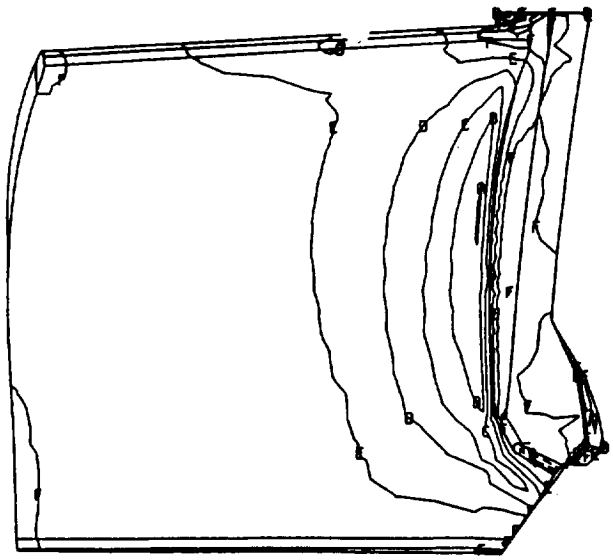

Legend	Ksi	MPa
A	46.00	317.2
B	37.00	255.1
C	28.00	193.1
D	19.00	131.0
E	10.00	69.0
F	1.00	6.9
G	−8.00	−55.2
H	−17.00	−117.2
*Max	46.91	323.4
*Min	−18.20	−125.5

*Denotes hidden

TE90-2153

• Stress profile

Figure 44. Temperature and stress profiles, Kyocera SN252 Si_3N_4 airfoil: 20-bladed gasifier turbine rotor, 3-D model, worst case transient condition.

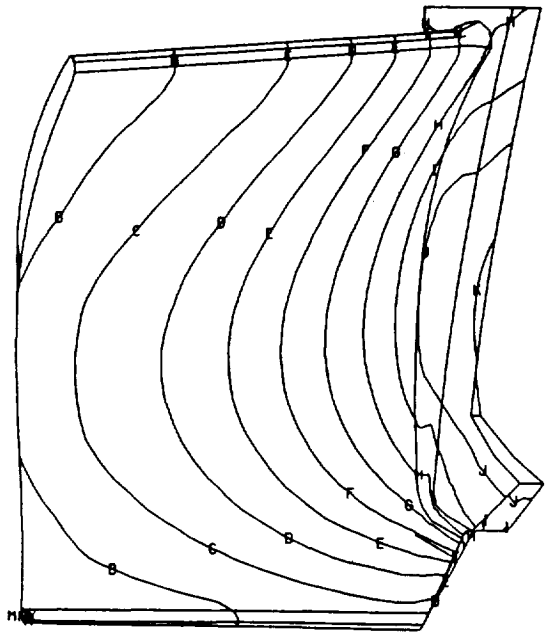

Legend	°F	°C
A	2300.00	1260.0
B	2200.00	1204.4
C	2100.00	1148.9
D	2000.00	1093.3
E	1900.00	1037.8
F	1800.00	982.2
G	1700.00	926.7
H	1600.00	871.1
I	1500.00	815.6
J	1400.00	760.0
K	1300.00	704.4
Max	2302.91	1261.6
*Min	1277.67	692.0

*Denotes hidden

• Temperature profile

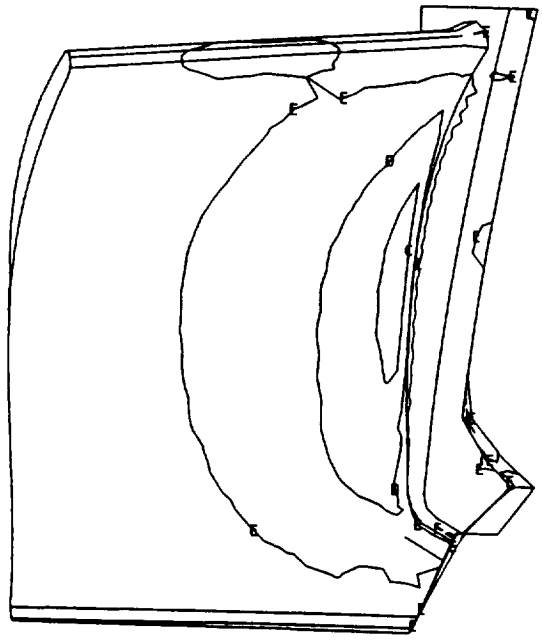

Legend	Ksi	MPa
A	90.00	620.6
B	70.00	482.7
C	50.00	344.8
D	30.00	206.9
E	10.00	69.0
F	−10.00	−69.0
*Max	93.22	642.8
*Min	−21.77	−150.1

*Denotes hidden

• Stress profile

TE90-2154

Figure 45. Temperature and stress profiles, Kyocera SN252 Si_3N_4 airfoil: 15-bladed gasifier turbine rotor, 3-D model, worst case transient condition.

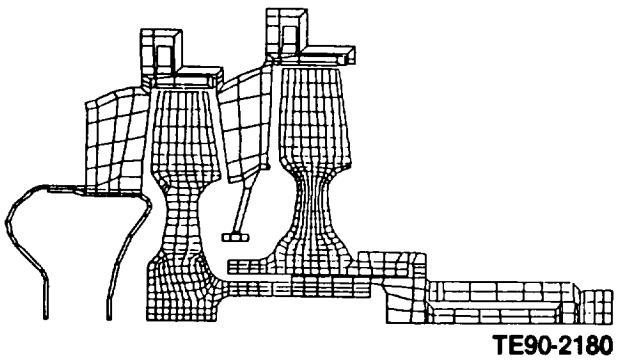

Figure 46. Preliminary power turbine FEM model (reference Figure 6).

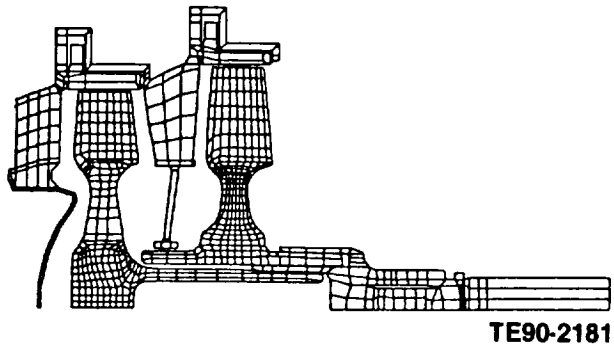

Figure 47. Interim power turbine FEM model.

nor and effects of the changes could easily be incorporated into the model. The revised model, as presented in Figure 47, was utilized to analyze and produce interim design data.

Temperatures were first calculated for the steady-state maximum power 1371°C (2500°F) gasifier rotor inlet temperature operating condition. The predicted temperature distribution for the power turbine assembly is presented in Figure 48. These temperatures were then input into the stress model to perform a deflection analysis. A possible deflection plot for the assembly is illustrated in Figure 49; the deflections are exaggerated on this plot and the parts do not experience the interference that appears. Clearances at the positions depicted in Figure 50 are tabulated in Table VII for both cold and hot (1371°C [2500°F] maximum power) conditions.

The power turbine aerodynamic design was finalized during the last quarter of the year. Minor modifications were incorporated into the model described above (Figure 47) to bring it into compliance with the final aerodynamic design. These modifications included adjustments to the radial and axial dimensions of the gas path, associated changes to shafting and bearing housings, and a revision of the first-stage nozzle/diaphragm design. This final model configuration is illustrated in Figure 51. Temperatures resulting from start-up to steady-state operation were simultaneously calculated for both static and rotating components using this model. Materials used in the various substructures are listed in Table VIII.

Static component steady-state temperatures and corresponding stresses were calculated for the 1371°C (2500°F) maximum power condition. The static component finite element grid used in both steady-state and transient thermal and stress analyses is presented in greater detail in Figure 52. This model consists of eight separate substructures constrained so as to accurately transmit loads occurring at their interfaces. The predicted steady-state maximum power temperature distribution and resulting stress profile for each of the substructures (exposed to steady-state maximum power conditions) are presented in Figures 53 through 60.

Table VII.
Power turbine assembly axial clearances.

Location	Cold clearance mm	Cold clearance in.	Hot clearance mm	Hot clearance in.
1	5.19	(0.2044)	4.67	(0.184)
2	3.68	(0.1449)	3.15	(0.124)
3	3.48	(0.1371)	4.55	(0.179)
4	3.56	(0.1403)	4.67	(0.184)
5	5.53	(0.2177)	4.29	(0.169)
6	5.74	(0.2259)	4.52	(0.178)

Table VIII.
Substructure material table used in analysis.

Substructure	Material type	Material
Sleeve	2	Metal
PT shaft	2	Metal
PT 1	4	SN252 Si_3N_4
Blade 1	4	SN252 Si_3N_4
PT 2	5	SN220M Si_3N_4
Blade 2	5	SN220M Si_3N_4
V1 shroud	3	Metal
Vane 1	3	Metal
V1 hub	1	Metal
R1 shroud	6	SN251 Si_3N_4
V2 support	3	Metal
Vane 2	3	Metal
R2 shroud retaining ring	3	Metal
R2 shroud	6	SN251 Si_3N_4

Legend	°F	°C
A	200.0	93.33
B	400.0	204.44
C	600.0	315.56
D	800.0	426.67
E	1000.0	537.78
F	1200.0	648.89
G	1400.0	760.00
H	1600.0	871.11
I	1800.0	982.22
J	2000.0	1093.33
Max	2190.3	1199.08
Min	199.5	93.08

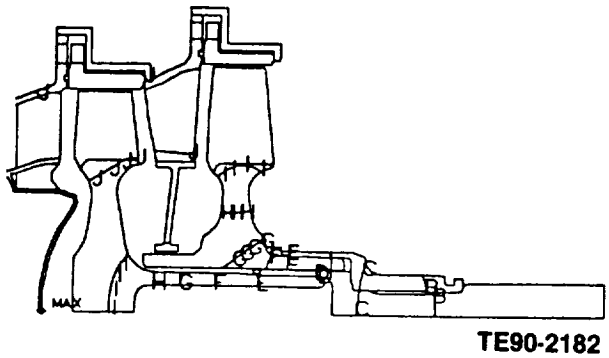

Figure 48. Power turbine assembly temperature distribution, maximum power steady-state operating condition.

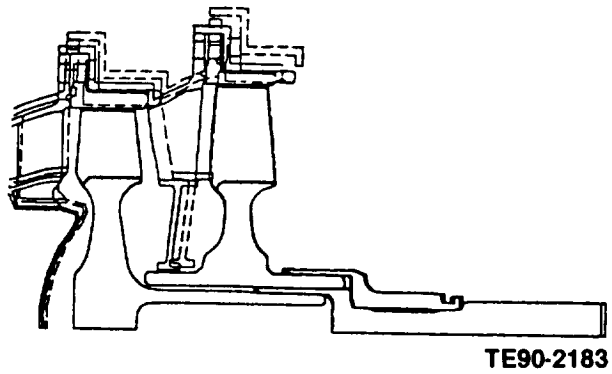

Figure 49. Power turbine assembly static stress deflection plot.

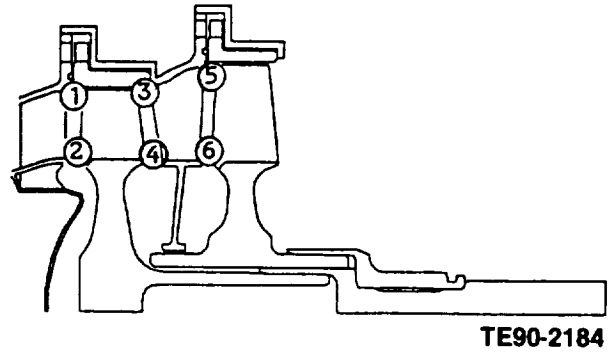

Figure 50. Power turbine axial clearance locations associated with values listed in Table VII.

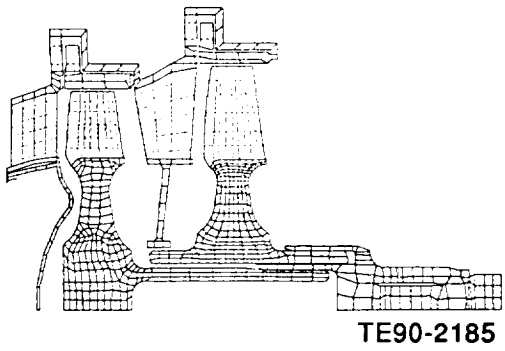

Figure 51. Final power turbine FEM model (reference Figure 6).

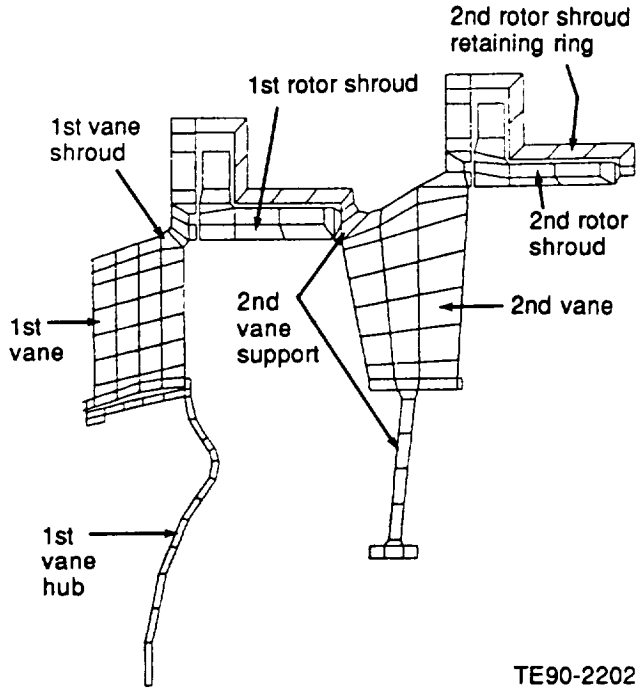

Figure 52. Power turbine static component FEM stress and thermal model (reference Figures 6 and 51).

Legend

	°F	°C
A	1800.0	982.22
B	1840.0	1004.44
C	1880.0	1026.67
D	1920.0	1048.89
E	1960.0	1071.11
F	2000.0	1093.33
G	2040.0	1115.56
H	2080.0	1137.78
I	2120.0	1160.00
Max	2127.6	1164.23
Min	1789.7	976.48

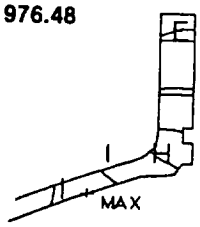

Legend

	Ksi	MPa
A	3.0	20.68
B	6.0	41.37
C	9.0	62.05
D	12.0	82.74
E	15.0	103.42
F	18.0	124.11
G	21.0	144.79
H	24.0	165.47
I	27.0	186.16
Max	27.7	190.75
Min	.2	1.26

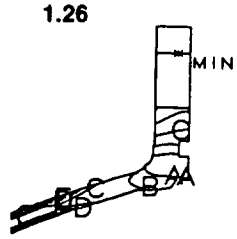

TE90-2203

Figure 53. Temperature and stress distributions: power turbine first vane shroud, maximum power steady-state operating condition (reference Figure 52).

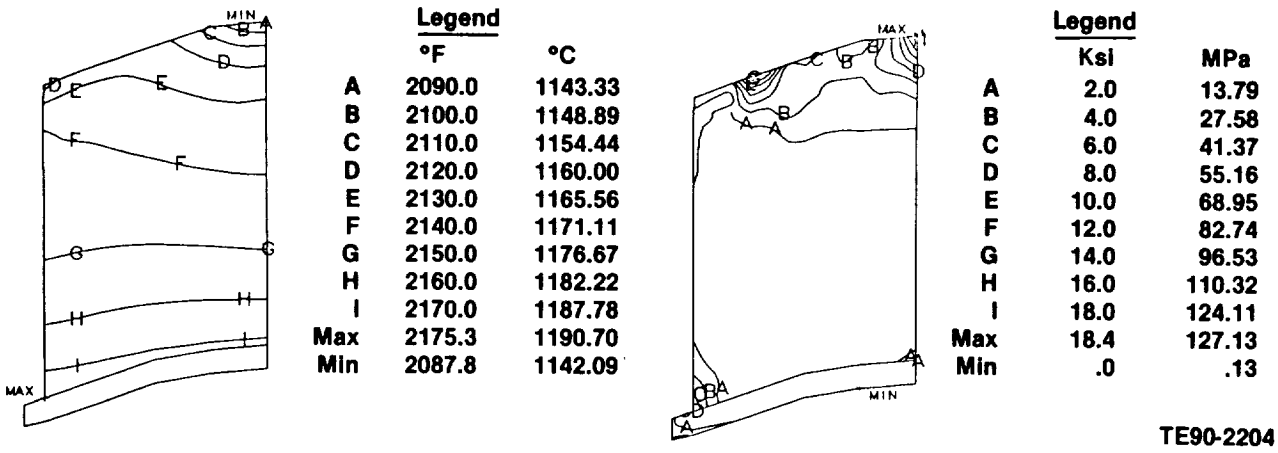

Legend	°F	°C
A	2090.0	1143.33
B	2100.0	1148.89
C	2110.0	1154.44
D	2120.0	1160.00
E	2130.0	1165.56
F	2140.0	1171.11
G	2150.0	1176.67
H	2160.0	1182.22
I	2170.0	1187.78
Max	2175.3	1190.70
Min	2087.8	1142.09

Legend	Ksi	MPa
A	2.0	13.79
B	4.0	27.58
C	6.0	41.37
D	8.0	55.16
E	10.0	68.95
F	12.0	82.74
G	14.0	96.53
H	16.0	110.32
I	18.0	124.11
Max	18.4	127.13
Min	.0	.13

Figure 54. Temperature and stress distributions: power turbine first vane, maximum power steady-state operating condition (reference Figure 52).

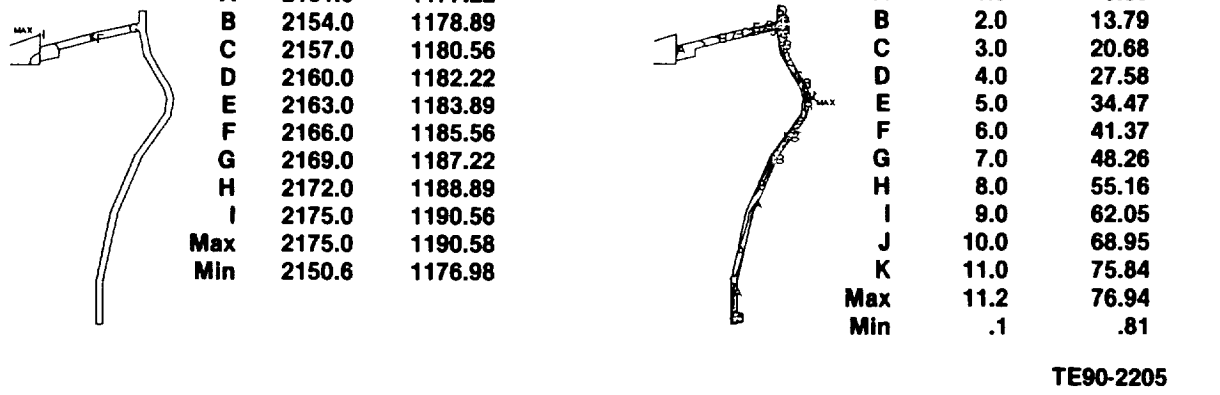

Legend	°F	°C
A	2151.0	1177.22
B	2154.0	1178.89
C	2157.0	1180.56
D	2160.0	1182.22
E	2163.0	1183.89
F	2166.0	1185.56
G	2169.0	1187.22
H	2172.0	1188.89
I	2175.0	1190.56
Max	2175.0	1190.58
Min	2150.6	1176.98

Legend	Ksi	MPa
A	1.0	6.89
B	2.0	13.79
C	3.0	20.68
D	4.0	27.58
E	5.0	34.47
F	6.0	41.37
G	7.0	48.26
H	8.0	55.16
I	9.0	62.05
J	10.0	68.95
K	11.0	75.84
Max	11.2	76.94
Min	.1	.81

Figure 55. Temperature and stress distributions: power turbine first vane hub, maximum power steady-state operating condition (reference Figure 52).

The first-stage nozzle assembly, shown as two components in Figures 53 and 54, is actually one casting. The structure has been subdivided into two components so that the temperature and stress levels can be presented in greater detail. The sheet metal diaphragm (hub) shown in Figure 55 is attached to the first-stage vane casting by welding and clamping. Stress levels in the first-stage vane and hub are moderate at the maximum power steady-state operating condition.

The ceramic first-stage rotor tip shroud (Figure 56) is mounted to the first-stage vane via crosskeys and retained in place by the second-stage vane assembly. Stress levels in the ceramic shroud are very low during maximum power steady-state operation.

The second-stage vane assembly, shown as two components in Figures 57 and 58 is also a one-piece casting. The structure has been subdivided to provide greater detail similar to the first-stage nozzle analysis. The diaphragm in the second-stage vane (lower detail in Figure 57) is an integral part of the vane casting. Stress levels in the second-stage vane assembly are also moderate at the maximum power operating condition.

The ceramic second-stage rotor tip shroud (Figure 60) is mounted to the second-stage vane by crosskeys

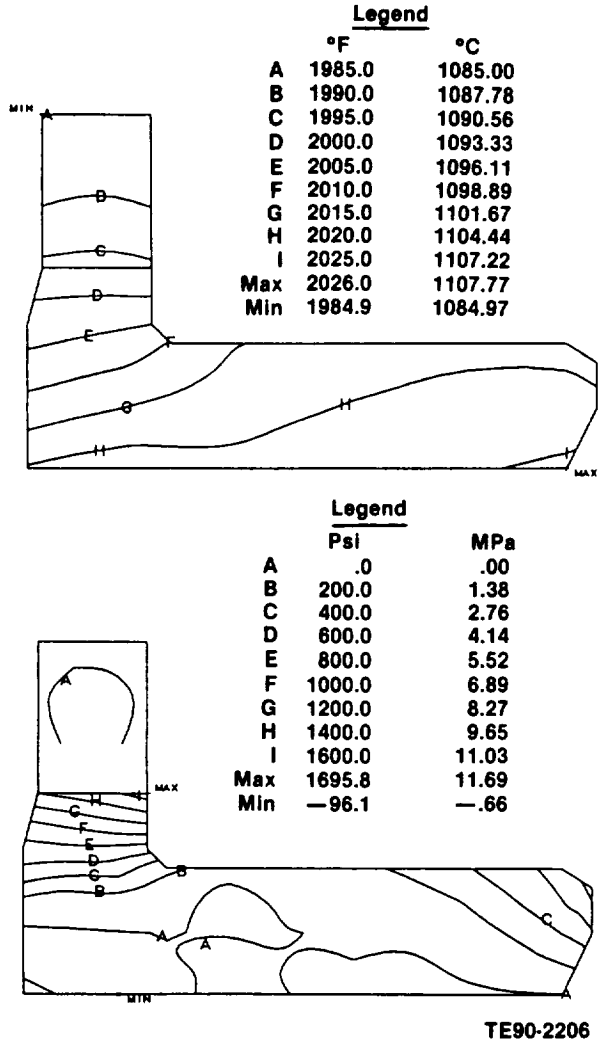

Figure 56. Temperature and stress distributions: power turbine first rotor shroud, maximum power steady-state operating condition (reference Figure 52).

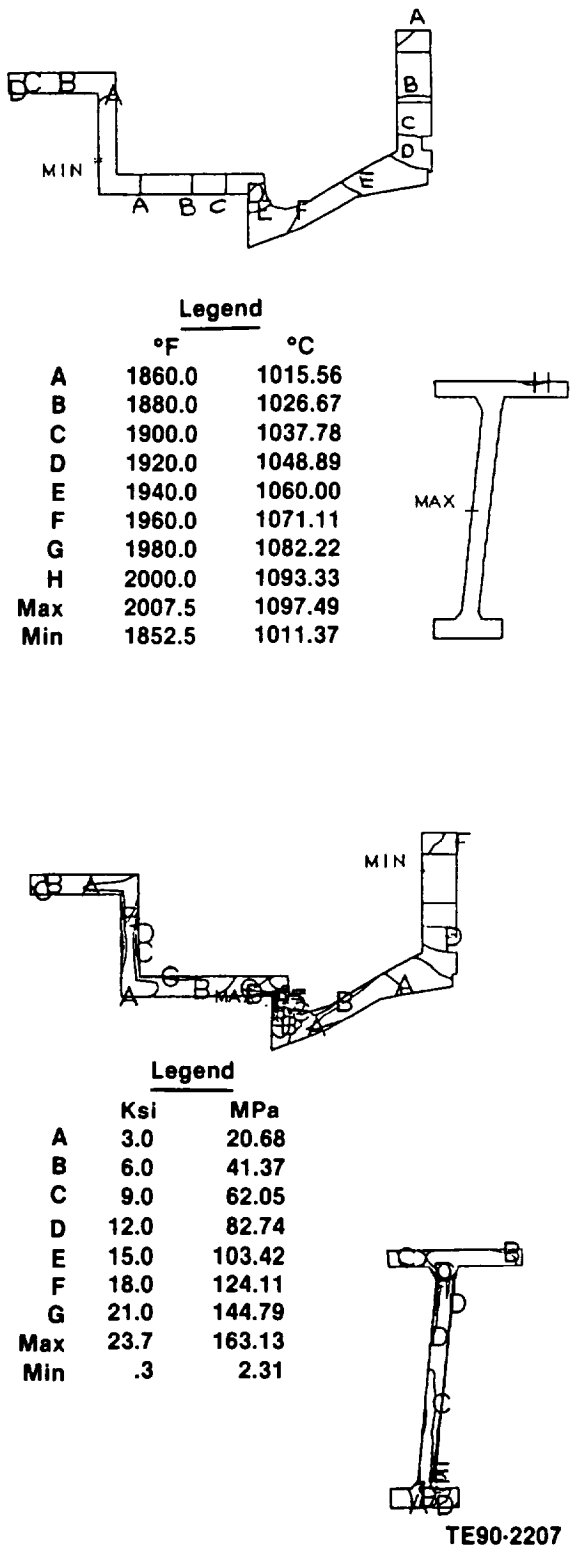

Figure 57. Temperature and stress distributions: power turbine second vane support, maximum power steady-state operating condition (reference Figure 52).

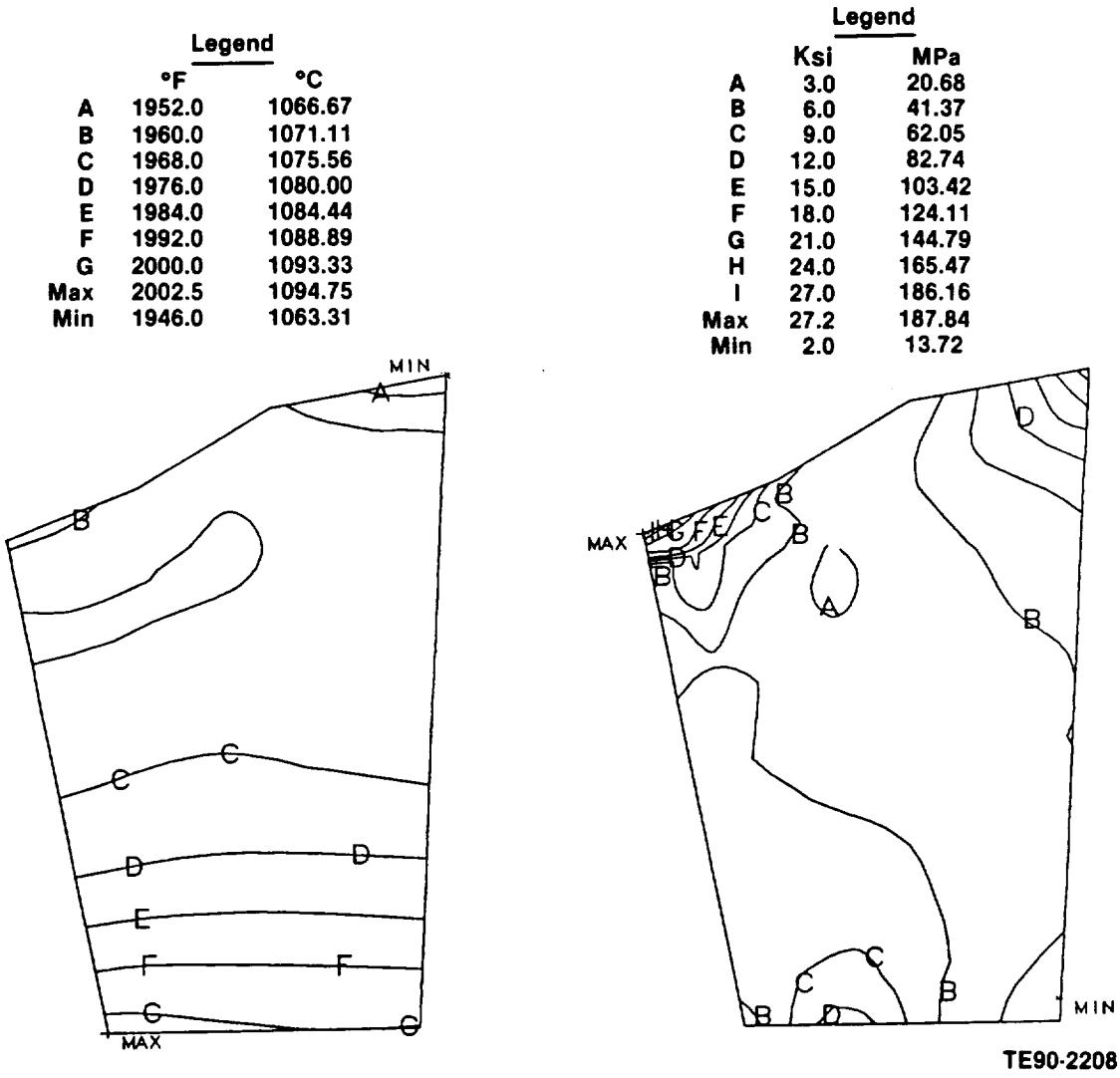

Figure 58. Temperature and stress distributions: power turbine second vane, maximum power steady-state operating condition (reference Figure 52).

(similar to the first stage) and retained in place by the retaining ring shown in Figure 59. Stress levels in the ceramic shroud are very low at the maximum power operating condition.

Temperatures within the power turbine static components were also calculated for several slices in time during cold start to maximum power operation. Stresses in each component were then calculated at the specified conditions. The most severe operating condition for the *ceramic components* occurs at steady-state maximum power. However, the *metallic components* encountered peak (local) stresses during the transient portion of the start-up. The peak (local) stress in each metallic component is illustrated in Figure 61 as a function of its corresponding temperature at various times during the transient cycle up to the steady-state maximum power operating condition. The 0.2% yield and ultimate strength of NX188 material (the material from which these components are fabricated) are also depicted in this same figure. As indicated in the figure, peak stresses (localized) in most of the metallic components exceed the material yield strength (at corresponding temperature) momentarily during the transient cycle and then recede to levels less than yield strength at steady-state operation. These transient results, in view of the available material data for NX-188, were considered unacceptable.

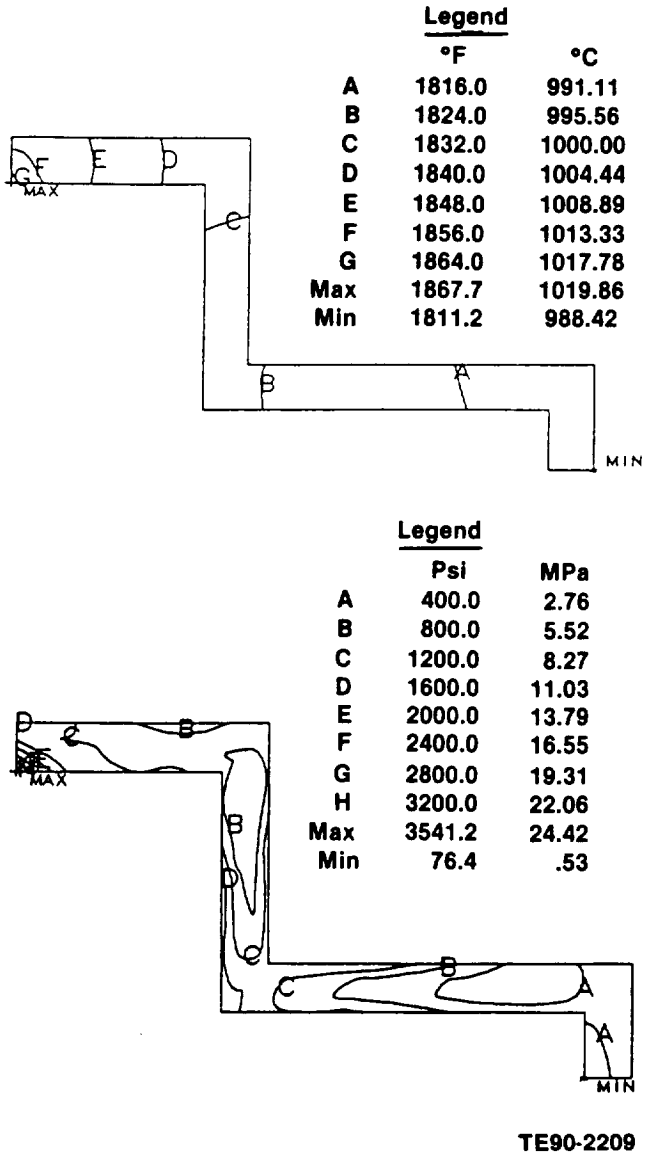

Figure 59. Temperature and stress distributions: power turbine second rotor shroud retaining ring, maximum power steady-state operating condition (reference Figure 52).

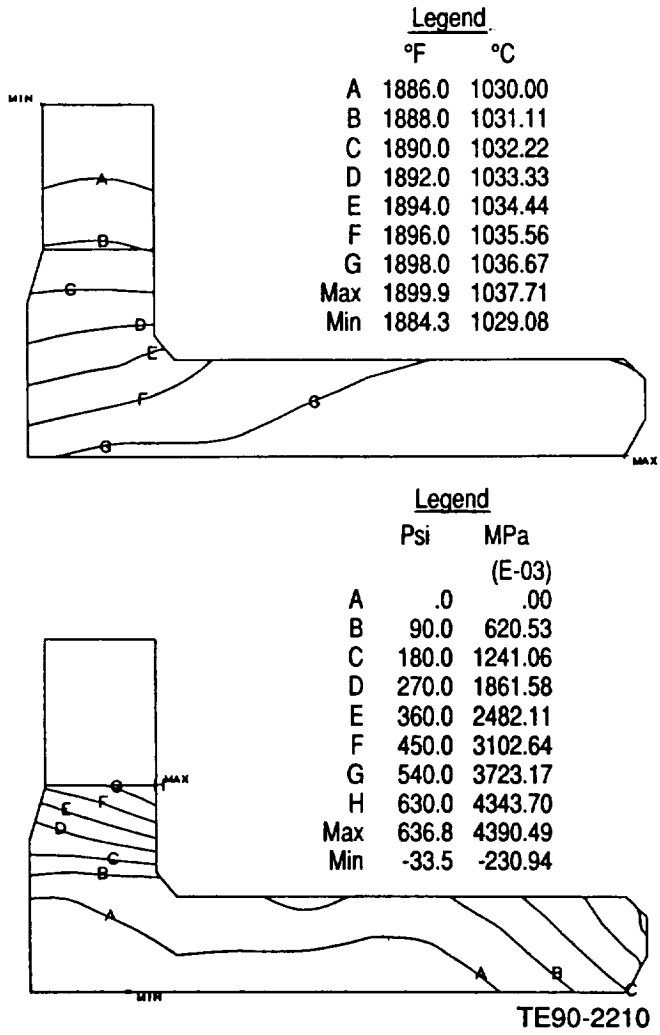

Figure 60. Temperature and stress distributions: power turbine second rotor shroud, maximum power steady-state operating condition (reference Figure 52).

A modified transient cycle was then developed by increasing idle time and employing a more moderate acceleration to maximum power so that stress levels remained below the material yield strength throughout the transient condition. The resulting transient, called the "Test Stand Transient," is presented in Figure 62. The time from cold start to maximum power is increased to 64 sec in this new test-stand only schedule. The resulting relationship between the NX-188 component stresses and the material strength corresponding to the test stand transient is illustrated in Figure 63. The temperature distributions and resulting stresses for the most "severe condition," which occurred at 65 sec, are presented in Figures 64 through 71. Rapid accelerations and sustained high speeds may require modification of the metal component designs, the incorporation of power turbine cooling, or the substitution of more ceramic components. Future plans include further analysis of other ceramic static power turbine components. Initial testing will utilize the "test stand transient" to ensure that excessively high stresses are not encountered in the metallic power turbine static structure as presently designed.

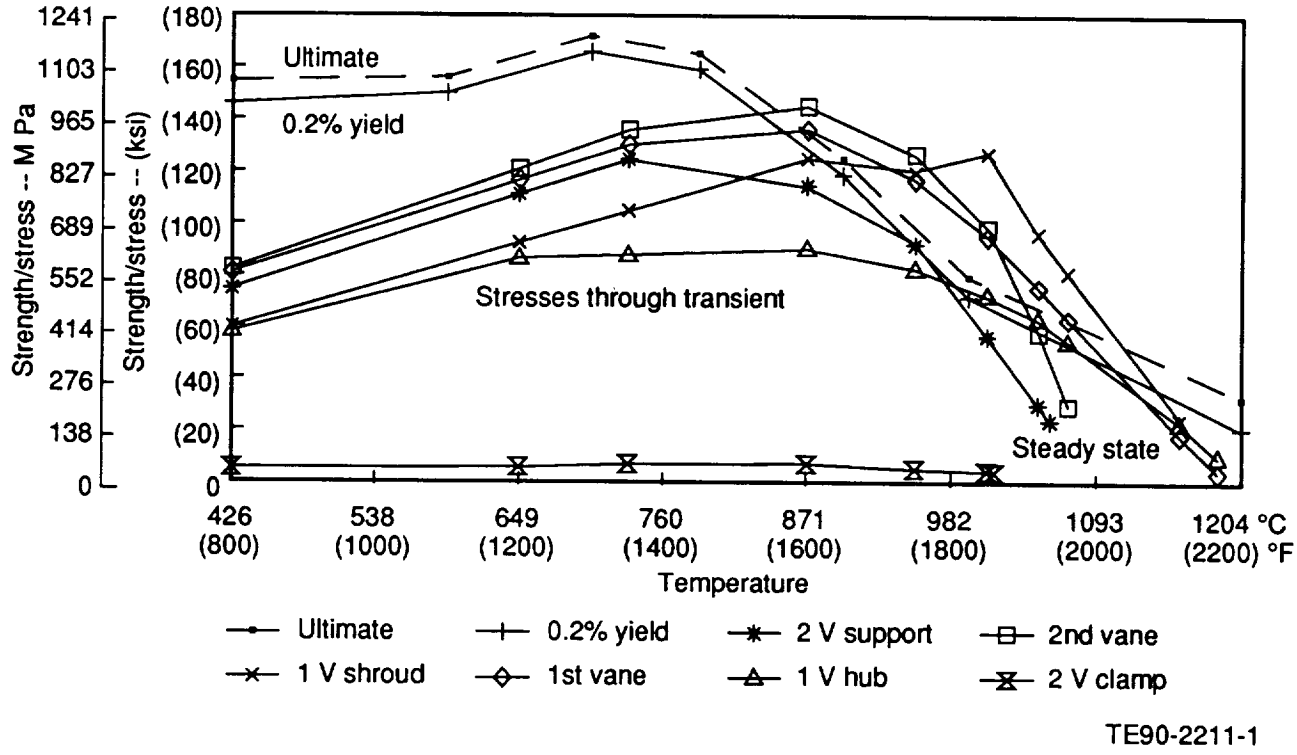

Figure 61. Original power turbine static component stress summary during transient operation.

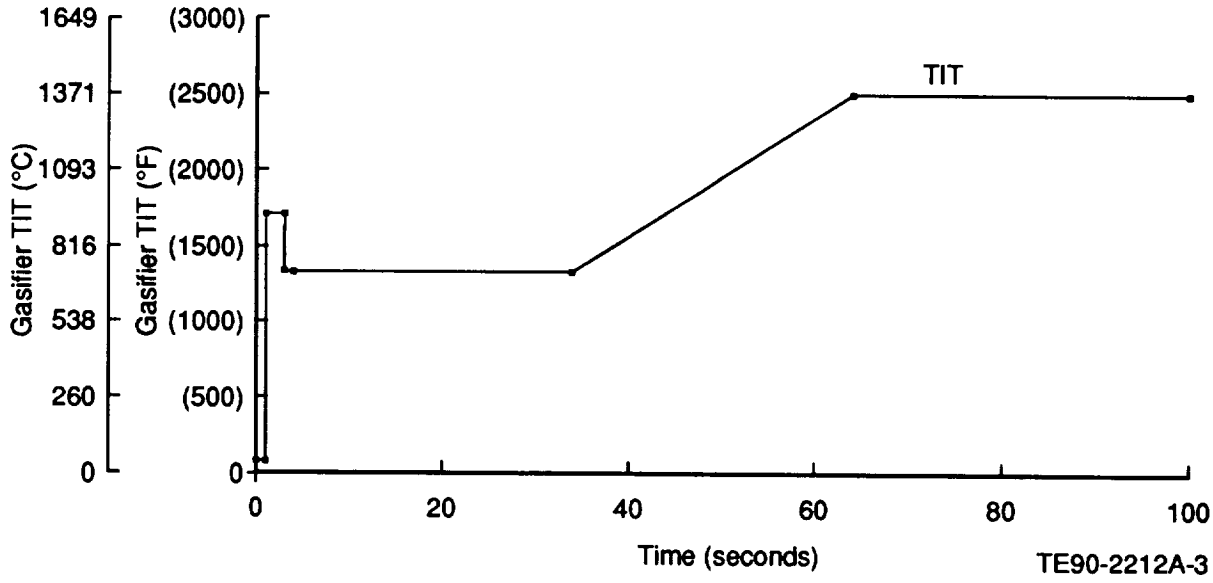

Figure 62. Test stand transient definition.

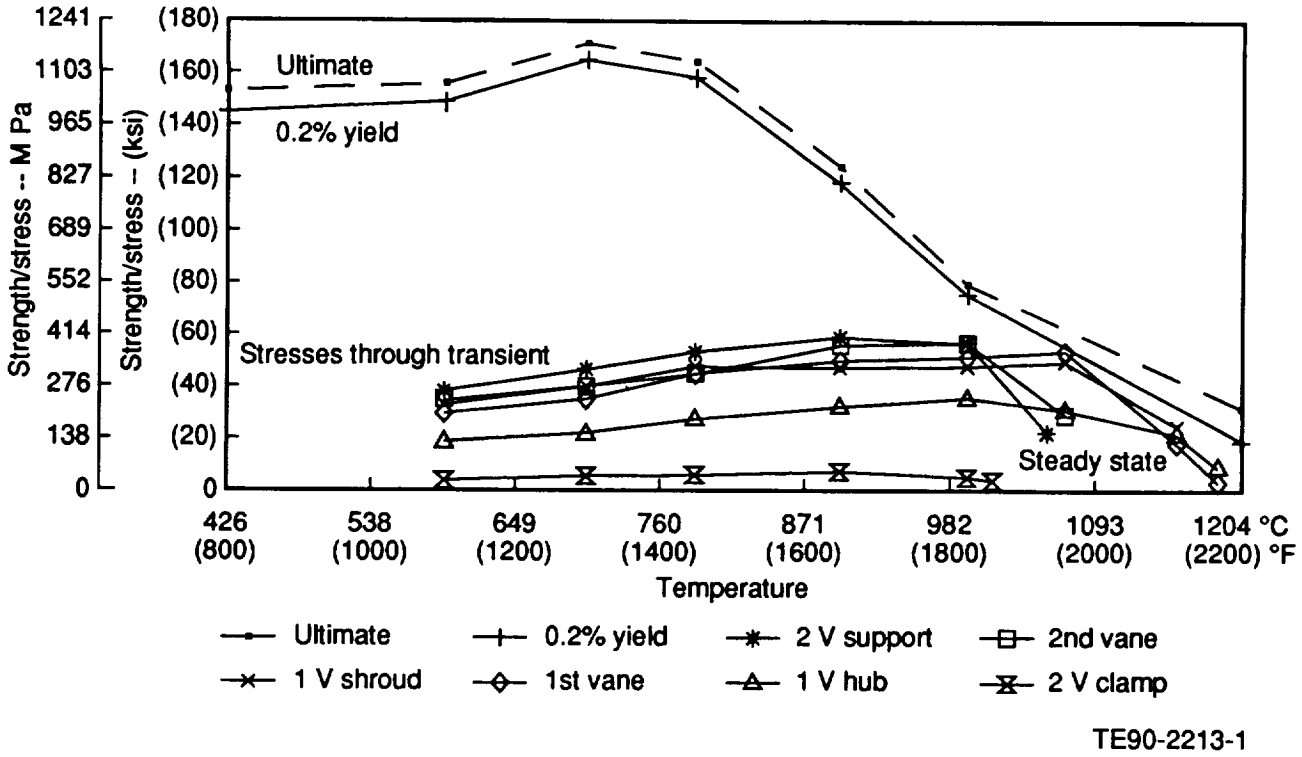

Figure 63. Revised power turbine static component stress summary during "test stand transient" operation.

Temperatures and stresses in the first-stage vane assembly are presented in Figures 64 through 66. Stresses very near yield still exist at the trailing edge of the vane at the outer shroud.

The temperatures and stresses in the second-stage power turbine vane are illustrated in Figures 68 and 69. Peak stresses (about 413 MPa [60 ksi]) exist at the leading edge of the vane and in the center portion of the outer shroud. Very low stresses exist in the second-stage shroud retaining ring as indicated in Figure 70.

The first- and second-stage rotor tip shrouds are currently the only two ceramic components in the static structure of the power turbine. In the design analysis, SN251 (Si_3N_4) material was specified for these components. Actual components will be fabricated of SN252 (Si_3N_4) material, which is very similar to SN251. These ceramic shrouds provide improved aerodynamic power turbine performance due to the close tip clearance control achieved by having expansion characteristics compatible with the ceramic rotors. The temperature and stress profiles in the two rotor tip shrouds, as presented in Figures 67 (first stage) and 71 (second stage), indicate that the maximum stress in both shrouds is very low. The probability of survival summary for these components is presented in Table IX. As previously stated, the most severe operating condition for these ceramic parts occurs at steady-state maximum power operation.

Table IX.
Ceramic shroud survivability summary.

Stage	Material	Goal POS	SS POS	Minimum POS* through transient
1	SN251 Si_3N_4	0.9980	0.9999	0.9999
2	SN251 Si_3N_4	0.9980	0.9999	0.9999

*Minimum POS for both shrouds occurs at steady-state condition.

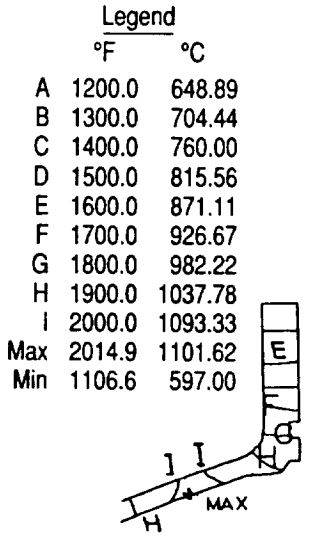

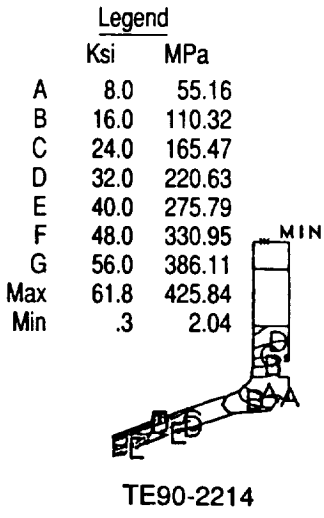

TE90-2214

Figure 64. Temperature and stress distributions: power turbine first vane shroud, worst case test stand transient condition.

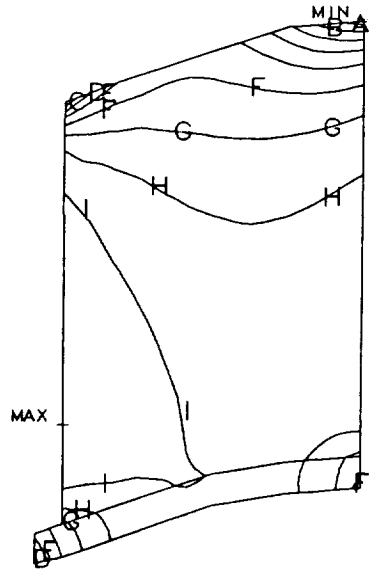

Legend

	°F	°C
A	1920.0	1048.89
B	1940.0	1060.00
C	1960.0	1071.11
D	1980.0	1082.22
E	2000.0	1093.33
F	2020.0	1104.44
G	2040.0	1115.56
H	2060.0	1126.67
I	2080.0	1137.78
Max	2098.3	1147.92
Min	1909.8	1043.24

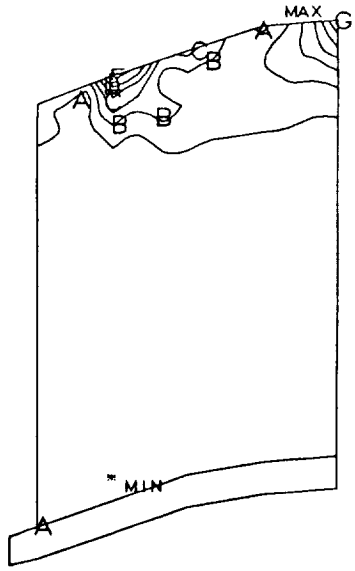

Legend

	Ksi	MPa
A	7.0	48.26
B	14.0	96.53
C	21.0	144.79
D	28.0	193.05
E	35.0	241.32
F	42.0	289.58
G	49.0	337.84
Max	50.4	347.72
Min	.1	.56

TE90-2215

Figure 65. Temperature and stress distributions: power turbine first vane, worst case test stand transient condition.

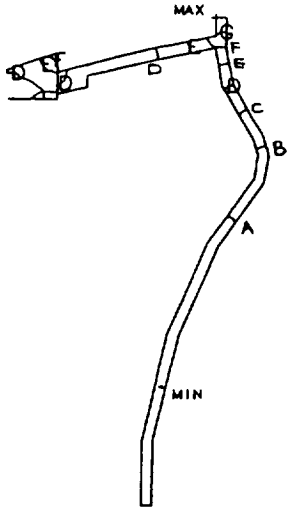

Legend	°F	°C
A	1830.0	998.89
B	1860.0	1015.56
C	1890.0	1032.22
D	1920.0	1048.89
E	1950.0	1065.56
F	1980.0	1082.22
G	2010.0	1098.89
Max	2034.3	1112.40
Min	1810.2	987.89

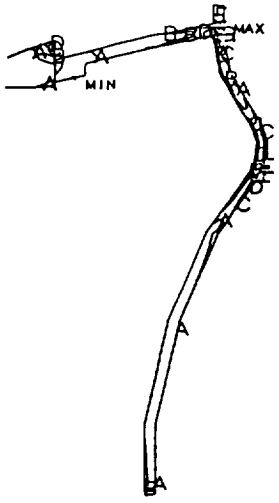

Legend	Ksi	MPa
A	4.0	27.58
B	8.0	55.16
C	12.0	82.74
D	16.0	110.32
E	20.0	137.90
F	24.0	165.47
G	28.0	193.05
H	32.0	220.63
Max	34.4	237.30
Min	.5	3.26

TE90-2216

Figure 66. Temperature and stress distributions: power turbine first vane hub, worst case test stand transient condition.

Legend	°F	°C
A	1430.0	776.67
B	1440.0	782.22
C	1450.0	787.78
D	1460.0	793.33
E	1470.0	798.89
F	1480.0	804.44
G	1490.0	810.00
H	1500.0	815.56
Max	1505.5	818.60
Min	1427.0	775.02

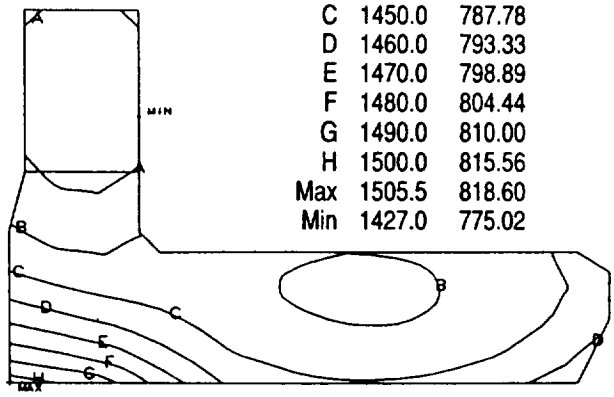

Legend	Psi	MPa
A	-400.0	-2.76
B	.0	.00
C	400.0	2.76
D	800.0	5.52
E	1200.0	8.27
F	1600.0	11.03
G	2000.0	13.79
H	2400.0	16.55
Max	2491.5	17.18
Min	-467.6	-3.22

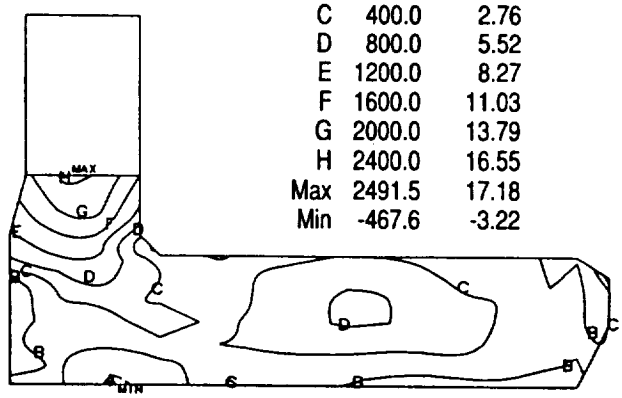

TE90-2217

Figure 67. Temperature and stress distributions, power turbine first rotor shroud, worst case test stand transient condition.

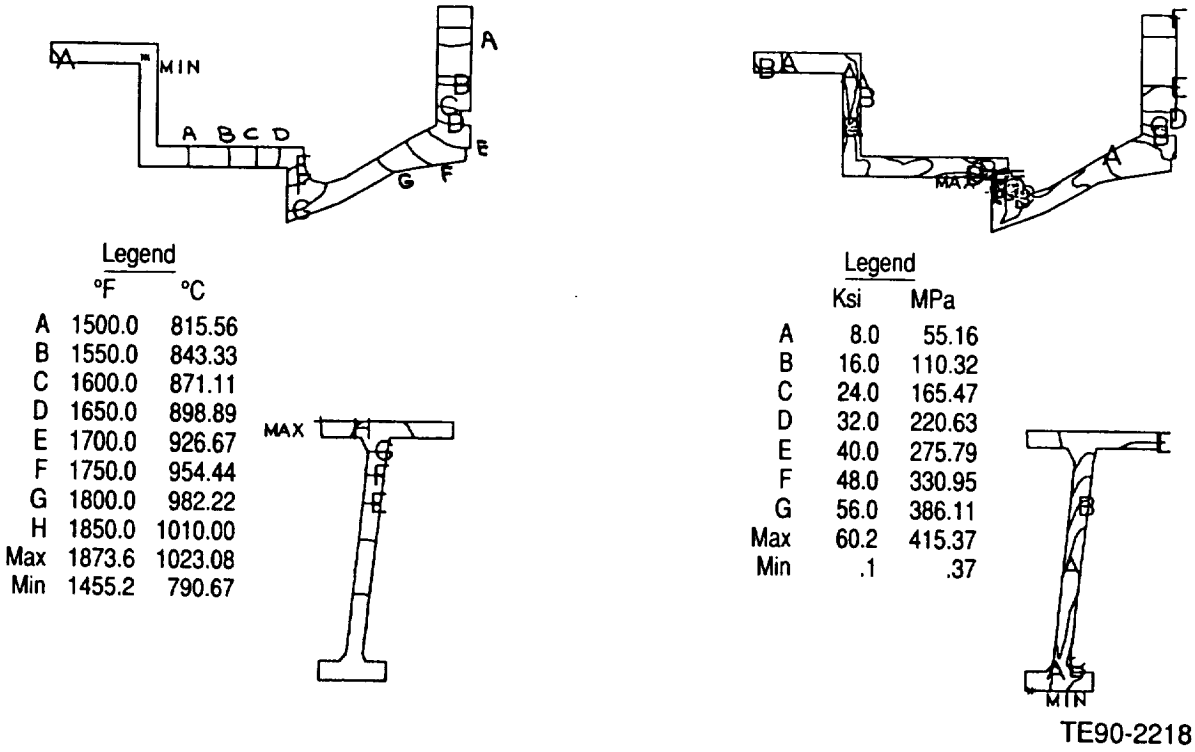

Figure 68. Temperature and stress distributions: power turbine second vane support, worst case test stand transient condition.

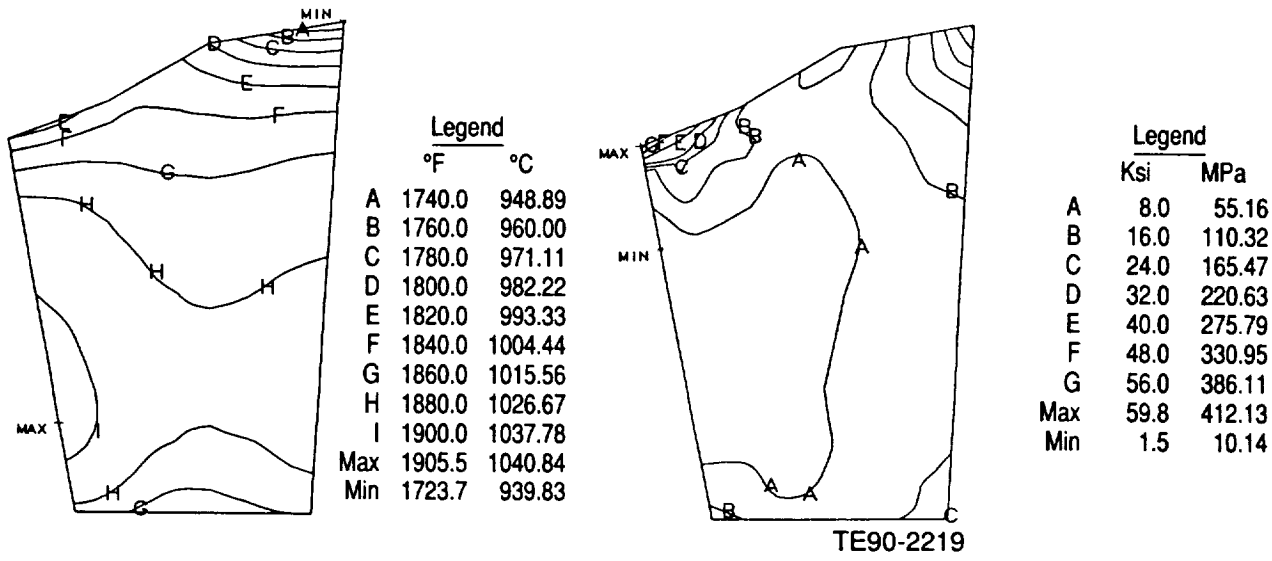

Figure 69. Temperature and stress distributions: power turbine second vane, worst case test stand transient condition.

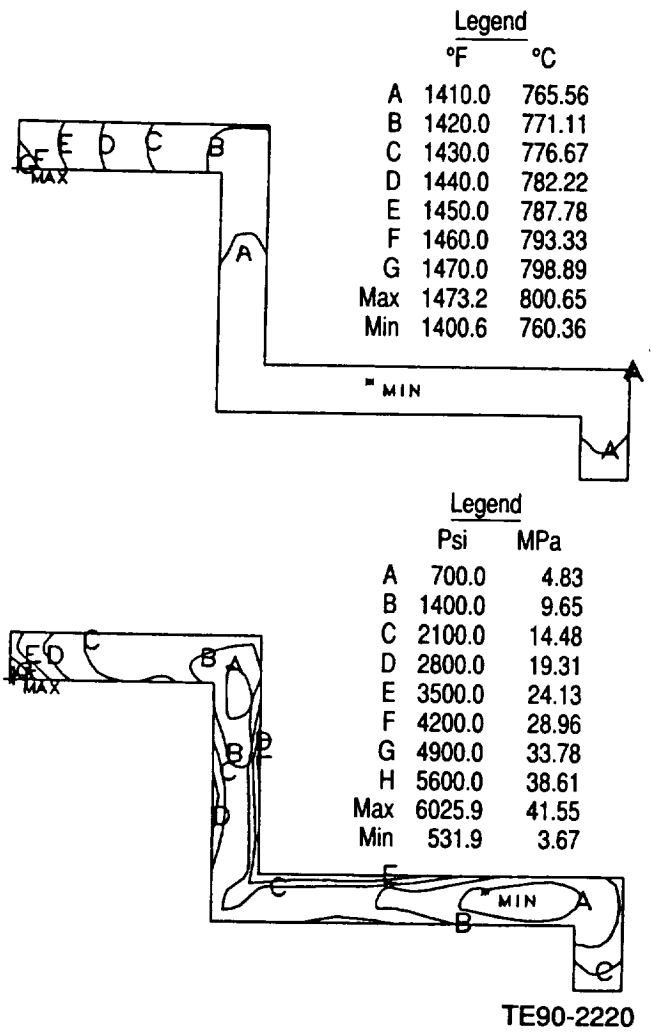

Figure 70. Temperature and stress distributions: power turbine second rotor shroud retaining ring, worst case test stand transient condition.

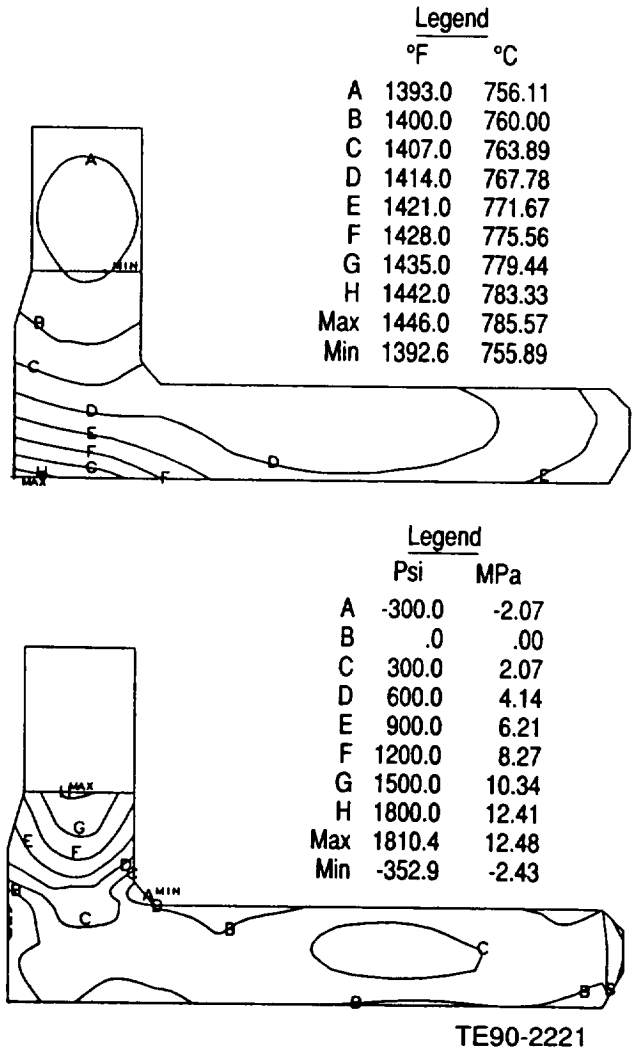

Figure 71. Temperature and stress distributions: power turbine second rotor shroud, worst case test stand transient condition.

Rotors. The rotating component finite element grid used for both steady-state and transient thermal and stress analyses is presented in detail in Figure 72.

The maximum power turbine shaft design speed was set at 110% N_2 or 62,700 rpm. This value corresponds to the transmission shift speed at wide open throttle engine operating conditions.

A summary of the predicted maximum temperatures, maximum principal stresses, radial expansions/deflections, and POSs occurring within the ceramic power turbine rotors during steady-state and transient start-up conditions is presented in Table X.

The first-stage power turbine rotor and the gasifier rotor exhibit similar temperature and stress characteristics due to their design similarity. The first-stage power turbine rotor was modeled using Kyocera's SN252 silicon nitride material. The temperature gradients incurred by this rotor during steady-state and start-up transient conditions display the same trends as those observed in the gasifier rotor, although, as expected, thermal and stress gradients are not as severe. Temperature gradients from the rotor rim to the shaft are 649°C (1200°F) and 743°C (1370°F) for steady-state and transient conditions, respectively (Figures 73 and 74). These temperature gradients and the centrifugal loading produce maximum principal stresses of 294 MPa (42.7 ksi) in the forward wheel

Table X.
Ceramic power turbine rotor analysis summary.

	First stage	Second stage
Material	SN252 Si_3N_4	SN220M Si_3N_4
Steady-state conditions		
• Maximum temperature--°C (°F)	1137.5 (2079.5)	1049.9 (1921.8)
• Maximum principal stress--MPa (ksi)	186.9 (27.1)	313.0 (45.4)
• Radial expansion/deflection--mm (in.)	0.21 (0.0082)	0.22 (0.0087)
• POS	0.9997	0.9742
Start-up transient conditions		
• Time of maximum principal stress (sec) (after start-up)	30	30
• Maximum temperature--°C (°F) (at maximum stress condition)	1133.6 (2072.4)	1047.7 (1917.9)
• Maximum principal stress--MPa (ksi)	294.4 (42.7)	340.6 (49.4)
• Radial expansion/deflection--mm (in.)	0.14 (0.0055)	0.15 (0.0060)
• POS	0.9883	0.9691
• POS goal	0.9853	0.9862

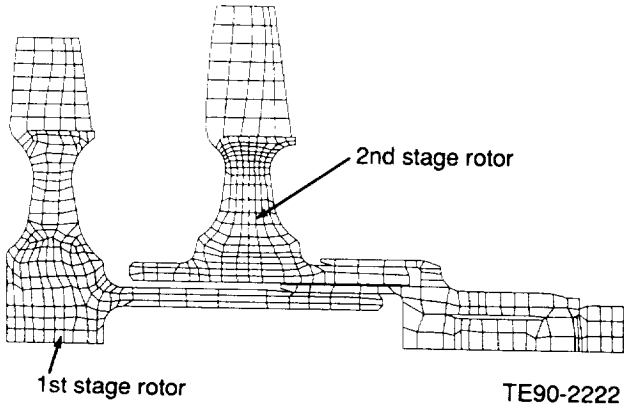

Figure 72. FEM grid of power turbine rotating components (reference Figures 6 and 51).

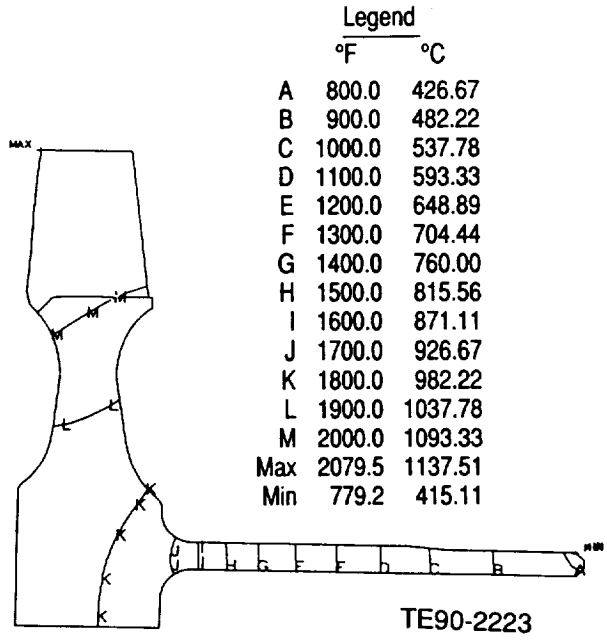

Figure 73. First-stage power turbine rotor temperature profile, maximum power steady-state condition, SN252 material.

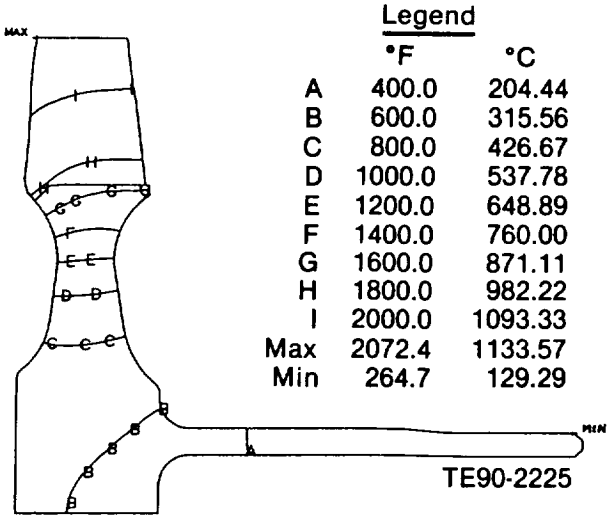

Figure 74. First-stage power turbine rotor temperature profile, 30 sec after start-up, SN252 material.

face of the first-stage rotor during the transient condition (Figure 75), but are much lower during steady-state operation (Figure 76). Radial stresses in the rotor wheel are the main components of the maximum principal stress profile. The predicted POS of this rotor during both steady-state and transient start-up conditions exceeds the design goal.

Because of the bore through the second-stage ceramic power turbine rotor, the POS of this rotor was anticipated to be low. Subsequent analysis used

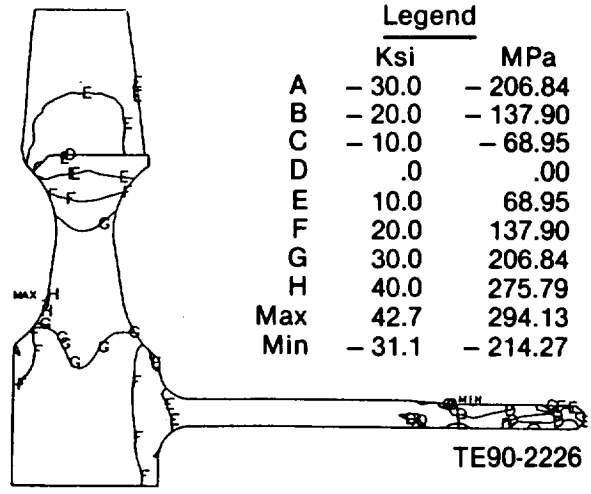

Figure 75. First-stage power turbine rotor maximum principal stress profile, 30 sec after start-up, SN252 material.

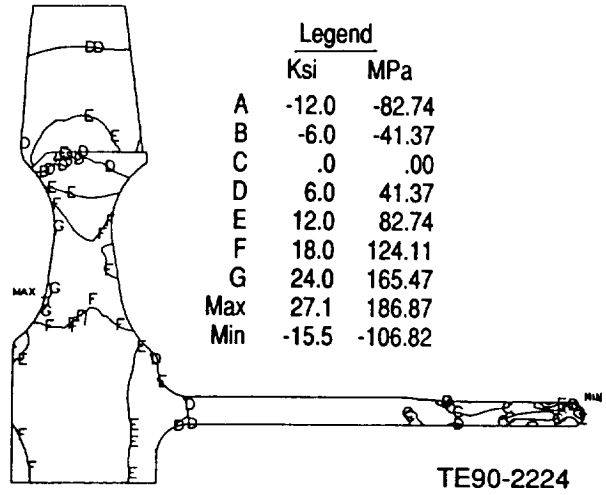

Figure 76. First-stage power turbine rotor maximum principal stress profile, maximum power steady-state operating condition, SN252 material.

Kyocera's SN220M silicon nitride material. Temperature gradients from the rotor rim to the shaft are approximately 593°C (1100°F) for both the maximum power and transient operating conditions (Figures 77 and 78). These gradients are less than those observed in the first-stage power turbine rotor. The stress profiles calculated for steady-state and transient operation (Figures 79 and 80) indicate a maximum principal stress of 341 MPa (49.4 ksi) in the bore of the second-stage rotor during the transient start-up acceleration. The maximum principal stress levels are somewhat lower during the steady-state condition. Again, these stresses are caused by the combination of centrifugal loading due to the turbine blades and the thermal gradient through the rotor. Tangential stresses, due to the hole through the center of the second-stage rotor, are the main component of the maximum principal stress profile. Because the predicted POS of this rotor is lower than the design goal, a material change to a stronger silicon nitride is being considered.

Since good performance has been demonstrated with the gasifier rotor shaft attachment scheme, the power turbine rotor shaft attachments were modeled and designed in the same manner. The attachment temperatures for the first-stage assembly during steady-state (the worst case) vary from 426°C (800°F) to 537°C (1000°F). The second stage has steady-state attachment assembly temperatures varying from 399°C (750°F) to 537°C (1000°F).

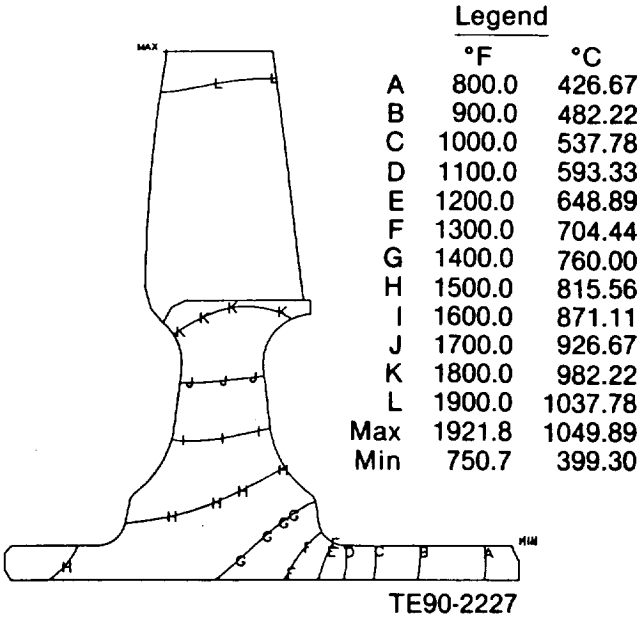

Figure 77. Second-stage power turbine rotor temperature profile, maximum power steady-state operating condition, SN220M material.

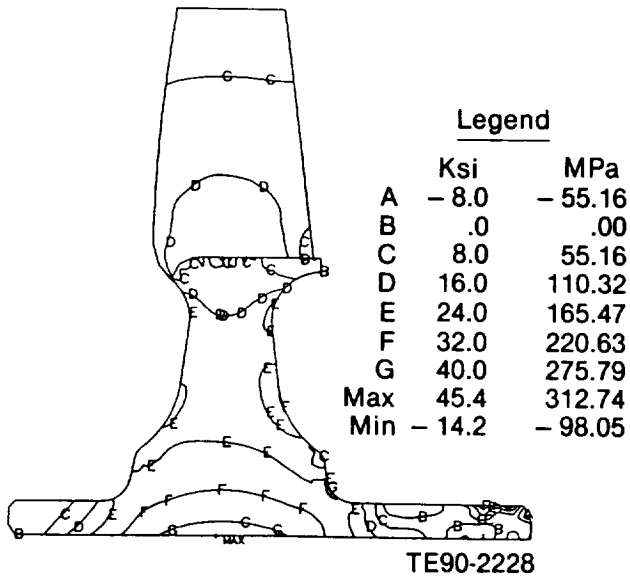

Figure 79. Second-stage power turbine rotor maximum principal stress profile, maximum power steady-state operating condition, SN220M material.

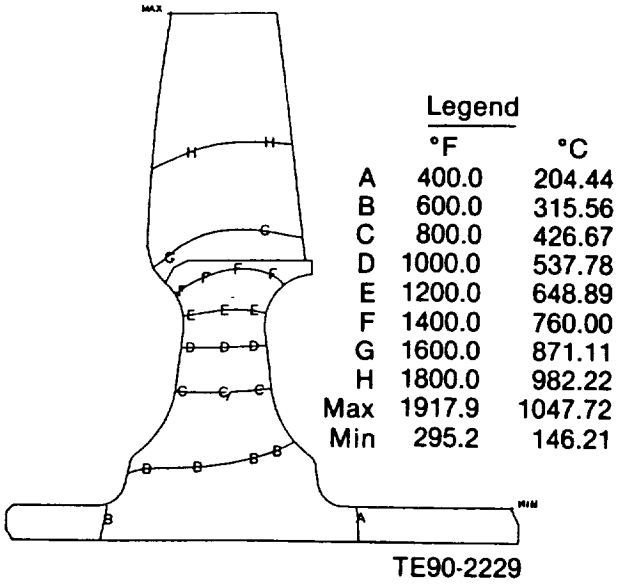

Figure 78. Second-stage power turbine rotor temperature profile, 30 sec after start-up, SN220M material.

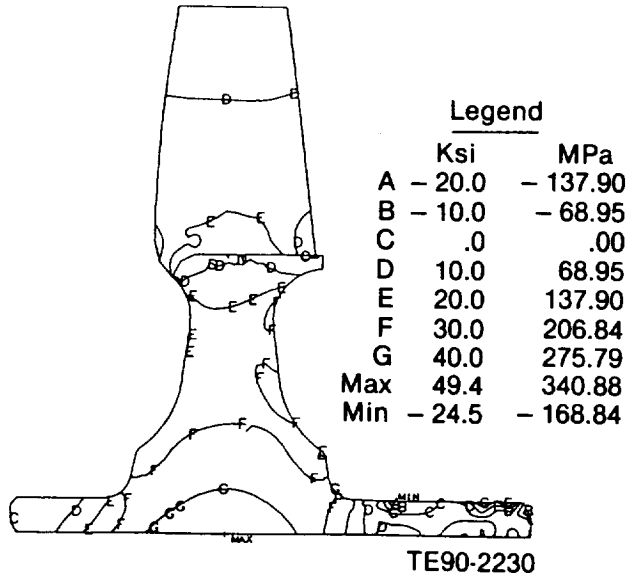

Figure 80. Second-stage power turbine rotor maximum principal stress profile, 30 sec after start-up, SN220M material.

III. MATERIALS CHARACTERIZATION AND CERAMIC COMPONENT FABRICATION

The materials characterization and ceramic component fabrication sections describe the ongoing ceramic material and component fabrication, characterization, and development activities, which are a key focus of the ATTAP program. The ceramic materials subsection documents the results of characterization and qualification of candidate ceramic materials and components being developed for advanced gas turbine engines. This includes characterizations of material properties (e.g., densities, fracture strengths, microstructures, fracture toughnesses), results of failure analyses of rig/engine tested components, and nondestructive evaluation results. The ceramic component fabrication subsection describes the ongoing ceramic component process development activities at the selected ceramic suppliers, including Carborundum, Manville, GTE Laboratories, Corning, Garrett Ceramic Components, and Ceramics Process Systems. Allison's approach to ceramic component technology development continues to be one of subcontracting process development to the domestic ceramic manufacturing community and working in an iterative development loop with those suppliers in areas of component design, fabrication, characterization, and rig/engine data feedback. While basic ceramic materials development is not a part of the ATTAP program, the program integrates material developments from Oak Ridge programs, supplier in-house activities, and other sources as they become available for component fabrication efforts.

3.1 MATERIALS AND COMPONENT CHARACTERIZATION

3.1.1 Material Properties and Microstructure

Objective/Approach

The materials and component characterization efforts have focused on the testing and evaluation of candidate ceramic materials and components for use in the ATTAP AGT-5 automotive gas turbine engine test-bed. The primary objective of this task is to establish a database of appropriate material characteristics to support the design, development, and testing of hot section ceramic components, and to generate understanding of the material characteristics for iterative development and refinement with the ceramic component suppliers. Characterization work is performed not only on materials and components of current development focus, but also on new or emerging materials, processes, and suppliers to assess candidates for subsequent component development activities. In addition, characterization of nondomestic materials and components helps in the continual assessment of the state of the art. The material characterization activities have focused on microstructural, density, fracture toughness, and flexural strength evaluations of various candidate ceramic materials. Fracture surface analysis is used to determine the nature and location of the strength-controlling defects. In addition, the time dependent strength characteristics and oxidation resistance are evaluated for select materials.

Accomplishments/Results

The ceramic materials and components that were characterized include the following:

- GTE Laboratories AY6 Si_3N_4
- GTE Laboratories PY6 Si_3N_4
- NGK Spark Plug EC-152 Si_3N_4
- Carborundum alpha-SiC rotor hubs

In addition, high temperature oxidation testing of various ceramic materials was also conducted.

Discussion

GTE Laboratories AY6 Silicon Nitride. Evaluation of the material characteristics of GTE AY6 Si_3N_4 was conducted. The AY6 Si_3N_4, containing 6% Y_2O_3 and 1.5% Al_2O_3 as sintering additives, was produced using Ube Si_3N_4 powder and the processing facilities at the GTE Labs Prototype Engineering Center. A total of 200 test bars were fabricated by injection molding and hot isostatic pressing (HIP). One hundred test bars were received with all four surfaces machined, with an additional 100 test specimens supplied with three sides machined and the remaining surface having an as-fired (as-HIPed) surface condition. The average density measured 3.254 gm/cc (0.117 lb/in.^{3}), 99.8% of theoretical density.

The flexural strength characteristics of the AY6 Si_3N_4 material are summarized in Table XI. The average room temperature strength of test bars

Table XI.
Strength characteristics of GTE Labs injection molded and HIPed AY6 silicon nitride.

Temperature--°C (°F)	Strength--MPa (ksi) Machined	As-Fired
25 (77)	1121.75 (162.69)	640.89 (92.95)
1000 (1832)	940.00 (136.33)	518.71 (75.23)
1150 (2102)	755.97 (109.64)	494.99 (71.79)
1250 (2282)	644.82 (93.52)	457.21 (66.31)

evaluated with a machined surface condition measured 1121.75 MPa (162.69 ksi) with a Weibull modulus of 16.0. The primary fracture origins were extremely small surface flaws as indicated in Figure 81. The secondary strength-controlling flaws were observed to be "large" beta-Si_3N_4 grains at or near the surface as shown in Figure 82. Machined bars tested at a temperature of 1000°C (1832°F) had an average strength of 940.00 MPa (136.33 ksi). The average strength of machined specimens tested at 1150°C (2102°F) was 755.97 MPa (109.64 ksi), while the average strength recorded at a temperature of 1250°C (2282°F) was 644.82 MPa (93.52 ksi). The primary fracture origins observed in the AY6 Si_3N_4 specimens tested at elevated temperature were small surface flaws similar to those of the room temperature tests.

Test bars evaluated with an as-fired surface condition had an average room temperature fracture strength of 640.89 MP (92.95 ksi) with a Weibull

TE90-2083

Figure 81. Typical fracture origin (small surface flaw) observed in GTE AY6 Si_3N_4 test bars.

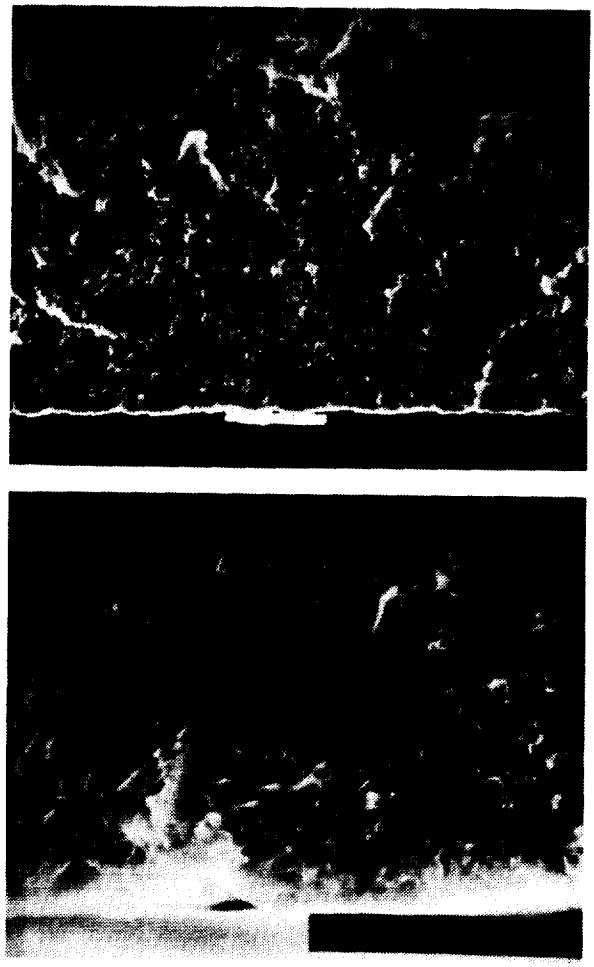

TE90-2084

Figure 82. Secondary fracture origin ("large" beta-Si_3N_4 grain) observed in machined GTE AY6 Si_3N_4 test bars.

modulus of 7.5. The primary fracture origins were observed to be shallow surface depressions/pits such as those shown in Figure 83. Secondary strength-controlling features were observed to be shell-shaped regions at the specimen surface. These latter origins, shown in Figure 84, are the result of impact damage, presumably associated with the removal of the ASEA glass encapsulation material required for HIPing. The strength of the as-fired AY6 Si_3N_4 material at a temperature of 1000°C (1832°F) averaged 518.71 MPa (75.23 ksi), with average strengths of 494.99 MPa (71.79 ksi) and 457.21 MPa (66.31 ksi) measured at temperatures of 1150°C (2102°F) and 1250°C (2282°F), respectively. The fracture origins of the test specimens at elevated temperature were similar to those of the room temperature specimens, i.e., surface depressions and pits.

The fracture toughness (K_{IC}) of the GTE AY6 silicon nitride measured 8.4 $MPa \cdot m^{1/2}$ (7.6 $ksi \cdot in.^{1/2}$) as determined through use of the single-edged notched beam (SENB) method.

GTE Laboratories PY6 Silicon Nitride. Evaluation of the material characteristics of GTE PY6 Si_3N_4 was also conducted during this reporting period. The PY6 Si_3N_4, containing 6% Y_2O_3 as a sintering additive (no alumina), was produced using Ube Si_3N_4 powder and the processing facilities at the GTE Labs Prototype Engineering Center. A total of 100 test bars were fabricated by injection molding and HIPing. Fifty test bars were received with all four surfaces machined, with an additional 50 test specimens supplied with three surfaces machined

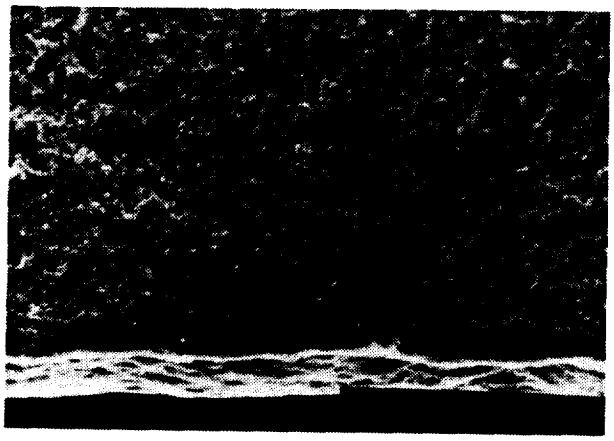

TE90-2085

Figure 83. Typical fracture origin (surface depression) observed in GTE AY6 Si_3N_4 test bars evaluated with an as-HIPed surface.

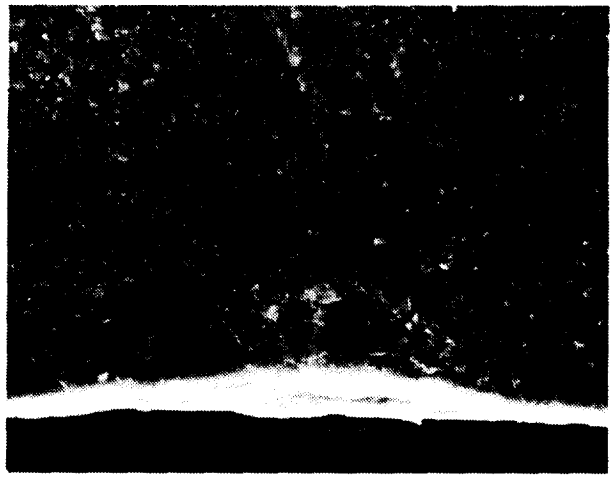

TE90-2086

Figure 84. Secondary fracture origin (shell-type feature) indicative of mechanical/impact damage in GTE AY6 Si_3N_4 as-HIPed test bars.

and the remaining surface having an as-fired (as-HIPed) surface condition. The average density measured 3.262 gm/cc (0.118 $lb/in.^3$), 99.8% of theoretical density.

The flexural strength characteristics of the PY6 Si_3N_4 material are summarized in Table XII. The average room temperature strength of test bars evaluated with a machined surface condition measured 965.37 MPa (140.01 ksi) with a Weibull modulus of 11.5. The primary fracture origins were extremely small surface flaws as indicated in Figure 85. The secondary strength-controlling flaws were observed to be metallic inclusions, consisting primarily of iron silicides, as shown in Figure 86. Machined bars tested at a temperature of 1000°C (1832°F) had an average strength of 827.06 MPa (119.95 ksi). The average strength of machined specimens tested at 1150°C (2102°F) was 678.54 MPa (98.41 ksi), while average strengths of 632.48 MPa (91.73 ksi) and 593.25 MPa (86.04 ksi) were measured at temperatures of 1250°C (2282°F) and 1371°C (2500°F), respectively. The primary fracture origins observed in the PY6 Si_3N_4 specimens tested at elevated temperature were small surface flaws similar to those of the room temperature tests.

Test bars evaluated with an as-fired surface condition had an average room temperature fracture strength of 807.54 MPa (117.12 ksi) with a Weibull modulus of 7.9. The primary fracture origins were observed to be shallow surface depressions/pits

Table XII.
Strength characteristics of GTE Labs injection molded and HIPed PY6 silicon nitride.

Temperature--°C (°F)	Strength--MPa (ksi) Machined	As-Fired
25 (77)	965.37 (140.01)	807.54 (117.12)
1000 (1832)	827.06 (119.95)	550.22 (79.80)
1150 (2102)	678.54 (98.41)	519.06 (75.28)
1250 (2282)	632.48 (91.73)	526.36 (76.34)
1371 (2500)	593.25 (86.04)	510.09 (73.98)

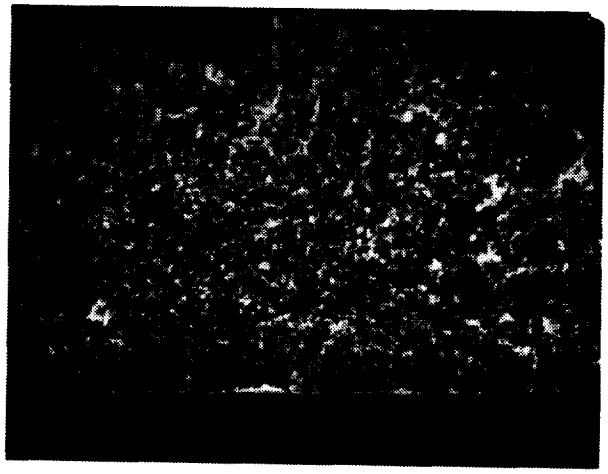

TE90-2087

Figure 85. Primary fracture origin (small surface flaw) observed in GTE PY6 Si_3N_4 machined test bars evaluated at room temperature.

such as those shown in Figure 87. Secondary strength-controlling features were observed to be shell-shaped regions at the specimen surface. These latter origins, shown in Figure 88, are also the result of impact damage, presumably associated with the removal of the ASEA glass encapsulation material required for HIPing. The strength of the as-fired PY6 Si_3N_4 material at a temperature of 1000°C (1832°F) averaged 550.22 MPa (79.80 ksi), with average strengths of 519.06 MPa (75.28 ksi), 526.36 MPa (76.34 ksi), and 510.09 MPa (73.98 ksi) measured at temperatures of 1150°C (2102°F), 1250°C (2282°F), and 1371°C (2500°F), respectively. The fracture origins of the test specimens at elevated temperature were similar to those of the room temperature specimens, i.e., surface depressions and pits.

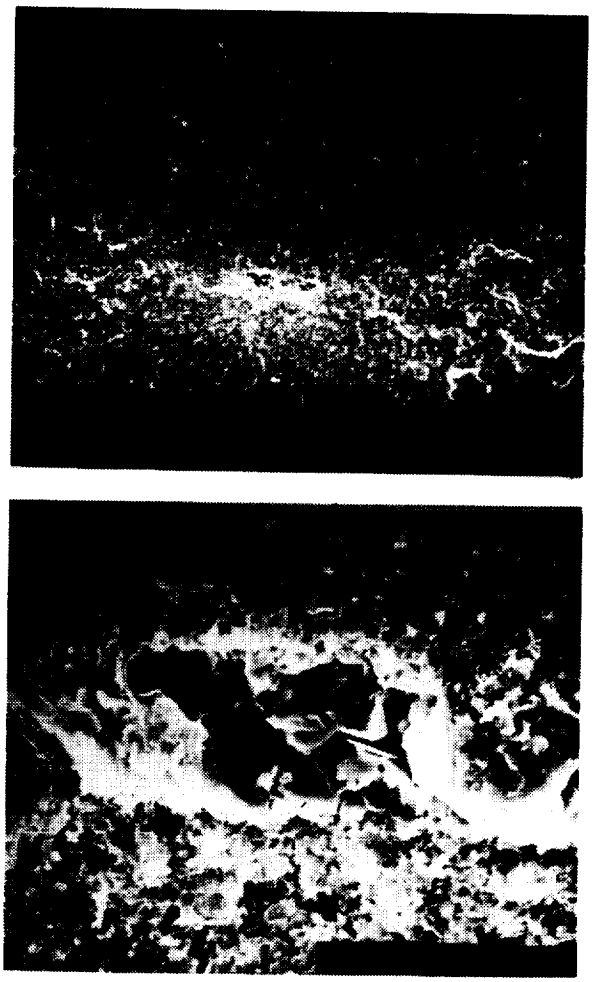

TE90-2088

Figure 86. Secondary fracture origin (metallic inclusion - Fe, Si) observed in GTE PY6 Si_3N_4 machined test bars.

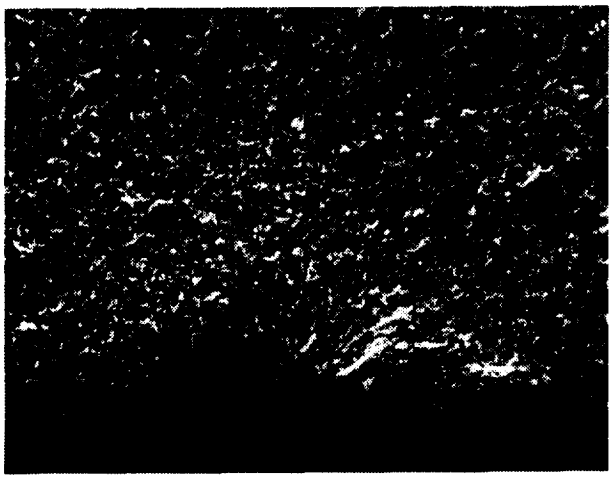

TE90-2089

Figure 87. Typical fracture origin (surface depression) observed in GTE PY6 Si_3N_4 test bars evaluated with an as-HIPed surface.

TE90-2090

Figure 88. Secondary fracture origin (shell-type feature) indicative of mechanical/impact damage in GTE PY6 Si_3N_4 as-HIPed test bars.

The fracture toughness (K_{IC}) of the GTE PY6 silicon nitride measured 6.4 $MPa \cdot m^{1/2}$ (5.8 $ksi \cdot in.^{1/2}$) as determined through use of the SENB method.

NGK Spark Plug EC-152 Silicon Nitride. The material characteristics of NGK Spark Plug EC-152 Si_3N_4 were also evaluated. The EC-152 Si_3N_4 is a sialon material containing Al_2O_3, Y_2O_3, and AlN as sintering additives. The EC-152 Si_3N_4 was produced using a two-step gas pressure sintering (GPS) process. The test bars were first cold isostatic pressed and sintered under low nitrogen pressure and subsequently subjected to increased nitrogen pressure and higher temperatures where densification was completed. The representative microstructure of the material, which had been polished and over-etched in a caustic solution, is presented in Figure 89. The material consists primarily of prismatic Si_3N_4 grains (0.5-2 micron (0.00002-0.00008 in.) in diameter). The average density measured 3.254 gm/cc (0.117 $lb/in.^3$), 99.8% of theoretical density.

The flexural strength characteristics of the EC-152 Si_3N_4 material are summarized in Table XIII. All specimens were tested with a machined tensile surface condition. The average room temperature strength measured 1059.69 MPa (153.69 ksi) with a Weibull modulus of 8.7. The material strength averaged 928.00 MPa (134.59 ksi) at 1000°C (1832°F), 685.02 MPa (99.35 ksi) at 1250°C (2282°F), and 584.01 MPa (84.70 ksi) at 1371°C (2500°F). The primary fracture origins observed in the EC-152 Si_3N_4 specimens were small surface flaws and internal pores as shown in Figure 90.

Carborundum Sintered α-Silicon Carbide Rotor Hubs. Characterization of the material strength of Carborundum injection molded sintered SiC and sinter/HIPed SiC axial turbine rotor hubs was conducted during this reporting period. The axial turbine rotor hubs were fabricated using the generic axial turbine rotor molding tool, modified to have the same cross section as the test-bed engine configuration rotors. A total of 18 rotors were evaluated:

TE90-2091

Figure 89. Microstructure of NGK Spark Plug EC-152 Si_3N_4--polished and etched.

Table XIII.
Strength characteristics of NGK spark plug isostatic pressed and gas pressure sintered EC-152 Si_3N_4.

Temperature--°C (°F)	Strength--MPa (ksi)
25 (77)	1059.69 (153.69)
1000 (1832)	928.00 (134.59)
1250 (2282)	685.02 (99.35)
1371 (2500)	584.01 (84.70)

4 sintered and 14 sinter/HIPed. The HIPed rotors were the result of an L4 (4-level Taguchi) experimental test matrix involving various combinations of HIPing temperature and time. The details of the HIPing test matrix are summarized in Table XIV. Seven HIP runs were conducted, with two rotor hubs from each of the process trials being evaluated.

Evaluation of the rotor hubs consisted of room temperature strength characterization of both test bars sectioned from the components and actual hub spin testing to failure. The results of these evaluations are summarized in Table XV.

The average density of the four sintered rotor hubs measured 3.150 gm/cc (0.114 lb/in.^{3}), 98.1% of theoretical density. The room temperature strength of test bars cut from two hubs averaged 398.12 MPa (57.74 ksi). The typical strength-controlling fracture origins were observed to be surface and internal pores as indicated in Figure 91. The average burst speed of the two sintered hubs was 107,500 rpm.

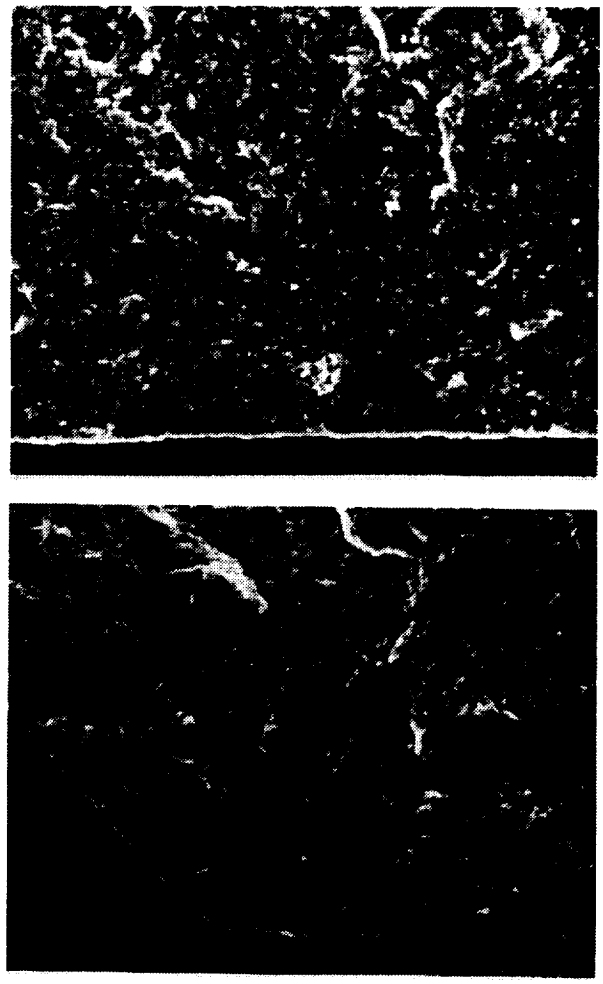

TE90-2092

Figure 90. Typical failure origins (small surface flaws and internal pores) observed in NGK Spark Plug EC-152 Si_3N_4.

Table XIV.
Carborundum SiC rotor hub HIPing test matrix.

Run No.	Time--minutes	Temperature--°C (°F)	Pressure--MPa (ksi)
1	60	2100 (3812)	207 (30)
2	105	2050 (3722)	207 (30)
3	15	2150 (3902)	207 (30)
4	60	2100 (3812)	207 (30)
5	105	2150 (3902)	207 (30)
6	15	2050 (3722)	207 (30)
7	60	2100 (3812)	207 (30)

Table XV.
Characterization results for Carborundum sintered and sinter/HIPed SIC rotor hubs.

Run No.	Rotor No.	Burst speed	Test bars cut from rotors Strength--MPa (ksi)	Weibull modulus
Sintered	2-3	102,600		
	9-3	112,400		
	1-3	---	380.81 (55.23)	4.46
	6-3	---	415.42 (60.25)	8.05
	Average	107,500	398.12 (57.74)	
HIP-1	7-2	131,500		
	2-1	---	415.49 (60.26)	6.83
HIP-2	10-1	109,000		
	1-1	---	504.51 (73.17)	11.36
HIP-3	15-2	125,200		
	13-1	---	419.56 (60.85)	5.67
HIP-4	11-1	126,400		
	5-1	---	475.13 (68.91)	5.29
HIP-5	4-2	130,700		
	5-2	---	453.62 (65.79)	6.78
HIP-6	16-2	131,300		
	16-1	---	483.20 (70.08)	5.37
HIP-7	14-1	145,500		
	8-1	---	516.78 (74.95)	8.21
	Average	128,500	466.93 (67.72)	

Finite element analysis of the bladeless rotors predicts an average burst speed of 117,500 rpm assuming typical SiC test bar properties, i.e., an average strength of 380 MPa (55 ksi) and a Weibull modulus of 9.

The average density of the 14 sinter/HIPed rotor hubs measured 3.163 gm/cc (0.114 lb/in.^{3}), 98.6% of theoretical density. The room temperature strength of test bars cut from the hubs averaged 466.93 MPa (67.72 ksi). These values ranged from a low of 415.49 MPa (60.26 ksi) for HIP run No. 1 to a maximum value of 516.78 MPa (74.95 ksi) for test bars cut from a rotor from HIP run No. 7. The typical fracture origins were observed to be surface pores and flaws as depicted in Figure 92. The size and frequency of the pores were found to be lower in the HIPed rotor hubs when compared with the sintered hubs. Test bars from the HIP-5 rotor hub, which was subjected to the highest HIPing temperature (2150°C [3902°F]) and longest process time (105 minutes), were observed to have fracture origins propagating from large SiC grains (see Figure 93). Existence of these grains indicates that maximum values of HIPing temperatures and process time have been achieved, and these should not be exceeded for optimizing mechanical and microstructural properties. The average burst speed for the HIPed rotor hubs measured 128,500 rpm, ranging from a low value of 109,000 rpm for HIP-2 to a maximum speed of 145,500 rpm for HIP-7. The average burst speed of the HIPed SiC rotor hubs measured 109% of the mean speed predicted from finite element analysis. This speed is equivalent to a test bar strength of 455 MPa (66 ksi), which correlates well with the modulus of rupture (MOR) results obtained on test bars sectioned from the HIPed rotor hubs. Photographs taken of the rotors at the moment of burst indicated fracture typically originating from the high stress region at the shaft/hub

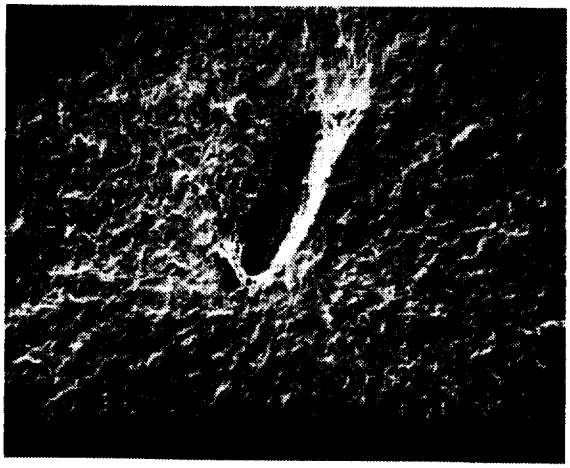

(A)

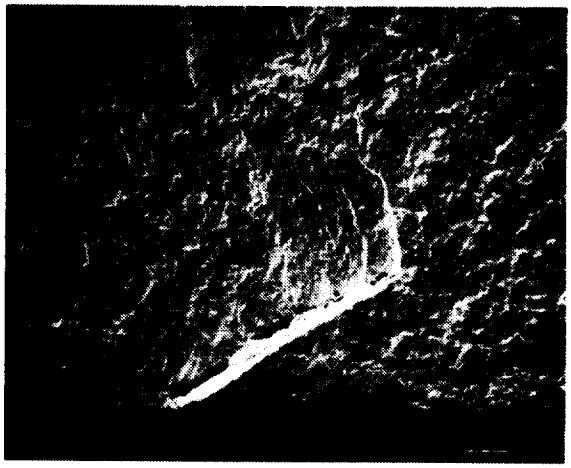

(B)

TE90-2093

Figure 91. Typical fracture origins observed in CBO sintered SiC rotor hubs: (a) internal pore, (b) surface pore.

area. Figure 94 shows a typical rotor burst at 131,500 rpm.

High Temperature Oxidation Testing. Characterization was undertaken of the oxidation behavior of ceramic materials being used for component development and parts-buy activities in the ATTAP program. The materials evaluated included Carborundum alpha-SiC (injection molded and sintered), Garrett Ceramic Components (GCC) GN-10 Si_3N_4 (isostatic pressed and HIPed), Kyocera SN251 Si_3N_4 (isostatic pressed and sintered), Kyocera SN252 Si_3N_4 (slip cast and sintered), and NGK Spark Plug EC-152 Si_3N_4 (isostatic pressed and gas pressure sintered).

TE90-2094

Figure 92. Typical fracture origin (surface flaw) observed in CBO sintered/HIPed SiC rotor hubs.

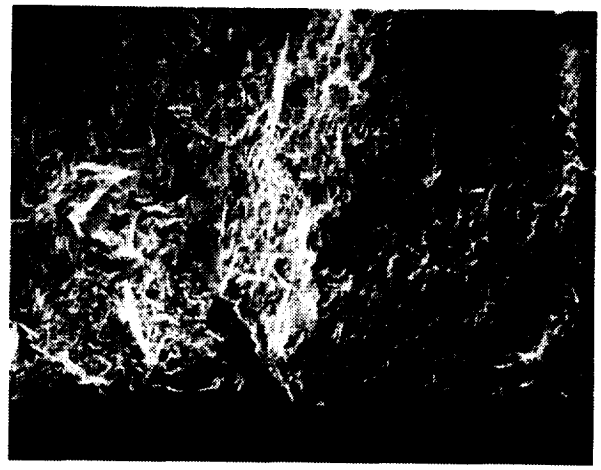

TE90-2095

Figure 93. Typical fracture origin (large SiC grain) observed in CBO SiC rotor hubs HIPed at 2150°C (3902°F) for 105 min.

The test specimens consisted of MOR test bars which were placed on platinum screens and heated in air for 500 hr at 1250°C (2282°F) with additional test specimens oxidized for 500 hr at 1371°C (2500°F). After testing, the weight gains were recorded and the surface morphology and chemistry of the oxide and the interface were investigated by scanning electron microscopy and energy dispersive X-ray analysis (EDS). The test bars were then fractured at room temperature and subjected to fractographic analysis to determine the

Figure 94. CBO HIPed SiC rotor hub burst at 131, 500 rpm.

location and nature of the strength-controlling flaws.

Figure 95 shows the general appearance of the specimens before and after the oxidation testing conducted at 1250°C (2282°F). Table XVI summarizes the room temperature (RT) strength results of both as-received and oxidized test bars. All of the specimens were tested with a machined surface.

The Carborundum a-SiC test bars exhibited no visible exterior change after oxidation at 1250°C (2282°F). A thin uniform layer of glassy oxide was observed forming on the surface with an average thickness of 2.9 microns (0.00012 in.). The average weight gain was 0.04%. The room temperature fracture strength after initial oxidation averaged 373.16 MPa (54.12 ksi), a 5.1% decrease compared with the strength of 393.36 MPa (57.05 ksi) measured on the as-received specimens. After exposure at 1371°C (2500°F), the thickness of the glassy oxide layer measured 5 microns (0.0002 in.) with an average weight gain of 0.12%. The room temperature strength after this increased oxidation averaged 351.51 MPa (50.98 ksi), a 10.6% decrease. The strength-controlling flaws, shown in Figure 96, were observed to be small surface and subsurface pores.

The GCC GN-10 Si_3N_4 test bars had an average weight gain of 0.20% after exposure at 1250°C (2282°F). An uneven glassy layer with localized nodules averaging 100 microns (0.004 in.) in diameter formed on the surface of the test bars. The average thickness of the glassy layer was 25 microns (0.001 in.). However, localized deep oxidation up to 80 microns (0.0032 in.) in depth with large gas bubbles was observed at some sites. The average room temperature strength following initial oxidation was 646.06 MPa (93.70 ksi), a decrease of 14.3% relative to the strength of 753.62 MPa (109.30 ksi)

Table XVI.
Results of oxidation at 1250°C (2282°F) and 1371°C (2500°F) for 500 hr for carious xeramic materials.

	RT strength, MPa (ksi)		
Material	As-received	1250°C (2282°F)	1371°C (2500°F)
CBO SiC	393.36 (57.05)	373.16 (54.12)	351.51 (50.98)
GCC GN-10 Si_3N_4	753.62 (109.30)	646.06 (93.70)	578.42 (83.89)
Kyocera SN251 Si_3N_4	680.95 (98.76)	622.00 (90.21)	546.02 (79.19)
Kyocera SN252 Si_3N_4	633.44 (91.87)	594.14 (86.17)	522.92 (75.84)
NGK EC-152 Si_3N_4	1059.69 (153.69)	659.99 (95.72)	401.91 (58.29)

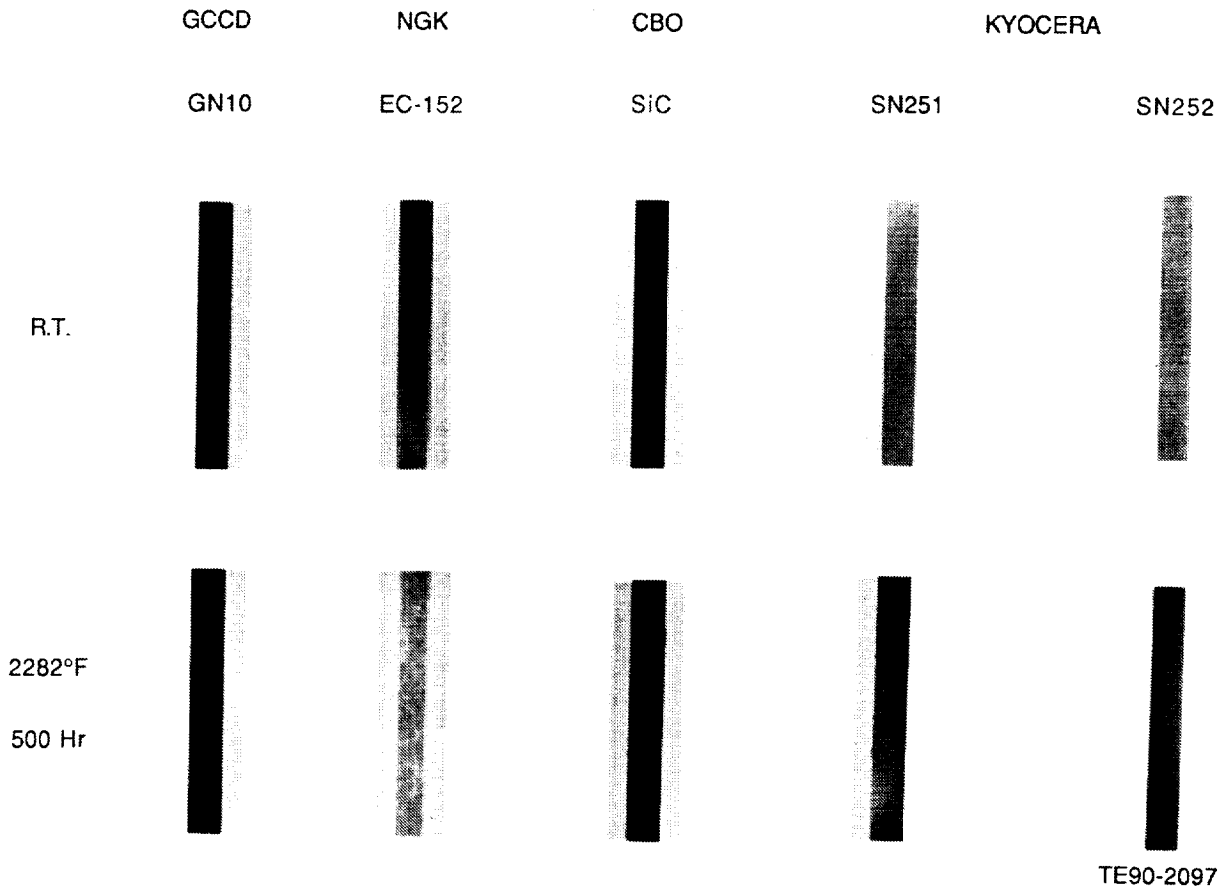

Figure 95. Results of oxidation in air at 1250 °C (2282 °F) for 500 hr.

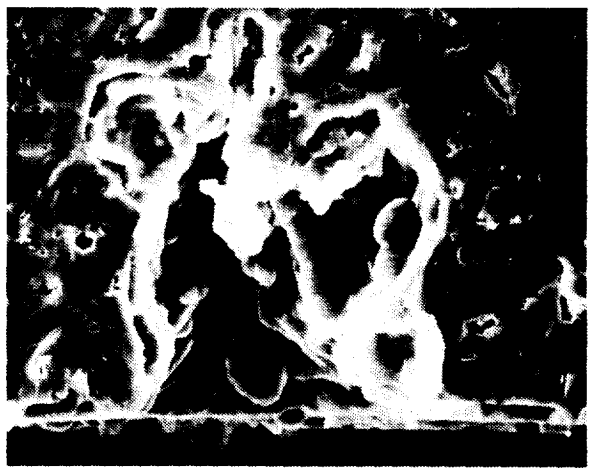

Figure 96. Typical fracture origin (surface pore) observed in CBO SiC oxidized for 500 hr at 1371 °C (2500 °F).

recorded for the as-received specimens. Exposure at 1371°C (2500°F) resulted in an average weight gain of 0.32% with a glassy layer averaging 35 microns (0.0014 in.) in thickness forming on the specimen surface. The average room temperature strength after this exposure measured 578.42 MPa (83.89 ksi), a 23.3% decrease. The typical fracture origins, shown in Figure 97, were observed to be from gas bubbles in the localized regions of heavy oxidation.

Only a slight discoloring on the exterior surface was observed for the Kyocera SN251 Si_3N_4 test bars after oxidation. A uniform glassy layer with an average thickness of 4.9 microns (0.0002 in.) was formed on the surface of the specimens after exposure at 1250°C (2282°F). The average weight gain was 0.07%. The average room temperature strength of the material exposed to the 1250°C (2282°F) temperature measured 622.00 MPa (90.21 ksi), a decrease of 8.7% compared with the strength of 680.95

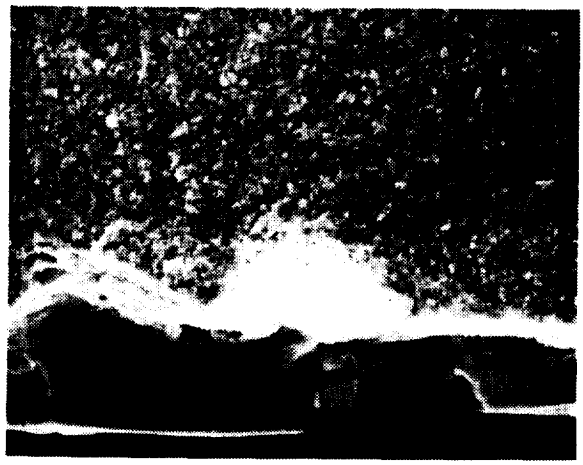

TE90-2099

Figure 97. Typical fracture origin (glassy bubble at surface) observed in GCCD GN-10 Si_3N_4 oxidized for 500 hr at 1371°C (2500°F).

MPa (98.76 ksi) for the as-received material. Material oxidized at a temperature of 1371°C (2500°F) formed a glassy layer averaging 8 microns (0.00032 in.) in thickness with an overall weight gain of 0.13%. The average strength of the material following the high temperature oxidation was 546.02 MPa (79.19 ksi), a 19.8% decrease. The oxidized test bars failed from large Si_3N_4 grains at the surface of the specimens as shown in Figure 98.

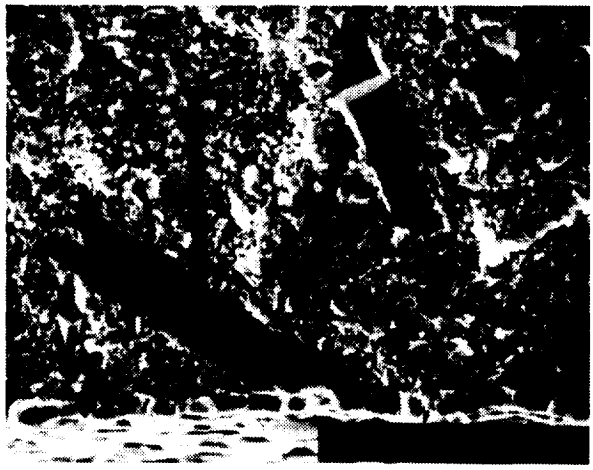

TE90-2100

Figure 98. Typical fracture origin (large Si_3N_4 grain at surface) observed in Kyocera SN251 Si_3N_4 oxidized at 1371°C (2500°F) for 500 hr.

The results obtained for the Kyocera SN252 sintered reaction bonded Si_3N_4 material were similar to the SN251 Si_3N_4 material. A very slight discoloring was observed on the exterior surface of the test bars after oxidation. A uniform thin glassy layer with an average thickness of 3.1 microns (0.00012 in.) was observed after exposure at 1250°C (2282°F). The average weight gain measured 0.04%. The fracture strength of the oxidized material averaged 594.14 MPa (86.17 ksi), 6.3% lower than the strength of 634.13 MPa (91.97 ksi) obtained for the as-received material. Specimens oxidized at 1371°C (2500°F) formed a glassy surface layer approximately 8 microns (0.00032 in.) in thickness with a weight gain of 0.13%. The strength of these exposed specimens averaged 522.92 MPa (75.84 ksi), a 17.5% decrease. The typical fracture origins were surface and near surface large Si_3N_4 grains shown in Figure 99.

The NGK Spark Plug EC-152 Si_3N_4 material exhibited a surface color change from gray to white-gray after oxidation at 1250°C (2282°F). The discoloration penetrated into the interior of the specimen for a depth of 50 microns (0.002 in.). However, the thickness of the surface glassy layer measured only 15 microns (0.0006 in.). The average weight gain was 0.10%. The strength of the oxidized material averaged 659.99 MPa (95.72 ksi), a significant decrease (37.7%) compared with the strength of 1059.69 MPa (153.69 ksi) measured for the as-received material. The oxidation of this material was more severe at a temperature of 1371°C (2500°F). A layer of heavy glass formation, mea-

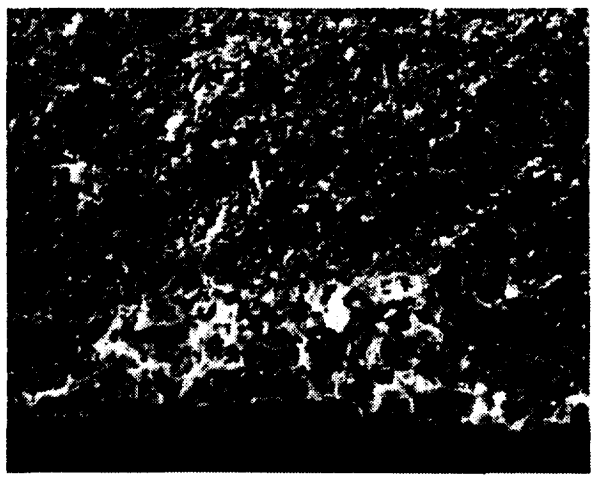

TE90-2101

Figure 99. Typical fracture origin (surface Si_3N_4 grains) observed in oxidized Kyocera SN252 Si_3N_4.

suring 200-300 microns (0.008-0.012 in.) in depth, was observed on the surface. A cross section of the EC-152 material oxidized at 1371°C (2500°F) is shown in Figure 100. The average weight gain was 0.88%. The strength of the specimens exposed at this temperature averaged 401.91 MPa (58.29 ksi), a 62.1% decrease. The typical fracture origins in the oxidized specimens were surface flaws and pores at the oxide surface layer as shown in Figure 101.

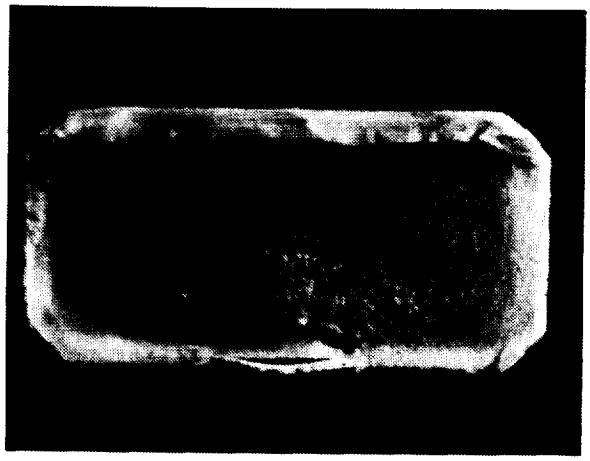

TE90-2102

Figure 100. Cross section of NGK EC-152 Si_3N_4 oxidized for 500 hr at 1371°C (2500°F).

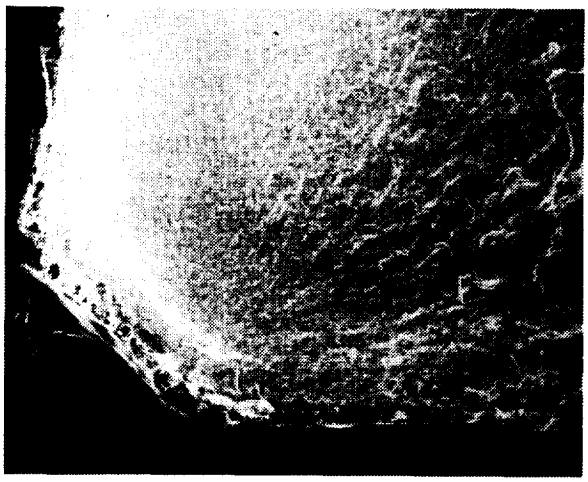

TE90-2103

Figure 101. Typical fracture origin (surface flaw) observed in oxidized NGK EC-152 Si_3N_4.

3.1.2 Inspection, Nondestructive Evaluation

Objective/Approach

The primary objective of this effort is to develop nondestructive evaluation techniques that are capable of detecting discrete flaws and microstructural variations in test specimens and candidate turbine engine components.

Feasibility studies were conducted in 1989 to determine the sensitivity of X-ray computed tomography (CT) to detect process induced volumetric defects and density variations in the gasifier rotor of the AGT-5 test-bed engine. In tomographic imaging, projection data are used to construct the cross-sectional images of a given object. The object under examination is irradiated by a beam of X-rays from various angular positions. For each beam position the intensity of emerging radiation is measured electronically using scintillation detectors. All measurements from a single position constitute a projection. The sum of all projections is computer analyzed to reconstruct a cross-sectional image of the object.

Accomplishments/Results

It was demonstrated that X-ray CT can detect process induced 600 micron or larger sized flaws in silicon nitride gasifier rotors with 0.75% or better sensitivity (defined as flaw depth divided by part thickness in the flaw location).

Discussion

Six silicon nitride rotors, manufactured by Ceramics Process Systems (CPS), were examined by microradiography at Allison using the Fein Focus system. A large number of voids were detected both in the hub and blades of all the rotors. A positive image of a typical radiograph is presented in Figure 102. This rotor, S/N CPS-7, was only 82% theoretically dense. The existing flaws are believed to have resulted from a low-cost silicone mold and are not to be construed as indicative of the final quality attainable using the CPS Quickset injection molding process. The CPS-7 rotor was characterized using two computed tomography systems, namely the LAM/DE system of ARACOR and the Model 101B of Scientific Measurement Systems (SMS). The following paragraphs describe each system and the results obtained from them.

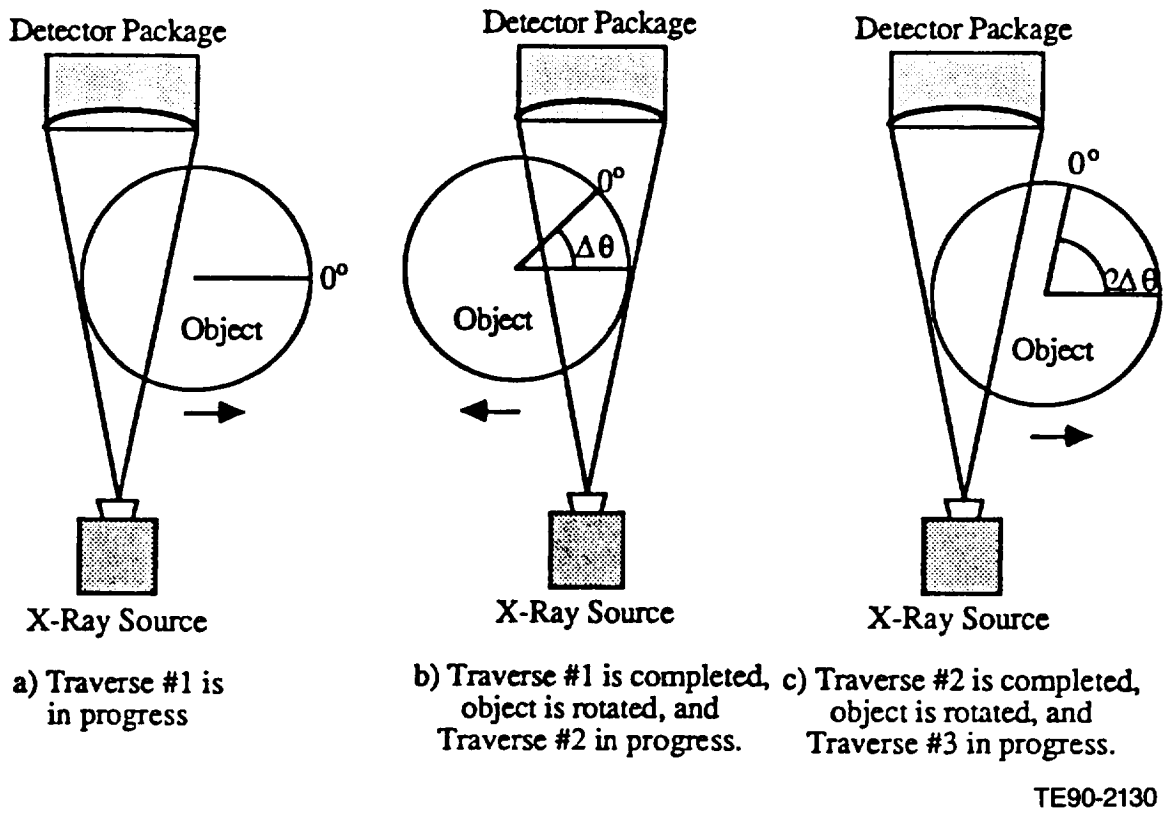

Figure 103. Second generation CT scanner schematic--translate/rotate scan geometry.

A long vertical branching crack, which probably resulted from gating defects in the molding process, is depicted in an axial slice near the rotor centerline in Figure 106. This is the same flaw observed in the radial slice previously depicted in Figure 105. A radial density profile through the blade up to the rotor center at 6.5 mm along the axial axis is presented in Figure 107. The average blade and hub densities were about 2.8 and 3.2 gm/cc, respectively. The density at a detected 918 micron void in the blade dropped to 2.6 gm/cc.

SMS Model 101B System. The SMS Model 101B utilizes a 420 KV 3 mA Phillips X-ray tube. The beam spot size of this system is 1.5 mm x 1.5 mm. The detectors are collimated to 0.432 mm x 0.432 mm size. The rotors were scanned with a slice width of 0.5 mm providing a true spatial resolution of 225 micron. The data were collected over a 512 x 512 pixel matrix. A radial and an axial CT slice of the CPS-7 rotor are presented in Figure 108. Flaws are present at the root of almost every blade, as well as in the shaft.

A sectioned view of the CPS-7 rotor, which indicates the presence of a vertical branching crack in the shaft (which was detected by both CT systems evaluated) is presented in Figure 109. It was concluded that both the ARACOR and the SMS systems are capable of detecting process induced flaws in ceramic rotors. However, the images from the SMS system appear to be somewhat sharper due to the smaller slice thickness used. Both systems, however, appear to have similar flaw detection sensitivity. Future work will concentrate on fabricating reference standard rotors possessing controlled smaller flaws (produced through use of an excimer laser) to determine the sensitivity of the CT systems. The best of these systems will be used to characterize engine quality rotors.

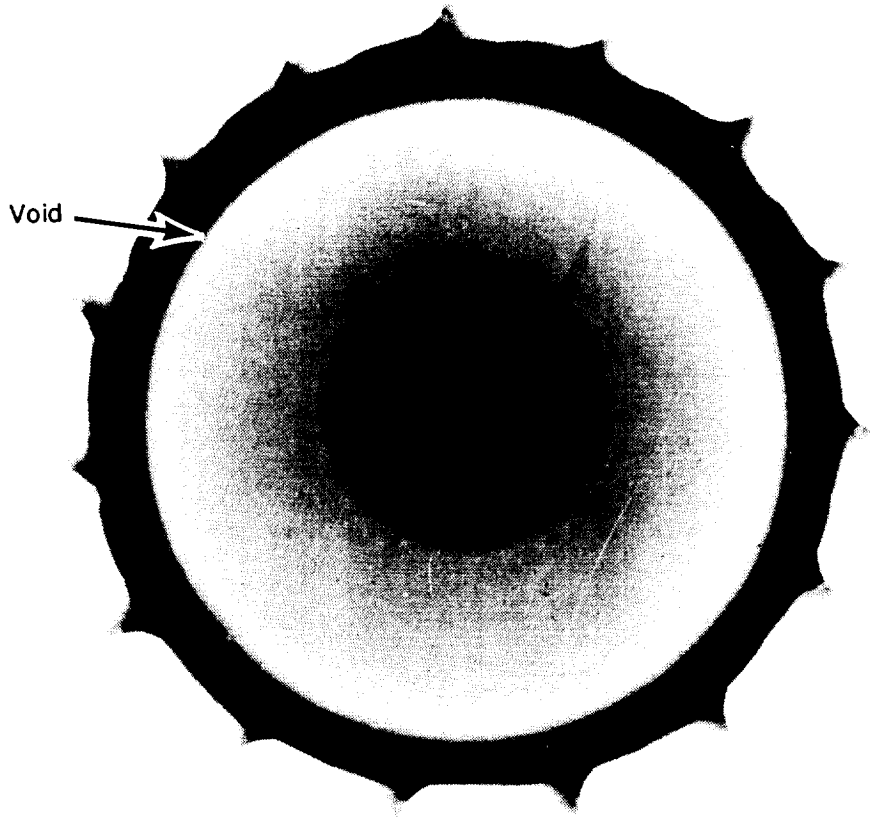

Figure 102. Microradiograph positive, CPS-7 sintered Si_3N_4 rotor.

LAM/DE System. The LAM/DE system was designed and developed by ARACOR for the U.S. Air Force. This is a second generation machine whose translational-rotational scan geometry is schematically illustrated in Figure 103. For this geometry, an object is translated past an X-ray beam, rotated, and translated past the X-ray beam again. This process is repeated until the part has been rotated a full 180 deg. Each translation is referred to as a traverse. LAM/DE incorporates a 420 KV Isovolt X-ray source and is capable of scanning a part 20 in. in diameter, 22 in. in length, and 110 lb. The slice thickness can be adjusted from 1 mm to 15 mm.

The silicon nitride rotor was scanned overnight at 420 KV using a slice thickness of 1.2 mm. Twenty-seven (27) radial slices of data along the rotor axial axis (height if rotor stood on hub end) were collected at increments so as to provide significant overlap in data collection and to preclude any flaw omission. A 512 x 512 pixel matrix was used to collect the data. The corresponding resolution aperture width was 1.2 mm. A typical presentation of the collected data attained with four radial slices between 5 and 6.5 mm along the axial axis (which are approximately at a cross section through the axial center of the rotor) appears in Figure 104. A large number of flaws are visible at the 6.5 mm slice. The smallest detected flaw in this figure is about 600 microns in diameter. Figure 105 depicts a data slice taken at a "height" of 9.5 mm which clearly indicates that two voids near the outer edge about 600 microns apart can be resolved. A half-moon crack and a void near the axis are also visible in the image presented in Figure 105. These data translate into a CT thickness sensitivity and resolution (minimum distinguishable distance between adjacent flaws) for the detected voids of about 1.1% through the hub and 0.75% through the blades.

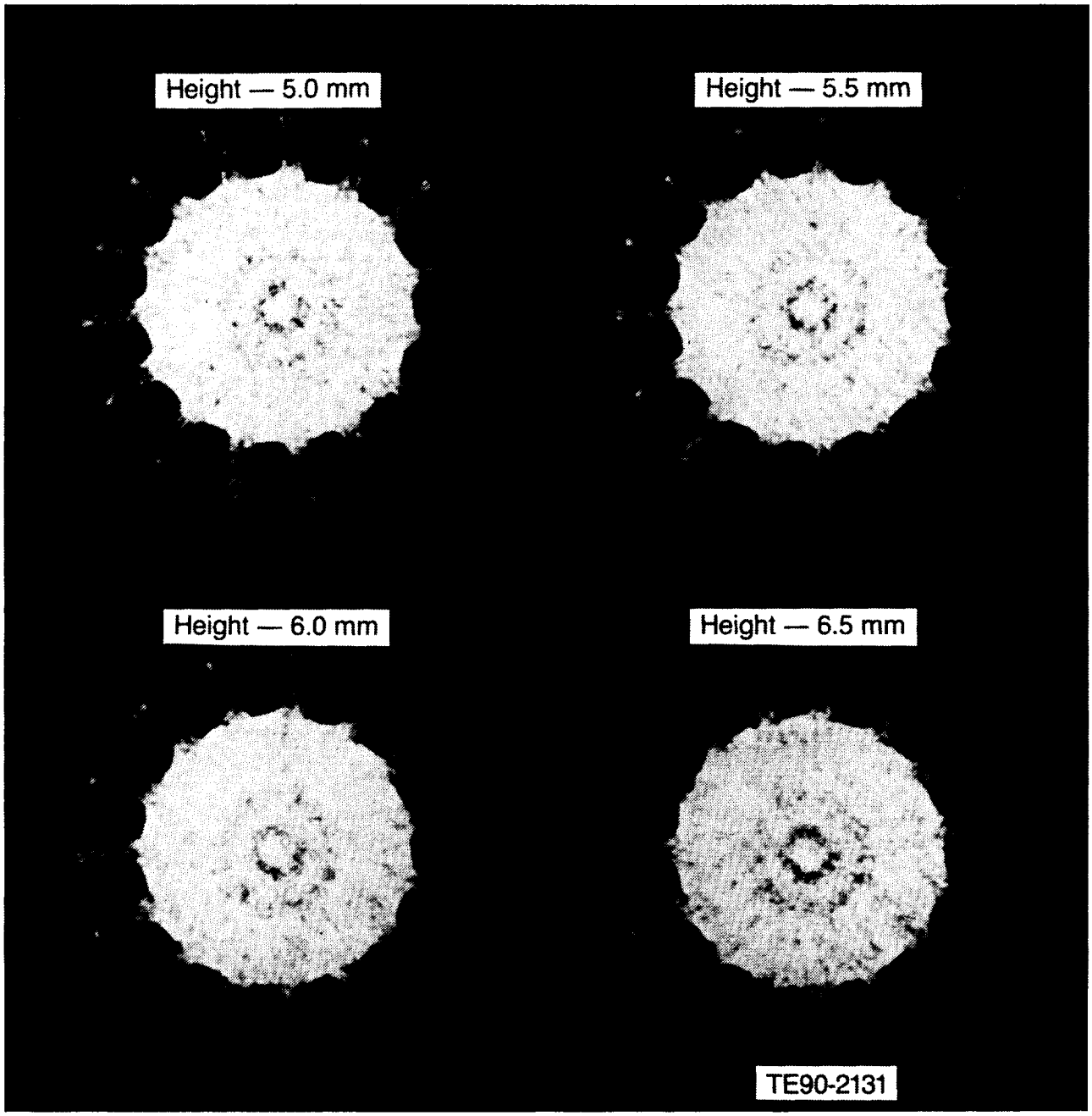

Figure 104. CT images at 5.0, 5.5, 6.0, and 6.5 mm heights--CPS-7 rotor.

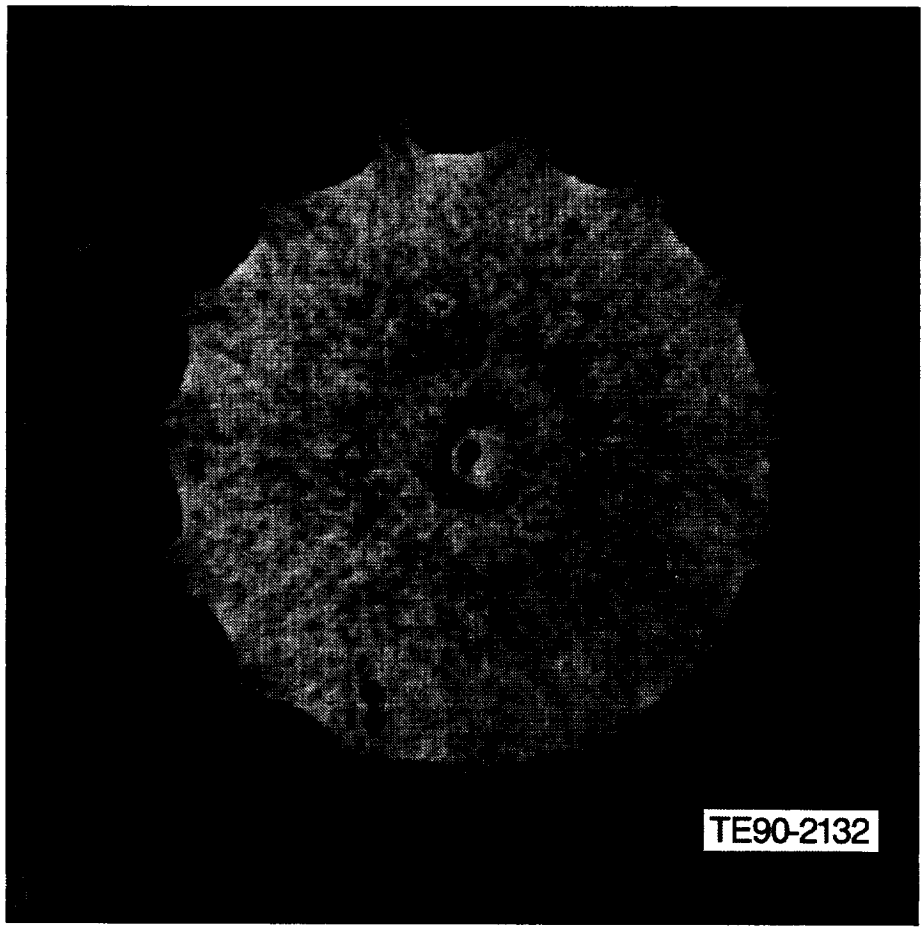

Figure 105. CT image at 9.5 mm height--CPS-7 rotor.

Figure 106. CT image at axial slice through CPS-7 rotor.

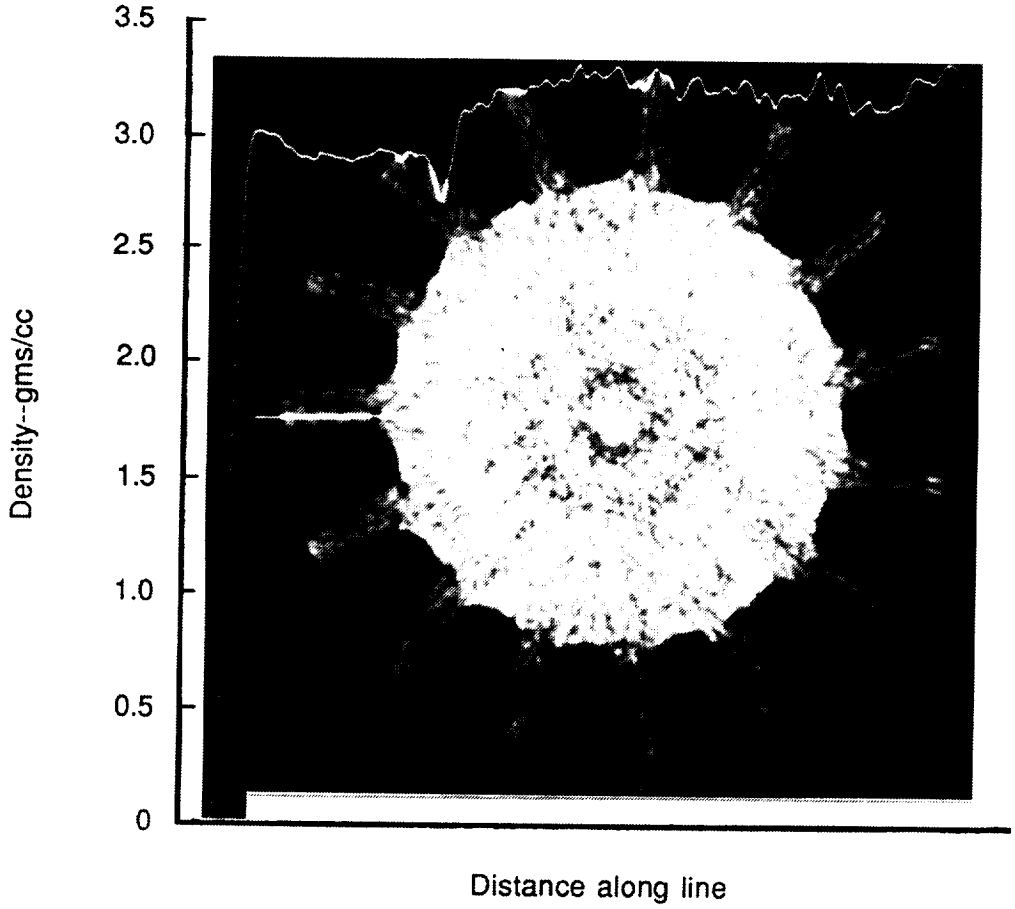

Figure 107. CT image and density profile at 6.5 mm height--CPS-7 rotor.

3.1.3 Failure Analysis

Objective/Approach

Failure analysis details the results of fractographic analyses of ceramic components that experienced unscheduled damage during rig/engine testing and evaluation. Fractographic analysis is one of the most powerful tools used in the failure analysis of an engine or rig tested component. A careful study of the general and detailed features of the topography of a fracture, by visual assessment and by scanning electron microscopy provides a wealth of information concerning the failure origin and the failure mode(s). Analysis of hardware failures allows the separation of design features from material deficiencies, defects, or nonoptimum fabrication procedures and can suggest appropriate corrective measures.

Accomplishments/Results

- Examinations were conducted on a Kyocera SN252 Si_3N_4 gasifier turbine rotor which had exhibited airfoil chipping after rig testing.
- Blade chipping was a result of impact fractures (foreign object damage [FOD]).
- The rotor is in good condition and can be used in further rig/engine tests.

Discussion

Kyocera Gasifier Turbine Rotor Used in Rig Development. A Kyocera slip cast SN252 silicon nitride AGT-5 test-bed engine design gasifier turbine rotor, P/N 5-67200, S/N 0001-2, was used in shakedown testing of a hot gas generator rig. The rotor had been run at 100% gasifier speed at turbine inlet temperatures up to 1200°C (2192°F); an addi-

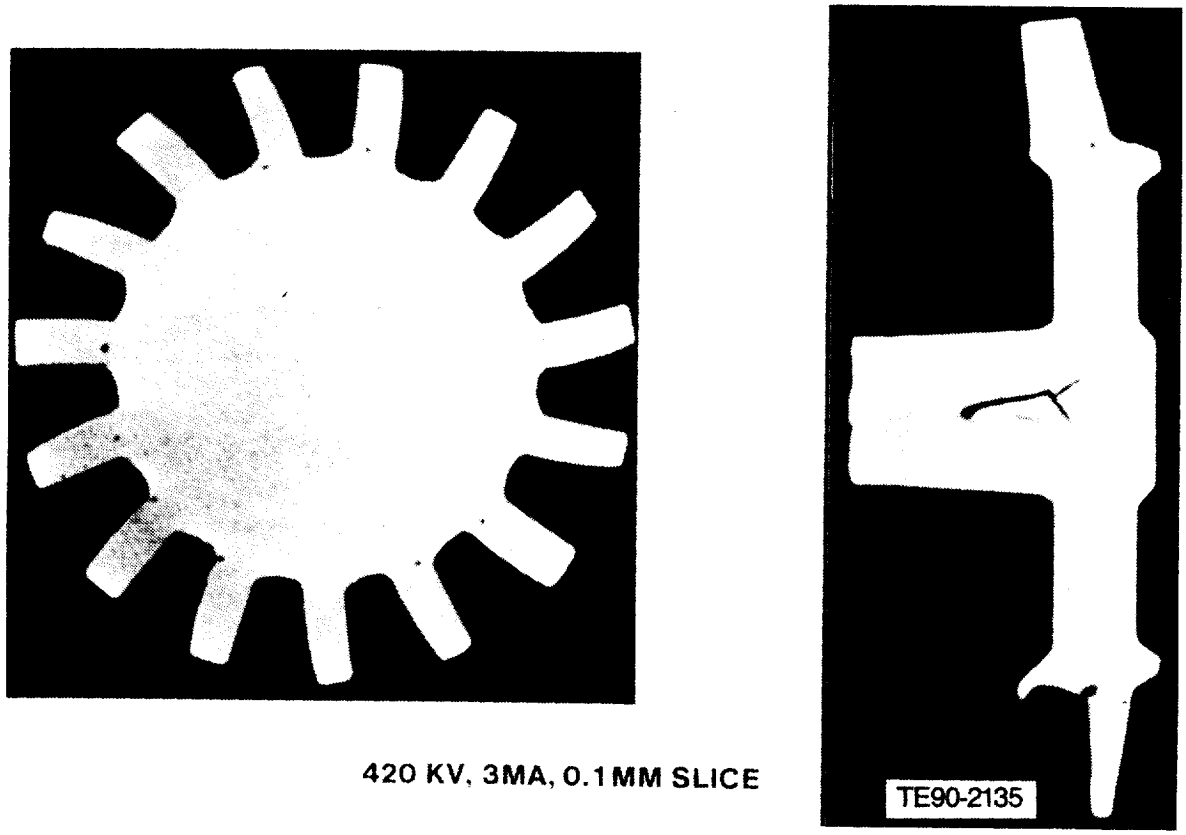

Figure 108. X-ray computed tomography of CPS-7 sintered Si_3N_4 gasifier rotor.

tional 2 hr were accumulated on the durability cycle. Total part time in the gasifier rig was 222.8 hr. Following teardown of the gasifier hot rig for inspection and maintenance, chipping was observed on the airfoils of the Kyocera rotor as shown in Figure 110. Fourteen of the twenty blades suffered damage at the leading edge tip as illustrated schematically in Figure 111. The blades were numbered for identification. Thirteen blades, numbers 1-4, 6, 9-11, 13-15, 19, and 20 had impact fractures at the leading edge tip. The representative impact fractures had a shell-like appearance as shown in Figure 112. The origins of the impact fractures were on the suction side of the airfoils. Blade number 12 had a long narrow fracture that was different from the impact fractures of the other blades.

Dark glossy marks on the leading edge tips of the undamaged blades (see Figure 113) indicate that the rotor had rubbed against the metallic shroud. Additionally, another type of rub/wear feature appeared on two groups of consecutive blades. Figure 114 shows the blade tips of the two groups, numbers 19 through 5 and numbers 12 through 14. These marks indicated that hard particles, probably silicon nitride debris from the impact fractures, were caught between the blades and the shroud. The impact fractures were probably the result of either the blade tip rub or FOD from the particle containment screen that had failed in a prior rig test using this rotor.

All the blades were coated with a light brown color film, which is typical of silicon nitride components tested at high temperatures in conjunction with metallic components. All impact fracture surfaces were coated with this brown film indicating that the impact fractures were not a recent occurrence. The fracture surface of blade number 12 had a much lighter brown coating indicating that the fracture occurred at a later time than the impact fractures of the other airfoils.

The rotor was determined to be in engine quality condition. It was returned for further workhorse use in rig evaluation without repair/blending of the damaged areas.

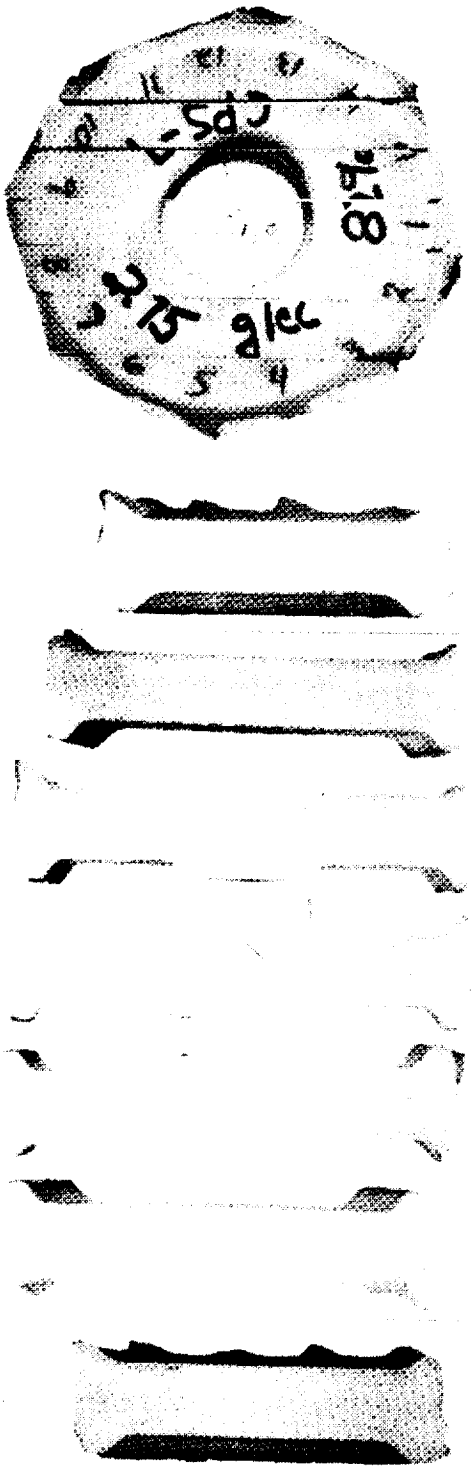

TE90-2136

Figure 109. Sectioned views of CPS-7 rotor indicating presence of internal crack in the shaft region.

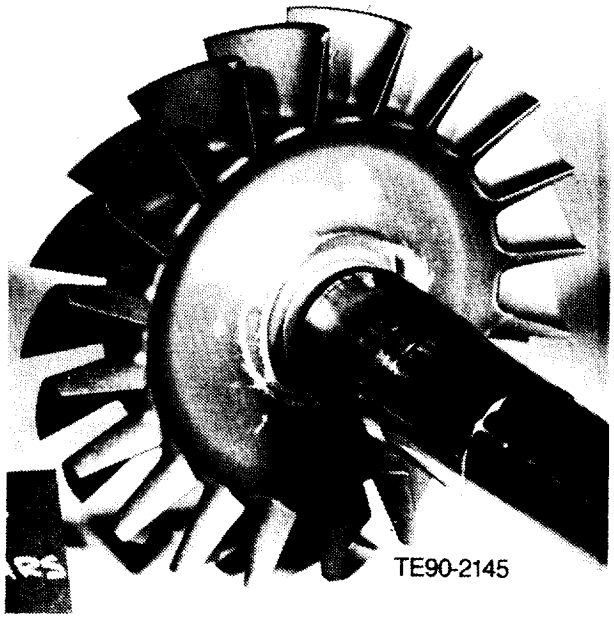

TE90-2145

Figure 110. Kyocera 20 blade gasifier rotor after 222.8 hot rig test hours.

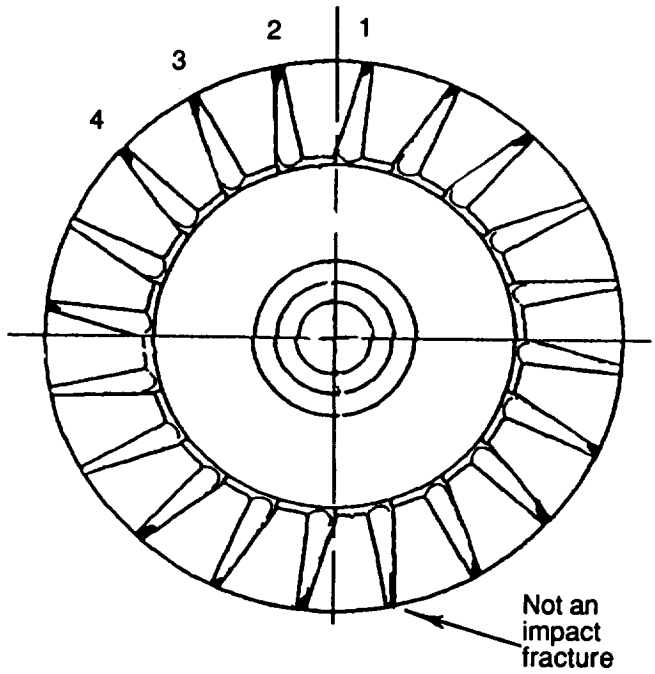

TE90-2146

Figure 111. Schematic diagram of impact fractures at leading edge tips--Kyocera 20 blade rotor.

Blade #2

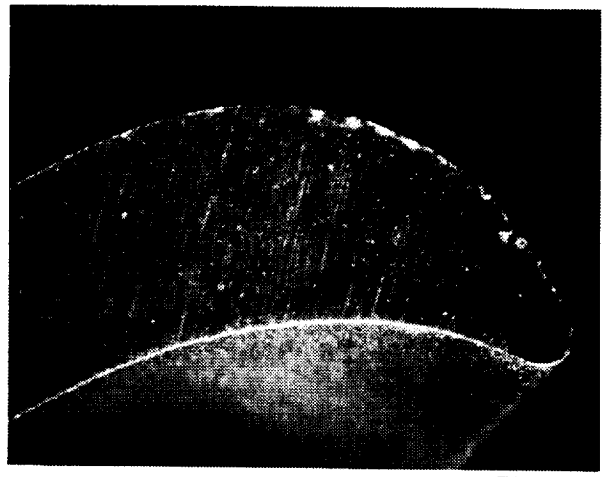

Blade #5

Blade #3

TE90-2147

Figure 112. Representative leading edge fracture caused by impact (magnification = 18X).

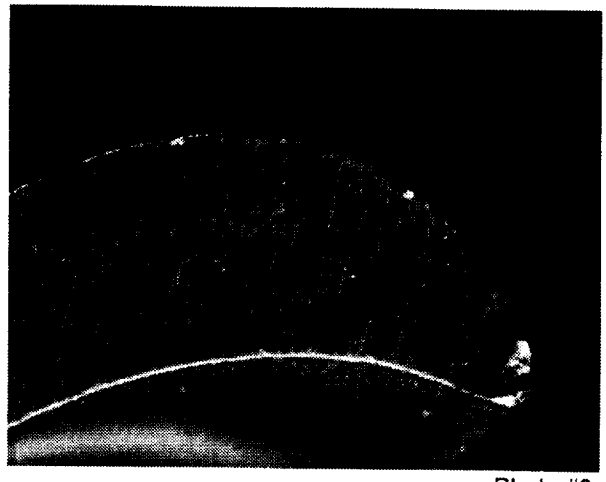

Blade #8

TE90-2148

Figure 113. Representative leading edge tip rub marks (dark bands) (magnification = 18X).

3.2 CERAMIC COMPONENT PROCESS DEVELOPMENT AND FABRICATION

This subsection details the ongoing ceramic component process development and fabrication activities at the selected ceramic component developers, including Carborundum, Manville, GTE Laboratories, Corning, Garrett Ceramic Components, and Ceramics Process Systems. Allison's approach to ceramic component development continues to be one of subcontracting process development to the domestic ceramic manufacturing community and working in an iterative development loop with those suppliers in areas of component design, characterization, and rig/engine data feedback.

The major focus of the component development activities at Carborundum included injection molded SiC gasifier turbine rotors, vane set development, and slip cast SiC scrolls. Manville's efforts concentrated on development and fabrication of ceramic thermal insulation for test rigs and engines. The development activities at GTE Laboratories focused on injection molded Si_3N_4 gasifier turbine rotors and vanes, as well as studies addressing toughened Si_3N_4 material systems using both microstructural and SiC whisker reinforcements. Corning was involved in extruded alumino-silicate regenerator disk specimens. Garrett Ceramics Components' effort was focused on the development and fabrication of gasifier turbine rotors using pressure slip cast

Figure 114. Abrasive marks on the midchord of the blade tips.

GN-10 Si_3N_4. The efforts at Ceramics Process Systems addressed Si_3N_4 gasifier turbine vane platform fabrication using their Quickset injection molding process.

3.2.1 Carborundum

Objective/Approach

The ceramic component development efforts being conducted with The Carborundum Company (CBO) consist of three major tasks: improved SiC rotor processing, vane set development, and slip casting. The rotor processing and vane set development tasks have focused on injection molding of sintered alpha-SiC, while the slip casting efforts have been directed toward slip cast sintered α-SiC for scroll fabrication. Prior efforts conducted in CY 1988 pertaining to ceramic/ceramic joining and chemical vapor deposition (CVD) of SiC on SiC/TiB_2 were deleted from the 1989 work plan.

Accomplishments/Results

- Process parameters were established for axial rotor fabrication, with delivery of the initial 15 SiC rotors.
- The vane injection molding tool was designed and received; vane fabrication remains active.
- Slip development efforts resulted in significant improvements in strength and castability.
- Scroll fabrication efforts are continuing.

Discussion

Improved Rotor Processing. The improved rotor processing activities consisted of those areas relating to successful fabrication of injection molded sintered a-SiC axial turbine rotors. These include: SiC process development, injection mold variable optimization using the generic (bladeless) axial rotor tool and flow modeling, and engine configuration rotor fabrication.

An SiC dry powder processing matrix was completed in 1989. The goal of this experiment was to evaluate different powder types as well as milling times, mill loading, and processing aids to determine the powder/processing combination providing the highest packing density. The powder responses were evaluated using scanning electron microscopy (SEM), particle size distribution, surface area, apparent density, tap density, and compaction density. Modulus of rupture (MOR) strength results were obtained on machined and annealed test bars in the SiC process development effort. The average density, MOR, and Weibull modulus obtained from 20 test bars of each composition at two different sintering temperatures, T° (the standard sintering temperature) and T°-25°C (T°-77°F), are presented in Table XVII.

Table XVII.
CBO SiC sintering test matrix results.

Fired at T°

Composition	A	B	C	D	E
Density, gm/cc (lb/in.^{3})	3.148 (0.114)	3.142 (0.113)	3.144 (0.114)	3.147 (0.114)	3.144 (0.114)
MOR, MPa (ksi)	394.4 (57.2)	347.5 (50.4)	387.5 (56.2)	367.5 (53.3)	425.4 (61.7)
Weibull modulus	7.5	4.7	4.8	5.0	6.5

Fired at T° -25°C (T°-77°F)

Composition	A	B	C	D	E
Density, gm/cc (lb/in.^{3})	3.139 (0.113)	3.117 (0.112)	3.102 (0.112)	3.103 (0.112)	3.092 (0.112)
MOR, MPa (ksi)	377.8 (54.8)	366.8 (53.2)	415.8 (60.3)	408.2 (59.2)	441.3 (64.0)
Weibull modulus	7.9	6.0	3.9	5.1	11.5

Legend:
- A: Experimental powder, standard polymer level
- B: Experimental powder, 2% less polymer
- C: SX-05, molding conditions same as A, B, and E
- D: SX-05 baseline
- E. SX-09 baseline

At T°C the SX-09 composition yielded the highest MOR while the two SX-05 composition sets and the experimental composition sets had approximately the same average strength. The Weibull modulus was generally lower for the machined test bars relative to as-fired specimens, which is contrary to previous SX-05 data. No significant difference in strength was observed for the two temperature levels, although the T°-25°C (T°-77°F) condition resulted in a more uniform microstructure. Based on these results, the baseline SX-05 composition and the T°-25°C (T°-77°F) temperature were selected for subsequent rotor fabrication activities.

A statistically designed molding matrix was conducted using the generic (bladeless) axial rotor tool to determine the molding variable values required to reduce knit lines on the surface of the rotor hub prior to receipt of the 15-bladed engine rotor fabrication tool. The design for this Taguchi-type experimental matrix is shown in Table XVIII. Two levels of nine molding variables were selected for the matrix evaluation. The variables included mold temperature, melt temperature, fill velocity, back pressure, pack pressure, pack time, shot size, hold pressure, and hold time. An L16 orthogonal array was used since this is the smallest two-level design matrix with interaction information that can be used with greater than 7 but less than 16 control variables.

Five parts were molded at each condition to establish equilibrium conditions with the exception of mold temperature and melt temperature, which took somewhat longer for stabilization. The last three rotor hubs from each of the 16 treatment combinations were processed through sintering to determine the effects of the rotor molding variables

C-2

Table XVIII.
CBO rotor molding test matrix.

Yates order	TC	Run order	Mold temp.	Melt temp.	Vel.	Back press.	Pack press.	Pack time	Shot size	Hold press.	Hold time
1	(1)	7	1.00	1.00	1.00	1.00	1.00	1.00	1.00	1.00	2.00
2	a	2	1.17	1.00	1.00	1.00	1.25	1.00	1.07	1.25	1.00
3	b	16	1.00	1.10	1.00	1.00	1.25	2.00	1.00	1.25	1.00
4	ab	12	1.17	1.10	1.00	1.00	1.00	2.00	1.07	1.00	2.00
5	c	13	1.00	1.00	1.40	1.00	1.25	2.00	1.07	1.00	1.00
6	ac	1	1.17	1.00	1.40	1.00	1.00	2.00	1.00	1.25	2.00
7	bc	15	1.00	1.10	1.40	1.00	1.00	1.00	1.07	1.25	2.00
8	abc	11	1.17	1.10	1.40	1.00	1.25	1.00	1.00	1.00	1.00
9	d	5	1.00	1.00	1.00	4.00	1.00	2.00	1.07	1.25	1.00
10	ad	3	1.17	1.00	1.00	4.00	1.25	2.00	1.00	1.00	2.00
11	bd	4	1.00	1.10	1.00	4.00	1.25	1.00	1.07	1.00	2.00
12	abd	10	1.17	1.10	1.00	4.00	1.00	1.00	1.00	1.25	1.00
13	cd	9	1.00	1.00	1.40	4.00	1.25	1.00	1.00	1.25	2.00
14	acd	14	1.17	1.00	1.40	4.00	1.00	1.00	1.07	1.00	1.00
15	bcd	8	1.00	1.10	1.40	4.00	1.00	2.00	1.00	1.00	1.00
16	abcd	6	1.17	1.10	1.40	4.00	1.25	2.00	1.07	1.25	2.00

on component density and dimensions. One rotor hub from each of the runs was placed in bake and each of the three bakes was sintered independently. The sintering arrangement randomized the run number rotor hub position in the furnace. After sintering, densities and measurements were obtained on the rotor hubs and the effect of each of the nine molding variables on those properties was analyzed.

Statistical analysis of the rotor molding test matrix (L16 orthogonal array) was completed using ANOVA-TM software. Statistical analysis showed that the mold temperature-velocity interaction, pack time, and mold temperature levels explained about 33% of the raw data variation for flow lines, while the mold temperature-velocity interaction, mold temperature, velocity, and pack time explained about 61% of the signal-to-noise ratio variation for flow lines. High pack time, high mold temperature, and low velocity are preferred to minimize flow lines on the surface of the rotor hubs. Mold temperature explained 73% of the green weight variation, with the lower mold temperature preferred. A cooler mold causes the material to cool more rapidly resulting in increased shrinkage permitting additional material to be packed into the mold cavity. The sintered differences were, however, minimal. Hold time was a major contributor toward diametral variation. The shorter hold time was preferred for meeting both the shaft outer and inner target diameters as well as minimizing diametral variability. A lower green density is achieved with a short hold time resulting in a greater shrinkage. Possibilities exist for fine tuning dimensions by adjusting hold times. One factor that consistently showed up as a major contributor to dimensional variation and out-of-roundness was pack time, with the low level generally preferred to minimize these conditions. The overall preferred factor levels resulting from this experiment, as they effect different properties, are listed in Table XIX.

After completion of the L16 rotor hub experimental array, a HIPing test matrix was conducted such that at least 1 rotor hub from each of the 16 runs was represented. A randomized L4 orthogonal array with three center points, as presented in Table XX, was used. The seven runs each contain three rotor hubs. The arrangement was such that a high HIP hold time rotor hub was on the top shelf and a low HIP hold time rotor hub was on the bottom shelf. HIP hold time levels were selected because that control variable had the greatest impact on the rotor dimensions. The response variables in-

Table XIX.
Preferred factor levels for CBO SiC rotors.

- Flow lines
  - $Velocity_L$ x mold $temp_H$
  - Pack $time_H$
  - Mold $temp_H$
  - $Velocity_L$
- Density
  - Melt $temp_H$
- Hub diameter
  - Mold $temp_H$
  - Hold $time_L$
  - Back $pres_L$ x melt $temp_L$
  - $Velocity_H$ x melt $temp_L$
- Hub diameter
  - Back $pres_H$
  - $Velocity_H$

L = low

H = high

cluded density, dimensions, and computed tomography inspections. The experimental results generally suggested lower temperatures and longer HIP hold times as the optimum conditions to fabricate acceptable rotors. The lower HIP temperatures also minimized grain growth.

The rotor hub density and computed tomography (CT) results before and after HIPing are shown in Table XXI. The average CT density differential between the outer hub region and the core was 8.0% in the sintered rotor hubs, compared with the 1.6% difference observed in the HIPed rotors, suggesting a dramatic core density improvement. Tomographs of the rotor hub before and after HIPing are shown in Figures 115 and 116 respectively. The CT rotor hub density level and uniformity were substantially improved by HIPing.

Table XX.
SiC rotor hub HIP matrix.

Run No.	Time at temp--min	Maximum temp--°C(°F)
1	60	2100 (3812)
2	105	2050 (3722)
3	15	2150 (3902)
4	60	2100 (3812)
5	105	2150 (3902)
6	15	2050 (3722)
7	60	2100 (3812)

Table XXI.
Results of rotor hub HIPing experiment.

Run No.	Density, gm/cm^3 ($lb/in.^3$) HIPed	As-fired	Δ	CT density difference, % As-fired	HIPed	Δ
1	3.159(0.114)	3.147(0.114)	.012	8.8	1.2	7.6
2	3.166(0.114)	3.156(0.114)	.010	7.1	1.8	5.3
3	3.165(0.114)	3.150(0.114)	.015	7.5	1.7	5.8
4	3.164(0.114)	3.147(0.114)	.017	9.8	1.5	8.3
5	3.166(0.114)	3.157(0.114)	.009	6.6	2.1	4.5
6	3.162(0.114)	3.148(0.114)	.014	8.3	1.3	7.0
7	3.161(0.114)	3.145(0.114)	.016	8.2	1.4	6.8

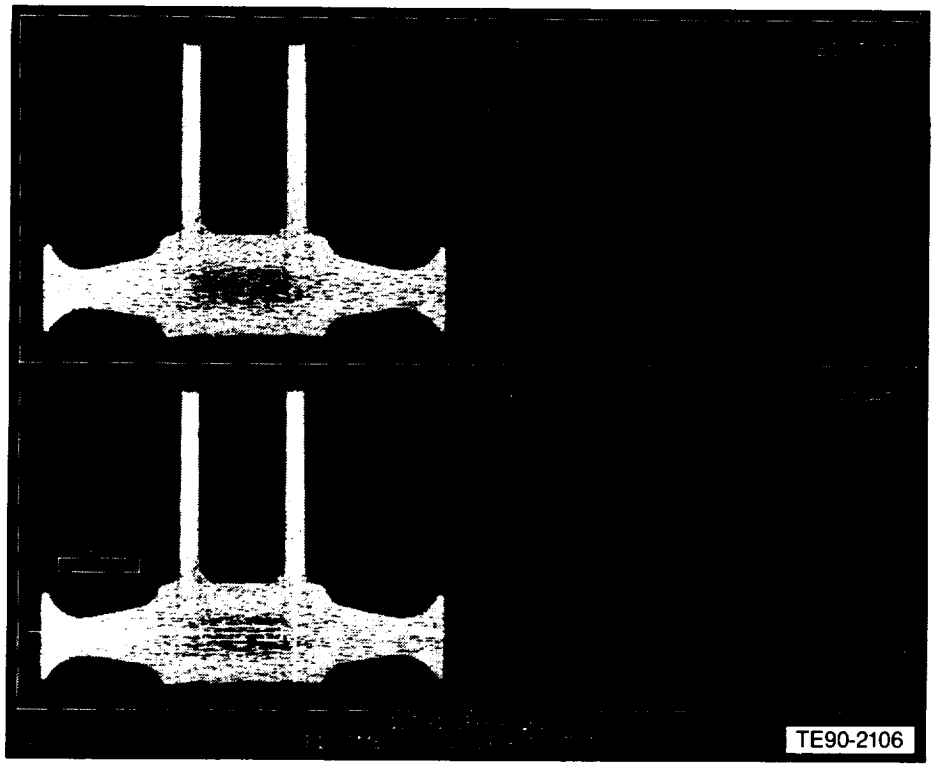

Figure 115. Computed tomograph of as-sintered CBO SiC rotor hub.

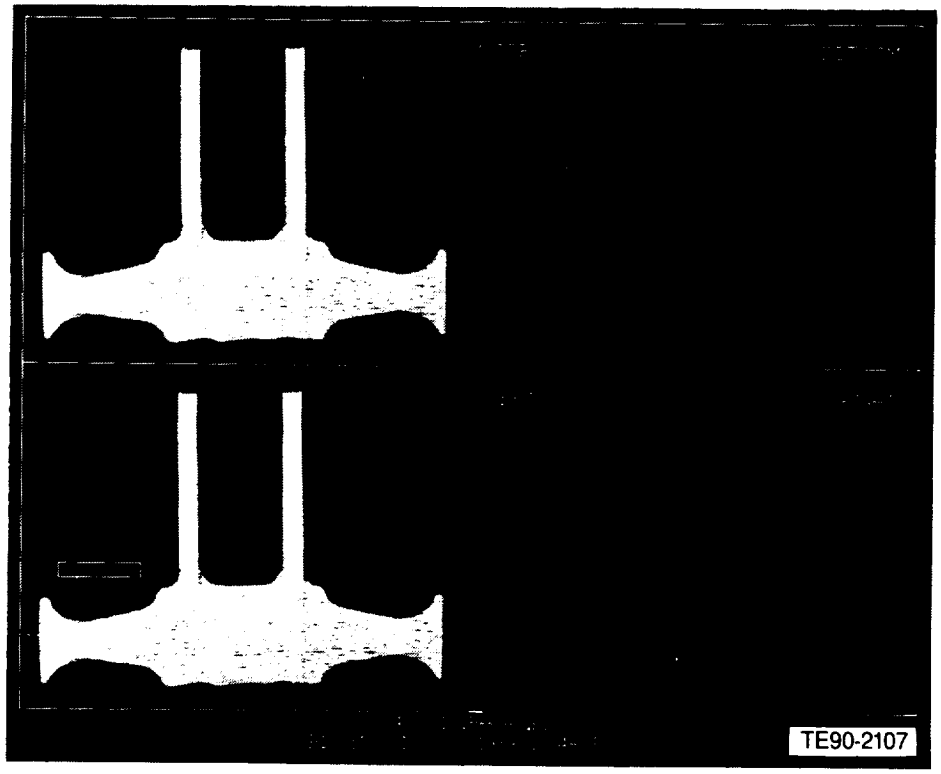

Figure 116. Computed tomograph of post-HIPed CBO SiC rotor hub.

Six sintered rotor hubs and fourteen sintered/HIPed rotor hubs (two from each of the HIPing experiments) were characterized at Allison. Characterization efforts on both the sintered and HIPed rotor hubs consisted of strength evaluation of test bars cut from the rotor hubs and spin testing to failure. The results of this evaluation are presented in the Materials and Component Characterization section of this report.

The 15-bladed engine configuration injection molding tool for Carborundum development was received from the tooling subcontractor in February. Two major problems were evident: the lever arm that actuates the sliders in the scroll plate was too stiff, and the cartridge mold heaters were underpowered. The tool was returned to the tooling vendor for modification of the scroll plate lever arm. After correction of the tool problems, baseline axial rotor molding began in April. The molding procedures were based on the recommended rotor hub factor levels for flow lines and recommended factor levels (mold temperature and velocity profile) from the finite element flow analysis. Molding variable levels were investigated using short shot molding procedures. The short shots were not as uniform as those made for the rotor hub using the generic rotor tool. The nonuniformity involved differences in the sprue bushing. The hub molding trials used a standard size conventional sprue bushing whereas the bladed engine configuration rotor had a larger size modified sprue bushing. Three additional sprue bushings were ordered and machined and a sprue bushing short shot matrix was run in early April. The results of the short shots are shown in Figure 117 where the blades are just starting to form on the rim. The standard size conventional and larger size conventional sprue bushings produce a uniform flow pattern. With the bulbous extension between the sprue and the hub as originally designed in the modified sprue bushing, some inconsistencies developed that led to knit lines between the blades on the rim.

A total of 46 rotors were molded under invariant conditions in April. After molding six rotors for equipment stabilization, 15 consecutive acceptable rotors were molded. A total of 29/40 rotors (72.5%) passed visual inspection after molding. Following the initial rotor molding effort, a total of 30 product-of-the-mold engine configuration rotors were processed through sintering and nondestructive evaluation (NDE). Five were rejected due to flaws discovered through X-ray analysis. The majority of the surface knit lines were located on the hub o.d. near the blade leading edge and on the hub radius near the shaft and sprue. A total of 16 rotors were HIPed, 15 of which were serialized as FX78499 through FX78513. The average density of the rotors increased from 3.157 gm/cc (0.114 lb/in.^{3}) to 3.171 gm/cc (0.115 lb/in.^{3}) due to the HIPing process.

As a result of flow finite element analysis and the Taguchi L16 matrix experiment, which identified mold temperature as a determining factor for rotor quality, a series of experiments was conducted with heated molds. The goal of this effort was to heat the mold to the melt temperature of the molding compound to obviate flow lines. It appears that mold temperature is the dominant factor affecting flow lines in molded rotors, despite the fact that sprue size provided the highest correlation in the L16 test matrix. When the temperature of the mold was heated above the normal mold temperature, the flow lines virtually disappeared.

The first group of rotors molded with the heated mold showed that the flow lines between the blades could be eliminated. Subsequent optimization resulted in a group of 29 rotors molded in early November that had an average visual quality rating of A-, which is the highest achieved to date. None of the rotors were lower than B+ in quality, which indicates only minor surface imperfections that can be easily removed/cleaned. The rotors were molded using a screen pack in compounding and the larger sprue bushing to minimize shear rates and stresses. The injection velocity in the blades was also reduced. The molded rotors have a shiny and more homogeneous surface appearance than rotors produced from earlier molding trials. These rotors will be sintered in January 1990.

Vane Set Development. Development activities were conducted to address the fabrication of injection molded sintered alpha-SiC vanes for the gasifier turbine. A single-cavity vane tool was ordered in May 1989. The initial molding of the SiC gasifier turbine vanes was conducted in June 1989 to evaluate the tool. As the sprue and the runner configuration adjacent to the sprue were not entirely within specification, the tool was returned for rework. Hence, additional moldings were conducted using the modified tool. Nine parts were sintered in late June to determine proper fixturing. Subsequent sintering runs included 90 parts, 36 parts, and 72 parts, all in July. Fifteen vanes were

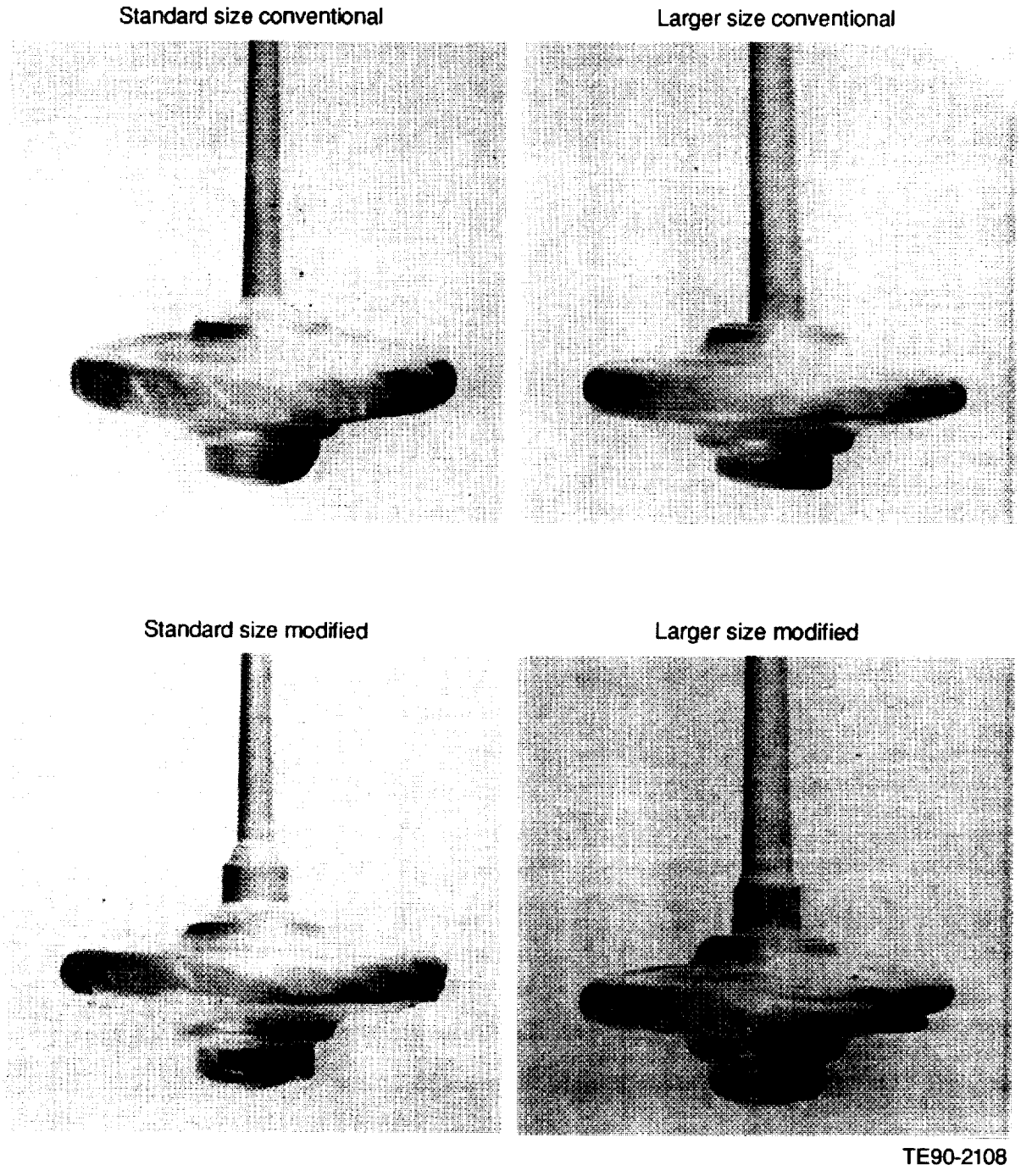

Figure 117. CBO rotor short shot, sprue bushing evaluation.

received at Allison in July for dimensional assessment. Inspection of these vanes revealed that the chord length, particularly at the vane foot, was short by approximately 0.002 to 0.005 in. The maximum twist was about 1 deg, with a typical twist of 10 to 30 angular minutes. These deviations were all considered to be acceptable.

A total of 75 sintered α-SiC gasifier turbine vanes were provided to Allison in early November. Initial inspection of the vanes revealed small indications at the vane leading and trailing edges; these are associated with removal of the flash at the tool parting lines. Additional vanes with modified flash removal procedures are currently being processed for delivery in early 1990.

Slip Casting. The objectives of the slip casting development task involve improvement of the properties of the sintered α-SiC slip cast parts based on processing variables, and fabrication of slip cast scrolls to be evaluated in rig and engine test activities. Scroll fabrication trials also provide information on process yields and component properties leading to final engine scroll development. The slip development activities focused on the fundamentals of each processing step, with the goal of improving casting yields and structural integrity by decreasing microstructural and macrostructural flaws. All development work was conducted using an alpha-SiC aqueous slip with a bimodal particle size distribution. The shapemaking development activities initially concentrated, as described, on fabrication of prototype scrolls. Information resulting from this effort relating to mold design and fabrication, dimensional control, and process yields were incorporated into the final design of the engine configuration scroll. Following definition of the scroll design, efforts focused on fabrication trials of the scroll to determine casting characteristics and properties and to produce engine quality scrolls for engine test-bed testing and evaluation.

The slip development efforts concentrated on powder beneficiation to remove unwanted ionic species, dispersion improvements through adjustments in chemical levels to increase the state of dispersion and binder additions that improve the plasticity and handling strength of the green parts. A number of statistically designed experiments were conducted to determine the influence of various material and processing variables as they effect the final slip quality. Variables under investigation include dispersant type and level, slurry pH, binder type and level, and ionic conductivity.

Two prototype configuration scroll models were initially designed and fabricated at Carborundum. One mold was produced with a low density plaster in the shroud area to facilitate formation of a thicker wall to provide for extra machining stock. A number of casts were made with both the standard and beneficiated slip. Following initial mold break-in, the castings were judged successful; lack of mold or shape-related problems indicated a mold pattern that fit well the model design. The model, green, and sintered prototype scroll parts are shown in Figure 118.

Five prototype scrolls were subsequently processed through sintering to densities of 3.09-3.11 gm/cc (0.112 lb/in.^{3}), 96-97% of theoretical density; no sintering cracks were observed. Earlier design experiments provided information on improving presintering and sintering procedures; however, the best results were observed at or beyond the envelope of the design conditions investigated. Therefore, a statistically designed experiment to investigate the effects of various processing factors on scroll density and dimensions was conducted. A central composite Taguchi-type experiment was designed entailing three to five different operating levels using five factors. The factors for both experiments were as follows:

Experiment I	Experiment II
Slurry pH	Casting time
Presinter 1	Bake temperature
Presinter 2	Presinter 1
Furnace position	Presinter 2
Furnace temperature	Furnace hold time

Slurry pH, bake temperature, and the two presinter variables were determined to be the most significant variables affecting sintered density. Casting time was judged to be the most important factor in the production of desired wall thickness. The experiments indicated that near theoretical density was possible to achieve by operating with intermediate presinter conditions. However, interaction with bake temperature prevents achieving ideal conditions in all cases. These presinter conditions and problems have been confirmed in the manufacture of other commercial SiC products.

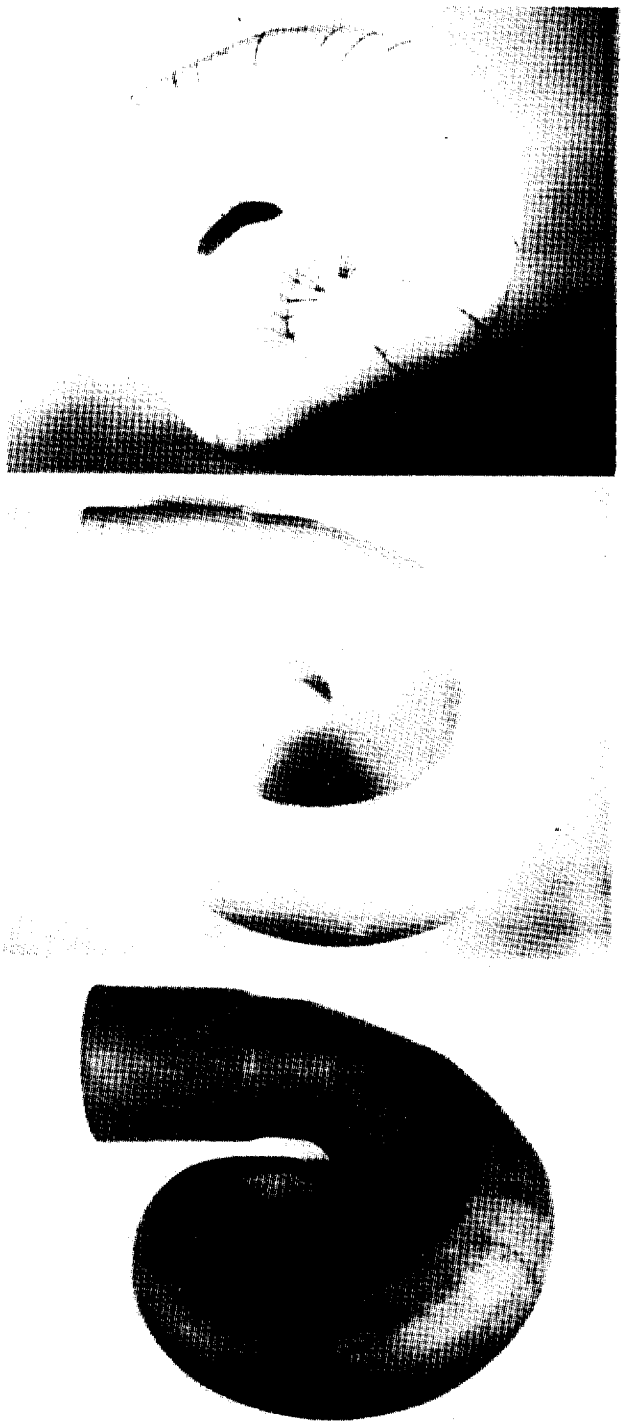

TE90-2109

Figure 118. CBO scroll model (top), green part (middle), and sintered part (bottom).

ORIGINAL PAGE
BLACK AND WHITE PHOTOGRAPH

The machined AGT-5 engine configuration master scroll model was received from the tooling subcontractor in June; two plaster molds were fabricated for scroll casting. A total of 16 parts have been cast to date. Breakage rate in handling during the initial casts was relatively high; however, only two parts actually cracked within the molds. One scroll was successfully sintered to a density of 3.124 gm/cc (0.113 lb/in.^{3}). A modified casting method is now being investigated that further increases stock for grinding in the shroud area of the scroll. This method will be optimized during subsequent experiments. Initial engine configuration scroll delivery is anticipated in early 1990.

Difficulties with the fineness of the two SiC powders used to produce casting slip were also encountered. The major difficulty involved adhesion of the cast parts to the surface of the plaster molds, resulting in damaged components. Samples of eight sublots of powder dating back to 1985 were analyzed for particle size distribution. The range of lot percentages falling into any one particulate size channel varied as much as 10% between lots. The powder with the least adhesive tendencies (and therefore, yielding the most success in casting the scroll) was determined to be the most coarse. The other sublots were all finer, particularly the one with which the problem was first discovered. There does not, however, appear to be a coarse powder lot available that matches the characteristics of that used in the optimization experiments. Therefore, the most coarse lot available has been chosen for subsequent scroll casting efforts.

A test matrix was also initiated in which the bimodal SiC powder blend is varied in both grit size and ratio. Parts are being cast at three pH levels within each blend, with the relative green density measured and correlated with particle size distribution of the feeds and milled slurry. All of the parts will then be sintered and densification variations correlated.

The sintered densities of slip cast components have increased from less than 3.00 gm/cc (0.108 lb/in.^{3}) to the current average of 3.11 gm/cc (0.112 lb/in.^{3}) over the past two years. A commercial slip cast SiC component was machined into test bars measuring 50.8 mm x 6.35 mm x 3.18 mm (2 in. x 0.25 in. x 0.125 in.) and the room temperature strength evaluated. The results of this evaluation are summarized in Table XXII. The non-annealed average strength of 462 MPa (67 ksi) represents a significant

Table XXII.
Strength characteristics of CBO slip cast SiC.

Sample No.	Annealed	No. of Specimens	Strength--MPa (ksi)
1	Y	8	468.9 (68.0)
1	N	8	459.9 (66.7)
2	Y	8	475.8 (69.0)
2	N	8	464.7 (67.4)
Average		32	467.5 (67.8)

increase in the strength of slip cast SiC. Lower strength values observed were usually due to processing related flaws. The samples have been submitted for fractography to determine the types of processing flaws present and to provide direction for further process improvements.

3.2.2 Manville

Objective/Approach

Efforts at Manville are aimed at developing an injection moldable insulation for automotive gas turbines capable of low cost, high volume production. The approach is to modify the insulation material system for improved injection molding properties while developing the injection molding process for both simple and complex engine components. In addition to the development of the molding process, several other developmental items have been addressed including insulation/metal hardware bondability and erosion resistance. Efforts have focused on refinements of the binder system, thermal characterization, injection molding, mold release and release agents, surface abrasion resistance, and mixer scale-up studies.

Accomplishments/Results

- evaluated various formulations of insulations to decrease heat transfer; the thermal conductivity of the insulation with silicon carbide used as the radiation blocker found to be lower than that of formulations with magnesium oxide; further, the high temperature shrinkage of this new compound was less than that of other formulations
- denser insulation mixes found to enhance molding and mold release agents determined to aid the molding process; mold redesign efforts also determined that back pressure helps to fill out the mold while increased draft angles of the gasifier housing contour proved necessary for proper mold release
- raw materials used in the insulation process, such as Polyox water soluable resin, identified as having a shelf life limitation
- developed a surface hardening material (two-part colloidal liquid system) and application technique for improved abrasion/erosion resistance
- determined that the insulation to metal bond appears to be independent of metal surface treatment; bond-line failure is believed to result from insulation material separation from the metal surface during application and occurs prior to drying

Discussion

Insulation Formula Development. Preliminary experimental formulations were prepared with silicon carbide powder (fines) in place of the magnesium oxide powder as the radiation blocking agent. Small bar test samples were first made to check density and drying shrinkage of this new formulation. Results are presented in Table XXIII.

The moldability, mold release, dry shrinkage, and density appear to be comparable with previous formulations. The last sample listed above was a 25.4 cm x 25.4 cm x 1.27 cm (10 in. x 10 in. x 1/2 in.) test plaque prepared for thermal conductivity testing in the High Temperature Heat Meter and the High Temperature Calorimeter. Thermal conductivity test results are reported in Table XXIV for this insulation sample which has silicon carbide as the radiation blocking agent.

Table XXIII.
Density and drying shrinkage of SiC based insulation.

Dry percent silicon carbide	Moldability	Mold release	Dry shrinkage percent Length	Width	Dry density Kg/M^3	lb/ft^3
5.3%	Excellent	Excellent	0.2%	1.0%	330	(20.6)
10.1%	Excellent	Excellent	0.2%	2.5%	354	(22.1)
14.4%	Excellent	Very good	0.0%	0.6%	353	(22.0)
14.4%	Excellent	Very good	0.1%	0.7%	370	(23.1)
14.4% (thermal sample)	Excellent	Excellent	0.5%	0.6%	361	(22.5)

Table XXIV.
Thermal conductivity test results for SiC based insulation formulation.

Sample	Hot face temperature-- °C (°F)	Cold face temperture-- °C (°F)	Mean temperture-- °C (°F)	Apparent thermal conducitivty-- W/m°K (Btu-in/hr ft^2°F)		Test density kg/m^3(lb/ft^3)
			Tested in high temperture heat meter--ASTM C-518			
6195-46-4 Silicon Carbide	371 (700)	260 (500)	316 (600)	0.072	(0.50)	393 (24.5)
	593 (1100)	482 (900)	538 (1000)	0.097	(0.67)	
			Tested in high temperature calorimeter--ASTM C-201			
6195-46-4 Silicon Carbide	704 (1299)	65 (149)	384 (724)	0.075	(0.52)	375 (23.4)
	813 (1495)	78 (173)	446 (834)	0.085	(0.59)	
	934 (1713)	93 (199)	513 (956)	0.095	(0.66)	
	1037 (1899)	111 (231)	574 (1065)	0.108	(0.75)	
	1064 (1948)	114 (238)	589 (1093)	0.113	(0.78)	

The high temperature shrinkage of this sample was less than 1% while the thermal conductivity of this formulation, with silicon carbide as the radiation blocker, was lower than that of formulations with magnesium oxide. The formulation has been selected for use as the engine test-bed insulation.

Injection Molding Development. Injection molding tests were conducted to evaluate mold filling and mold release agents. The testing was performed at the General Motors Technical Center using a molding injection cylinder. The insulation was forced into the injection cylinder from a vertical, air pressurized Ladish pipe through a three way valve. The insulation was then injected onto the gasifier housing with a female mold attached. The female mold was first coated with Teflon for evaluation as a potential mold release agent. Using the formulation currently being applied by hand, the first injection failed to fill out the entire mold; insulation within the mold was absent opposite the in-gate and also stuck to the upper cone. The second injection trial was applied through a new in-gate placed one third of the way around from the first in-gate. The insulation in this trial did fill the entire mold cavity, including the uppercone, but still stuck to the female mold in the upper cone portion.

The female mold was next sprayed with a dry lubricant (Sherwin Williams Sprayon Products "Dry Lubricant") and a metal plate was bolted over the top of the mold cone opening to provide back pressure for the molding. The increased back pressure resulted in a total fill of the mold with a significant reduction of voids within the insulation. When the female mold was removed, however, the entire cone area was torn off and the insulation separated in a number of other areas. The data from these trials indicates that while the increased back pressure led to better fill-out of the mold and to a more dense and consistent application of the insulation, the spray release agents did not work as intended.

The next series of injection molding trials applied insulation to which less water was added in the base formulation so that both density and stiffness of the wet material would be increased. This insulation was then injected into the gasifier housing mold using the Teflon coated female mold (cleaned of the sprayed-on release agent). The injection site used the previous in-gate and the cone area top plate provided back pressure as described above. This denser insulation completely filled out the cavity and the webbing of the housing, but firmly stuck to the base of the housing and the cone portion of the female half of the mold.

Additional testing was conducted with this denser insulation material to evaluate mold release agents from Chem-Trend, Inc. The first mold release agent was a silicone in methylene chloride solution (MR515) wiped onto the Teflon coated female mold half. The insulation again pulled off of the female mold cone portion in the area where very little draft angle exists relative to the desired insulation shape. Subsequent trial tests using various combinations of mold release agents yielded similar results until a combination of silicone and soap (RCTW9011) in a water base was applied to the female mold half and a washer sized to fit the cone opening of the female mold was bolted to the housing. The washer was designed to replace the back pressure plate but still hold the insulation in place at the top of the cone when the female half was removed. Results of this trail indicated the insulation completely filled the cavity and considerably less insulation was removed on the female mold at the cone area. The last trial combined results of the second trial in which the female mold was wiped and sprayed with MR515 with the new washer installation. This trial resulted in the best molding; the entire cavity filled out, the insulation surface had few voids, and insulation did not separate from the housing in the cone area. There was, however, some evidence of insulation cracking in areas with very small draft angles.

Conclusions from these trials indicate that the denser insulation mix yields a better mold; proper release agents can aid in the molding process; back pressure helps fill out the mold; and further, the mold needs to have some minimum draft angle for the material to properly release from the mold. As a result of the above conclusions, the gasifier housing insulation contour has been redesigned to increase both the insulation thickness in appropriate areas and the draft angles where feasible. The increased thickness will provide more thermal protection and the increased draft angles permit easier release of the female mold half.

Raw Material Shelf Life. During molding trials, insulation was prepared from the raw materials that were on hand at the GM Tech Center. The molding characteristics of the wet insulation were significantly different from prior samples. The wet mass de-watered easily and the surface ripped when worked by hand. One or more of the organic components were suspected of deteriorating with age. The material suppliers were contacted regarding the shelf-life of their respective products. Polyox, a water soluble resin, was identified as the most likely shelf-life limited material. Polyox has a shelf-life of eight months to a year when exposed to air at ambient temperatures. As Polyox ages, the long polymer chains cleave and the material no longer functions as desired. A fresh sample of Polyox was received from Union Carbide, and subsequent insulation prepared using the new Polyox exhibited normal handling and molding characteristics.

An additional problem regarding the mixing components composing the wet insulations was identified. The compounding and blending of the insulation component specifies discrete mixing times and mixing speeds. If the components are mixed for longer than specified times or at higher than specified speeds, the wet insulation may exhibit the same molding deficiencies as observed with aged Polyox. The long polymer chains within the components may be breaking down with too long or too intense mixing. Further, the drying shrinkage was found to increase, resulting in decreased bonding to

the metal surface and, therefore, decreased dry insulation integrity.

A series of test batches was prepared at Manville to compare aged Polyox with fresh Polyox and to reconfirm that specified mixing times and mixing speeds were optimal. The results of the tests are detailed in Table XXV. While the GM Tech Center's old Polyox had deteriorated, the Manville old Polyox had not, and performed similar to Manville new, or fresh, Polyox. All three samples of Polyox performed poorly when subjected to higher mixing speeds. In all cases, the poor performance was evidenced by unsatisfactory molding characteristics and by increased drying shrinkage. The mixing procedure used at the General Motors Technical Center has been revised to focus on the proper mixing speeds.

Abrasive/Erosion Resistance. Hot rig tests at General Motors using in-place moldable insulation indicated that the insulation surface was eroding in areas in direct contact with the engine's hot working fluid. Previously, colloidal silica had been either spray or brush applied to the insulation surface to create a "hard" coating to withstand erosion. These coatings, however, formed a thin skin which either cracked at high temperature or was friable and easily eroded. A two-part colloidal liquid system was developed and applied to the surface of dried insulation, hardening the insulation to a depth of about one millimeter. The technique consists of applying either an acid or base stabilized colloid to the surface, allowing it to soak into the surface, and then applying the opposite colloid, thus gelling them in the surface layer. Upon drying, the surface layer, to a depth of about

Table XXV.
Polyox evaluation: effects of aging and mixer speed.

Polyox/ mixer speed	Moldability	Mold release	Dry shrinkage percent Length	Width	Dry density Kg/m^3	(lb/ft^3)
MVL old/normal	Excellent, normal consistency	Excellent	0.1%	1.0%	367	(22.9)
MVL old/high	Very good, rips when worked	Excellent	0.7%	1.6%	381	(23.8)
MVL new/normal	Excellent, normal consistency	Excellent	0.2%	0.7%	378	(23.6)
MVL new/high	Excellent, rips when worked	Excellent	0.4%	2.3%	362	(22.6)
GMTC old/normal	Good, rips when worked	Excellent	0.6%	3.3%	396	(24.7)
GMTC old/high	Poor, de-waters well, rips when worked	Excellent	0.8%	2.3%	377	(23.5)

GMTC = GM Tech Center
MVL = Manville

one millimeter, becomes significantly harder than the untreated insulation. The surface remained hard and intact upon exposure to 1800°F soaking heat in a furnace. This surface hardening technique has been demonstrated and appears to provide improved erosion resistance.

Insulation to Metal Bond. The bond between the insulation and the engine castings was evaluated by molding insulation bars on various cast plates which had been subjected to various surface treatments. The treatments included: resin impregnation (LOCTITING), sandblasting, stripping with paint stripper, hot and/or cold degreasing with chlorathene, and various combinations of these treatments. In all cases, the wet molded insulation following drying was firmly bonded to the metal plates. This result indicates that prior bond deficiencies observed between the insulation and various engine parts is likely not due to the condition of the metal surfaces of the parts. A bond-line failure is probably a result of material separation from the metal surface during the application of the wet insulation before drying. Hand molding techniques need to be carefully assessed to determine if this is truly the mechanism leading to the insulation-to-metal bonding failures.

3.2.3 GTE Laboratories

Objective/Approach

The objectives of GTE Laboratories' ATTAP ceramic development efforts are: to develop turbine rotors and vanes with state-of-the-art material properties for evaluation in AGT-5 rig and engine test-bed test activities, and to improve current materials and processes to enhance the resistance of the ceramic rotors to impact damage/failure within such rig/engine environments. To accomplish these objectives, a three phase technical effort is being conducted. In Task I, the process technology is being developed for fabrication of AY6 and PY6 Si_3N_4 axial turbine rotors and PY6 Si_3N_4 vanes. The remaining two technical efforts address the requirement for improved impact resistance in turbine rotors. In Task II, the fracture toughness of monolithic PY6 Si_3N_4 is being increased by microstructural modifications. Task III addresses toughness improvements of PY6 Si_3N_4 by the incorporation of SiC whisker reinforcement.

Accomplishments/Results

- PY6 Si_3N_4 gasifier turbine vanes were fabricated and delivered.
- AY6 and PY6 Si_3N_4 test bars were fabricated and delivered.
- Process parameters were established for axial rotor fabrication.
- HIPing test matrix was designed and conducted.
- PY6 Si_3N_4 turbine rotors with 30 v/o SiC whiskers were fabricated.

Discussion

Task I–Rotor Shape Making Development/Turbine Vane Fabrication. The objectives of this task are to establish and demonstrate reliable AY6 and PY6 Si_3N_4 rotor fabrication processing methodology, and to develop and fabricate PY6 gasifier turbine vanes. The specific goals for 1989 were the following:

- fabrication of AY6 and PY6 Si_3N_4 test bars
- fabrication of PY6 Si_3N_4 turbine vanes
- development and demonstration of rotor shape making capabilities required for rotor fabrication

Recent improvements in mechanical properties of GTE AY6 and PY6 Si_3N_4 produced within the GTE Prototype Engineering Center have resulted in a requirement for a new mechanical properties data base to be generated at Allison for these materials. GTE supplied modulus of rupture specimens of both materials in 1989. The test bars were fabricated using identical processing conditions compared with the component fabrication efforts, with one side left in the as-fired (as-HIPed) condition to allow determination of the strength characteristics of both the as-fired and machined surfaces. A total of 200 AY6 bars and 100 PY6 bars were delivered to Allison in September. The results of Allison's characterization of these test bars are reported in subsection 3.1.1 of this annual.

Companion test bars, which failed NDE inspection, were evaluated at GTE Laboratories. The test bars were 50.8 x 6.35 x 3.18 mm (2 x 0.25 x 0.125 in.) and were tested with a crosshead speed of 0.5 mm/minute (0.02 in./minute). For the as-fired property testing, the bars were ground flat under

the outer knife edges to ensure a uniform load distribution. The results of these tests are listed in Table XXVI. The average strength values are adequate for both the as-HIPed and machined surfaces; however, the low Weibull modulus values observed in several cases reflect that these parts were rejected by NDE for delivery to Allison. Inspection of several low strength as-HIPed bars revealed that large surface pits acted as the primary fracture origins. In practice, actual components with similar defects would not be considered acceptable for delivery and engine testing. One interesting observation is the nearly equivalent room temperature strengths of the as-HIPed AY6 and PY6 samples. There is an obvious material difference between AY6 and PY6, as demonstrated by the room temperature strengths obtained from the machined samples. The fact that the as-HIPed surface strengths did not significantly differ between AY6 and PY6 indicates a common source of flaw origins. Since the as-HIPed surface strengths are substantially less than the machined surface strengths, it is assumed that the failure origins are surface related in the as-HIPed samples. Initial analysis of the fracture surfaces supports this assumption. A preliminary conclusion may be that the current fabrication process (in particular HIPing) produces a surface roughness (defect size) that limits the room temperature strength of current AY6 and PY6 Si_3N_4 to approximately 690 MPa (100 ksi).

The oxidation resistance of machined AY6 and PY6 Si_3N_4 test bars and that of as-HIPed PY6 Si_3N_4 turbine vanes has been measured. All the oxidation tests were performed in air for 500 hr. The PY6 samples were oxidized at 1350°C (2462°F) and the AY6 samples at 1000°C (1832°F) and 1200°C (2192°F). The results of the oxidation of AY6 test bar fragments are shown in Figure 119. The weight increase per unit area at 1200°C (2192°F) behaved in a parabolic manner typical of silicon nitride. At 1000°C (1832°F) there was essentially no noticeable oxidation weight gain. While the PY6 bar fragment oxidized at 1350°C (2462°F) behaved in the typical parabolic manner, the four PY6 as-HIPed vanes all showed slight weight losses for the first 100 hr of oxidation, as indicated in Figure 120. This initial period of weight loss was followed by oxidation weight gains over the next 400 hr at a rate approximately equal to that of the machined test bar fragment. The reason for the initial weight loss is unknown. Observation of the oxidized samples showed no indication of gas evolution or catastrophic oxidation behavior. In fact, the oxidized vanes looked unchanged except for a shiny "glazed" surface finish.

Fabrication of the gasifier turbine vanes progressed well. The vane injection molding tool was received from the tooling vendor in May. Over 300 PY6 Si_3N_4 vanes were molded and both internal and surface inspections indicated the green parts to be high quality. A conservative processing scheme has been demonstrated that yields fully dense vanes without any residual alpha-Si_3N_4 and with an acceptable as-HIPed surface finish. However, attempts are in progress to understand the as-HIPed surface characteristics of the vanes in greater detail. This is particularly important because the vanes have a high as-HIPed surface-to-volume ratio, and encounter high surface stresses during transient engine operation.

Table XXVI.
GTE mechanical property evaluation of AY6 and PY6 Si_3N_4 test bars.

Material	Temperature --°C (°F)		Strength --MPa (ksi)		Weibull modulus	No. of samples
AY6 (machined)	25	(77)	1088.0	(157.8)	6.0	10
AY6 (machined)	1200	(2192)	600.6	(87.1)	8.7	8
AY6 (as-HIPed)	25	(77)	597.8	(86.7)	10.8	14
AY6 (as-HIPed)	1200	(2192)	462.0	(67.0)	17.2	10
PY6 (machined)	25	(77)	962.5	(139.6)	15.6	8
PY6 (machined)	1400	(2552)	421.3	(61.1)	----	4
PY6 (as-HIPed)	25	(77)	673.6	(97.7)	7.5	10
PY6 (as-HIPed)	1400	(2552)	381.3	(55.3)	5.7	8

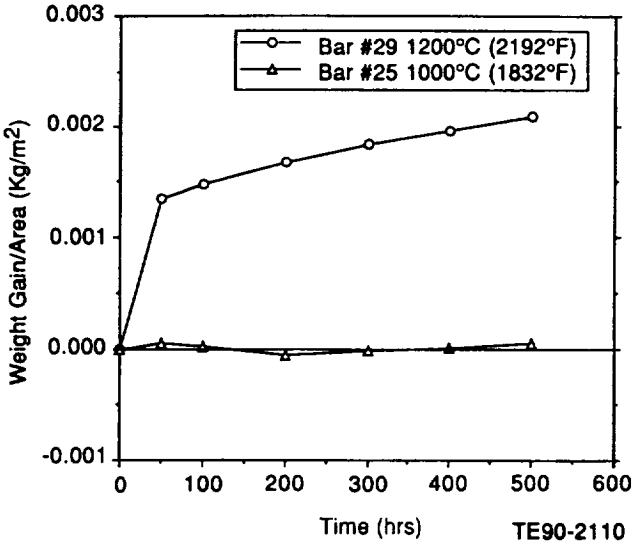

Figure 119. Oxidation of GTE AY6 Si_3N_4 test bars in air.

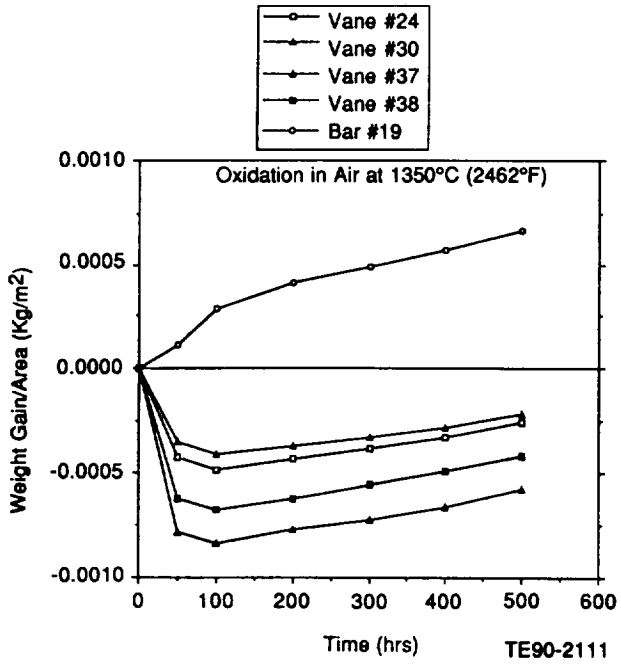

Figure 120. Oxidation of GTE PY6 machined test bars and AGT-5 vanes in air at 1350°C (2462°F).

Approximately 200 vanes were successfully HIPed, from which 50 were selected for machining and delivery. Rigorous microfocus X-radiography was used to identify parts for delivery. An evaluation of vanes processed through HIPing has shown that the thin cross section and high surface area of the vanes did not affect the material during densification. The fracture toughness and microstructure (crystalline phase and grain size) of the vanes was comparable to those of rotor hub material. Fifty vanes were received by Allison in October 1989 for dimensional and NDE evaluation. These inspections revealed the vanes to be of acceptable quality with no observable defects.

Rotor fabrication efforts have concentrated on the receipt, troubleshooting, and fine-tuning of the injection molding tool; fabrication and delivery of 10 AY6 and 10 PY6 Si_3N_4 gasifier turbine rotors; and development of green machining techniques for the rotor shaft. The rotor injection molding tool was received from the tooling vendor in March. Preliminary inspection of the tool revealed several problems that necessitated returning the tool to the vendor for modification. In an attempt to minimize delay caused by returning the tool, approximately 20-25 rotors were to be processed with the as-received tool to begin binder removal and HIPing trials. However, during molding with the as-received tooling, difficulties were encountered with the tool and processing was terminated. Revisions to the tool were completed and the tool returned to GTE in June.

Approximately 100 AY6 Si_3N_4 rotors were molded for green machining, binder removal, and HIPing studies. The primary focus of the rotor fabrication effort has been on binder removal. As a result of the change to Ube silicon nitride powder from the prior SN502, the cracking tendency of large cross-section parts, such as the AGT-5 test-bed rotors, during the binder removal step has increased significantly, requiring additional efforts to adapt the process for the turbine rotor configuration. Green machining of the shaft area has also impacted the cracking problem. Resolution of these two technical issues has been the primary focus of the Task I efforts and has resulted in a delay of rotor delivery. Modifications to the binder removal schedule resulted in a substantial decrease in AGT-5 rotor hub cracking. Cracking, and often complete separation, of the shaft and stub at the rotor hub fillet remains an issue. This shaft-related cracking appears largely unaffected by the changes made to the binder removal cycle, the solids loading level, and the silicon nitride particle size distribution. These observations, in conjunction with the different appearance of this crack relative to types typically associated with the binder removal process, indicates that the shaft cracking may be related to molding or the shaft green machining operation.

Activities are ongoing to address each of these potential problem areas.

To minimize part stress during the mold opening operation, the injection molding tool has been reworked to draw polish the blade insert surfaces; to increase the taper on the shaft and reference stub; and to increase the fillet radius on the shaft and reference stub shaft. This series of modifications has been completed and rotors have been successfully molded in the revised mold. These components are currently proceeding through the binder removal process.

It has also been noted that the shaft crack appearing after binder removal often occurs at the base of the green machined shaft hole. Stresses generated during green machining may be contributing to the crack generation. To evaluate this hypothesis, several of the recently molded rotors will be put through binder removal with completely unmachined shafts or with shafts containing only a small diameter pilot hole. Should this alleviate the shaft cracking, the initial deliverable rotors will be processed in this manner and the final shaft configuration will be diamond ground after densification.

To provide the highest material strength characteristics for engine rotors, an activity has been included to profile machine the rotor hub prior to delivery. Longer term efforts in ATTAP and/or in GTE internally funded programs will seek to improve the strength of as-fired AY6 and PY6 Si_3N_4 and eliminate the need for hub machining.

Task II--Toughened Monolithic Rotors. The objective of this task is to identify process conditions for increasing the fracture toughness of monolithic PY6 Si_3N_4. The basic mechanism for achieving improved fracture toughness has involved microstructural modifications, specifically focusing on increasing the average grain size. By increasing the grain size of Si_3N_4, resistance to crack growth increases because the crack is deflected more by propagation around the grains.

A test matrix of the hot isostatic pressing (HIPing) process for PY6 silicon nitride was conducted to study the effect of different densification times, pressures, and temperatures on microstructure and material properties. The initial three cycles were designed to determine general relationships of HIP conditions and resultant microstructures prior to a more complete HIP parametric study. The results of this test matrix are summarized in Table XXVII. SEM examination indicated different microstructures resulted from each of the HIP cycles, indicating that sufficient flexibilitv exists in the process variability to warrant a study of toughness adjustment via process modifications. However, no significant differences were measured in the fracture toughness. Consistent with the fracture toughness measurements, no significant strength differences were observed between the three HIP cycles, although the strength of the HIP-4 cycle bars was slightly lower than those of the HIP-1 and HIP-2 bars. Similar to the hot pressed billets, all HIPed materials exhibited high values for the Weibull moduli. Compared to hot pressed PY6 Si_3N_4, however, the HIPed PY6 showed higher room tempera-

Table XXVII.
Mechanical properties of experimental HIP cycle material.

HIP cycle	Temperature	Pressure	Time	Fracture toughness MPa-$m^{1/2}$ (ksi-$in.^{1/2}$)	25°C (77°F) strength MPa (ksi)	1400°C (2552°F) strength MPa (ksi)
HIP-2	Standard	Low	Standard	4.5 (4.1)	909 (132)	447 (65)
HIP-1	Standard	Standard	Standard	4.6 (4.2)	1016 (147)	502 (73)
HIP-4	High	Low	Standard	4.7 (4.3)	865 (125)	388 (56)
HIP-5	High	Standard	Standard	NM	690 (100)	285 (41)
HIP-6	High	Standard	Long	4.2 (3.8)	775 (112)	348 (50)
HIP-7	Standard	Standard	Long	4.7 (4.3)	NM	NM

Note: NM = not measured

ture strength but lower retention of strength at elevated temperatures. The hot pressed PY6 Si_3N_4 billets retained 60-70% of their room temperature strength at 1400°C (2552°F), while the HIPed PY6 Si_3N_4 material retained only 50% of the room temperature strength at 1400°C (2552°F). In addition, almost all of the HIPed bars tested at 1400°C (2552°F) exhibited minor deflection before failure, while the bars machined from hot pressed billets failed without yielding. SEM examination of hot pressed and HIPed microstructures revealed a significantly larger average grain size (approximately five times larger) in the hot pressed material compared with the HIPed material. This large difference in grain size may account for the different strength and toughness behavior between hot pressed and HIPed material.

Two additional HIP cycles were conducted based on the results obtained for the initial three HIP runs, which indicated that the higher HIP pressure used in the standard GTE HIP cycle (HIP-1) may be necessary to attain high strengths. The HIP-5 and HIP-6 cycles were designed to promote sufficient grain growth (using high temperature and high pressure) to increase material fracture toughness. However, evaluation of HIP-6 material showed no increase in fracture toughness compared with the previous HIP samples. In addition, the high temperature and pressure used in the HIP-5 and HIP-6 cycles resulted in significantly lower fracture strengths at both room temperature and 1400°C (2552°F).

Material evaluation of the HIPed samples showed slight decreases in density compared with HIP-4 material, suggesting that dedensification may have occurred at the highest temperature. Detrimental surface reactions (pitting) were also noted on the HIP-5 and HIP-6 samples. These results indicate a possible limit to the HIP temperature and pressure conditions for densifying PY6 Si_3N_4 material due to thermodynamic reactions.

To further pursue the concept of increasing material fracture toughness through grain growth during HIP densification, an additional experimental HIP cycle (HIP-7) was conducted for an extended time period to grow the Si_3N_4 grains and thereby improve fracture toughness. However, the measured fracture toughness did not increase as significantly as anticipated. Microstructural analysis has provided a possible explanation for this behavior. Polished and etched sections were prepared and examined via SEM. The SEM micrographs revealed that grain growth did occur by extending the HIP time with all other processing conditions remaining constant. However, it was qualitatively apparent that the grain growth occurred via Ostwald ripening resulting in lower aspect ratio grains and enlarged triple points of the glassy phase.

A similar plateau of fracture toughness improvement with grain growth has been noted for hot pressed PY6 Si_3N_4. Analysis of the hot pressed materials revealed alterations in the intergranular phase chemistry and distribution with increased hot pressing time. There is evidence to suggest that the grain boundary phase of HIPed PY6 Si_3N_4 also changes depending on the HIPing parameters. This confirms the need for further investigation of not only the Si_3N_4 grain development but also the thermodynamic reactions that take place in the intergranular phase during the HIP cycle. Thermodynamic analyses are currently being initiated using a slightly modified version of the NASA-Lewis CE83 computer program and available thermodynamic data for the silicon nitride-yttria system.

The following information was gained from the initial HIP cycle experimental matrix which will contribute toward future HIP cycle design and optimization:

- Most of the material fracture toughness is developed in the early stages of the HIP cycle.
- Strength and surface quality are better for the lower of the two tested HIP temperatures.
- Changing HIP temperature affects mechanical properties more than changing HIP pressure.

To measure the effects of changes in starting powder size distribution on material properties and microstructural development, isopressed PY6 Si_3N_4 billets (approximately 25 mm [1 in.] diameter x 25 mm [1 in.] length) were prepared as listed in Table XXVIII. The billets of various powder size distributions were then HIPed under the same conditions as sample injection molded rotors. Test bars were prepared from each billet and were evaluated for fracture toughness. X-ray diffraction analyses were then conducted to quantitatively measure the degree of alpha-to-beta-Si_3N_4 conversion for each billet. The correlation, as presented in Figure 121, between beta content and fracture toughness is relatively low. This supports the concept that control

Table XXVIII.
Particle size distributions of PY6 Si_3N_4 starting powders used for isopressed billets.

Powder ID	Description of particle size distribution
Ube A	A particle size distribution weighted toward the coarse end
Ube B	A broad particle size distribution
Ube C	Similar to Ube A, but increased amount of fine Si_3N_4
Ube D	A narrow size distribution of fine particles
Ube E	A narrow size distribution of coarse particles

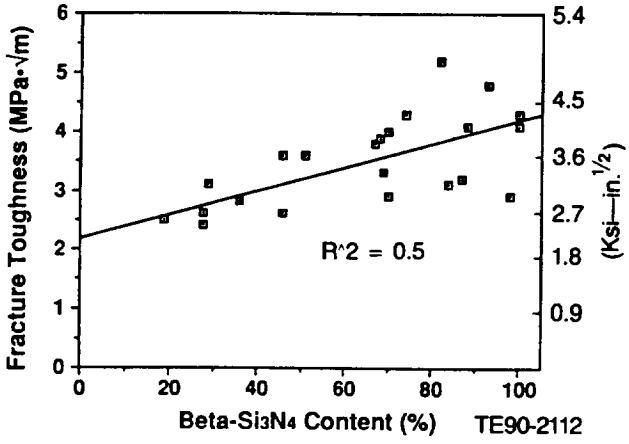

Figure 121. Fracture toughness versus beta-Si_3N_4 content for HIPed PY6 billets.

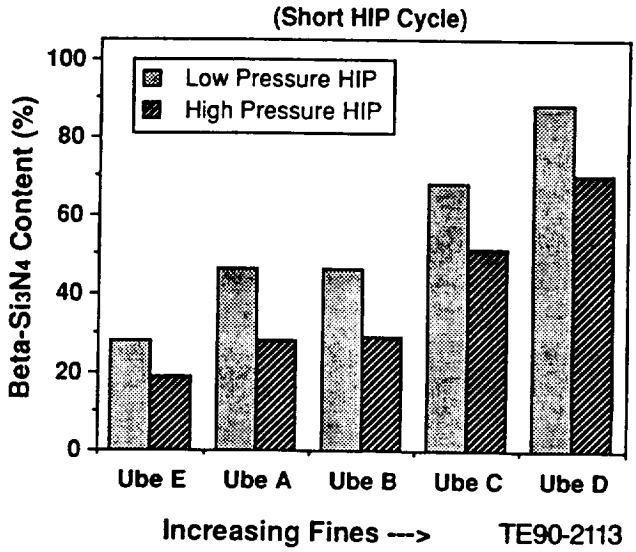

Figure 122. Beta-Si_3N_4 conversion versus initial powder size for HIPed PY6 billets.

of a combination of factors, primarily Si_3N_4 grain morphology and the intergranular phase characteristics, is required for optimal fracture toughness.

The amount of alpha-to-beta-Si_3N_4 conversion increases with the fineness of the initial powder size distribution as indicated in Figure 122. Also, for the HIPing time tested, there was a greater dependence of final beta content on initial particle size at the lower HIPing temperature than at the higher HIP temperature. The data confirm the trend noted for the experimental HIP runs performed on rotor sections in that the role of HIPing pressure on alpha-to-beta conversion appears to be minor relative to that of HIPing temperature. The respective influences of each parameter on Si_3N_4 grain morphology will be investigated further through qualitative microstructural analyses on test bar fracture surfaces from each billet.

Task III–Toughened Composite Rotors. The objective of this task in 1989 was to evaluate the densification kinetics, material properties, and fabricability of PY6 Si_3N_4 containing 30 v/o SiC whiskers. Improvements in fracture toughness, strength, and creep resistance were demonstrated in GTE's CTAHE project for additions of SiC whiskers in an AY6 Si_3N_4 matrix. At 30 v/o whisker additions, a 40% increase in fracture toughness and a 25% increase in fracture strength were observed. However, whisker reinforcement also decreased the densification rate of the composite material by limiting particle rearrangement. To evaluate the concept of whisker reinforcement of the PY6 Si_3N_4 matrix, which contains less densification additives than the AY6 Si_3N_4, the feasibility of attaining

near theoretical density must first be demonstrated. If densification is possible, notable improvements in material properties must then be observed to establish the benefit of utilizing whisker-reinforced PY6 material for ATTAP rotors.

A dust containment/collection system for working with SiC whisker containing powders has been tested at GTE and found to be more than adequate for protection of the operator and the environment. Using this system, PY6 Si_3N_4 with 30 v/o SiC whiskers was successfully compounded at the standard solids loading level to provide approximately 1.5 kg (3.3 lb) for initial injection molding and HIP trials. For future Task III activities, a 7.2 kg (15.8 lb) batch of PY6 Si_3N_4 has been sent to ACMC for blending with 30 v/o SiC whiskers.

Several thick cross-section test samples of PY6 Si_3N_4 with 30 v/o SiC whiskers were successfully injection molded. Two of these samples have been processed through binder removal and hot isostatic pressing. Both samples were over 99% dense after HIPing and show only slight distortion during densification. Test bars were machined from a HIP densified injection molded thick cross section of PY6 Si_3N_4 with 30 v/o SiC whiskers, and the mechanical properties will be evaluated.

The compounded material used to mold these parts did not flow well and the as-molded quality of the samples was marginal. To address this issue, a silicon nitride particle size distribution, identified for monolithic ceramics in Task I as having a higher flow rate, was blended with the 30 v/o SiC whiskers. This mixture was compounded with a binder system identified in a GTE proprietary binder study as enhancing flow properties in injection molding. The combination gave excellent flow properties. Subsequent tests showed that both the new binder system and the revised powder particle size distribution contributed to the enhanced flow. The revised formulation now provides injection molding feedstock with comparable flow properties to the monolithic PY6 Si_3N_4 material, enabling the use of whisker-containing material for complex rotor fabrication trials. Sufficient material will be compounded with the new binder system and new powder to injection mold several PY6 Si_3N_4 AGT-5 gasifier rotors containing 30 v/o SiC whiskers. The molding of this material is scheduled for early 1990, with an evaluation of the densification distortion observed for the whisker-containing PY6 rotors to be made in March 1990.

3.2.4 Corning

Objective/Approach

Efforts at Corning, Inc, continue for the purpose of developing a reliable, low cost, extruded ceramic regenerator disk capable of operating at RPD conditions. Initial effort has been focused on a segmented disk formed from multiple extruded pieces cemented together. During 1989 Corning developed an extrusion process for an ultra-low expansion aluminum silicate (AS) rectangular ceramic regenerator matrix which can be scaled to make cemented modular disks. Initially, small 4 x 6 x 7.6 cm (1.5 x 2.4 x 3.0 in.) AS samples were provided to Allison for determination of characteristic properties and thermal cyclic performance. These samples were later expanded to include lower cost magnesium aluminum silicate (MAS) pieces having lower expansion and reduced porosity characteristics than previously available in this material.

Accomplishments/Results

- delivered samples of extruded AS and MAS matrix for Allison testing

Discussion

Corning designed and produced an extrusion die, developed the batch preparation, extrusion, firing, leaching, and refiring processes for an AS matrix with 202 cells/cm^2 (1300 cells/$in.^2$) of rectangular shape with 2:1 aspect ratio and 0.13 mm (0.0053 in.) wall thickness. Samples were delivered to Allison for thermal cyclic tests in December 1989. Cross-corner compressive test results of interim AS samples are reported in subsection 4.2.4. Corning also supplied samples of a 26% porous, reduced thermal expansion MAS made with the same die. The MAS had 147 cells/cm^2 (950 cells/$in.^2$), 0.12 mm (0.0047 in.) thick long walls and 0.15 mm (0.0059 in.) thick short walls. The lower MAS cell count was due to less firing shrinkage. Cyclic thermal testing for both materials simulating engine acceleration-deceleration cycles will be conducted early in 1990 to determine material characteristics and strength retention.

3.2.5 Garrett Ceramic Components

Objective/Approach

A technical development effort with Garrett Ceramic Components Division (GCCD) was initiated in December 1988. The objective of this activity is to develop and deliver engine-quality silicon nitride AGT-5 gasifier turbine rotors for test and evaluation. GCCD is tailoring its pressure slip casting techniques and proprietary mold technology to develop and fabricate GN-10 Si_3N_4 rotors. In Phase I, subscale GN-10 Si_3N_4 rotors were produced to establish a processing and properties baseline for axial turbine rotors. In Phase II, the techniques developed in Phase I are being scaled-up to produce ful!-scale engine quality
GN-10 Si_3N_4 AGT-5 rotors.

Accomplishments/Results

- Casting parameters were established for pressure slip casting GN-l0 Si_3N_4 axial turbine rotors.
- HIPing parameters were developed for the rotors.
- Appropriate statistical process control (SPC) and inspection procedures were developed for the rotors.

Discussion

Phase I--Subscale 15-Bladed AGT-5 Rotor. Initial activities for the GN-10 Si_3N_4 axial turbine rotor fabrication were conducted using molds fabricated from an existing plastic AGT-5 rotor. These rotors were undersize by approximately 16%. The tooling and slip casting molds for two casting orientations (A--primary shaft down, B--primary shaft up) were completed and used for rotor fabrication. A total of 50 rotors were cast from 31 different mill batches.

The results determined from casting the configuration B subscale rotors are: (1) pressure casting time is approximately 6 hr; (2) slip casts fully, no gelling on top of shaft observed; (3) incomplete blade casting (two-thirds of required height); and (4) during mold removal, most of the blades become detached (break off) from the hub.

The blade filling and casting problems were found to be related to the mold configuration B (primary shaft up) and the casting speed and time. The use of this casting orientation was terminated when the configuration A tooling and molds were completed. All subsequent casting trials were conducted using the configuration A arrangement.

The results determined from casting the initial configuration A subscale rotors were: (1) pressure casting time is approximately 4 hr; (2) slip casts fully, no gelling on top of shaft observed; (3) fuller blade casting (three-fourths of required height); (4) during mold removal, some of the blades still become detached from the hub; and (5) hub cracking and shaft detachment were noted for several rotors.

These experiments showed that the blade, hub, and shaft casting rates were different for the two configurations. The different casting rates were a contributing factor to the cracks appearing in the hub and shaft sections. It was also a cause of blade detachment, since differential shrinkage of a portion of the rotor creates stresses that can generate cracks.

A number of experiments were conducted to isolate and eliminate the casting problems, with the end goal being the establishment of a standard casting procedure that yields rotors with a full complement of blades. The focus of these experiments has been to (1) equilibrate the casting rates in the blades and hub by changing the dewatering surfaces, (2) develop a better process for removing the rotor from the mold, (3) eliminate blade cracking, and (4) estimate rotor casting rates.

The results of these experiments have yielded: (1) modification of the shaft/hub/blades dewatering surfaces to ensure that the blades cast fully, blades remain attached to the hub, and casting and shrinkage cracks are minimized; (2) modification to the mold that reduces the stress applied to the hub/blade interface when the cast rotor is removed from the mold, thus eliminating stresses on the blades; and (3) the appearance of a correlation between slip viscosity and casting rate in which the viscosity appears to control the casting rate of this part geometry considerably more than anticipated.

Five rotors were glass encapsulated HIP densified and sectioned into test bars for strength determination. The strength characteristics of the rotor test bars are summarized in Table XXIX. The average room temperature strength was 693.2 MPa (100.5 ksi), with an average strength of 560.2 MPa (81.2

Table XXIX.
Strength characteristics of GCCD GN-10 Si_3N_4 rotor test bars.

Temperature--°C (°F)	Strength--MPa (ksi)	
25 (77)	693.2	(100.5)
1204 (2200)	560.2	(81.2)
1371 (2500)	384.8	(55.8)

ksi) recorded at 1204°C (2200°F) and 384.8 MPa (55.8 ksi) obtained at 1371°C (2500°F).

A total of five rotors were fabricated using this current standard mold and mold removal technique and received by Allison. Rotors from this initial fabrication effort have a minimum of 13 of 15 blades attached to the hub, the shaft attached to the hub, and a minimum of surface cracks. An example of these rotors is shown in Figure 123.

Phase II--Full-Scale AGT-5 Rotor Fabrication. The processing procedures and NDE techniques established in Phase I were used as the baseline for fabrication of full-scale 20 bladed AGT-5 gasifier turbine rotors. A total of 61 development rotors have been cast to date while a variety of casting parameters have been changed during the casting process. These experiments were designed to establish a standard casting procedure by which full-scale AGT-5 engine test-bed turbine rotors can be fabricated. Slip procedures have progressed through 15 revisions during rotor casting activities. An example of the initial full-scale rotor casting efforts is shown in Figure 124.

The major problem still present in the fabrication of engine quality rotors is the attainment of complete and defect-free blade trailing edges during the casting process. Typically, this region either did not cast fully or a series of spall lines were observed on the cast blade tip edges. It was determined from the earlier experimental castings of the full-scale AGT-5 rotor that the rotor geometry, pattern and mold quality, and casting technique all contributed to this problem. Additional experiments were performed to determine the causes of this problem and to develop the casting process required to fabricate engine quality rotors. Mold quality has been improved and the casting fixtures modified to eliminate problems associated with the partial blade casting and blade detachment. A series of rotors was cast with the modified procedures and defect-free blade trailing edges are now routinely obtained.

However, with the modified casting procedures a former problem, associated with many of the ear-

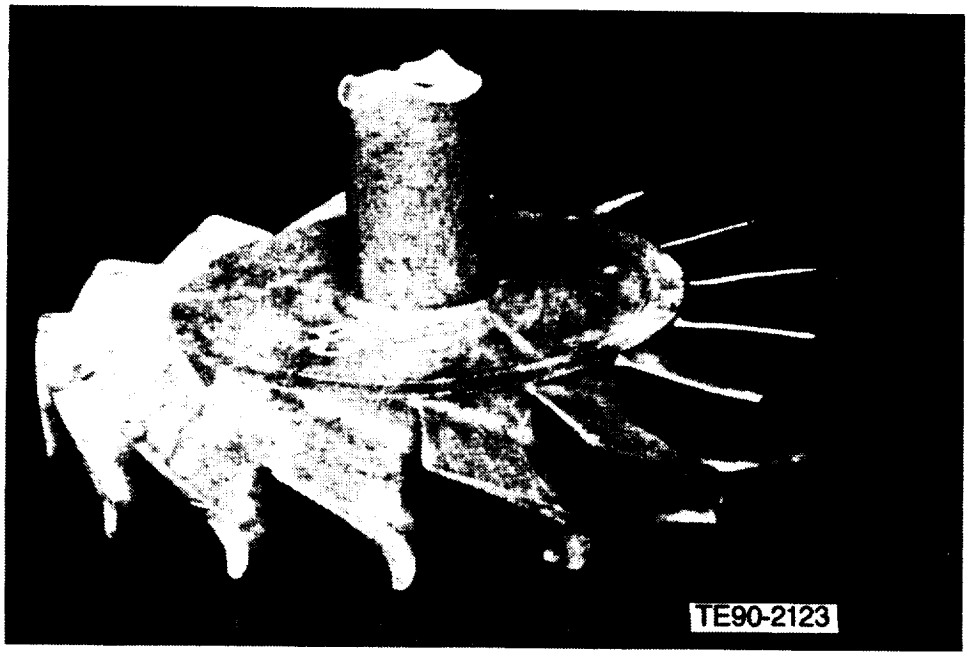

Figure 123. GCCD GN-10 Si_3N_4 subscale rotor.

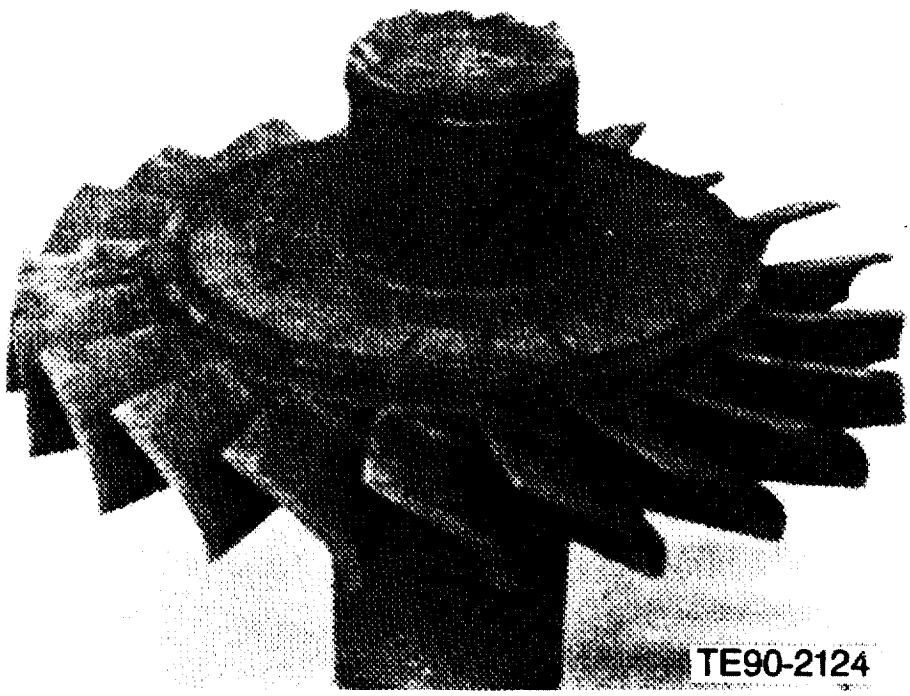

Figure 124. As-cast GCCD GN-10 Si_3N_4 full-scale rotor.

lier full-scale rotors, has resurfaced. This problem, involving the existence of one or two large internal hub cracks, is currently being addressed. The sharp, straight nature of these cracks suggests that they are not casting or drying cracks, but are cracks that develop during stresses generated during mold removal.

Two rotors, No. 53 and No. 55, have been glass encapsulation HIP densified. Rotor No. 53 was delivered to Allison in November 1989 for dimensional evaluation and will be sectioned into MOR test bars for strength determination. Rotor No. 55 is currently being machined into test specimens at GCCD. Room and high temperature flexural testing will be done to verify the properties of the Revision 15 rotor casting process.

Bisque machining of the two rotor hub faces and drilling of a hole in the primary shaft are required to obtain the required as-processed dimensions. Two rotors, No. 67 and No. 75, bisque machined and HIPed, are currently being dimensionally evaluated. Rotor No. 67 will be supplied to a machining vendor to perform final machining trials to assist in design of the proper fixturing for diamond grinding.

3.2.6 Ceramics Process Systems

Objective/Approach

A development program with Ceramics Process Systems (CPS) was initiated in April 1989 for development and fabrication of gasifier turbine vane platforms. The platforms will be fabricated using the Quickset (CPS patented process) injection molding process for CM200 sialon material. The configuration incorporates a center section with approximately the same cross section as the gasifier turbine rotor; this center section will be machined out to provide test specimens for material characterization activities. The vane pockets will be molded integrally with the vane platform, eliminating the requirement for ultrasonic machining.

Accomplishments/Results

- The vane platform tool was designed and fabricated.
- Initial Quickset injection molding of vane platforms was conducted.
- Characterization of the CM200 sialon material was conducted.

Discussion

The effort with CPS has concentrated on the development and fabrication of Quickset injection molded gasifier vane platforms. Although the program began in April, the vane platform design was not fully definitized until August 1989. This configuration, shown in Figure 125, incorporates a center section with approximately the same cross section as the gasifier turbine rotor. The injection molding tool was ordered in August 1989 and was delivered in October.

While the final vane platform configuration was being determined, a developmental vane platform tool (PD-1) was designed and fabricated during the months of July and August. This tool has the same overall geometry as the engine configuration vane platform but lacks the vane pockets. Process engineering was conducted using the PD-1 tool, with initial vane platform molding trials in September. Over 30 PD-1 vane platforms were Quickset injection molded and sintered to full density. Radiographic and visual inspections of the components revealed no cracks or voids. Recent efforts have focused on initiating a development process specification and procedure for vane platform molding, as well as investigating the microstructural uniformity and dimensional control and variation.

The engine configuration vane platform molding tool (VSP-2) was received by CPS in October. From approximately 50 moldings, 20 VSP-2 platforms were processed through the Quickset process and were sintered. Mold qualification was evaluated for: (1) proper mold filling during injection, (2) proper evacuation of air from the tooling during injection, (3) lack of molding textures resulting from nonuniform mold filling, and (4) lack of part distortion and cracking due to demolding. The tool dimensions met the specifications.

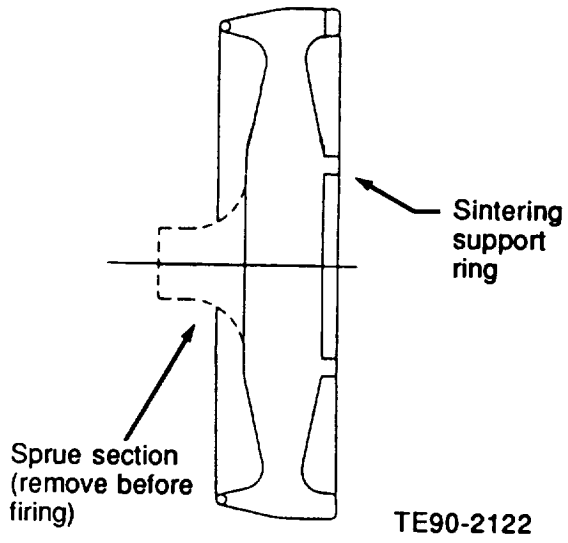

Figure 125. CPS vane platform configuration.

Visual and internal sectioning of the as-molded parts indicated good quality, with no evidence of molding textures or demolding defects and a uniform internal microstructure. However, numerous indications were visible on the components after both the drying and sintering operations. Small swirl textures on the platform surface were observed near the sprue area. A more gradual taper was placed on the sprue insert resulting in the elimination of the swirls. Molding textures were observed to vary as a function of mold temperature and injection pressure and were not directly related to the tool configuration.

The molded vane platforms showed no indication of deformation or cracking after demolding. However, initial drying studies showed significant cracking at the base of each vane pocket. The VSP-2 tooling alignment was remeasured to determine if the pocket cracking was due to poor insert tracking during withdrawal of the tool. The insert tracking met specification; however, there was concern about trapping solids in the vane insert mechanism. To remedy this concern, the tool was hard coated with a nonwetting coating which should prevent solids penetration into the insert track and eliminate binding of the insert withdrawal mechanism.

Characterization of the CM200 sialon material is being conducted concurrently with the component fabrication development efforts. Microstructural evaluation and mechanical property determinations were carried out on CM200 test bars cut from PD-1 hub sections. The flexural strength results are summarized in Table XXX. Both pressureless sintered and sintered/annealed test bars were evaluated. The average strengths of the sintered test bars measured 741.9 MPa (107.6 ksi), 529.5 MPa (76.8 ksi), 352.3 MPa (51.1 ksi), and 353.7 MPa (51.3 ksi) at temperatures of 25°C (77°F), 1200°C (2192°F), 1300°C (2372°F), and 1371°C (2500°F), respectively. At temperatures above 1200°C (2192°F), the sintered-only flexural strengths exhibited a significant decrease due to the amorphous grain boundary phase in the CM200 mate-

Table XXX.
Flexural strength of CPS CM200 sialon.

Temperature--°C (°F)	Strength, MPa (ksi)	
	Sintered	Sintered/annealed
Room	741.9 (107.6)	630.2 (91.4)
1200 (2192)	529.5 (76.8)	515.7 (74.8)
1300 (2372)	352.3 (51.1)	519.2 (75.3)
1371 (2500)	353.7 (51.3)	430.9 (62.5)

rial. Efforts in the postsintering annealing step have concentrated on heat treatment operations intended to result in recrystallization of the grain boundary phases to provide additional strength retention at elevated temperatures. The current annealing operation resulted in average strengths of 630.2 MPa (91.4 ksi), 515.7 MPa (74.8 ksi), 519.2 MPa (75.3 ksi), and 430.9 MPa (62.5 ksi) at temperatures of 25°C (77°F), 1200°C (2192°F), 1300°C (2372°F) and 1371°C (2500°F), respectively. Additional efforts are continuing to provide further improvements in high temperature strength and oxidation resistance.

Microstructural evaluation of the CM200 sialon material is also being conducted at the Oak Ridge National Laboratory (ORNL) High Temperature Materials Laboratory (HTML). High temperature X-ray diffraction, differential scanning calorimetry, differential thermal analysis, transmission electron microscopy, and energy dispersive spectroscopy analysis methods are being employed to characterize the CM200 material and to provide a baseline standard for use in evaluating subsequent material/process iterations.

IV. COMPONENT RIG DEVELOPMENT AND TEST

4.2 COMPONENT RIG TESTING

The objective of this activity is to develop the necessary test procedures and to conduct rig testing of the ATTAP development ceramic components and assemblies. All ceramic components are rig proof tested prior to AGT-5 test-bed engine testing. Rig tests of the ceramic components are generally conducted with more instrumentation than normally available within a test-bed engine. Critical data provided by rig testing are used in the development and verification of the ceramic design methodology. Currently two component rigs, the hot gasifier rig and the regenerator cyclic sample rig, are being utilized.

4.2.3 Turbine Rotor Rig Test

4.2.3.3 Hot Gasifier Rig Test

Objective/Approach. Hot gasifier rig testing is used to screen/proof test and evaluate structural ceramic components (namely combustors, gasifier turbine components, and regenerators) prior to introduction into the AGT-5 test-bed engine(s). The rig has build-time, accessibility, instrumentation, and cost benefit advantages compared to the full engine test-bed. The rig has also been designed to simulate the engine environment so that ceramic components are subjected to nearly the same operating conditions as if they were installed within the test-bed engine. Developmental rig evaluation is continuing until domestic ceramic components become available for testing.

Accomplishments/Results.

- accumulated 401 hr of test time with ceramic rotors
- retired a ceramic rotor in engine-ready condition after 364.9 test hours (engine and rig)
- accumulated 348.6 test hr on a second ceramic rotor without failure
- attained 1204°C (2200°F) at 100% N_1 (gasifier speed)
- successfully tested ceramic rotor/ceramic shroud assembly
- evaluated bearing system designs for heat rejection to oil
- measured critical rig component surface temperatures
- designed and implemented new air inlet system

Discussion

Ceramic Rotor Design Evaluation and Rig Development. Four hundred and one hours of rig testing of two ceramic gasifier turbine rotor designs (15- and 20-blade) have been accumulated on four different rotors during the second year of ATTAP as outlined in Table XXXI. Evaluation of these rotor designs added valuable information to the program by verifying design parameters and FOD-survivability, as well as by providing material evaluation in components. These rotors simultaneously served as workhorse components for rig shakedown and development to high temperature capability. The original 15-blade-design rotor (background data to ATTAP) is of Kyocera's SN250M Si_3N_4,

Table XXXI.
Gasifier rig accumulated test time.

Rotor S/N	No. of blades	Material	Hours on test	Remarks
5K8	15	SN250M	34.9	Not heat treated. 364.9 hr total (330 hr previously accumulated on engine test-bed)
5K12	15	SN252	11.5	
5K22	20	SN252	348.6	
5K24	20	SN252	5.8	

while the other three rotors are of Kyocera's SN252 Si_3N_4. A 15-blade-design rotor (5K8) was run in an engine for 330 hr prior to being transferred to the hot gasifier rig. During engine testing, some of which was unattended for extended periods, the rotor was run to 75% N_1 and 1885°F. It also successfully ingested combustor-produced hard carbon and metal chips from a deteriorating combustor dome during its first 40 hr of operation. Only minimal rotor damage was sustained: a small chip at the trailing edge tip of one blade. After being transferred to the hot gasifier rig, the rotor incurred a rub after 8 hr of testing due to a power interruption to the rig's oil pump. The rotor was not damaged. Maximum running conditions in the hot gasifier rig were 90% N_1 and 989°C (1812°F). The rotor was "retired" in engine-ready condition with 364.9 total test hours so that evaluation of the 20-blade rotor design could commence.

A 20-blade-design rotor (5K22) was operated (with a metal rotor shroud) for a total of 348.6 hr in the gasifier rig, including 840 starts. During the first 34 hr of test, the rotor sustained fracture damage on 13 of the 20 airfoils (minor chips in blade leading edge tips), as a consequence of either the failure of a particle containment screen or a tip rub. Analysis of these results is presented in subsection 3.1.3. The rotor was inspected and returned to service without blending of the chips. During the balance of the testing, the rotor successfully ingested insulation broken away from the engine block and metal chips from a deteriorating combustor dome. No additional damage was sustained and the rotor is in engine-ready condition. Maximum test conditions were 100% N_1 and 1204°C (2200°F). Remarkably, this design/component sustained multiple distress conditions in service and maintained overall structural integrity.

Development hardware for the gasifier rotor consisting of a hybrid metal/ceramic nozzle assembly, as shown in Figure 126, was designed to withstand 1204°C (2200°F) turbine inlet temperature while maintaining tip clearances approaching those which would occur in an all-ceramic gasifier stage. During initial testing of this hybrid assembly, the 15-blade-design rotor (5K12) rubbed the ceramic shroud at 82% N_1. Inspection revealed no visible or measurable damage to the ceramic components. The only evidence of a rub was a shiny band on the shroud at the wheel blade tip location. A mislocated bearing caused an unstable operating condition which allowed the rotor to rub the shroud. The problem was corrected and the gasifier rig was operated at 1204°C (2200°F) and 100% N_1. Turbine inlet temperature as a function of gasifier speed is illustrated in Figure 127. Multiple curves repre-

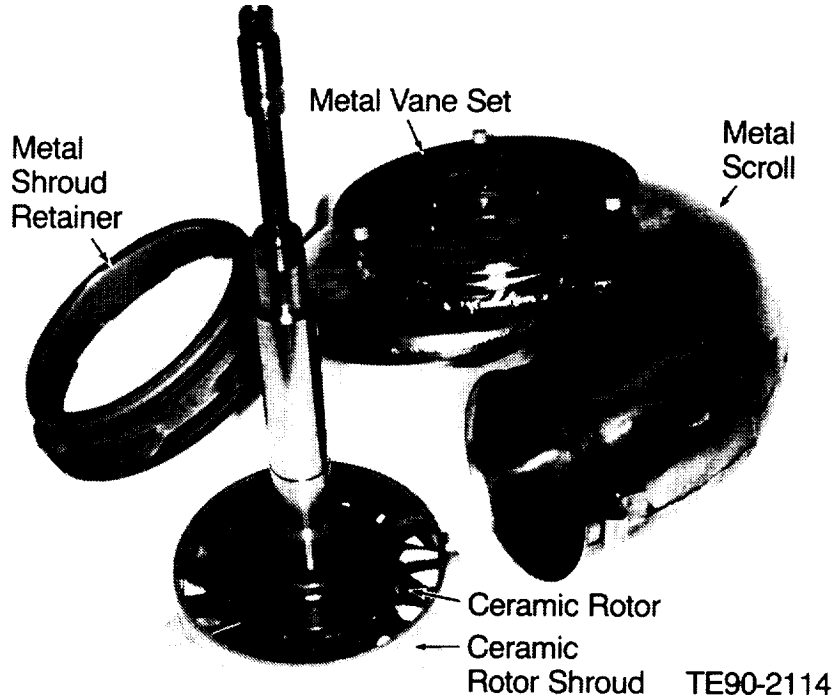

Figure 126. Hybrid metal/ceramic gasifier turbine hot flow-path components.

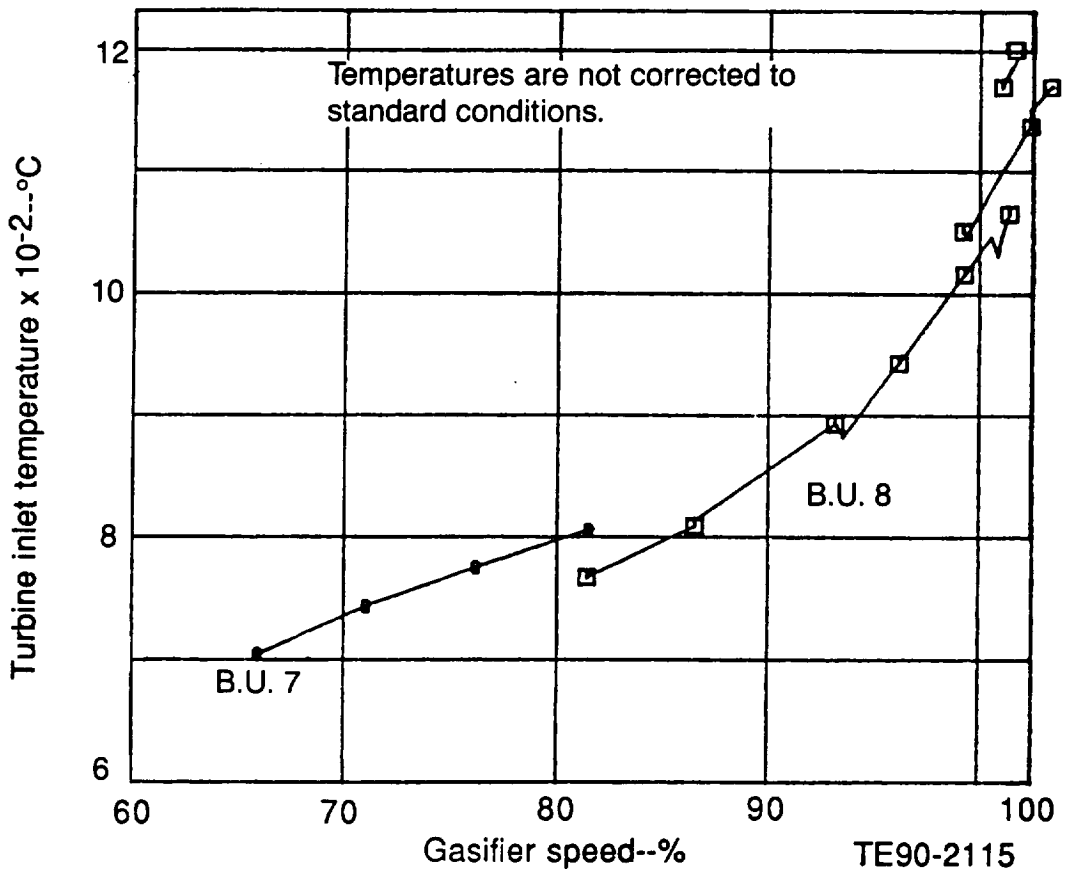

Figure 127. Turbine inlet temperature as a function of gasifier speed for rig testing using ceramic rotor/shroud.

senting various combinations of different gasifier speeds and levels of inlet throttling are depicted. A total of 5.5 hr was accumulated with this particular rotor/shroud combination. An additional 5.8 hr were accumulated with another rotor (20-blade-design, 5K24) and shroud combination without incident during evaluation of bearing designs and measurement of critical rig component surface temperatures. Total time accumulated (rig plus engine) on the above ceramic rotors was 730.8 hr; a maximum turbine inlet temperature of 1204°C (2200°F) was achieved.

Oil and Component Temperatures in the Gasifier Environment. Two different bearing cartridge designs were tested to determine the amount of heat rejection to the lubricating oil. One of the designs utilized a "shrink fit" bearing cartridge and the other an insertable cartridge that also included a thermocouple (T/C) installed to measure the bore temperature. Results of both bearing cartridge design tests are presented in Figure 128. Peak TIT with the new insertable cartridge was 1143°C (2089°F) while the original design was evaluated at a level of 1075°C (1967°F). Shaft mechanical speed throughout both tests was approximately 100% design speed. The tests indicated that the older design has the better ability to conduct heat away from the oil. Oil temperature rise at the same TIT is 34°C less while oil discharge temperature is reduced a similar amount with the old design as compared to results obtained using the new design. The modifications (larger annulus) to the insertable cartridge were not entirely nonbeneficial, however, as there was no evidence of excessive oil or material temperatures. The bearing housing temperature near the new bearing, as measured by the T/C, was relatively low. Increased oil temperatures are not considered desirable, however, so additional development of this design is required.

Some component surface temperatures have also been measured. The locations in which thermal data were acquired are indicated in Figure 129. The three temperatures of primary interest are the scroll/nozzle flange temperature, the bearing housing temperature (T7R5), and the scroll/nozzle ring

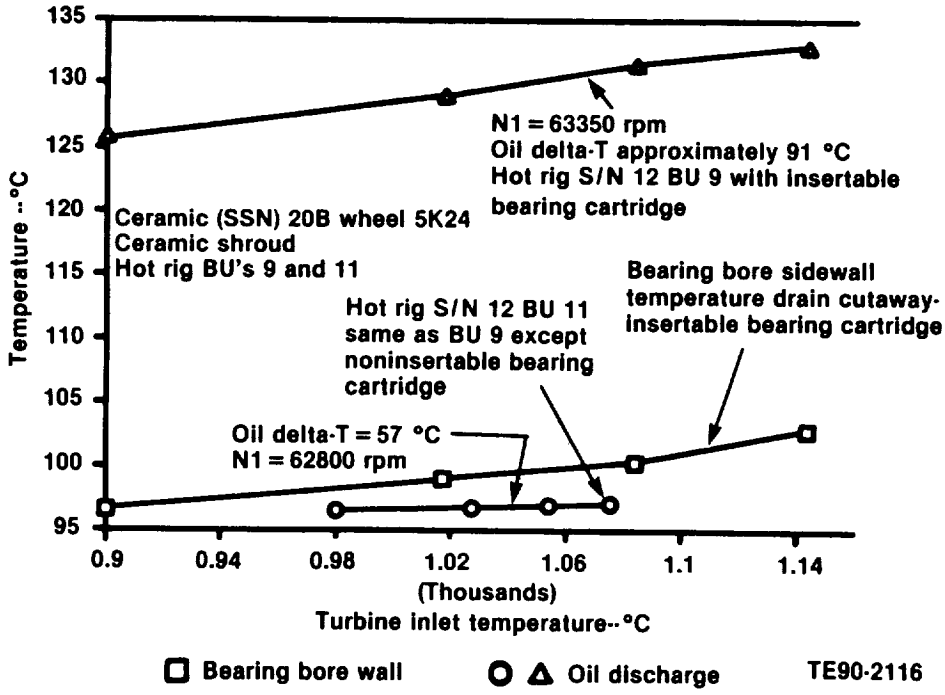

Figure 128. AGT-5 gasifier rig bearing oil drain and bore temperatures.

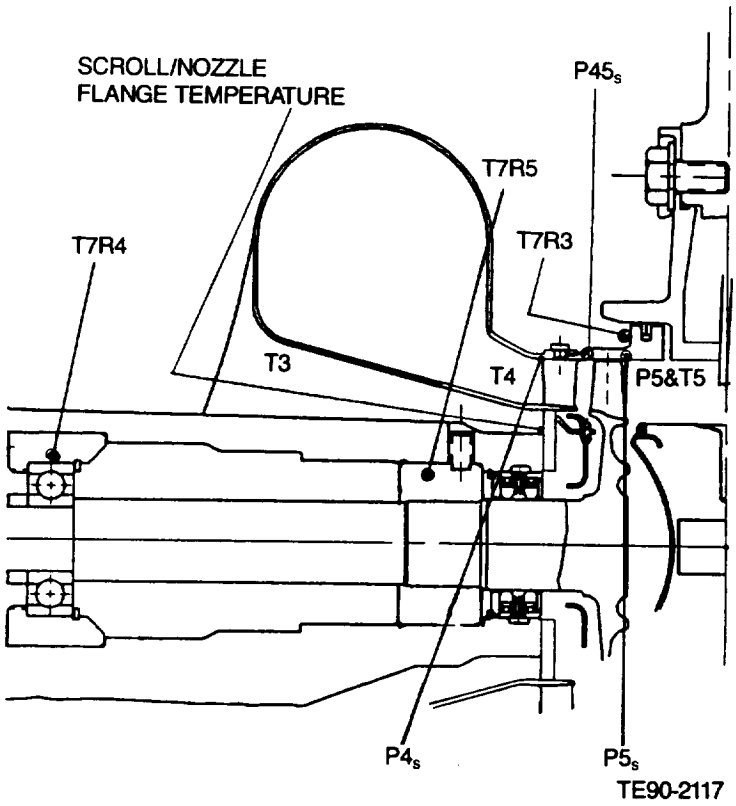

Figure 129. Gasifier rig instrumentation locations--partial.

groove flange temperature (T7R3). The nozzle flange temperature as a function of TIT is illustrated in Figure 130. At the indicated rate of temperature rise, this area should remain relatively cool at 1371°C. Bearing carrier and scroll/nozzle ring groove flange temperatures as functions of TIT are presented in Figure 131. The bearing carrier temperature is virtually the same as the oil drain temperature. The scroll/nozzle flange temperature is affected by both the burner inlet temperature (T_3) and the hotter TIT. The flange temperature appears to operate at a temperature level increased above that of the burner inlet temperature by 30% of the differential between TIT and T_3.

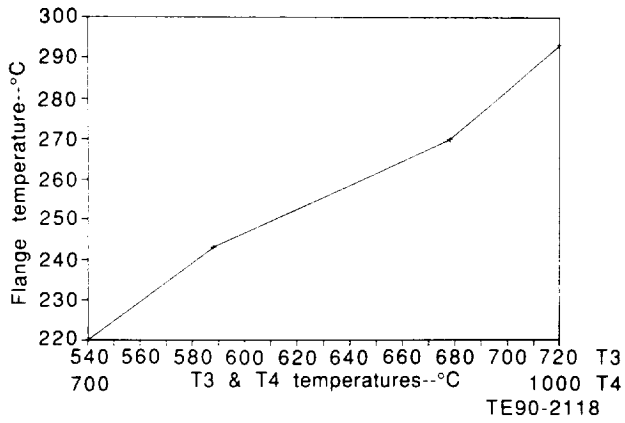

Figure 130. Gasifier scroll/nozzle flange temperature as a function of TIT.

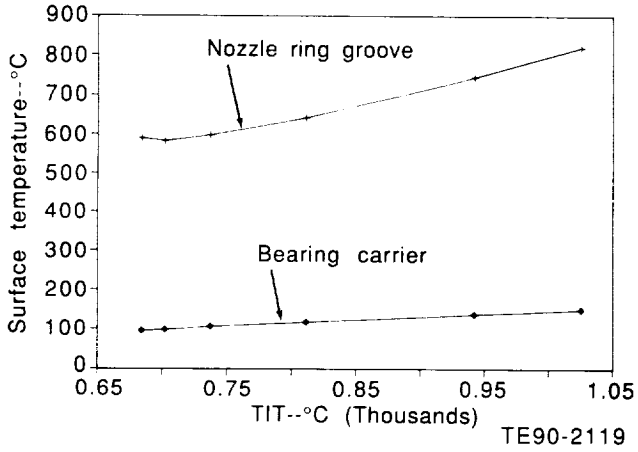

Figure 131. Gasifier scroll/nozzle ring groove and bearing carrier temperatures as a function of TIT.

Air Inlet System. The original air intake system for the gasifier hot rig utilized an axial inlet as illustrated in Figure 132. To better simulate engine start-up thermal gradients with the rig, the rig intake system was redesigned. The new design, as presented in Figure 133, starts the rig exactly like the engine, but uses a vertical air entry. This system is now fully functional.

4.2.4 Regenerator Rig Test

Objective/Approach

The objective of this activity is to evaluate candidate ceramic and metal regenerator matrix samples by characterizing the effects of cyclic thermal exposure on these materials/structures. Characteristics are thus determined both initially and after exposures. A burner rig is used to simulate engine acceleration/deceleration thermal cycles. Candidate metal matrices are assessed for oxidation, cracking, and distortion. Ceramic matrices are assessed for loss of strength.

Accomplishments/Results

- an acceptable simulation of engine full throttle acceleration-deceleration thermal cycles was achieved
- an Fe20Cr5Al-Ce catalytic converter metal alloy was found to have excessive oxidation, cracking, and deformation after only 4,000 of 10,000 required cycles
- a Haynes 214 nickel base metal alloy was judged to have tolerable oxidation, cracking, and distortion after the required 10,000 cycles
- NGK-Locke MAS ceramic matrix was determined to have lost all flexural strength in bars cut from the hot face, after 10,000 thermal cycles
- Corning extruded rectangular AS ceramic matrix was determined to have initial cross-corner compressive strength of 1.35 MPa (196 psi) (average of four samples), before thermal exposure

Discussion

Thermal Cycle Definition and Damage Mechanisms. A gas burner rig was used to simulate engine full throttle acceleration-deceleration cycles on 4 x 6 x 7.6 cm (1.5 x 2.4 x 3.0 in.) regenerator

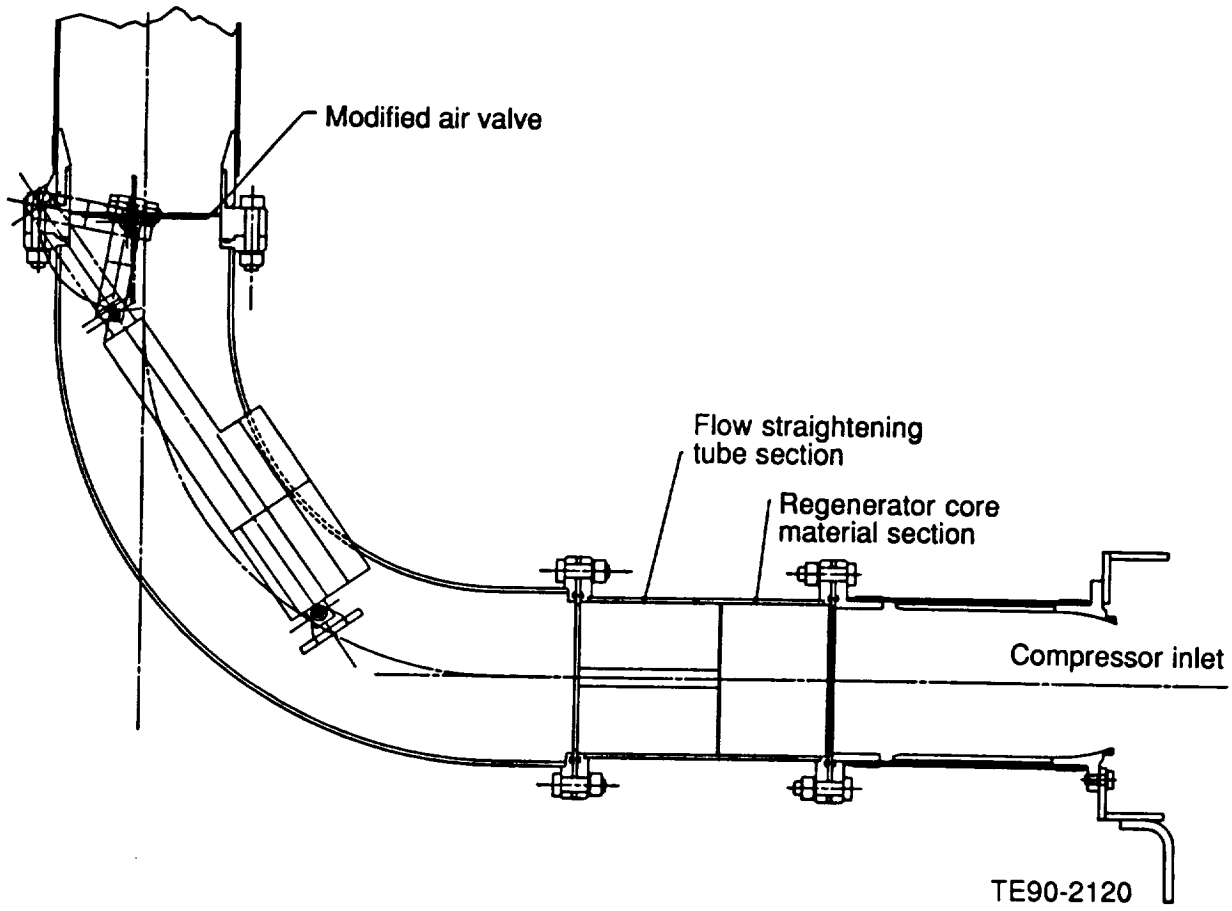

Figure 132. Original inlet throttling system--AGT-5 hot gasifier rig.

matrix samples. This rig is operated at higher mass flow per unit area than the actual regenerator in order to achieve required response rates, so a heat transfer model was used to calculate a commensurate reduction in peak temperature so that matrix hot face response would be very close to that in an engine. The resulting gas temperature schedule is as follows:

- peak temperature--1110°C (2030°F)
- full power temperature--977°C (1790°F)
- idle period--13.5 sec
- peak temperature spike width--1.4 sec
- full power period --5.0 sec, 9000 cycles
  --20.0 sec, 1000 cycles

Allison has previously shown that thermal cyclic exposure is the most life limiting condition for both metal and ceramic regenerator matrix materials. Cyclic oxidation of metal and cyclic crack growth of ceramics were previously identified as the damage mechanisms. Current testing has revealed thermal fatigue and distortion to also be metal damage mechanisms. Cracking and distortion damage have always been evident, but were not recognized to be separate from oxidation damage until highly oxidation resistant Haynes 214 was tested.

Fe20Cr5Al-Ce Converter Alloy Cyclic Test Results. Testing of this candidate was terminated after 4000 cycles due to severe hot face distortion and cracking. The material was also partially oxidized. Heat transfer performance would be considered unsatisfactory due to extreme distortion (Figure 134). About 80% of the cells have cracks extending 0.6 to 1.2 cm (1/4 in. to 1/2 in.) deep into the side of the cell formed by the slightly corrugated separator strip while 10% have similar cracks in the wall formed by the more deeply corrugated strip.

Flexure in the slight corrugations of the separator strip caused by the cyclic thermal gradients is apparently causing thermal fatigue in the convolutions. The separator convolutions are necessary to

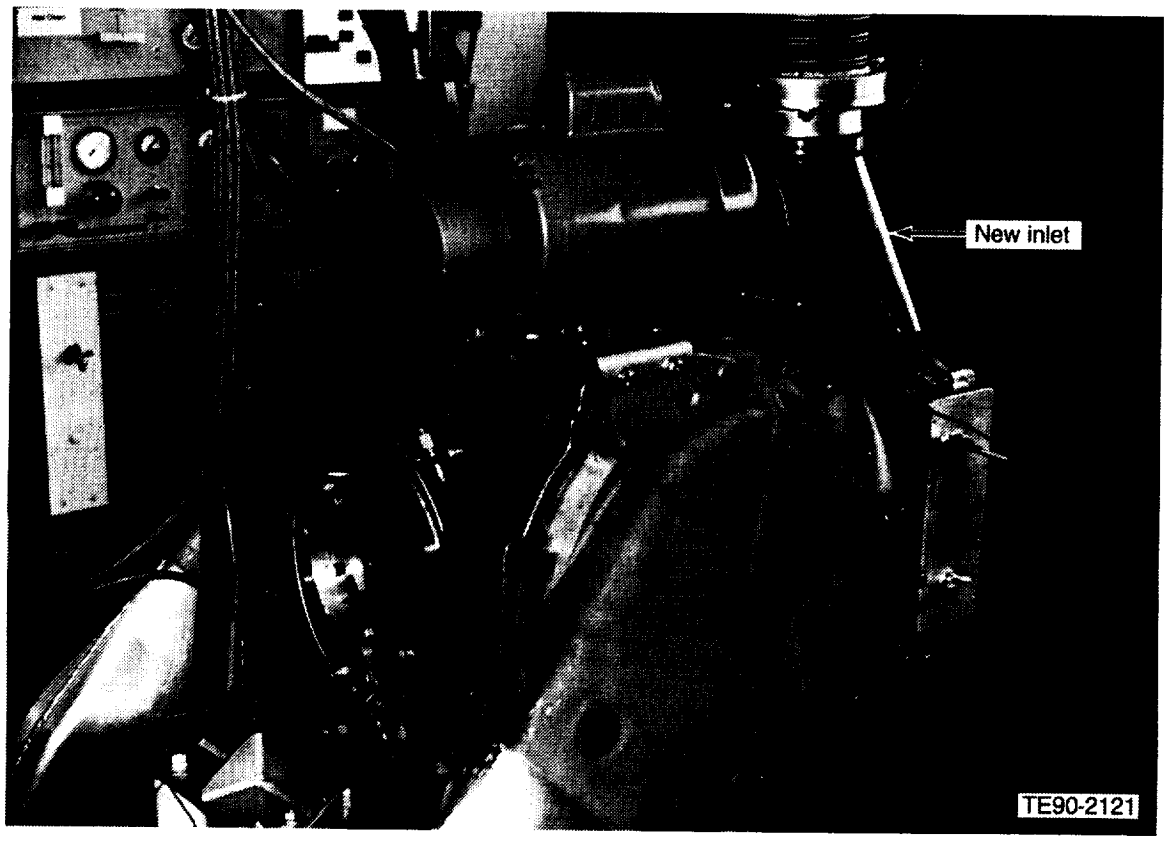

Figure 133. Hot gasifier rig with modified engine intake system.

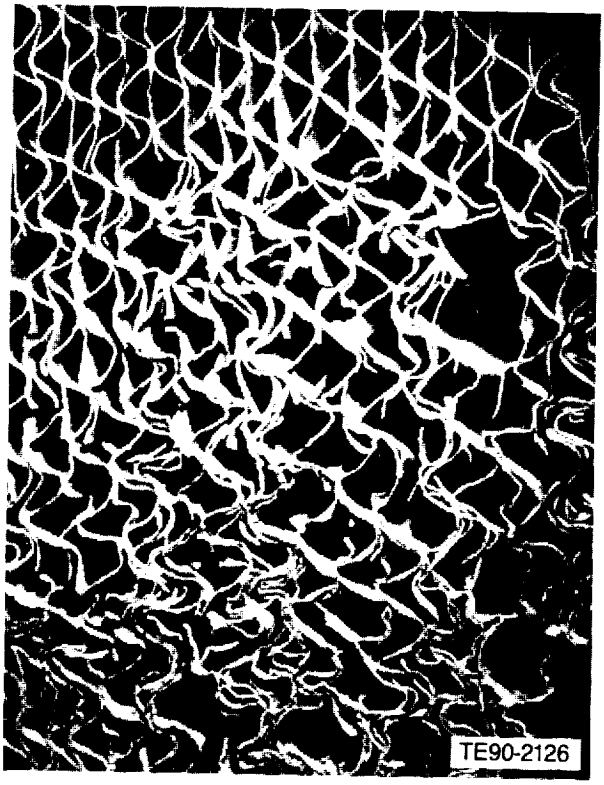

Figure 134. Fe20Cr5Al-Ce converter alloy after 4000 thermal cycles.

absorb high differential expansion during steady-state regenerator operation.

About half of the wall leading edges, in the area of high distortion, are oxidized through their full thickness and inward for a depth approximately equal to the thickness (refer to Figure 135). This oxidized material flaked away when lightly probed, while adjacent material remained ductile. The wall surfaces showed evidence of oxide spalling; some walls were reduced to half their original thickness. Spalling was evident to about 1 cm (0.4 in.) depth. These results show that the hot strength and oxidation resistance of this alloy are not adequate.

Haynes 214 Alloy Cyclic Test Results. Inspection of this matrix sample after 9000 cycles showed minor distortion and extensive cracking, but negligible oxidation (see Figure 136). This amount of distortion would not prevent satisfactory operation; however, a material with higher hot strength would be desirable. Haynes 230 and Hastelloy S are considered good candidates. About 60% of the cells have a crack in the wall formed by the flat strips, while about 10% have cracks in the hex strip. This

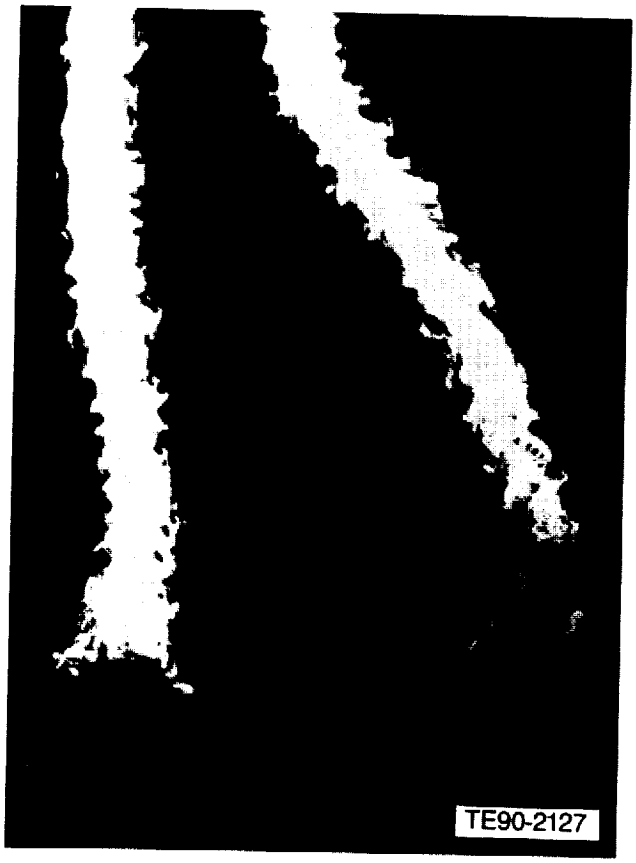

Figure 135. Typical Fe20Cr5Al-Ce converter alloy leading edges after 4000 thermal cycles.

hexagonal matrix was used for expediency and is not advocated for regenerators. An additional 1000 cycles were tested with dwell time at full power increased from 5 sec to 20 sec, typical of vehicle use. Visual distortion, cracking, and oxidation increased slightly more than that pictured at 9000 cycles. Photomicrographs have been made which show that most walls are oxidized to a depth of 0.5 mil. Even with typical 2 mil stock, this leaves enough sound material to ensure that the disk surface would not be rubbed away by seals, limiting disk life as has occurred in the past. Distortion and cracks, which were seen to extend 1/2 in. deep in the flow direction, are considered tolerable.

Hastelloy S and Haynes 230, which have three times the strength of Haynes 214 but two and six times the oxidation rate, respectively, will also be rig evaluated.

NGK MAS Ceramic Matrix Cyclic Test Results. A sample of NGK extruded rectangular "modified" MAS (magnesium aluminum silicate) regenerator matrix has been tested for MOR 4 point bend

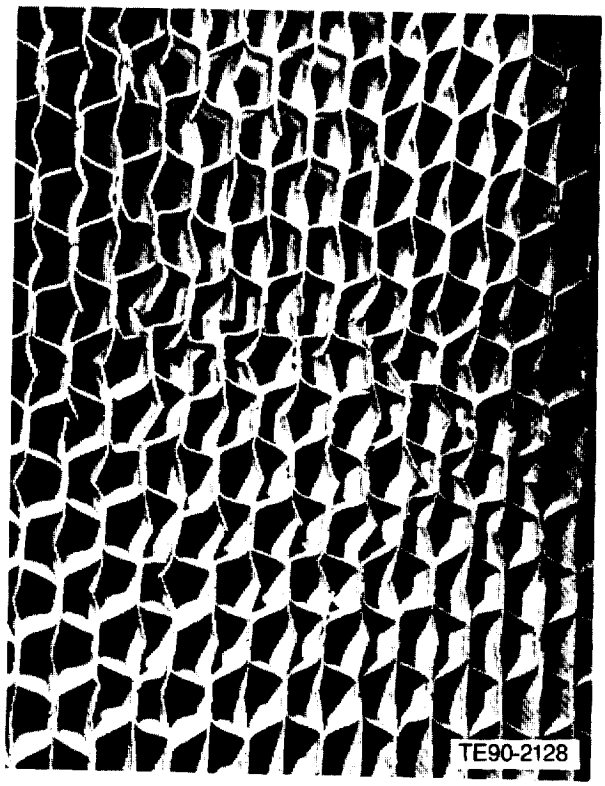

Figure 136. Haynes 214 alloy hot face after 9000 thermal cycles.

strength following exposure to 10,000 simulated full throttle acceleration-deceleration thermal cycles. Three 1.3 cm^2 (1/2 $in.^2$) test bars cut from the hot face show almost complete loss of strength. Two of the three fell apart before testing, one during machining and one during measuring. Three bars from the second 1/2 in. layer retained only one-third of their original strength. Progressive loss is indicated through the fourth layer (see Figure 137). The cold face retained only 63% of the original strength which probably resulted from temperature gradients near the cold face. This cold face strength loss probably would not occur in an actual engine. In the actual engine environment, where heat transfer takes place, the cold face never exceeds about 316°C (600°F). In the rig simulation, the cold face comes up to the full 982°C (1800°F) temperature because of the lack of heat transfer.

With the near complete loss of hot face strength, the NGK material would appear risky for engine endurance tests. However, it is possible that hot face cracks would not progress to catastrophic failure or result in prohibitive erosion from seal rubbing. It is worth noting that an earlier (1983) version of NGK MAS also lost all hot face strength

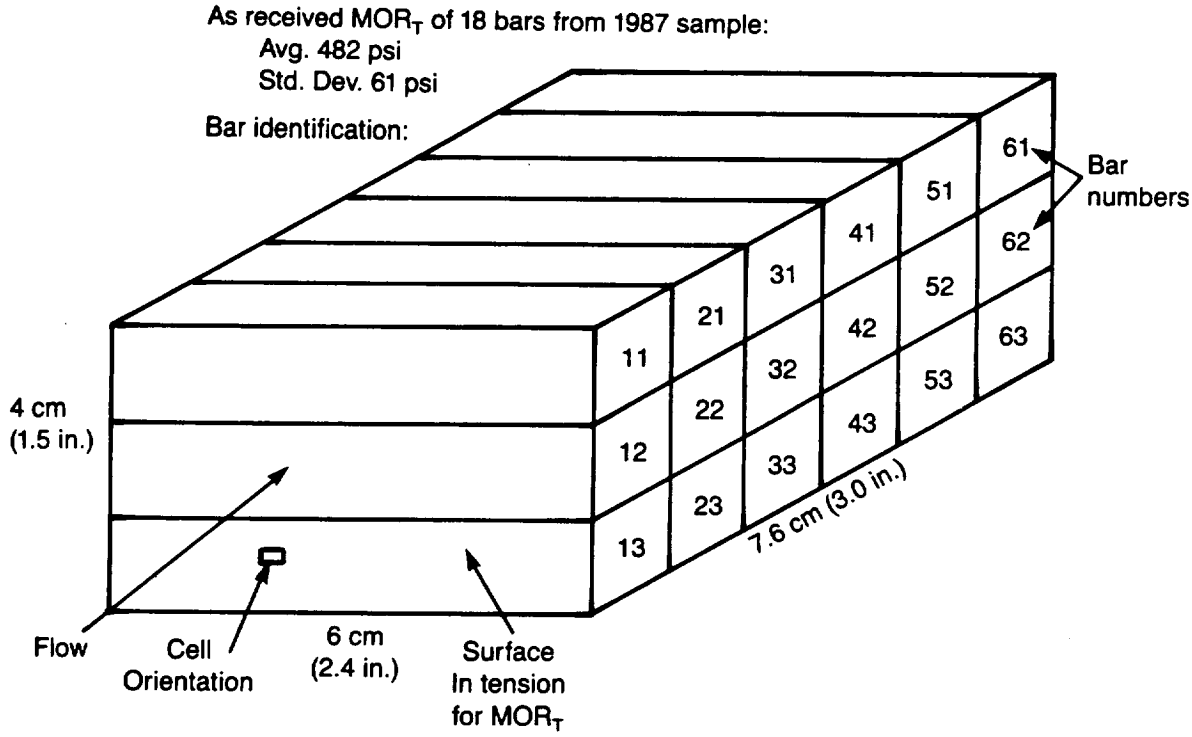

Bar No.	MOR Strength MPa	Psi	Notes
11	0.16	22.6	Hot face—fell apart, assumed load
12	0.15	21.8	Hot face—fell apart, assumed load
13	0.22	31.9	Hot face
21	0.57	82.9	
22	1.56	226.8	
23	1.27	183.9	
31	2.85	413.0	
32	3.11	451.1	
33	2.71	393.4	
41	3.07	444.8	
42	3.14	455.3	
43	3.04	441.1	
51	3.45	500.3	
52	3.44	498.9	
53	3.35	486.6	
61	2.03	294.0	Cold face—also affected
62	2.42	351.4	Cold face—also affected
63	2.05	297.3	Cold face—also affected

TE90-2125

Figure 137. NGK MAS regenerator matrix MOR strength following 10,000 full throttle thermal cycles.

when exposed to a simulated AGT-404 engine cycle, whereas Corning AS material lost only 43% of its strength after 10,000 cycles. To date, SEM examination has not been able to characterize or identify the damage; this effort continues. In 1983, light micro-examination appeared to show surface cracks in AS.

Corning Aluminum Silicate Ceramic Matrix Compression Test Results. Interim samples of Corning extruded rectangular aluminum silicate regenerator matrix have been compression tested with diagonal cross-corner loading. Four samples had cross-corner strengths of 163, 200, 202, and 219 psi averaging 1.35 MPa (196 psi). Cross-corner strength is the lowest of all directions and is typically only one-half of the lowest strength in line with walls. These strengths are expected to be sufficient for appreciable engine operation but may prove marginal after strength loss due to long term cyclical exposure. These samples were produced for another application and have 1070 cells/in.^{2} with 0.0114 cm (4.5 mil) thick long walls and 0.0137 cm (5.4 mil) thick short walls in lieu of the current goal of 1300 cells/in.^{2} and 0.0112 cm (4.4 mil) walls.

V. PERFORMANCE AND DURABILITY TESTING--TEST-BED ENGINES

5.2 DURABILITY TESTING

The objective of this activity is to conduct test-bed engine fabrication and testing in order to verify those advancements in ceramic component technology that address the achievement of program performance and durability goals. Ceramic component designs and integrity are to be ultimately verified at maximum engine steady-state and cyclic durability conditions. As the ceramic component technology improves, the test-bed engines are being modified to allow operation up to Reference Powertrain Design (RPD) conditions. Test efforts continue to be conducted that develop and demonstrate the durability and reliability of the test-bed engines, as well as of the ceramic components and designs. Both long-term cyclic and steady-state tests are being performed. Cyclic tests simulate the GM automotive gas turbine driving cycle (refer to subsection 5.2.3.2) while steady-state tests are being performed at idle, cruise, and full-power conditions.

5.2.3 Test-Bed Engine Fabrication and Test

5.2.3.1 Test-Bed Engine Fabrication

Objective/Approach

Test-bed engine fabrication activities support all engine test activities through instrumentation, build, and repair where necessary (see subsection 5.2.3.2). New engine component fabrication activities support the design/development efforts to evolve the AGT-5 to a high temperature durability test-bed engine.

Accomplishments/Results

During 1989 the following test-bed activities were achieved:

- A substantial portion of the test-bed engine fabrication effort has been devoted to the development of procedures and techniques that improve the installed insulation product within the engine; the ceramic technology portion of this work is reported in subsection 3.2.2.
- A test-bed engine was assembled with a modified gearbox to evaluate gearbox vibration, in response to an earlier investigation indicating higher than desired noise in the midspeed range; the modified arrangement will be tested in January 1990.

Discussion

An investigation was undertaken into the source of gearbox noise. There was concern that the noise might be indicative of a potential durability problem that would compromise ceramic component testing. Analysis of the data suggested that the gear case cover should be stiffened. Steps are in progress to revise the gear case cover and subsequently evaluate its behavior.

5.2.3.2 Test-Bed Engine Testing

Objective/Approach

The objective of this activity is to perform shakedown durability testing of the AGT-5 durability test-bed engine, high temperature durability verification of the test-bed, and evaluation of ceramic hot flow path components and engine insulation. This is accomplished through operation using the General Motors' gas turbine durability schedule and conduction of tests at steady-state idle, cruise, and full-power conditions.

Accomplishments/Results

- The designated durability engine accumulated 359.5 hr, 226.9 of which were on the durability schedule.
- The durability dynamometer was automated for unattended durability schedule testing.
- The reason for previously unexplained engine power variations was determined.
- Engine oil flow rate was parametrically investigated.

Discussion

Durability Schedule. The durability test schedule (Figure 138) has been designed to subject the automotive gas turbine to conditions considered extreme compared to the most severe expected field use. Nineteen accelerations, 24 decelerations, 9 starts/stops, and a 9-minute soakback are included during a single 60-minute cycle. Engines subjected to 1000 hr of testing using this accelerated schedule experience wear and operational characteristics comparable to 100,000 miles of typical automotive

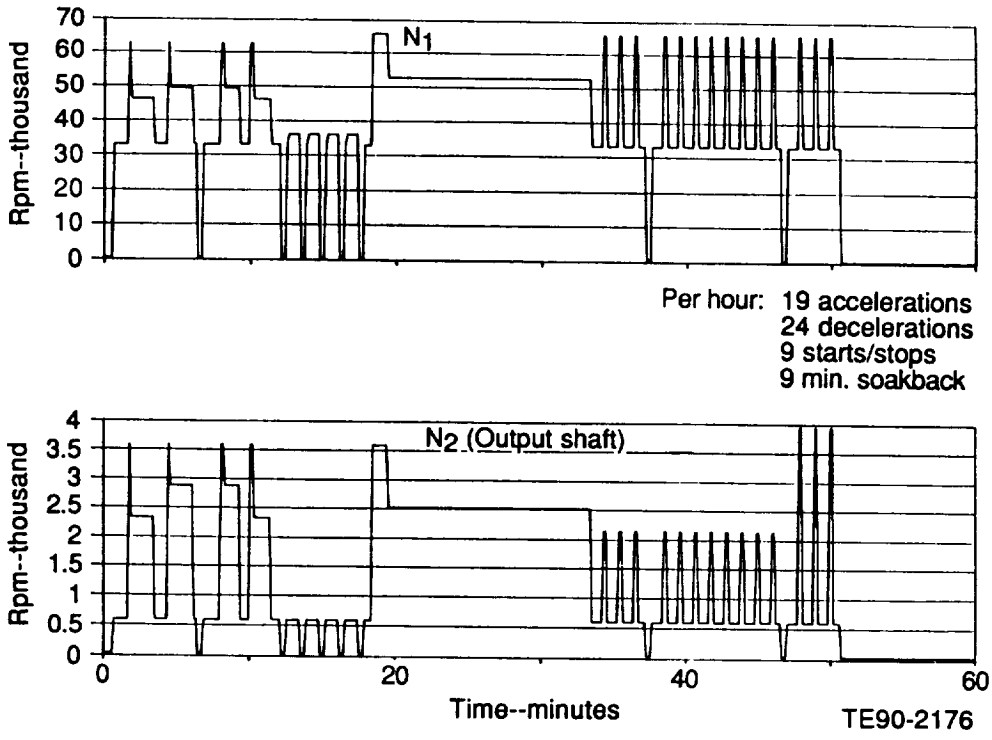

Figure 138. Durability test cycle for automotive gas turbine.

operation. The ATTAP goals are 100 hr of engine operation on this accelerated durability schedule in Year 4, and 300 hr in Year 5 (see Figure 1).

Gasifier and dynamometer (engine output) speeds are now controlled by the engine computer system, and with the addition of some test cell safety devices, unattended testing was demonstrated. This system uses the test cell data acquisition computer as the "command" for the engine computer. This overall system integrates engine speed and engine dynamometer load control. The benefit of this integration results in a synchronized test operation in which desired test data can be generated and recorded automatically at any point in the cycle.

Engine Airflow/Power Variation. A power check of the durability engine, utilizing an automotive intake system, indicated that both power and engine airflow were approximately 7-1/2% below design values. All previous airflow measurements used an axial, rather than an automotive intake. Appropriate calibration checks were made on all pressure transducers and thermocouples to ensure that the airflow computation was correct. Additionally, two ASME air nozzles were placed in series for redundant airflow measurement. The two airflow measurements were virtually identical verifying that airflow was indeed low. Various tests with the intake housing revealed that the filter orientation plays a major role in affecting engine airflow rate. This is thought to be due to the nonuniformity of paper folds in typical automotive filter elements, which can cause localized inlet pressure variation and promote nonuniformity of flow at the compressor inlet. Improved filter designs are being pursued with a supplier. It was thus confirmed that this power loss was not due to engine degradation, but rather to the inconsistency in the intake configuration.

Engine Oil Flow. A test-bed engine was installed in a dynamometer cell without an internal engine oil pump in order to run oil flow tests to determine desired actual engine oil flow rates. The engine was started and initially run at peak power points to establish baseline engine performance. Oil flow rates were then established at various pressures and temperatures (see Figure 139). These data will be utilized in making oil system modifications required by increased engine operating temperatures. Other engine test investigations included start-fuel schedule evaluations.

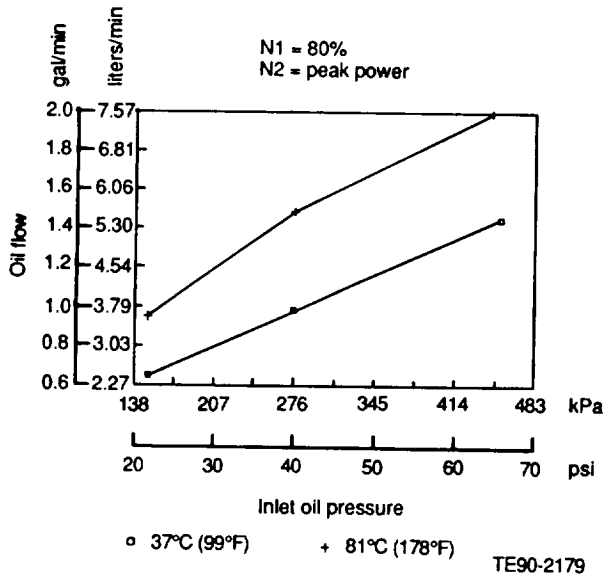

Figure 139. AGT-5 oil flow versus inlet oil pressure.

Engine Test Incident. Following 186.9 hr of test on the durability cycle, engine operation was discontinued due to excessive gearbox noise. Inspection revealed that a drive pulley nut had loosened. The engine was removed from the dynamometer and further inspection revealed that the loose nut allowed axial movement of a drive gear and shaft. During this axial movement the drive shaft came in contact with the first-stage reduction (bull) gear, thereby causing the excessive noise. The teeth on the high speed pinion gear were also chipped, apparently caused by secondary foreign object damage. An oily substance was also discovered in the gasifier housing compressor "pocket" and the gasifier diffuser back plate. An analysis of the substance revealed it to be engine lubricating oil, which had apparently leaked past the gasifier turbine carbon seal.

The engine was rebuilt and placed back on test. Total durability test hours increased to 226.9 hr; total engine test time now stands at 359.5 hr.

APPENDIX. TERMS AND DEFINITIONS

α	alpha
ACMC	Advanced Composite Materials Corporation
AES	Advanced Engineering Staff
AGT	automotive gas turbine/Advanced Gas Turbine
AS	aluminum silicate
ATTAP	Advanced Turbine Technology Applications Project
AVG	active variable geometry
BIT	burner inlet temperature
BOC	Buick, Oldsmobile, Cadillac
BOT	burner outlet temperature
BSFC	brake specific fuel consumption
BU	build
BVG	burner variable geometry
°C	degree centigrade
CBO	Carborundum
CCM	Contractors Coordination Meeting
cm	centimeter
CMC	ceramic matrix composite
CPS	Ceramics Process Systems
CTAHE	Ceramic Technology for Advanced Heat Engines
CVD	chemical vapor deposition
CVI	chemical vapor infiltration
CY	calendar year
DOE	Department of Energy
E	elastic modulus
ext	extruded
°F	degree Fahrenheit
FBN	fuel bound nitrogen
FCM	function control module
FE	fuel economy
FEM	finite element method
FOD	foreign object damage
FPI	fluorescent penetrant inspection
gal	gallon
GCCD	Garrett Ceramic Components Division of Allied-Signal Aerospace Company
GE	General Electric Company
gm	gram
GM	General Motors
GT	gasifier turbine
GTE	GTE Laboratories Inc
HIP	hot isostatic pressed
hp	horsepower
HTML	High Temperature Materials Laboratory
i.d.	inner diameter
$in.^2$	square inch
$in.^3$	cubic inch
IWC	inertia weight class
kg	kilogram
K_{IC}	fracture toughness
km	kilometer
kPa	kilopascal
ksi	kilopounds per square inch
kW	kilowatt
KYO	Kyocera America, Inc.
ℓ/L	liter
LAS	lithium aluminum silicate
LeRC	Lewis Research Center
m	Weibull modulus
MOR	modulus of rupture
N1	gasifier shaft speed, rpm
N2	power turbine shaft speed, rpm
NDE	nondestructive evaluation
NTC	Norton/TRW Ceramics
OCC	outer combustor case
o.d.	outer diameter
ORNL	Oak Ridge National Laboratory
POS	probability of survival
ppmw	parts per million by weight
psi	pounds per square inch
PSR	perfectly stirred reactor
RB	reaction bonded
RPD	reference powertrain design
rpm	revolutions per minute
RT	room temperature
SEM	scanning electron microscopy
SENB	single edge notched beam
SiC	silicon carbide
Si_3N_4	silicon nitride
SL	sea level
SMD	Sauter mean diameter
S/N	serial number
SPC	statistical process control
SS	steady-state
T/C	thermocouple
TEM	transmission electron microscope
THM125C	GM production automatic transmission

APPENDIX. TERMS AND DEFINITIONS (cont)

TIT	turbine inlet temperature
TVG	thermally actuated variable geometry
2-D	two-dimensional
v/o	volume fraction, percent
WOT	wide open throttle

1. Report No. NASA CR-187039	2. Government Accession No.	3. Recipient's Catalog No.
4. Title and Subtitle Advanced Turbine Technology Applications Project (ATTAP)-- 1989 Annual Report		5. Report Date 2 July 1990 6. Performing Organization Code
7. Author(s) Engineering Department, Allison Gas Turbine Division Advanced Engineering Staff, General Motors Technical Center		8. Performing Organization Report No. EDR 14585 10. Work Unit No.
9. Performing Organization Name and Address Allison Gas Turbine Division General Motors Corporation P.O. Box 420 Indianapolis, IN 46206-0420		11. Contract or Grant No. DEN 3-336 13. Type of Report and Period Covered Contractor Report January - December 1989
12. Sponsoring Agency Name and Address U.S. Department of Energy Conservation and Renewable Energy Office of Transportation Technologies		14. Sponsoring Agency Code DOE/NASA

15. Supplementary Notes
Annual Report, prepared under Interagency Agreement DE-A101-85CE50111.
Project Manager P. T. Kerwin, Propulsion Systems Division,
NASA Lewis Research Center, Cleveland, OH 44135

16. Abstract

ATTAP activities during the past year were highlighted by test-bed engine design and development activities; ceramic component design; materials and component characterization; ceramic component process development and fabrication; component rig testing; and test-bed engine fabrication and testing. Although substantial technical challenges remain, all areas exhibited progress. Test-bed engine design and development activity included engine mechanical design, power turbine flow-path design and mechanical layout, and engine system integration aimed at upgrading the AGT-5 from a 1038°C(1900°F) metal engine to a durable 1371°C(2500°F) structural ceramic component test-bed engine. ATTAP-defined ceramic and associated ceramic/metal component design activities completed include: the ceramic combustor body, the ceramic gasifier turbine static structure, the ceramic gasifier turbine rotor, the ceramic/metal power turbine static structure, and the ceramic power turbine rotors. The materials and component characterization efforts included the testing and evaluation of several candidate ceramic materials and components being developed for use in the ATTAP. Ceramic component process development and fabrication activities are being conducted for the gasifier turbine rotor, gasifier turbine vanes, gasifier turbine scroll, extruded regenerator disks, and thermal insulation. Component rig testing activities include the development of the necessary test procedures and conduction of rig testing of the ceramic components and assemblies. Four-hundred hours of hot gasifier rig test time have been accumulated with turbine inlet temperatures exceeding 1204°C(2200°F) at 100% design gasifier speed. A total of 348.6 test hr have been achieved on a single ceramic rotor without failure and a second ceramic rotor was retired in engine-ready condition at 364.9 test hr(330 hr of which were previously accumulated on an engine test-bed). Test-bed engine fabrication, testing, and development supported improvements in ceramic component technology that will permit the achievement of program performance and durability goals. The designated durability engine accumulated 359.3 hr of test time, 226.9 of which were on the General Motors gas turbine durability schedule.

17. Key Words (Suggested by Author(s)) automotive gas turbine, ceramic components, structural ceramics, engine configuration rotors, alternate propulsion systems, vehicular propulsion, alternate fuels, emissions, improved fuel economy	18. Distribution Statement Unclassified, unlimited		
19. Security Classif. (of this report) Unclassified	20. Security Classif. (of this page) Unclassified	21. No. of Pages 139	22. Price*

* For sale by the National Technical Information Service, Springfield, Virginia 22151